Research and Technology 1993

Annual Report of the Marshall Space Flight Center

NASA-TM-108420

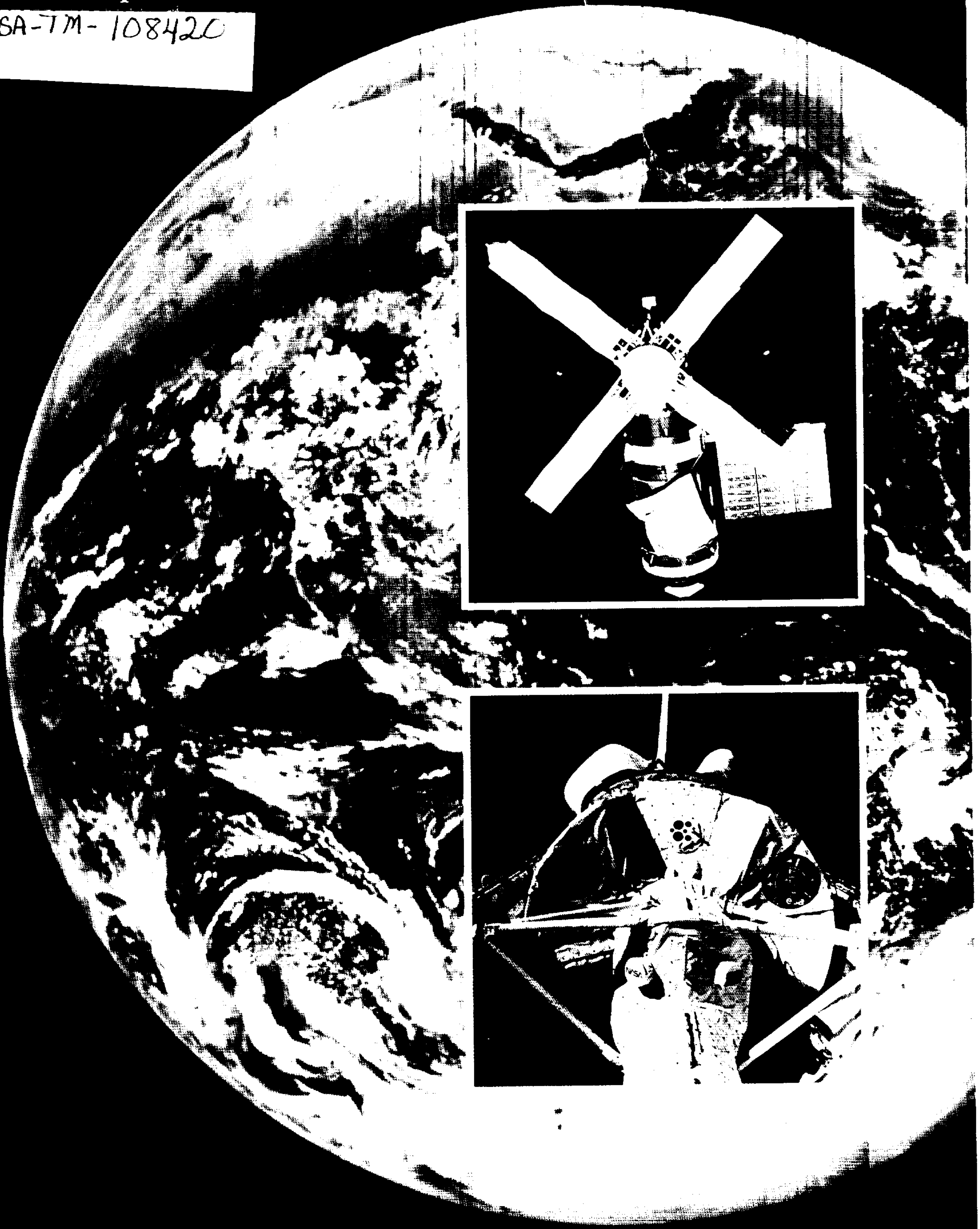

Salute to Skylab and Spacelab–Two Decades of Discovery

For further information regarding this report,
contact Dr. Gabriel R. Wallace, Director of the
Research and Technology Office, Mail Stop ER01,
Marshall Space Flight Center, AL 35812.
The telephone number is 205–544–4359.

NASA-TM-108420

230 p

Research and Technology 1993

Annual Report of the Marshall Space Flight Center

(NASA-TM-108420) RESEARCH AND TECHNOLOGY, 1993. SALUTE TO SKYLAB AND SPACELAB: TWO DECADES OF DISCOVERY Annual Report (NASA. Marshall Space Flight Center) 230 p

N95-10021

Unclas

H1/99 0013724

NASA TM–108420

National Aeronautics and
Space Administration

George C. Marshall Space Flight Center
Marshall Space Flight Center, Alabama 35812

Introduction

"...both leadership in technology and science and partnerships with other countries, those are the keys to our future as a people, to our standard of living, to our quality of life, as well as to our ability to continue the American tradition of exploring frontiers."

President Clinton
June 22, 1993

Twenty years ago, the challenge of putting a scientific laboratory into space led to the first Space Station—*Skylab.* Ten years ago, the first *reusable* space-based scientific laboratory—Spacelab—was launched aboard the Space Shuttle *Columbia.* On the anniversaries of these two highly successful missions, we are reminded of the numerous benefits that come from meeting such challenges. Both *Skylab* and Spacelab propelled the development of new technologies to overcome the limitations imposed by gravity and by space travel. In addition to spurring new innovations, our unique view from space has given us insights into the workings of our own planet—and our place in the cosmos—that otherwise would not have been possible. The Spacelab program continues to provide a workshop for new scientific investigation and information.

From its inception, the National Aeronautics and Space Administration has invested in technological developments that have led to improvements in life on Earth, in fields ranging from aviation and agriculture, to communications and computers, to medicine. Some recent technology transfer projects, as well as possible opportunities to work with MSFC resources, are highlighted in this book.

Research and Technology 1993: Annual Report of the Marshall Space Flight Center features articles by some of the scientists and engineers who help make programs such as *Skylab* and Spacelab come alive. The diverse work that has been accomplished over the past year continues the Center's tradition of technological innovation and scientific discovery and prepares us for whatever challenges the future may hold.

T. J. Lee

T.J. Lee
Director

Acknowledgments

The point of contact and coordinator at MSFC for this report is H.C. Stinson (ER41/205–544–7239). She was assisted by an editorial committee consisting of G.F. McDonough, C.R. Chappell, S.H. Morgan, W.C. Snoddy, and G.R. Wallace. Detailed editorial support and production assistance was provided by MSI, a Division of The Bionetics Corporation. The research and technology work at MSFC is a cooperative effort, however, due to space restrictions, it is impossible to list all those involved in the projects described in this report.

To assist the reader, the MSFC contact, office code, and telephone number are included at the beginning of each article. The sponsoring organization and university and commercial involvement are given at the end of each article. Please note that some sponsoring organizations have implemented name changes. An abbreviations and acronyms list, an alphabetical index of contacts, and an index of key words are presented at the end of this report.

Table of Contents

Space Physics

Astrophysics

Microgravity Science and Applications

Technology Programs

Avionics

Materials and Manufacturing Processes

Mission Operations

Propulsion and Fluid Management

Structures and Dynamics

Systems Analysis and Integration

Salute to Skylab and Spacelab

Two Decades of Discovery

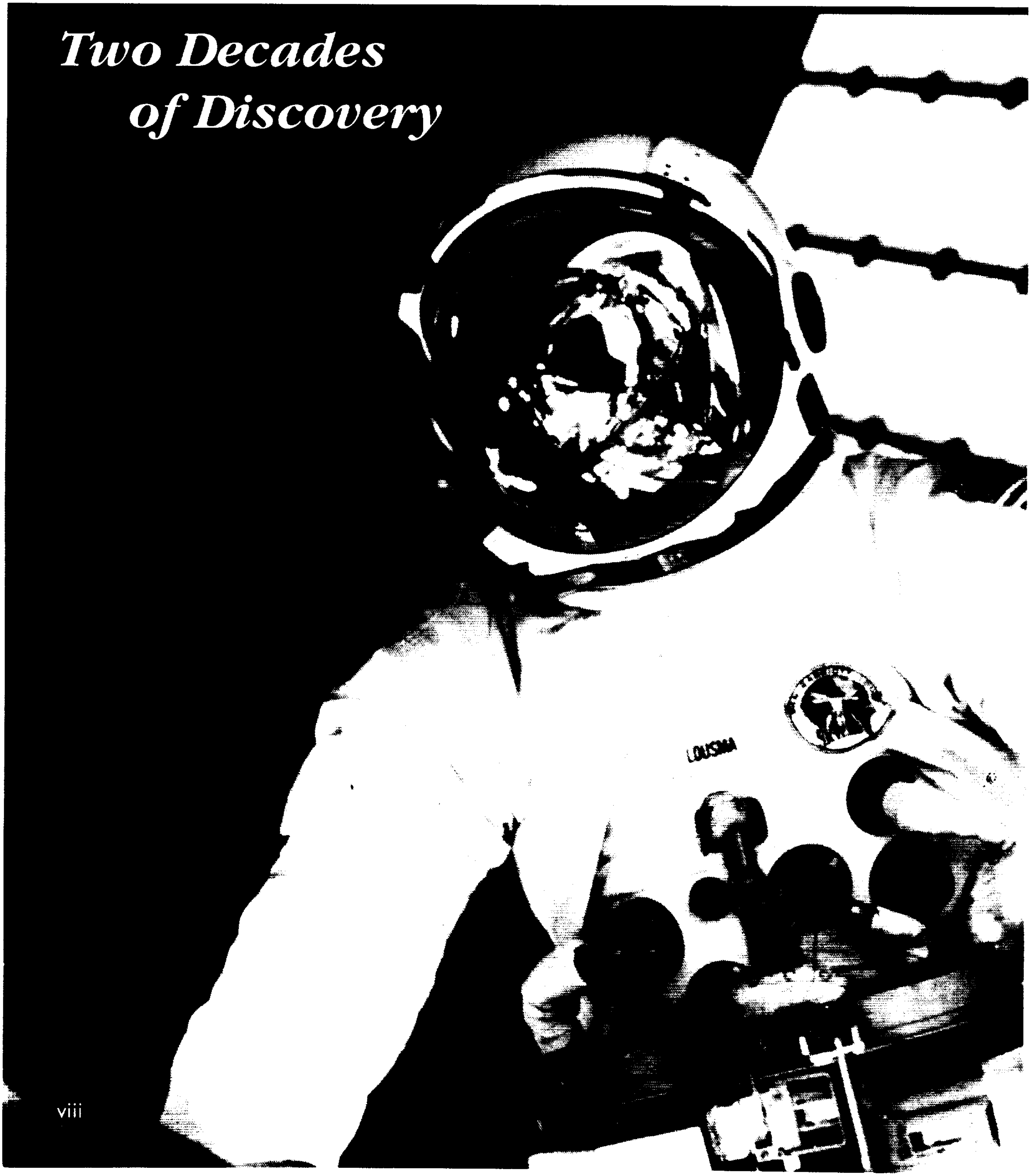

Since it was established in 1960, the roots of Marshall Space Flight Center's extensive research and technology base have been intertwined in the history of thousands of space-related projects and experiments. Skylab *and Spacelab, however, rank among its most successful programs. In 1993, the Marshall Center marked the twentieth anniversary of* Skylab *and the tenth anniversary of the first Spacelab mission, occasions to reflect on the significance of these two programs in the history of space flight.*

Astronaut Lousma looks homeward during a space walk outside *Skylab*, in orbit some 270 miles above Earth.

Skylab

America's First Space Station

The *Skylab* program objectives were to prove that humans could live and work in space for extended periods, and to expand knowledge of solar astronomy and Earth resources. *Skylab's* three different three-man crews spent a total of 171 days, 13 hours in Earth orbit, and performed more than 300 experiments.

The Marshall Center provided the four Saturn launch vehicles, directed many of the *Skylab* experiments, and developed all of the major *Skylab* components, including the *Skylab* workshop. Marshall worked closely with the prime contractor for the workshop unit to convert a Saturn IVB stage into a habitable module containing crew quarters and support systems, as well as some experiment area. Marshall Center employees built portions of the *Skylab* Apollo Telescope Mount in-house and worked closely with several contractors on a very precise attitude and pointing control system. This telescope became the first manned astronomical observatory designed for solar research from Earth orbit.

The Marshall Center was also closely involved in the design, development, and test activities for the *Skylab* airlock module. The module was attached to the forward end of the Skylab workshop and enabled crew members to make excursions outside the space station. In addition, Marshall Center workers designed and built the structure for the multiple docking adapter. The adapter, which was attached to the forward end of the airlock module, provided the docking port for the Apollo command and service module, the spacecraft that ferried each three-member crew from Earth to the space station.

The unmanned *Skylab* workshop/Apollo Telescope Mount combination was launched on May 14, 1973, by the Marshall-developed Saturn V—America's most powerful rocket. Unfortunately, trouble began approximately 63 seconds after the launch when a huge panel protecting the orbital workshop from micrometeoroids and solar radiation ripped off. Adding to the trouble, one of the solar arrays for providing power to the workshop was torn away, and a second array was only partially deployed.

All this meant one thing—the launch of the first *Skylab* crew, scheduled for May 15, would be delayed until methods could be devised to repair and salvage the workshop. Some troubleshooting teams at the Marshall Center and other NASA centers did not leave their posts for days. Finally, on May 25, the astronaut crew—prepared to implement NASA's plan to repair the workshop—was launched.

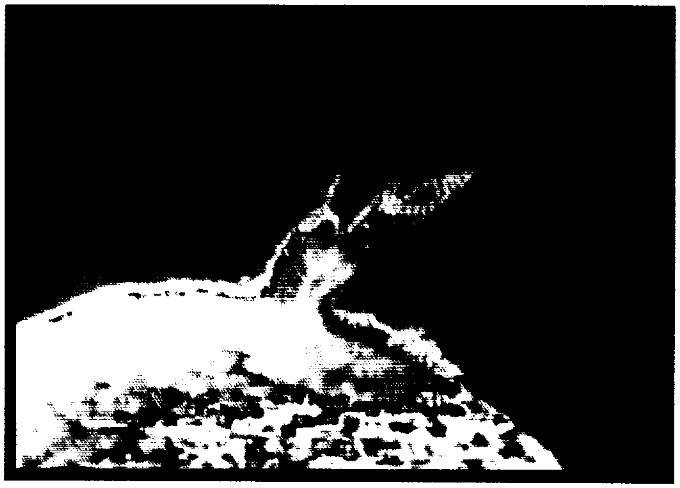

Skylab's telescopes logged 8½ months of solar observations, compared to less than 80 hours from all natural eclipses since 1839, when photographic records were begun.

As a result, the first *Skylab* mission was able to continue. The crew gathered data on some 80 percent of the planned solar experiments. They also achieved a major scientific accomplishment by monitoring a solar flare. They completed 11 of 14 planned Earth resources data runs and conducted a total of 16 medical experiments. The astronauts also gathered data from five student investigations before splashing down 28 days later, on June 22, 1973.

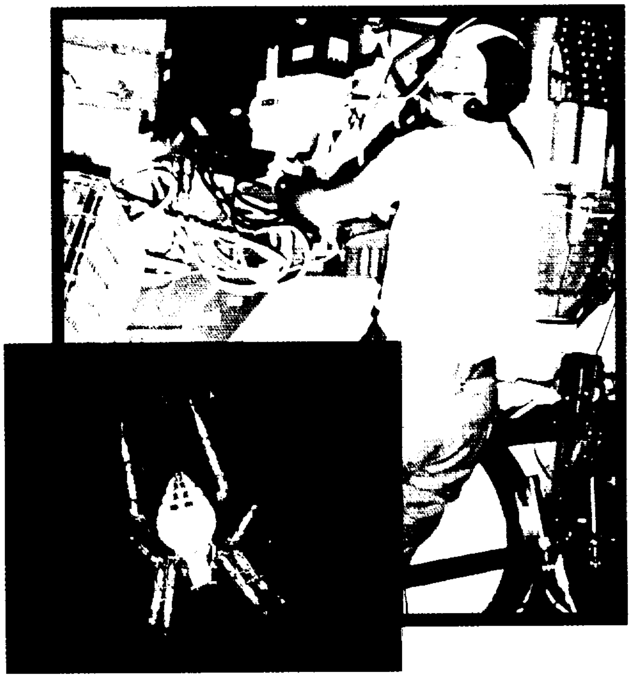

Astronaut Garriott operates a camera used for Earth observations. (Inset) Anita was one of the two spiders that flew as part of a student experiment investigating the role of gravity in web making.

The second manned *Skylab* crew was launched on July 28, 1973. By the tenth day, the crew was devoting about 19 hours a day to scientific experiments, but a week to 10 days later they were doing 27 to 30 hours of experiments each day. Although 26 Earth resources experiment passes had been planned, 39 were actually accomplished. In addition, some 206 hours of solar viewing had been planned, while 305 were logged. The medical experiments had included 327 planned runs, while 333 were accomplished. The mission also included the first orbital demonstration of astronaut-maneuvering equipment and a pair of common spiders, Arabella and Anita, were on board to determine their ability to spin webs without the influence of gravity, which they did once they grew accustomed to their new evironment. The second manned *Skylab* mission ended September 25, 1973, after 59 days in space.

A Saturn IB rocket carrying the third crew lifted off November 16, 1973. The astronauts continued the *Skylab* in-flight experiment program, including four extravehicular activities and the observation and documentation of the newly discovered Comet Kohoutek. The third crew also served as the source for important new medical data on how humans react to weightlessness in space. The mission ended after 84 days, on February 8, 1974, setting a new endurance record and reflecting our ability to live and work in space for extended periods of time.

Spacelab

A Short-Term Spaceborne Laboratory

As space shuttle development began at the Marshall Center in the 1970's, planners at the Center were studying ways to use the proposed new vehicle's capabilities for scientific research. Early studies at the Marshall Center had called for the development of a versatile, reusable laboratory facility. This facility would fit inside the payload bay of the shuttle orbiter and provide the crew of career astronauts (mission specialists) and members of the science community (payload specialists) with workbench space, power, computer support, and racks and storage for experiment equipment. The ninth flight of the shuttle, launched on November 28, 1983, carried Spacelab—a multiconfiguration spaceborne scientific laboratory—into orbit.

In 1970, the Marshall Center had requested proposals from industry for the preliminary design of a research and applications module as a way to provide versatile laboratory facilities for Earth-orbital research and applications work. In 1971, the Marshall Center began in-house studies on a laboratory called the Sortie Can, later renamed the Sortie Lab. The Sortie concept for Spacelab included a combination of habitable, pressurized modules in which scientists could conduct investigations and unpressurized pallets for instruments requiring direct exposure to space, such as telescopes.

In 1972, NASA began negotiations with the European Space Research Organization, the forerunner of the European Space Agency (ESA). This ultimately led to an agreement between NASA and ESA, with ESA assuming responsibility for funding, developing, and building Spacelab. Under this arrangement, Marshall Center did the feasibility and preliminary design work during the Sortie studies, and ESA did the engineering design and hardware development based on Marshall-defined requirements. Marshall, however, retained responsibility for technical and programmatic monitoring of Spacelab development activities, which involved 50 manufacturing firms in 10 European countries.

In addition to program management responsibilities, Marshall Center built related Spacelab flight components, including an optical window for scientific observations, and developed a pressurized transfer tunnel for passage of crew and equipment between the shuttle's orbiter cabin and the laboratory module, where astronauts and scientists could work in a shirt-sleeves environment.

Flight controllers and experiment scientisits direct Spacelab science activities from the Marshall Center.

The Marshall Center also was responsible for Spacelab's command-and-data-management subsystem and its high-data-rate multiplexer and recorder. In addition, a software development facility was established to develop and verify programs for Spacelab experiment components. Other contributions ranged from the development of ground support equipment to sophisticated scientific instruments.

The Spacelab program also required engineers and other specialists at the Marshall Center to perform systems analyses, design and develop integration hardware, oversee assembly and checkout, plan the flight timeline, conduct simulation and training exercises, and provide real-time support for the missions. Marshall's Payload Crew Training Complex became a training site for Spacelab mission specialists from the astronaut corps and payload specialists from the scientific community. Prior to the establishment of the Marshall Center Spacelab Mission Operations Control Center facility, Marshall mission managers monitored, controlled, and directed experiments aboard Spacelab from the Johnson Space Center.

The primary purpose of the first Spacelab mission was to demonstrate the scientific capability of the laboratory and to check the thousands of structural, mechanical, and electronic parts making up the laboratory. During the 10-day mission, the science crew conducted more than 70 separate investigations in life sciences, atmospheric physics, Earth observations, astronomy, solar physics, space plasma physics, and materials science and technology. Spacelab–1 was a truly international mission, with 14 countries participating.

Numerous Marshall-developed and managed experiments and investigations were on board. The Imaging Spectrometric Observatory was among the atmospheric and Earth observation experiments on Spacelab–1. It was designed to provide new insights into the varied reactions and energy transfer processes that occur in the Earth's environment. Another experiment, the Space Experiments with Particle Accelerators, was among the investigations in space plasma physics and was designed to carry out active and interactive experiments on and in the Earth's ionosphere and magnetosphere. Atmospheric Emission Photometric Imaging, another space plasma physics experiment, was used to observe faint optical emissions associated with natural and artificially induced phenomena in the upper atmosphere.

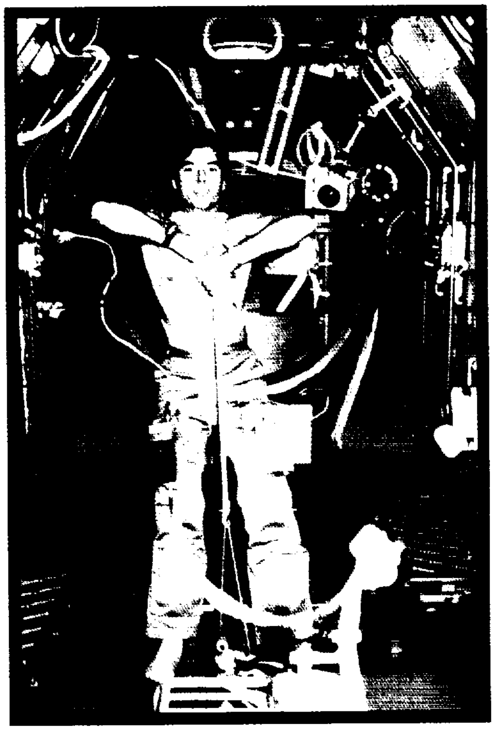

How the body reacts to weightlessness may provide clues to diseases on Earth. Here Spacelab–1 payload specialist Merbold exercises on orbit, while instruments measure his heart's performance.

Prior to the first Spacelab mission, the Far Ultraviolet Space Telescope (FAUST), a compact, wide-field-of-view instrument, had been used on rockets for brief astronomical observations. FAUST, however, was used on the first Spacelab mission to observe galaxies and quasars, and for joint observations with Spacelab–1 experiments. An investigation in materials science was called Tribological Experiments in Zero Gravity and was designed to observe wetting and spreading phenomena and fluid distribution patterns without the interference of gravity.

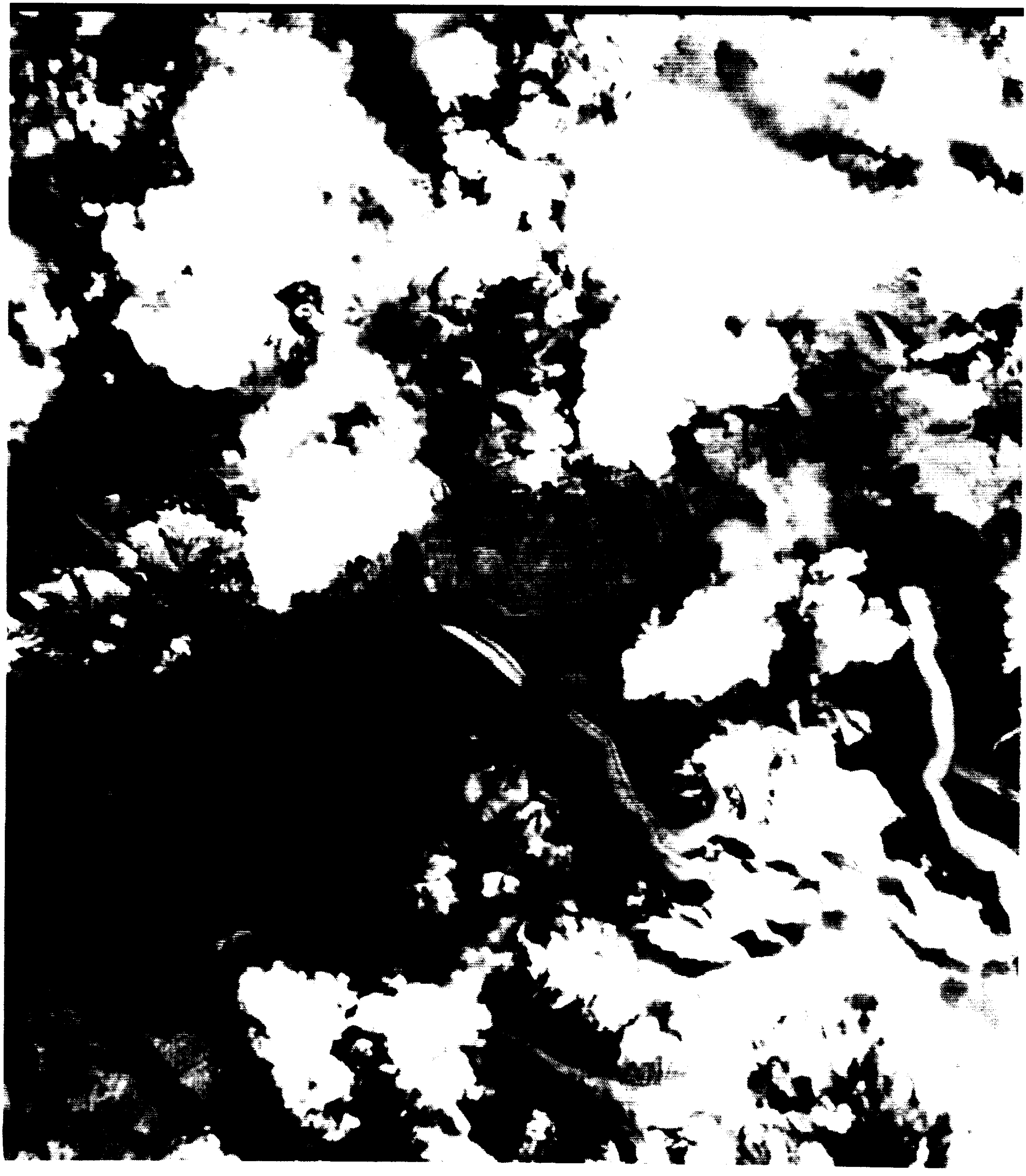

Both Skylab *and Spacelab–1 added new dimensions to the Marshall Center research and technology base. They left a legacy that opened up the field of scientific study in microgravity, where underlying physical properties and phenomena may be observed free from the masking effects of gravity. Information gained from Earth and celestial observations made from space have virtually rewritten textbooks and, in turn, opened up new fields of study.* Skylab *and Spacelab–1 helped identify and develop ideas and tools that would lead to improvements in research facilities in space, as well as contribute to the quality of life on Earth.*

Michael D. Wright/CN22
MSFC Historian
205-544-6840

■

A land of glaciers is one of countless images taken from space that have enhanced map making and navigation, assisted weather forecasting, and revealed natural resources on our planet.

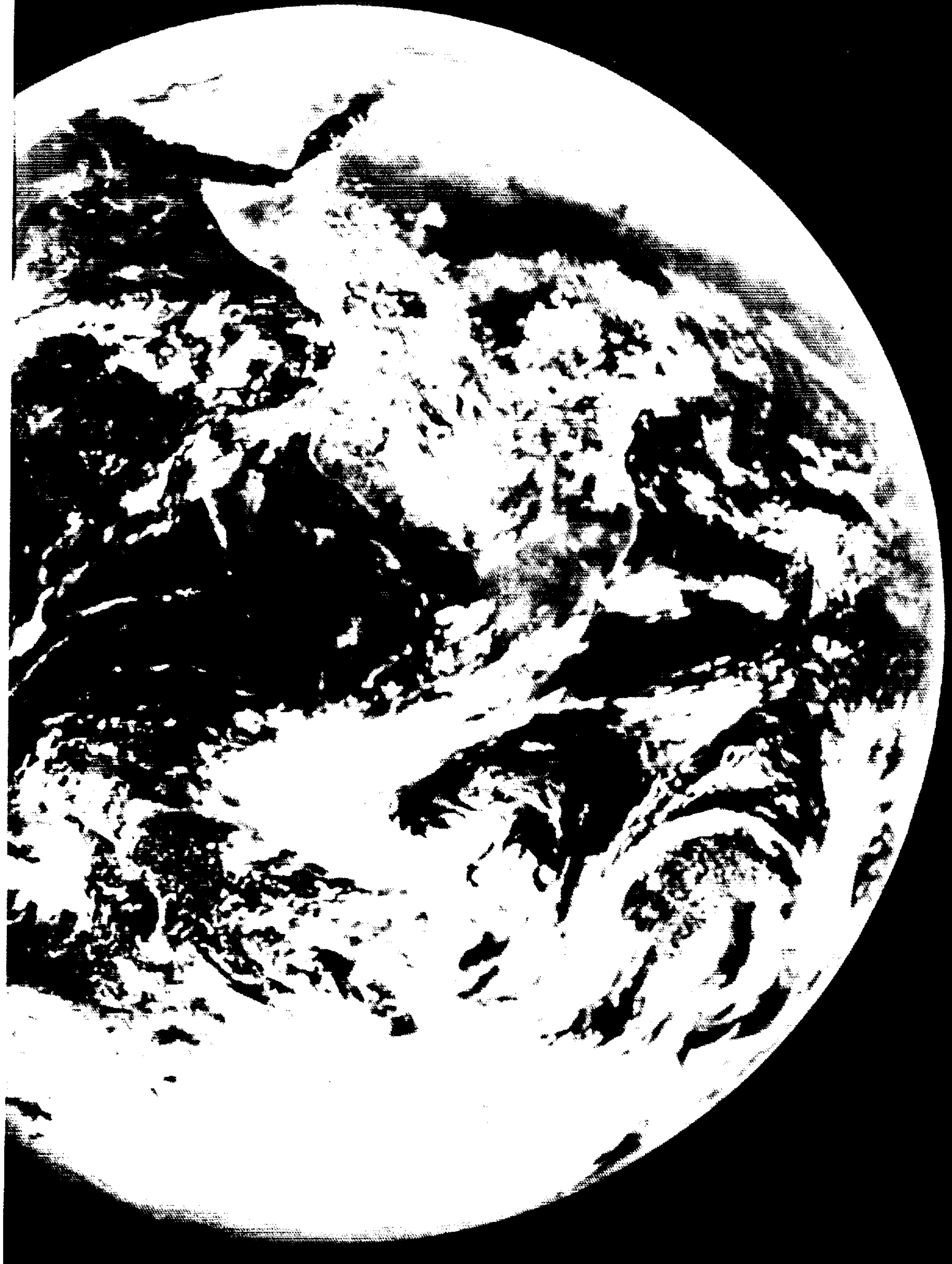

Advanced Studies

The advanced studies of the past have led to the observatory programs of today. *Skylab* and Spacelab are prime examples of programs which have included space-based observatories that have increased our understanding of the Earth and the universe.

We at NASA are concentrating on developing "new ways of doing business," which include the following promising studies:

- The Lunar Ultraviolet Telescope Experiment (LUTE) is being studied as a first step to developing a relatively low-cost astronomical telescope operating on the surface of the Moon, which will require no adjustments after its initial alignment and will rely on the very stable motion of the Moon to sweep out its observational swath across the sky.
- An advanced study was initiated to globally image the Earth's magnetosphere from space. The Inner Magnetosphere Imager (IMI) mission, in combination with internal measurements previously planned as a part of the Solar Terrestrial Physics program, will significantly enhance the understanding of magnetospheric processes. As a science mission, the technology developed could have immediate spinoffs to scientific applications, as well as the commercial optics industry.
- Solar Ultraviolet Radiation and Correlative Emissions (SOURCE) advanced studies are concentrating on defining a complement of instruments cost-compatible with the Small Explorer (SMEX) program and Lite Sat-type spacecraft. The main goal of the SOURCE missions is to develop proxy measurements which indicate solar activity of the same type that produces ultraviolet radiation within spectral regions that can be monitored from ground-based instruments.
- We are studying Geostationary Earth Observatories (GEO's) as an element of the NASA Mission to Planet Earth (MTPE) program. The GEO's will provide the temporal resolution measurements required to complement the Earth Observing System (EOS) and Earth Probe (EP) satellite portions of MTPE. Various instrument complements and spacecraft concepts are being developed.
- In an effort to reduce the onboard complexity of orbiting assets, we are conducting investigations of utilizing Space Laser Energy (SELENE) to transfer ground power to orbiting assets, based on the principle of photovoltaic conversion of high-power laser light to electricity.
- Considerable progress has been made in developing tether applications. Advanced studies are in process to expand the use of tethers to deorbit commercial payloads and to suspend sensors downward for atmospheric research. In addition, the tether systems will be utilized to boost scientific payloads to higher orbits than attainable by the launch vehicle, thus performing a low-cost transportation function.
- We are developing low-cost conceptual applications for utilizing the previously flown Long Duration Exposure Facility (LDEF) in a shortened version to fly a variety of science and engineering investigations.
- Space commercial activities utilizing the microgravity environment of both the space shuttle and the proposed space station are being studied, with the promise of revealing the underlying properties of materials, leading to improved manufacturing processes and scientific discoveries.
- The next generation of launch vehicles is being assessed with conceptual studies concentrating on single-stage-to-orbit (SSTO) and two-stage-to-orbit (TSTO) concepts. The goal of this activity is to identify the key technologies associated with these vehicles and the potential for reducing launch vehicle operating cost. Key technologies identified thus far include: reusable cryogenic tanks, vehicle health management and monitoring, autonomous flight control, operations enhancement technologies, and long-life low-maintenance thermal protection systems.

These advanced studies activities taken to completion will make a substantial contribution to our knowledge base and will greatly add to orbital operation and program flexibility.

James M. McMillion, Director
Program Development

Space Science

Astrophysics—Lunar Ultraviolet Telescope Experiment

Max E. Nein/PS02
205-544-0619

Robert O. McBrayer/PS02
205-544-1926

A small ultraviolet (UV) telescope has been identified by NASA's Office of Space Science (OSS) as a potential first step in the return of NASA astronomy missions to the Moon. The LUTE will use a 1-m UV telescope that can be emplaced on the lunar surface by an unmanned lunar lander with a payload capacity of approximately 400 kg. Typical lander configurations have been analyzed by NASA. The Russian Space Agency's Phobos lander is a candidate to be used for this type of payload.

The Lunar Ultraviolet Telescope is a simple, self-sufficient, transit telescope that achieves a wide field of view (FOV) with a compact optical system using lightweight mirrors (fig. 1). The focal plane instrument is a two-dimensional (2–D) mosaic of charge coupled devices (CCD's) arranged to cover the 1.4-degree FOV. The Lunar Ultraviolet Telescope will not track specific targets, but rather points continuously at a specified declination. It requires no adjustment after its initial alignment, relying on the very stable motion of the Moon to sweep out its observational swath across the sky.

The Lunar Ultraviolet Telescope has been proposed by principal investigator Dr. John McGraw of the University of New Mexico as an early, low-cost precursor experiment to future lunar observatories. The Lunar Ultraviolet Telescope, with its fast optical system (f/3), is a scientifically important UV telescope that can image a strip of the sky in the 0.1 to 0.35 μm wavelength regime. At the orbit of the Moon, the geocorona effect that obscures measurements in the Lyman-alpha radiation range is minimized in comparison to the situation in Earth orbit. Dr. Jack Burns of New Mexico State University is designing the Lunar Environmental Measurement package.

The LUTE technical concept is being analyzed and engineered by MSFC. Because of the expense of lunar payload transportation systems, it is important that the LUTE be designed as a lightweight flight experiment. This requires that weights for subsystems—such as the optics, communications, and data handling—and power are stringently controlled.

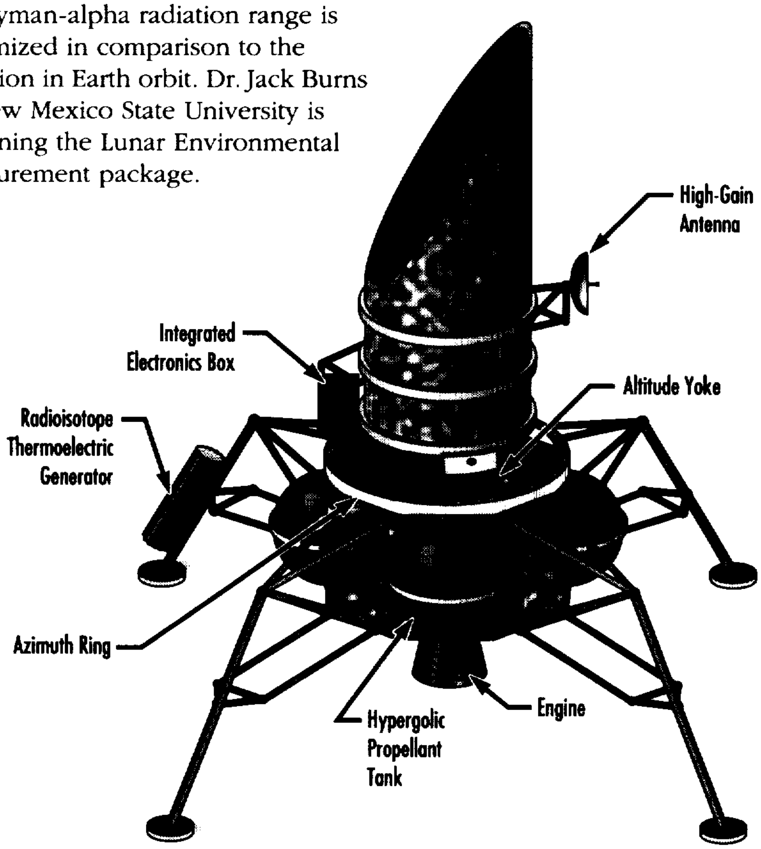

FIGURE 1.—The 1-m Lunar Ultraviolet Telescope.

A radioisotope thermoelectric generator (RTG) is necessary for electrical component survival during the lunar night and for operation throughout the lunar day-night cycles. An RTG for power generation is ideally suited because components and subsystem temperatures can be maintained at a tolerable level during the lunar night when temperatures drop to near 60 K, while keeping systems weight at a level commensurate with a photovoltaic power system. Trade studies of the LUTE subsystems are now being completed to optimize the design, to select the best lunar site for telescope placement, and to identify interfaces with potential lunar transportation systems.

Deployment of the LUTE on the Moon during this decade is technically and programmatically feasible. Although this constitutes a tight schedule, plans are being made to reduce the historically lengthy review phases occurring in the development of flight systems through the introduction of new ways of doing business. Typically, this approach is based on concurrent engineering and maximum use of computer aided design (CAD).

Sponsor: Office of Space Science

University Involvement: University of New Mexico and New Mexico State University

■

Inner Magnetosphere Imager Mission

C. Les Johnson/PS02
205-544-0614

Carmine E. DeSanctis/PS02
205-544-0618

In 1991, MSFC initiated a design study for a mission to globally image the Earth's magnetosphere from space. The IMI mission, which is scheduled to launch before the end of the decade, will obtain the first simultaneous images of component regions of the inner magnetosphere using extreme and far ultraviolet light, x rays, and energetic neutral atoms. Working with the NASA Headquarters-appointed science working group, the MSFC Program Development engineering design team is near completion of the mission Phase A study.

Progress in magnetospheric physics has shown that a static model built up over time from single-point particle and field measurements alone cannot adequately describe the complexity of the Earth's magnetospheric system. Further progress is contingent upon global observations of the entire system. A program to image the inner magnetosphere, combined with internal measurements conducted previously and planned as a part of the International Solar Terrestrial Physics Program, will significantly enhance understanding of magnetospheric processes.

Techniques to allow satellite imaging of important charged-particle populations in the magnetosphere have recently been demonstrated. Techniques to image the ring current with energetic neutral atoms are being optimized for space satellite use. The imaging of low-energy magnetospheric plasmas using solar radiation resonantly scattered from singly ionized helium (He^+) has also been demonstrated. Singly ionized oxygen (O^+) imaging of the plasmasphere and extended imaging of the near-Earth plasma sheet also appear to be feasible.

The baseline IMI mission calls for an instrument complement of seven imagers to be flown on a spin-stabilized spacecraft in an elliptical Earth orbit with an apogee of seven Earth radii, perigee of 4,800 km, and a 90-degree inclination. The strawman instruments, with a brief summary of their measurement characteristics, are listed in table 1.

TABLE 1.—*Strawman instruments for the baseline IMI mission spacecraft*

Instrument Name	Measurement(s)
Hot Plasma Imagers	Energetic neutral atoms with energies between 1 to 50,000 and 20,000 to 1,000,000 eV
He^+ 304 Plasmasphere Imager	Singly ionized helium with 304 Å light
O^+ 834 Plasmasphere Imager	Singly ionized oxygen with 834 Å light
Geocoronal Imager	Light with a wavelength of 1,216 Å
Auroral Imager	Light with wavelengths of 1,304 and 1,356 Å
Proton Auroral Imager	Light with a wavelength of 1,216 Å
Electron Precipitation Imager	X rays with energies of between 300 and 10,000 eV

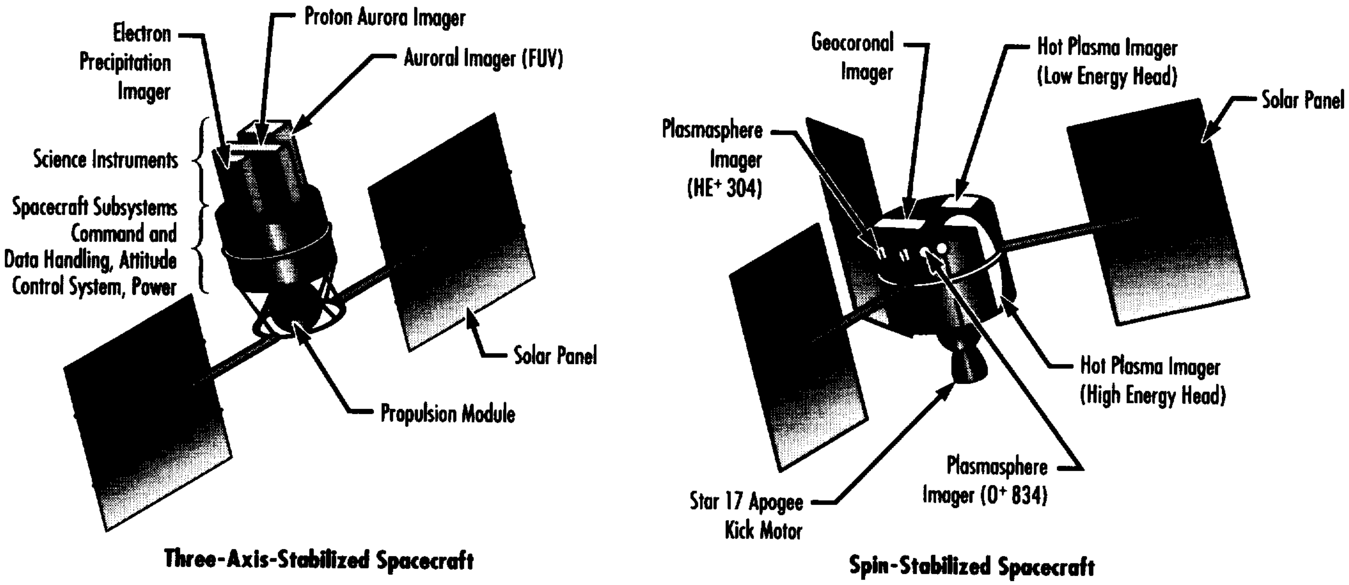

Three-Axis-Stabilized Spacecraft

Spin-Stabilized Spacecraft

FIGURE 2.—IMI dual spacecraft option.

Several spacecraft concepts have been thoroughly examined for the mission. The baseline concept is a single spin-stabilized spacecraft with a despun platform. The 1,300 kg spacecraft would be launched by a Delta II launch vehicle from the Western Test Range (Vandenberg Air Force Base, CA) and perform on orbit for 2 yr. The spacecraft would use body-mounted solar arrays to provide the 325 W of mission power and communicate the 59 kb/s data rate to the ground via the Deep Space Network. An optional configuration would divide the science instruments onto two smaller spacecraft. The first would be a small spin-stabilized spacecraft carrying the instruments borne by the spinning portion of the baseline concept. The second would be a three-axis-stabilized spacecraft carrying those instruments from the despun platform that require precise pointing to specific regions of the magnetosphere. These two spacecraft options are illustrated in figure 2.

The IMI mission will enhance our understanding of the near-Earth space environment and the coupling of this environment to the Sun. The mission instruments will drive the development of high-throughput, narrow bandwidth ultraviolet filters, high-reflectivity mirrors, and software useful in low signal-to-noise optical image processing. The technology developed for imaging the hot plasma with energetic neutral atoms will enhance scientists' basic understanding of thin-foil scattering and low-energy particle optics. The technology developed for the IMI could have immediate spinoffs to other scientific applications, as well as the commercial optics industry.

The scientific return from the IMI mission will open a new window on the plasma universe, providing a better understanding of the magnetospheric plasmas in the near-Earth environment, as well as those deep-space plasmas not previously measurable from the Earth. Such terrestrial and celestial plasmas will be imaged and understood in that context—not utilizing in situ particle and field measurements as were required previously.

Inner Magnetosphere Imager Scientific Rationale and Mission Concept. Vol. 1: Executive Summary. 1991. NASA, MSFC, AL.

Johnson, C.L., and Hermann, M. 1993. The Inner Magnetosphere Imager Mission. Society of Photo-Optical Instrumentation Engineers (SPIE) Aerospace Science and Sensing, Orlando, FL.

Wilson, G.R. 1993. *Inner Magnetosphere Imager (IMI) Instrument Heritage.* Contractor Report 4498. NASA, MSFC, AL.

Sponsor: Office of Space Science, Space Physics Division

■

Solar Ultraviolet Radiation and Correlative Emissions

Joseph R. Dabbs/PS02
205-544-0623

Carmine E. DeSanctis/PS02
205-544-0618

The SOURCE mission will give an accurate measurement of the extreme ultraviolet (EUV) solar flux from 1 to 122 nm. The EUV flux is required as an input to models of the Earth's atmosphere. In addition, the EUV flux data will complement and help explain the data from other satellite missions such as the Upper Atmosphere Research Satellite (UARS); Thermosphere, Ionosphere, Mesosphere, Electro-Dynamics (TIMED) Mission; and so forth. Finally, the SOURCE data will help to develop proxy measurements that can be used to accurately predict EUV flux when direct measurements are not available. SOURCE utilizes a mix of highly stable instruments and calibration techniques to obtain accurate measurements in a spectral range where detector drift and degradation tends to be severe. SOURCE instrumentation consists of spectroradiometric instruments and imagers that measure emissions from the solar chromosphere, solar transition region, and corona. Spatial resolution of 5 arc seconds (or better) is desired. The strawman payload that has been considered has a mass of 55 kg and requires approximately 100 W of electrical power and a telemetry rate of 400 kb (or less).

The main goal of the SOURCE mission is to develop proxy measurements that indicate solar activity of the same type that produces EUV radiation, but are in spectral regions that can be monitored from ground-based instruments. The data from SOURCE are extremely important, and it is possible to accomplish these goals in an economical manner by the use of small spacecraft and low-cost launch vehicles of existing design. Strawman instrument complements of 55-kg mass have been defined that meet the scientific goals and are compatible with "Lite Sat" type spacecraft in Sun-synchronous orbit at 400 km, which is reachable with small expendable launch vehicles such as the Pegasus or Conestoga.

Current activity has focused on redefining and reducing the complement of instruments that will guarantee the required accuracy at a cost compatible with the Small Explorer program constraints.

Sponsor: Office of Space Science

■

▮▮▮▮ Space Systems

Geostationary Earth Observatory Program

Vernon W. Keller/PS02
205–544–2470

The Geostationary Earth Observatories are a future element of NASA's Mission to Planet Earth program. They will provide the excellent temporal resolution measurements required to complement the other MTPE space observations.

The GEO element of MTPE is currently in the concept definition stage (Phase A). Based on the science requirements for the mission, a preliminary GEO remote sensing instrument complement has been defined. These instruments include optical imagers, atmospheric sounders, passive microwave sensors, and other passive sensors that require either excellent Earth viewing temporal resolution, or other attributes such as the nearly continuous view of the Sun (annually, 99 percent of the time), best attained from geostationary orbit.

Studies are addressing both the instrument design and the spacecraft required to accommodate them. Utilization of three-axis-stabilized spacecraft instead of "spinners" permits longer Earth viewing integration times and improved sensing efficiency, but places increased thermal demands on the spacecraft and its sensors, as well as more complex pointing control than is required with spin-stabilized satellites. This severe thermal environment is even more of a problem because the instrument optical systems are simultaneously being designed for high-spatial and high-spectral resolution. For example, meteorological imagers in the past have typically had a visible channel ground resolution of about 1 km in both low-Earth and geostationary orbits. This corresponds to about 1.3 mrad in low orbit and 28 μrad in geostationary orbit. One of the proposed new GEO imagers requires 100-m ground resolution in several visible and UV spectral bands.

To achieve such high performance, the new GEO instruments will need to incorporate technological advances beyond those used in current civilian designs. For example, since the imager telescope structure and optical elements such as the mirrors, which are exposed most directly to solar illumination, can undergo a temperature change on a three-axis-stabilized spacecraft from –10 to +70 °C in a period of a few hours, use of materials that exhibit high thermal stability, as well as good structural and optical performance and lightweight characteristics, is important to meet the new requirements. Silicon carbide's (SiC's) inherent properties of high-stiffness-to-weight, very high thermal stability over wide temperature excursions, excellent optical polish capability, and projected low cost make it an ideal candidate. A prototype 0.5-m diameter f/4 telescope that uses SiC for both optics and structure is currently being designed, developed, and performance tested over a wide temperature range. This effort is scheduled for completion in late 1994.

Advances not only in optics, but also in structures, detectors, coolers, coatings, pointing and control systems, and calibration technologies would significantly benefit the GEO program. Technologies of particular interest include: diffractive optics, tunable liquid-crystal optics, thermally stable optical coatings, infrared (IR) etalon interferometers, composite reflective elements, image motion compensation, and solar channel calibrators.

Koczor, R.J. 1993. Technology Needs for Geostationary Remote Sensors. SPIE 1952–15. Orlando, FL.

Sponsor: Office of Mission to Planet Earth

■

Space Laser Energy

Edward E. Montgomery/PS04
205–544–1767

Wireless power transmission research at MSFC is directed toward developing critical component technologies for the SELENE power beaming program. The objective of SELENE is to develop and demonstrate technologies needed for low-cost, reliable electrical power and propulsion for spacecraft, based on the principle of photovoltaic conversion of high-power laser light to electricity. It is a ground-to-space system utilizing near-visible wavelength technologies under development by NASA. The focus on the development of key component technologies in adaptive optics and high-energy lasers has resulted in several prototype hardware items over the last year.

The two main subsystems of a laser power beaming ground station will be a free electron laser (FEL) as a generator and a large segmented adaptive beam director that functions as the transmitter. Their key technologies were identified in reviewing cost goals set down for the first ground site. In the laser, the highest leverage potential was shown to be in the accelerator cost. For the beam director, the major driver was the segmented primary mirror.

The performance of an innovative induction linear accelerator module design constructed by Science Research Laboratories has been tested. Recently, this 1.0 MeV first accelerator section was installed on the beamline with an injector section to form a 1.5 MeV electron beam source. The development of this system was a jointly funded project by NASA and the U.S. Navy.

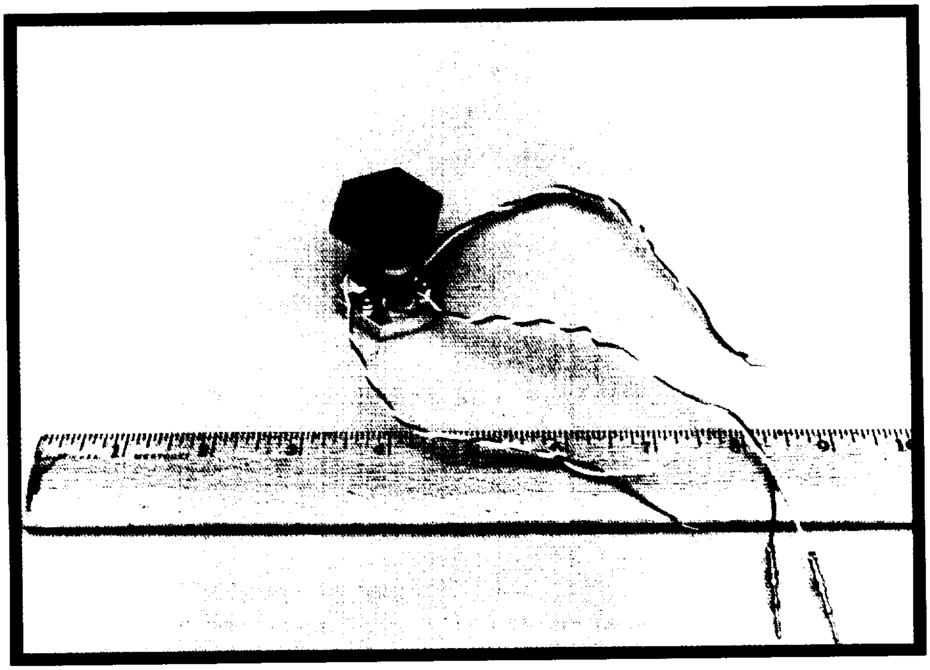

FIGURE 3.—Active mirror segment prototype design for an atmosphere compensation beam director.

In the beam director development program, MSFC has concentrated on developing the active mirror segments that will populate the primary mirror of the SELENE Cassegrain telescope configuration. A critical issue to be addressed in the design is the quality and economy in mass production of the small-scale (3 cm flat-to-flat), hexagonal, low figure error, mirror segments with embedded actuators sensors and electronics. Another issue is the ability of a controller to manage the dynamics of a multitude of simultaneous channels.

Several type I segment assembly prototypes were developed based on piezoelectric, electrostrictive, and electromagnetic actuators. Figure 3 contains a photograph of a completed type I segment with an electrostrictive actuator. Most of the type I segments designed and built this year were based on the type I design concept (Montgomery et al. 1993). In the type I system, an externally located wavefront sensor determines the aberration pattern in the atmosphere. That information is fed to a processor that contains the control algorithm and produces the commands for the segment actuators. The SELENE design team originated an innovative concept this year in which the wavefront sensor is an

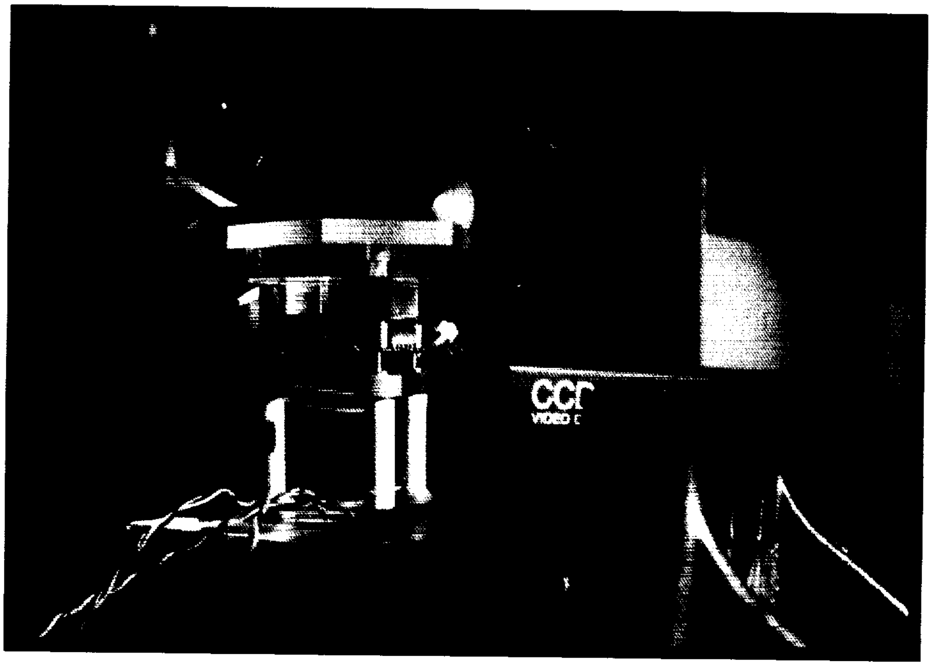

FIGURE 4.—Innovative active mirror segment concept utilizing an integral wavefront sensor.

integral part of each segment. These type II segments also include a second solid Cassegrain reflector element and a CCD camera. Figure 4 shows the prototype constructed using piezoelectric actuators.

The benefits of a laser power beaming system include extensions in the life of existing geostationary satellites by reducing battery discharge during the relatively short but frequent periods that they are in the Earth's shadow and unable to use solar arrays. Studies by Comsat, Inc., indicate a potential 20-percent extension in the total life of a satellite (Meulenberg 1992). Assuming the typical 24 transponders per satellite, current market rate for feed time, and a group of 22 satellites specifically identified for this service, there is a potential revenue stream of approximately $500 million per year.

Other applications include weight reductions in the power systems for future satellites and spacecraft. Highly efficient electric propulsion systems for orbital transfer vehicles would be possible. Spinoff benefits include waste treatment and large batch sterilization of medical supplies using the accelerator module technologies. The atmosphere compensation capability achieved through the active segments will be applicable to all ground-based telescopes and future space telescopes as well. Potential applications for the high-power laser component include repair of the ozone layer and removal of orbital debris.

Meulenberg, A. July 1992. Application of Laser Power Beaming to Commercial Communications Satellites. *Proceedings of the SELENE Advocacy Briefing and Progress Review.* NASA, MSFC, AL.

Montgomery, E.E.; Fawcett, S.C.; Redmon, J.W., Jr.; and Lindner, J.L. February 1993. SELENE Component Technology Test-Beds at MSFC. *First Annual Wireless Power Transmission Conference Proceedings,* Center for Space Power. College Station, TX.

Rather, J.D.G. July 16, 1992. Laser Power Beaming for Space Development: An Example of an Ongoing Advanced Research Technology Project at NASA. *Proceedings of the SELENE Advocacy Briefing and Progress Review.* NASA, MSFC, AL.

Sponsor: Office of Advanced Concepts and Technology

Commercial Involvement: Science Research Laboratories; Comsat, Inc.; Kaman Corp.; Forth, Inc.; AVX, Inc.; Shaeffer Magnetics, Inc.; and United Applied Technologies, Inc.

■

Space Station Advanced Programs

John M. Butler, Jr./PS04
205-544-4833

During 1993, MSFC continued studies of advanced concepts related to the evolution of the space station. The 1993 effort involved assessment of logistics elements, including the ability of such elements to be accommodated on expendable launch vehicles (ELV's). Current designs of space station logistics elements were examined to determine their potential usability on ELV's. Several types of mounting locations and arrangements for logistics carriers on ELV's were investigated, including: (1) cantilevered concepts (fig. 5), and (2) concepts utilizing strongbacks that provide carrier interfaces analogous to those in the space shuttle orbiter payload bay (fig. 6). Cantilevered concepts require some degree of structural modification to existing carriers; these were identified. Strongbacks add weight, but minimize impacts to existing carriers and also allow more logistics elements to be carried. Some strongback concepts allow elimination of the carriers, with the orbital replacement units being mounted directly on the strongbacks.

Engineering prototype development work continued during 1993 in: (1) the Environmental Control and Life Support System (ECLSS) Advanced Automation Project (AAP), and (2) the Space Station Module Power Management and Distribution (SSM/PMAD) system.

The ECLSS AAP work was coordinated closely with the Space Station Control Center Complex personnel this year, to facilitate implementation of this technology. Models of the Carbon Dioxide Removal Assembly (CDRA) and the Temperature and Humidity Control (THC) system have been developed and are being assessed by the control center engineers.

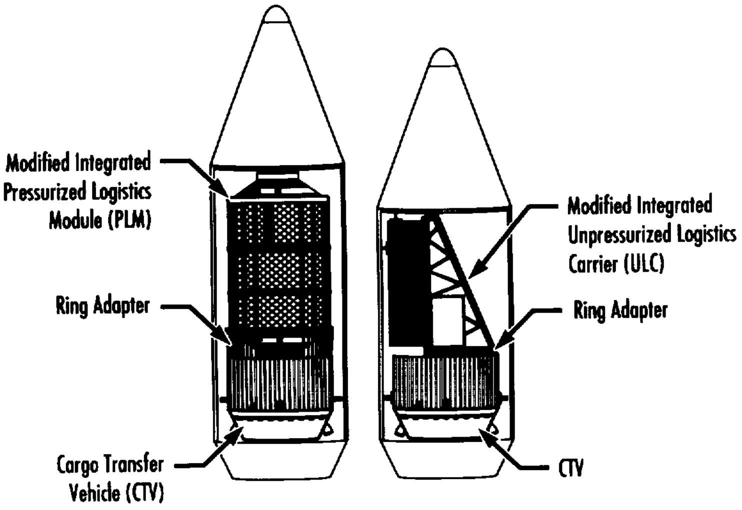

FIGURE 5.—Cantilevered carrier concepts.

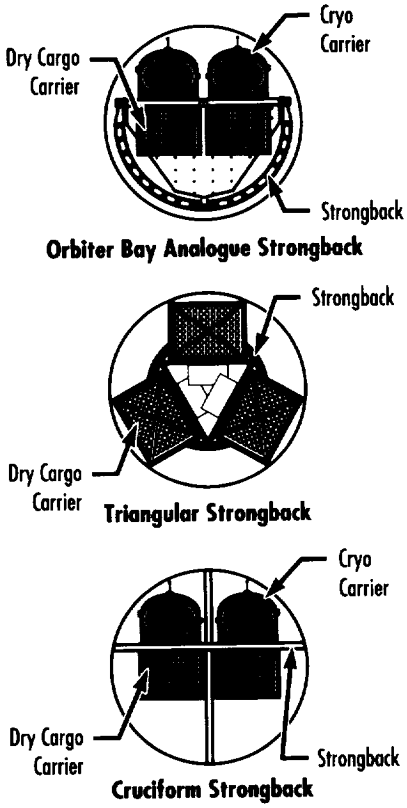

FIGURE 6.—Strongback carrier concepts.

The approaches and techniques proved in the SSM/PMAD test-bed system are now being integrated into the Electrical Power System (EPS) console software for the Johnson Space Center (JSC) Consolidated Control Center. Developed in cooperation with the Lewis Research Center (LeRC) and controllers at the Kennedy Space Center (KSC), an EPS console using these technologies is expected to enable better, less expensive operations than do current techniques.

Sponsor: Space Station Engineering Division

■

Tether Applications in Space

Charles C. Rupp/PS02
205–544–0627

John M. Butler, Jr./PS04
205–544–4833

Research into tether applications in space has the objective to develop the use of tethers in a broad range of space activities. NASA's first tether systems flew on *Gemini* 12 and 13 in the late 1960's, which demonstrated spin-stabilized and gravity-gradient-stabilized configurations of the *Gemini* manned spacecraft and the Agena docking target.

The first of the modern tethers, the Tethered Satellite System (TSS), flew on the space shuttle in 1992, and demonstrated the electrodynamic interaction of a tether system with the environment, and tether deployment and retrieval, as well as contributed to an understanding of tether dynamics, particularly in proximity operations with the shuttle. The second modern tether system, the Small Expendable Deployer System (SEDS), flew in March 1993, as a secondary payload on an Air Force Delta rocket, and demonstrated the low-tension deployment profile and the capability of a tether system to deorbit payloads from low-Earth orbit. A third tether system, the Plasma/Motor Generator (PMG), flew in June 1993, from another Air Force Delta rocket, and demonstrated the use of plasma contactors to enhance the electrical contact of the tether system to the plasma.

Planning and engineering support continue for follow-on SEDS missions. SEDS–2, scheduled for flight in 1994, will demonstrate a closed-loop control law to deploy the tether system in a stable local-vertical orientation. A third SEDS flight is planned to boost and release a student-developed satellite known as the Students for the Exploration and Development of Space Satellite (SEDSAT) to a higher orbit than that attained by the launch vehicle. Analysis of data from the first SEDS flight is leading to improved models of the SEDS deployment friction and to the development of closed-loop control laws for these future missions.

Potential scientific applications for tethers in the near future include the use of two SEDS-type deployers on a single spacecraft to deploy a dipole antenna for low-frequency communications system research. Other applications being studied include the use of a SEDS to deorbit commercial payloads and to suspend payloads downward for atmospheric research. Potential uses of tethers for transportation include deorbiting waste from the space station and deorbiting spent rocket upper stages to control the rising debris hazard to operational spacecraft.

Early in 1993, a nonadvocacy panel reviewed the TSS and SEDS flight results and the studies and plans for future tether applications. The panel findings favored a reflight of the TSS and more frequent SEDS flights. Additional coordination with potential user communities is recommended to disseminate information on the beneficial uses of tethers.

Sponsor: Office of Space Systems Development, Advanced Programs

■

A Long Duration Exposure Facility Follow-On Spacecraft Concept

Vernon W. Keller/PS02
205–544–2470

The successful flight, retrieval, and analyses of the Long Duration Exposure Facility experiments have demonstrated the value of long-duration space exposure for a broad spectrum of science and engineering investigations. The original LDEF was an excellent gravity-gradient spacecraft, but because of its 9-m length and 9,700-kg mass, it was difficult to manifest on the space shuttle in conjunction with other payloads for either launch or retrieval.

An LDEF follow-on spacecraft—LDEF II—has been conceptualized (fig. 7). Its short stowed length (~3 m) greatly improves shuttle manifesting opportunities, while still providing very large surface area exposure for experiments. Deployable "wings" on each end of the short, cylindrical main body of this new spacecraft provide the means for gravity-gradient stabilization while greatly increasing the spacecraft surface area. The center section of the spacecraft is oriented with the end faces of the 12-sided, 4.3-m-diameter cylinder perpendicular to the velocity vector, thus providing large areas for experiments in both the ram and anti-ram directions, as well as additional exposure area around the periphery of the cylinder. When deployed and properly oriented with the shuttle's remote manipulator system (RMS), both wings of the spacecraft are oriented edge-on to the direction of motion and lie

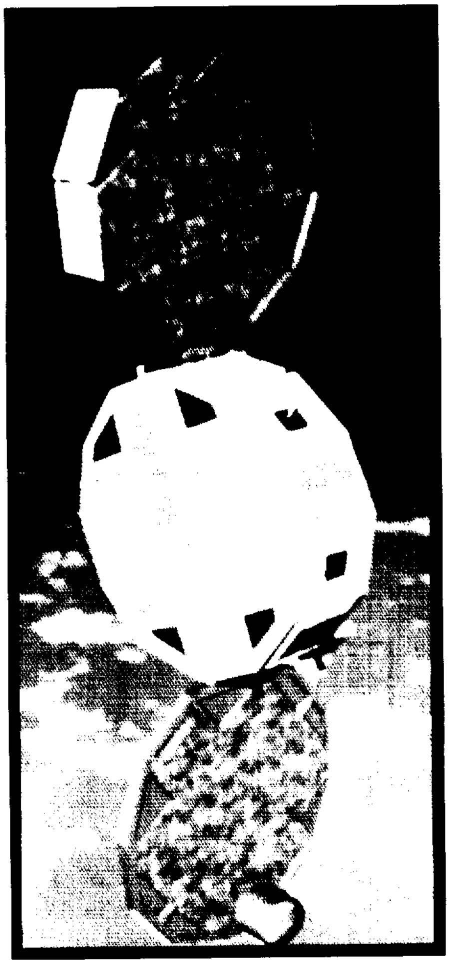

FIGURE 7.—LDEF II concept.

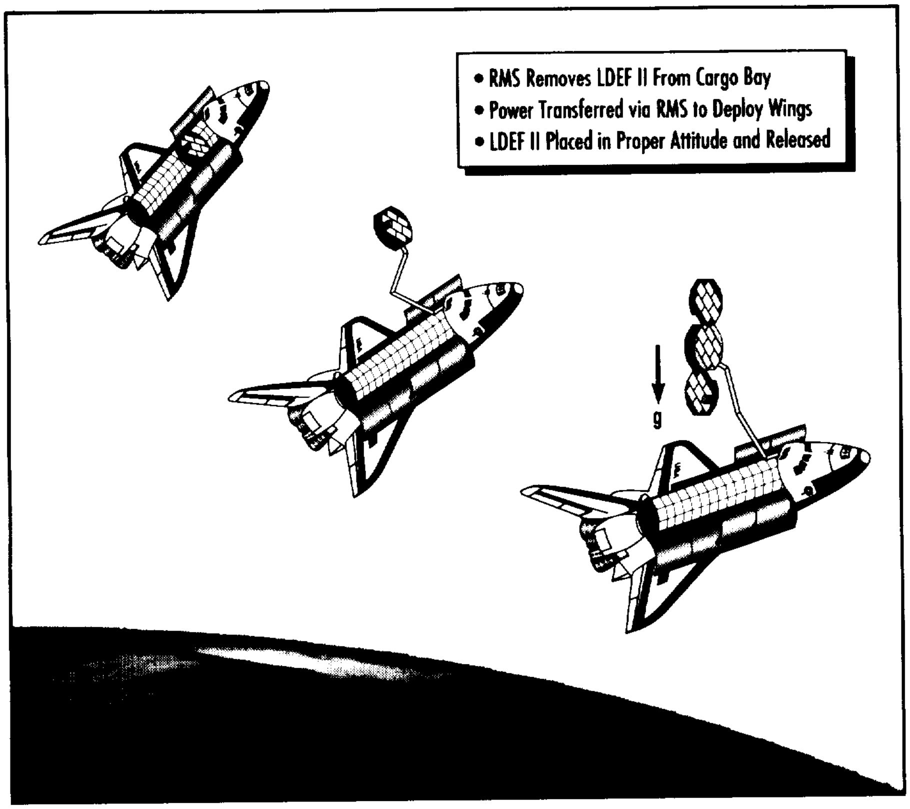

FIGURE 8.—LDEF II spacecraft deployment sequence.

in the plane that contains the local gravity (g) vector (fig. 8). Each of the relatively thin wings readily accommodates dual side exposure of heavy nuclei collector (HNC) glass plate stacks for cosmic ray detection. This is important since the HNC experiment requires a large surface area and is quite heavy. Space environmental effects experiments (materials, systems, biology, microgravity, etc.) can be accommodated on the center section of the spacecraft.

Flat surfaces mounted normal to, and on the periphery of, the wings provide additional areas in both the ram and anti-ram directions for cosmic dust, micrometeoroid, and orbital debris collection experiments, free of contamination from splatter off secondary surfaces.

The baseline spacecraft concept provides enhancements not available on the original LDEF, such as solar-array-generated electrical power and data telemetry. As presently envisioned and costed, this relatively inexpensive spacecraft will be an MSFC in-house-developed carrier with experiments supplied by various principal investigators (PI's) from government, academia, and industry. In-house design, construction, and integration of the spacecraft will provide valuable hands-on experience for a number of young NASA engineers. After exposure to the low-Earth orbit (LEO) space environment for approximately 3 yr, this free-flyer spacecraft will be retrieved by the space shuttle and the experiments will be removed and returned to the PI's for analyses and publication of results.

Sponsor: Program Development

■

Small Expendable Deployer System

James K. Harrison/FA34
205-544-0629

The Small Expendable Deployer System is a lightweight, spinning-reel-type system designed to deploy a payload attached to the end of a 20-km-long tether, which is cut and discarded after use. The key objectives are to validate the design concept and study the dynamics of the tether during and after deployment. SEDS weighs about 41 kg, including the tether weight of 7 kg. The tether is made from a high-strength, low-density polyethylene fiber called SPECTRA™. SEDS–1 flew on a Delta II launch vehicle in March 1993. SEDS–2 is scheduled to fly in 1994.

During flight, the 26-kg payload is deployed toward Earth (fig. 9). Payload instruments are an accelerometer, a tensiometer, and a magnetometer (for orientation information). The SEDS–1 experiment lasted about 2 h, ending when the tether was fully deployed. The tether was cut, allowing it and the payload to reenter the Earth's atmosphere. On SEDS–2, the tether will remain attached to the Delta II second stage and will reenter the atmosphere, along with the second stage, about a month after launch.

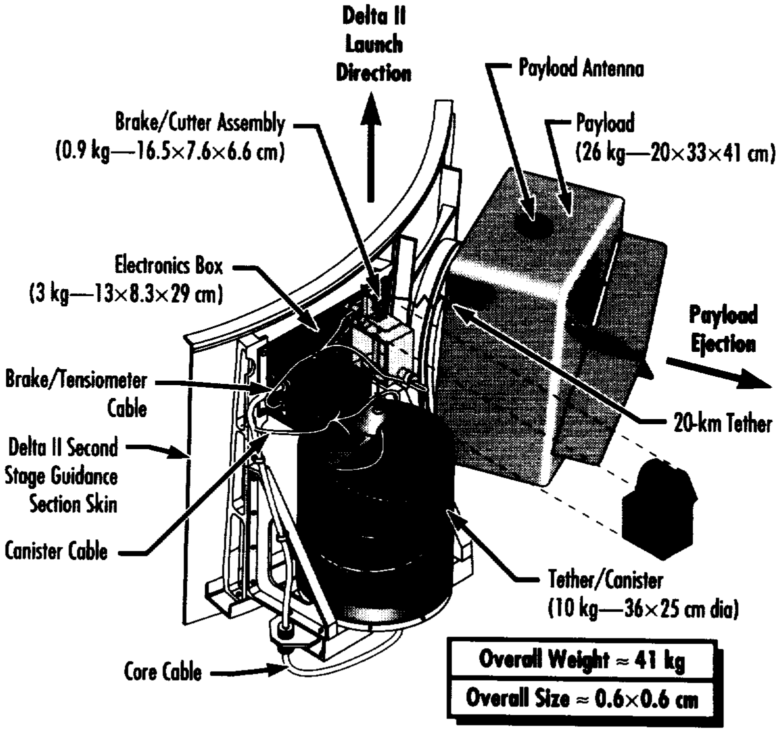

FIGURE 9.—SEDS–2 to be flown on a Delta II launch vehicle.

Numerous future tether applications of SEDS are being considered. One is the routine deorbiting of the space station waste materials, packaged in small, lightweight containers that can be folded for easy storage during space shuttle trips to the station. Another is the boosting of small payloads such as the University of Alabama in Huntsville student-built satellite called SEDSAT to higher orbits—from 185 by 740 km to 680 by 792 km. Another use of SEDS will be to place instruments in the 90- to 120-km altitude region for upper atmospheric research.

Sponsor: Office of Space Systems Development

■

Commercial Use of Space

Protein Crystal Analysis Equipment

Kaye Inman/PS05
205-544-2229

Kenneth R. Taylor/PS05
205-544-0640

Protein crystal growth in microgravity is one of the more promising commercial uses of the space environment. Protein crystals grown on the space shuttle are more defect-free and larger than those grown in ground-based laboratories due to the absence of gravity-driven sedimentation. Evidence to date indicates that crystals are degraded if subjected to the gravity force of reentry or if there are relatively long intervals between shuttle visits to the space station. For this reason, x-ray diffraction measurements made on orbit will significantly improve the scientific knowledge that can be gained from microgravity-grown protein crystals.

This Phase I Small Business Innovation Research (SBIR) study addressed the feasibility of an on-orbit x-ray crystal diffraction imaging system, providing on-orbit protein crystal diffraction imaging and data acquisition, given the space station power, volume, and weight constraints, and the radiation environment in orbit. An analysis of the interaction of unshieldable cosmic rays and protons with the x-ray detector found that a pulsed operating mode would reduce the background signal in the diffraction image data to an insignificant level.

The study concluded that a protein crystallographic imaging system, suitable to the constraints of space-based operation, is feasible. The major technological innovation required is the development of a compact, low-power x-ray generator combined with efficient x-ray optics. Recent work in grazing incidence optics indicates that substantial improvement of the optical efficiency of the x-ray collimating optics is possible by combining these optics with an improved microfocus x-ray tube having a smaller emitting area, if the space station experiments power budget can be met. The next logical step is to build and test a prototype system, including a 2,000 by 2,000 pixel solid-state x-ray camera for acquiring and digitizing the diffraction images (fig. 10) acquired with this type of CCD camera.

In addition to the space station, there is a substantial dual-use commercial market for both the high-efficiency x-ray source and the solid-state digital x-ray camera system being developed under this program. The x-ray generator and CCD camera would have immediate benefits for conventional ground-based protein diffraction, since use of these components would considerably advance the state of the art as it is now practiced on the ground. Even if crystallography in space were deferred, development of the high-efficiency x-ray tube, x-ray collimator, and camera can be justified for the immediate benefits they would confer upon the large x-ray crystallographic community.

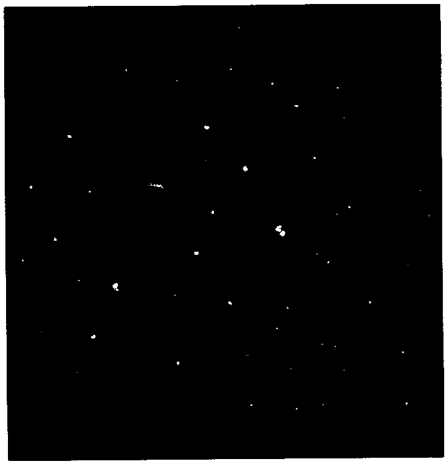

FIGURE 10.—Laue diffraction pattern of the enzyme protein crystal lysozome in a quartz capillary.

At the 1993 Crystallography Society meeting, approximately 1,000 attendees exhibited considerable interest in replacing photographic film and single-point x-ray detectors with this type of digital x-ray imaging camera. The more efficient x-ray source will make the crystallography laboratories more competitive with the synchrotron x-ray facilities, a real incentive to upgrade the current x-ray equipment in these numerous academic and industrial laboratories.

Sponsor: Office of Advanced Concepts and Technology, Small Business Innovation Research Program

Commercial Involvement: Princeton Scientific Instruments

■

IIII Transportation Systems

Access to Space: Advanced Technology Vehicle (Option 3) Focused Technology/Advanced Development Plan

Gene Austin/PT01
205-544-0633

This focused technology/advanced development plan is based upon an assessment of the current technology readiness levels (TRL's) for major systems and subsystems of advanced technology vehicles. The class of launch vehicles represented has the potential for major reductions in annual space launch vehicle operating costs. Single-stage-to-orbit and two-stage-to-orbit systems have been assessed in this process to ensure maximum flexibility for implementation when these technologies have been brought to maturity.

Tasks are presented that bring the most promising technologies to a TRL 6 (system or subsystem model demonstration in a relevant environment). A major consideration in the development of these tasks is low operational costs. Each vehicle concept being defined by the Advanced Technology Team stresses low operational costs, and the technology tasks have been developed with this same emphasis. The target for the development of this plan is technology maturity by the year 2000.

The advanced technology vehicle configurations assessed consist of the following general types:

- Single-stage-to-orbit: all rocket (SSTO R)
- Single-stage-to-orbit: air breathing plus rocket (SSTO A/R)
- Two-stage-to-orbit: air breathing plus rocket (TSTO A/R).

After reviewing each configuration, it was evident that there were several core technology areas that were essential for the development of all the concepts. These common enabling technologies include the following:

- Reusable Cryogenic Tanks:
  A common element of fully reusable vehicles that has not been explored in prior technology efforts is the development of long-life/low-maintenance reusable cryogenic tank systems. The cryogenic tank system includes both the tank structure and insulation. Included in this task is: the development of tank certification criteria; nondestructive evaluation (NDE) techniques; establishment of a materials data base; optimization of materials processing and fabrication; and the design, fabrication, and analysis of a large-scale cryogenic tank system (including structural and thermal cycling).

- Vehicle Health Management and Monitoring: Vehicle health management and monitoring, while successfully and widely utilized on high-performance military and commercial aircraft, is not as mature on space launch systems. Application of these existing techniques to launch vehicles permits real-time identification of vehicle subsystem status. Definition of critical items to be monitored and stored, development of data transfer techniques, "smart" management algorithms, and development of ground processing procedures are included in this task.

- Autonomous Flight Control:
  To achieve low-cost space transportation, most in-flight functions must be automated and control responsibility transferred to the vehicle. Autonomous flight control is both possible and near state of the art for ascent, reentry, and landing. On-orbit operations, such as routine rendezvous and docking at the space station, are also near state of the art and are

under development by NASA. This task objective is to develop and demonstrate these integrated techniques.

- Operations Enhancement Technologies: The focus on low operations cost approaches for space launch systems has resulted in an assessment of operations requirements derived from a series of studies and benchmark evaluations. Several key areas requiring further investigation include operable and reliable rocket engines, leak-free mechanical joints, and electromechanical actuators/electrohydraulic actuators.
- Long-Life/Low-Maintenance Thermal Protection System (TPS): The development of a long-life/low-maintenance TPS is required to decrease the operational costs of reusable vehicles. Tasks to investigate toughened rigid ceramic insulation (TUFI), tailored advanced flexible blanket insulation (TABI), carbon-silica carbide hot structures, and direct-bond reusable surface insulation are included in this activity.

These core technology requirements are shared by all three basic configurations being considered by the Advanced Technology Team. These technologies are also considered to be high-priority requirements for each configuration. It is possible to develop the specific technology tasks associated with these enabling technologies without having to select a given configuration or concept for development.

In addition to the core technologies discussed above, some enabling technologies are unique for the specific configurations being considered. For the SSTO R concept, the key technology requirement is for the development of a long-life, low-maintenance, advanced liquid oxygen/liquid hydrogen (lox/LH_2) engine derived from the space shuttle main engine (SSME). An alternate approach would be the development of appropriate technology for a tripropellant engine system (Russian RD701 design or equivilant).

For the SSTO A/R combination concept, several unique technology requirements exist. An extensive technology program is required for the air-breathing propulsion system, including the development of several flight experiments that will be used to demonstrate and calibrate ramjet/scramjet operations. In addition, this configuration uses an actively cooled TPS that will require an extensive technology program. Additional technology requirements include advanced material studies and studies relating to the production and transfer of slush hydrogen (H_2). Some technology development is required for the linear aerospike rocket engine system.

The TSTO A/R combination concept requires technology development of the turbojet/ramjet air-breathing propulsion system and an expander-cycle lox/LH_2 rocket engine system. Additional materials technology is required for titanium matrix composite materials used for control surfaces.

Sponsor: Office of Space Systems Development

■

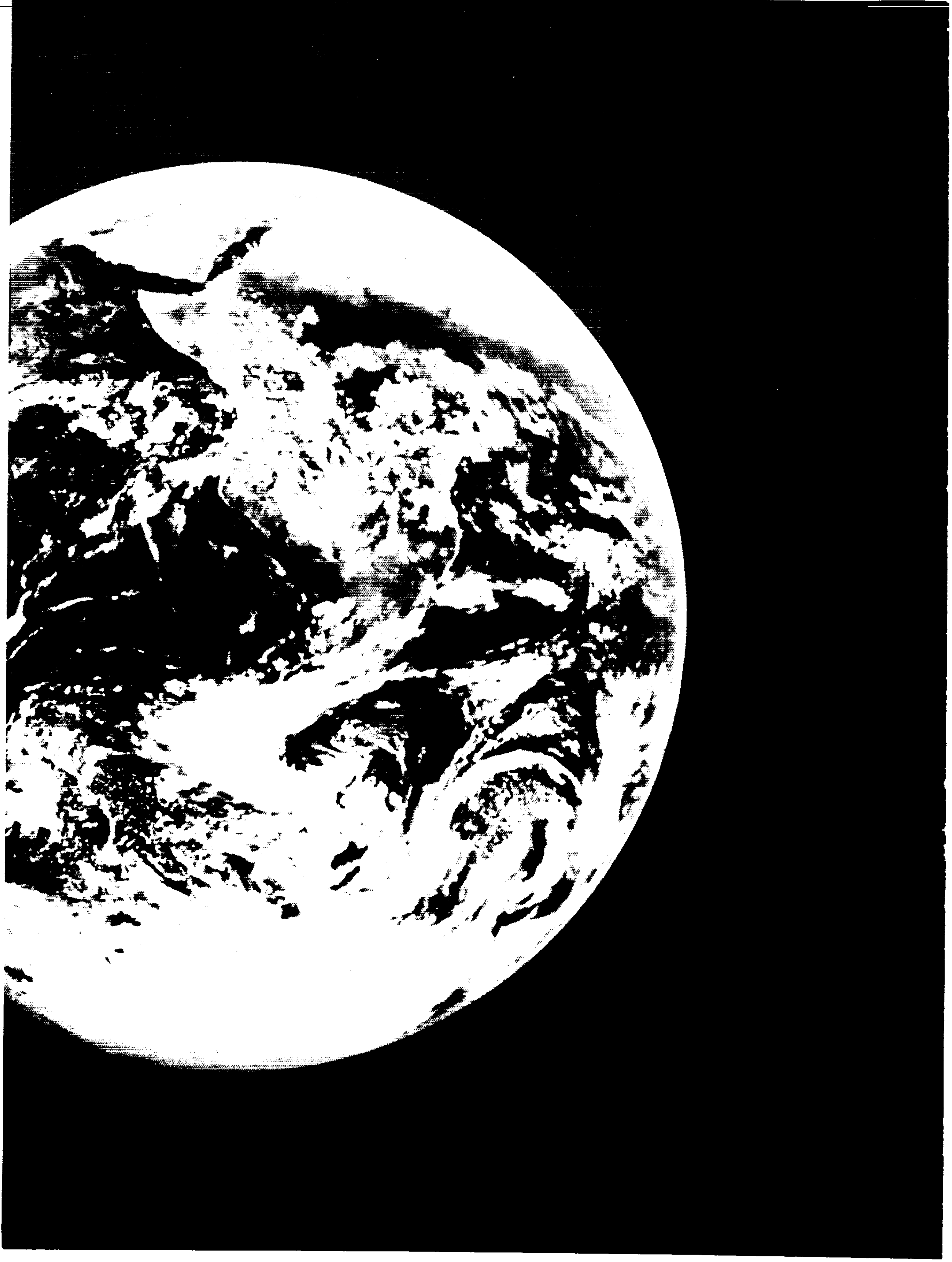

Research Programs

Skylab offered a large orbiting research platform to perform numerous investigations in space science. These included observations of the Sun, stellar and galactic astronomy, and comet observations; measurements of cosmic rays, isotopic abundances in the magnetosphere, neutron fluxes, and ultraviolet airglow in the Earth's atmosphere; and studies of the orbital environment. Space science research performed from orbit, pioneered during the *Skylab* missions, continued during the Spacelab era.

Today, space science research at MSFC has dramatically broadened from the days of *Skylab*, but remains highly selective, concentrating on centers of excellence in Earth and space science. Earth system science research includes investigations of the hydrologic cycle, global atmospheric modeling, aerosol backscatter experiments, lightning research, and global climate measurements, including those related to long-term global temperature changes. Many of these studies contribute to NASA's Mission to Planet Earth, a large-scale, unified study of our planet as a single, dynamic system.

Solar physics research is concentrated on understanding the mechanisms of solar variability. Space plasma physics research includes studies of the transport of energy from the solar wind toward the Earth, dissipating energy in the ionosphere and atmosphere, resulting in the escape of atmospheric gases in space.

Astrophysics research emphasizes x-ray and gamma-ray astronomy and cosmic-ray research. Exciting results from the Burst and Transient Source Experiment (BATSE) have revolutionized our understanding of gamma-ray bursts.

MSFC's leadership position in microgravity science evolved directly from the Center's historic role in the scientific utilization of crewed space systems. The first opportunity to perform long-duration, low-gravity experiments was during the flights of *Apollo* 14, 16, and 17, when several "suitcase" experiments were flown. The first opportunity to conduct experiments in a dedicated space-based facility was on the *Skylab* space station. With Spacelab, the program has expanded greatly. For example, over the past 8 years more than 50 payloads have been flown aboard Spacelab in the orbiting space shuttle.

Microgravity research at MSFC is focused on materials science and biophysics. An extensive ground-based and flight research program continues in electronic and photonic crystal investigations and protein crystal growth. The latter includes expanded work to determine the atomic structures of the human immunodeficiency virus (HIV) and HIV-related retroviruses.

Gregory S. Wilson, Director
Space Science Laboratory

Earth System Science

Numerical Modeling of Nonlinear Baroclinic Fluid Systems

Timothy L. Miller/ES42
205-544-1641

In developing an understanding of the processes that affect global change of the planet Earth, a component that offers one of the greatest challenges is the fluid system comprised of the atmosphere and oceans. Clearly, the objective of understanding this system is an important one since the atmosphere is the fluid system in which we live, which supplies the land with fresh water, and which shields life from harmful solar radiation. Due to the complex nature of this system and the difficulty in obtaining sufficient observational data on it, accurately predicting or even understanding its behavior for all but very short time periods remains an elusive goal. The goal of the research efforts described here is to develop a better understanding of the Earth system through the use of computer models that allow the study of the complicated behavior of a rather simple fluid system that is driven by horizontal temperature gradients and influenced by rotation.

One of the means for studying the behavior of the Earth's atmosphere and oceans is to conduct laboratory experiments in cylindrical and spherical containers where a fluid such as water is differentially heated and rotated. Depending upon the strength of the differential heating and the rate of rotation, the flow may be very simple—steady in time and axisymmetric in structure. For other values of the heating and rotation, the flow may be made of steady, regular waves, or it may be quite irregular and chaotic. Such experiments have been conducted in the laboratory, both at MSFC and elsewhere, and a numerical model developed at MSFC is being used to test the ability to predict the type of flow and to assist in the development of an understanding of such processes as heat and momentum transport. Studies are being performed additionally to help design future space-flight experiments using the Geophysical Fluid Flow Cell apparatus described below.

The model has been developed for the study of these flows (geophysical fluid flow simulator (GEOSIM)), and is able to study either spherical or cylindrical flows. Analysis of the flows proceeds in several steps: calculation of the axisymmetric flow (that which would be seen if no variations in longitude are allowed); calculation of the linear stability of that flow to three-dimensional (3–D) wave perturbations; calculation of the wave amplitude where interaction between the wave and the longitudinal mean flow is allowed; and, finally, the calculation of the fully nonlinear flow with full interaction between all components of the flow. The extent to which each of these steps can be directly applied to the actual flows depends upon the nonlinearity of the flow, which in turn depends upon the experimental parameters. For highly nonlinear flows, time series of images of the predicted flow are produced, and these are shown in computer animations to illustrate the interactions between various types of structures in the flow.

Recent work has placed emphasis on vacillatory flow in the baroclinic annulus experiments. The flow occurring in the gap between two concentric, co-rotating cylinders that are differentially heated is computed with high resolution and, typically, for several tens-of-rotational periods. For certain combinations of rotation rates and temperature differences, the resulting flow is 3–D and undergoes a periodic oscillation in the amplitude of the "wave" part of the structure. Agreement between the computer simulations and previous laboratory experiments is very good. The computer calculations allow the investigation of more cases than have been done experimentally. This work has resulted in the demonstration that a numerical model can be used to identify the boundaries of regions in parameter space that are deterministically predictable, as opposed to regions in which the result is highly sensitive to numerical and physical parameters. An investigation into the mechanics of the various flow regimes is continuing.

Miller, T.L.; Lu, H.I.; and Butler, K.A. 1992. A Fully Nonlinear, Mixed Spectral and Finite Difference Model for Thermally-Driven, Rotating Flows. *Journal of Computational Physics* 101:265–75.

Lu, H.I.; Miller, T.L.; and Butler, K.A. 1993. A Numerical Study of Wavenumber Selection in the Baroclinic Annulus Flow System. Submitted to *Geophysical Astrophysics Fluid Dynamics.*

Sponsor: Office of Mission to Planet Earth

■

Diagnostics of the Global Hydrologic Cycle

Franklin R. Robertson/ES42
205–544–1655

The prominent role of water in all three phases of the global hydrologic cycle distinguishes Earth's physical climate system from those of its planetary neighbors in the solar system. Moisture transport and phase changes constitute the essential link in converting incident solar radiation to kinetic energy of the atmosphere-ocean system. The thrust of this research program is to understand how the cycling of water, particularly within the Earth's atmosphere, helps determine the character of climate on different time and space scales. Near-term research centers upon understanding the role of hydrologic process in governing reservoirs of water on Earth (i.e., the mass cycling of water), and upon understanding the radiative implications of clouds and water vapor on climate variability. This approach carries an emphasis on merging remotely sensed data from space with conventional gridded analyses of atmospheric state variables (e.g., wind, temperature, and humidity) available from operational numerical weather and climate prediction centers.

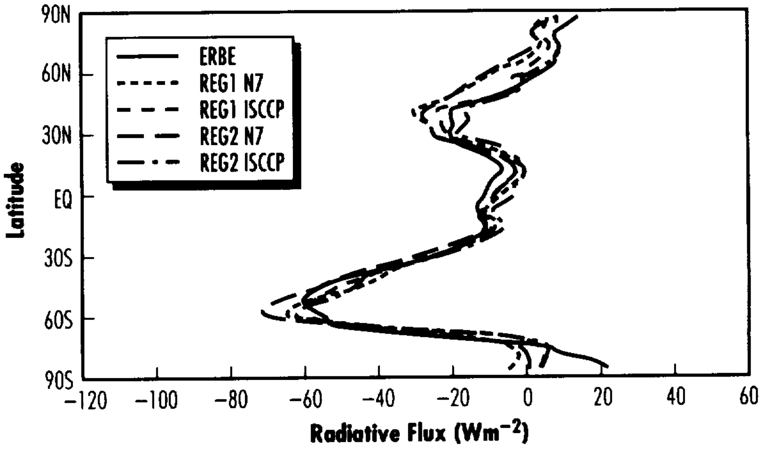

FIGURE 11.—Latitudinal distribution of zonal average net CRF obtained from three methodologies (ERBE, REG1, and REG2) and two cloud data sets (N7 and ISCCP).

One research effort examined the effects of clouds on global and zonally averaged temperatures. Low clouds tend to reflect more solar radiation than they trap terrestrial or long-wave radiation. This yields a net cooling effect on the Earth system. Conversely, high clouds tend to trap more terrestrial radiation than they reflect incident solar radiation. Earlier estimates suggested that the net effect of clouds, known as cloud radiative forcing (CRF), was to slightly cool the Earth's system. However, the amount of estimated cooling ranged from about 2 to 27 Wm^{-2}. Using three different methods of computing CRF from satellite solar and long-wave estimates, each employing data from February and March 1985, an estimate of approximately 17 Wm^{-2} net cooling was found. Furthermore, the largest disagreement between methods being 3.5 Wm^{-2}, we were able to demonstrate that earlier disagreements were primarily due to use of different data sets and analysis times.

From a water mass cycling standpoint, we have continued to investigate combining column-integrated atmospheric water vapor from the spaceborne Special Sensor Microwave Imager (SSM/I) with kinematic constraints from global gridded analyses (e.g., those produced by the European Center for Medium Range Weather Forecasts (ECMWF)) as a means of reconstituting vapor, cloud, and precipitation in three dimensions and in time. This basic formalism is what is termed a semiprognostic assimilation procedure, since only the evolution of the moisture fields is being predicted. Horizontal wind fields and vertical motions from ECMWF gridded analyses have been used to drive conservation equations for vapor, liquid, and ice. These equations, which also use bulk parameterizations of cloud microphysics (e.g., condensation, autoconversion, collection, precipitation evaporation, and fallout) are updated, or constrained in such a way that where SSM/I observations are available in space and time, the evolving model vapor is "nudged" to those values.

The moisture fields reconstructed from this methodology have been compared to available cloud climatologies such as the International Satellite Cloud Climatology Project (ISCCP). Such comparisons allow scientists to understand how cloud fields and water vapor distributions are governed by large-scale transport processes and ensemble convective processes (fig. 11).

Sohn, B.J., and Robertson, F.R. 1993. Intercomparison of CRF: A Zonal and Global Perspective. *Bulletin of the American Meteorological Society* 74:997–1006.

Sponsor: Office of Mission to Planet Earth

Mesoscale Modeling Related to the Hydrologic Cycle

William M. Lapenta/ES42
205-544-1667

The need to better understand the hydrologic cycle and the moist processes affecting that cycle, before the impact of observed Earth system changes such as increased carbon dioxide (CO_2) can be accurately predicted, is well documented. As a result, several scientists at NASA have been using a mesoscale modeling system, the Limited Area Mesoscale Prediction System (LAMPS), to aid in understanding more about the hydrologic cycle. With the importance of global change and as the observing phase of the Global Energy and Water Cycle Experiment (GEWEX) Continental International Project (GCIP) approaches, it is particularly appropriate that the hydrologic cycle be investigated, with special emphasis on the impact of smaller atmospheric scales. Below is a brief description of several ongoing projects at MSFC that employ LAMPS to better understand moist atmospheric processes associated with the hydrologic cycle.

It is well known that air-sea interactions have a profound impact on atmospheric circulations and, therefore, can affect the meridional atmospheric transport of heat and moisture. Such circulations include rapidly intensifying cyclones off the East Coast of the United States during winter months. The influence of air-sea interaction processes associated with sea-surface temperature patterns on these systems is currently being investigated. Differential heating and moistening of the lower atmosphere across the north wall of the Gulf Stream is thought to force mesoscale baroclinic circulations in the marine atmospheric boundary layer that provides an energy source for the explosively deepening cyclone. However, the above hypothesis is based primarily on statistical data and has not yet been confirmed through other scientific research techniques. Therefore, a series of sensitivity experiments using four-dimensional (4–D) data assimilation has been conducted over the past 2 yr using LAMPS to test this hypothesis. Significant findings include: (1) that a 4–D data assimilation can be successfully employed within a sensitivity test framework to investigate air-sea interaction processes, (2) the sea surface temperature gradient associated with the Gulf Stream's north wall forces a region of enhanced baroclinity within the atmospheric marine boundary layer through differential heat and moisture fluxes, (3) a negative correlation was found between the strength of the low-level baroclinity and cyclone intensity that directly opposes the hypothesis of many other investigators, (4) a positive correlation was found between cyclone intensity and reduced lower tropospheric stability, and (5) increased evaporative fluxes had a positive impact on cyclone intensification through subsequent latent heat release associated with precipitation processes.

Another LAMPS-related project involves the impact of sampling frequency on heat and moisture diagnostics. For many years, diagnostic studies of heat and moisture budgets for large-scale circulations have been studied by evaluating the difference between the large-scale heat and moisture tendencies and their associated advective fluxes calculated from the circulation and thermodynamic fields. In preparation for the CGIP, this project has focused on the impact of spatial and temporal sampling frequency on the diagnostic heat and moisture budgets for several convectively active systems over the midwestern United States. Mesoscale model simulations have been used to test the impact of "observation resolution" on the accuracy of the diagnostics. The observation resolution is varied by sampling the model simulations at various spatial and temporal intervals. Preliminary results to date include the following: (1) both heat and moisture budgets vary as spatial and temporal sampling is changed, and (2) individual vertical profiles of heating and moistening indicate that at least one of the quantities significantly affected by horizontal sampling is the horizontal advection term at midlevels.

Sponsor: Office of Mission to Planet Earth

■

Lightning Radiative Transfer Inversion Studies

William J. Koshak/ES43
205–544–8749

Measurements of cloud-top lightning optical waveforms have been collected from high-altitude U–2 aircraft flights above thunderstorms. A study of the diffuse, cloud-top lightning illuminations may provide some knowledge about the embedded lightning source emission (including the source brightness, rise-time characteristics, pulse width, and source location and geometry). Measurements of the cloud-top optical waveforms may also provide some useful knowledge about the microphysical state of the thundercloud within which the lightning source is embedded (e.g., properties such as the number distribution of cloud particle scatterers, the cloud particle composition, orientation, and spatial distribution). In addition, these measurements might be useful in retrieving the bulk electromagnetic properties of the cloud such as the bulk permittivity, ε, and permeability, μ.

Because thunderclouds are finite, three-dimensional, and multiple-scattering media, and because a lightning discharge is a spatially tortuous and a highly transient phenomena, MSFC currently employs complex radiative transfer modeling techniques. A Boltzmann transport model with diffusion approximations, commonly applied to the problem of nuclear reactor analyses, has been developed to track source photons throughout the thundercloud medium. Using this forward radiative transfer model, cloud-top waveforms have been generated that closely resemble actual U–2 optical pulse sensor (OPS) data sets.

To obtain useful information about the properties of the lightning source, the inverse transfer problem has been investigated. A theoretical study of this transfer problem has revealed that the source strength, $\boldsymbol{f}$, (in units of intensity: W/m^2/sr) is related to a set of intensity measurements, $\boldsymbol{g}$, via a linear matrix equation:

$$\boldsymbol{g} = A\boldsymbol{f} + \varepsilon \qquad (1)$$

where ε is a column vector of measurement errors and kernel truncation errors. The elements of the kernel matrix, A, are given by:

$$A_{ij} \equiv 8\sum_{l=1}^{\infty}\sum_{m=1}^{\infty}\sum_{n=1}^{\infty} \qquad (2)$$

$$\left[\varphi_{lmn}(r_i) - {}^{3D}\!/_{c}\,\Omega_i \bullet \nabla\varphi_{lmn}(r_i)\right]$$

$$\varphi_{lmn}(r_j)e^{-\lambda^2_{lmn}(t_i - t_j)}$$

where D is the diffusion coefficient, φlmn is an eigenfunction with corresponding eigenvalue, λlmn, V is the volume of the cloud, and the variables ($\boldsymbol{r}$, $\boldsymbol{\Omega}$, t) are the fundamental location, direction, and time variables, respectively, in the transfer problem. The eigenfunction and eigenvalue depend on the geometry of the cloud, and the diffusion coefficient depends on the cloud scattering properties. In effect, the kernel matrix contains all that is needed (given model assumptions) to relate measured optical signals to source emissions. A formal inversion of the kernel matrix provides a solution for the source location and brightness.

Sponsor: Office of Mission to Planet Earth

■

Defense Meteorological Satellite Program Optical Linescan System Data System Global Survey of Lightning

Steven J. Goodman/ES42
205-544-1683

This project is an effort to develop a climatology of lightning activity from the nighttime Defense Meteorlogical Satellite Program (DMSP) Optical Linescan System (OLS) images and to interrelate the lightning to the SSM/I brightness temperature and precipitation data base for the F8, F10, and F11 series. In addition, this research supports the design and development of a DMSP climate archive data base at the National Snow and Ice Data Center. Though the archive data are not yet routinely available to the user community, the Air Force Global Weather Central has been reliably copying DMSP data to 8-mm tapes and shipping them to the National Oceanic and Atmospheric Administration (NOAA) National Geophysical Data Center (NGDC) archives in Boulder, CO, since September 1992.

The F8 OLS lightning data were digitized for comparison with global rainfall estimates for the period August to November 1987. The F8 lightning map for August 1987 is shown in figure 12. MSFC scientists' participation in the WETNET Precipitation Intercomparison Project 1 (PIP1) consisted of submission of the Navy Cal/Val precipitation algorithm to serve as a baseline rainfall estimate covering the same August to November time period.

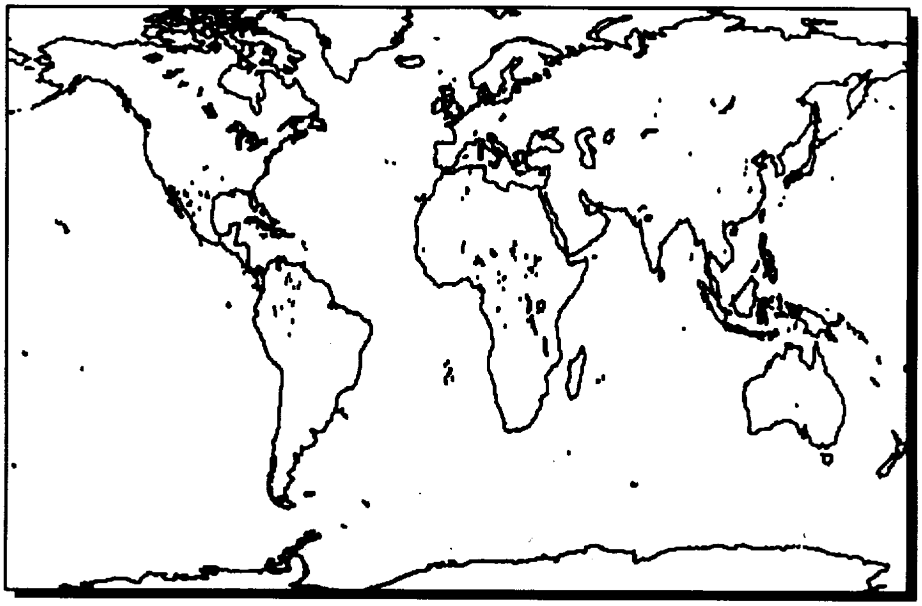

FIGURE 12.—Flag DMSP F8 OLS lightning August 1987 (ASC/DESC 0635/1835 UTC).

In order to ensure that the Cal/Val algorithm was implemented properly using the WETNET test data set, we compared the brightness temperatures derived from SSM/I antenna temperatures (TA's) using both Wentz and Navy methodologies. No statistically significant differences were found to exist, implying that the Cal/Val rainfall algorithm estimate is the same whether Wentz or Navy SSM/I brightness temperatures (TB's) are used as the input data to the algorithm (fig. 13). This result permits us to compare precipitation algorithms based on Wentz TB's with the operational Cal/Val algorithm. The goal is to ultimately compare the thunderstorm activity (derived from the OLS lightning data base) with the various algorithm estimates of rainfall. The value of this study to NASA's mission is to develop improved global rainfall estimates for the Mission to Planet Earth program. The practical benefit is that we believe we have discovered the major source of error in the current operational SSM/I rainfall algorithm used by the U.S. armed forces. We have suggested that the algorithm be recalibrated with another independent data set, such as the AMEDAS combined radar/rain gauge surface rainfall data base collected in Japan during the Algorithm Intercomparison Project 1 (AIP1) as part of the World Meteorological Organization (WMO) sponsored Global Precipitation Climatology Project. This can be accomplished using nonlinear regression modeling of the observed brightness temperatures against the surface rainfall data set in a like manner that was performed in the original development of the algorithm at the University of Wisconsin.

Initial intercomparisons show that the Cal/Val algorithm generally underestimates monthly rainfall by a factor of two when compared with other rainfall algorithms. It has been found that the chief source of error from the Cal/Val rainfall algorithm is attributable to the "ground-truth"

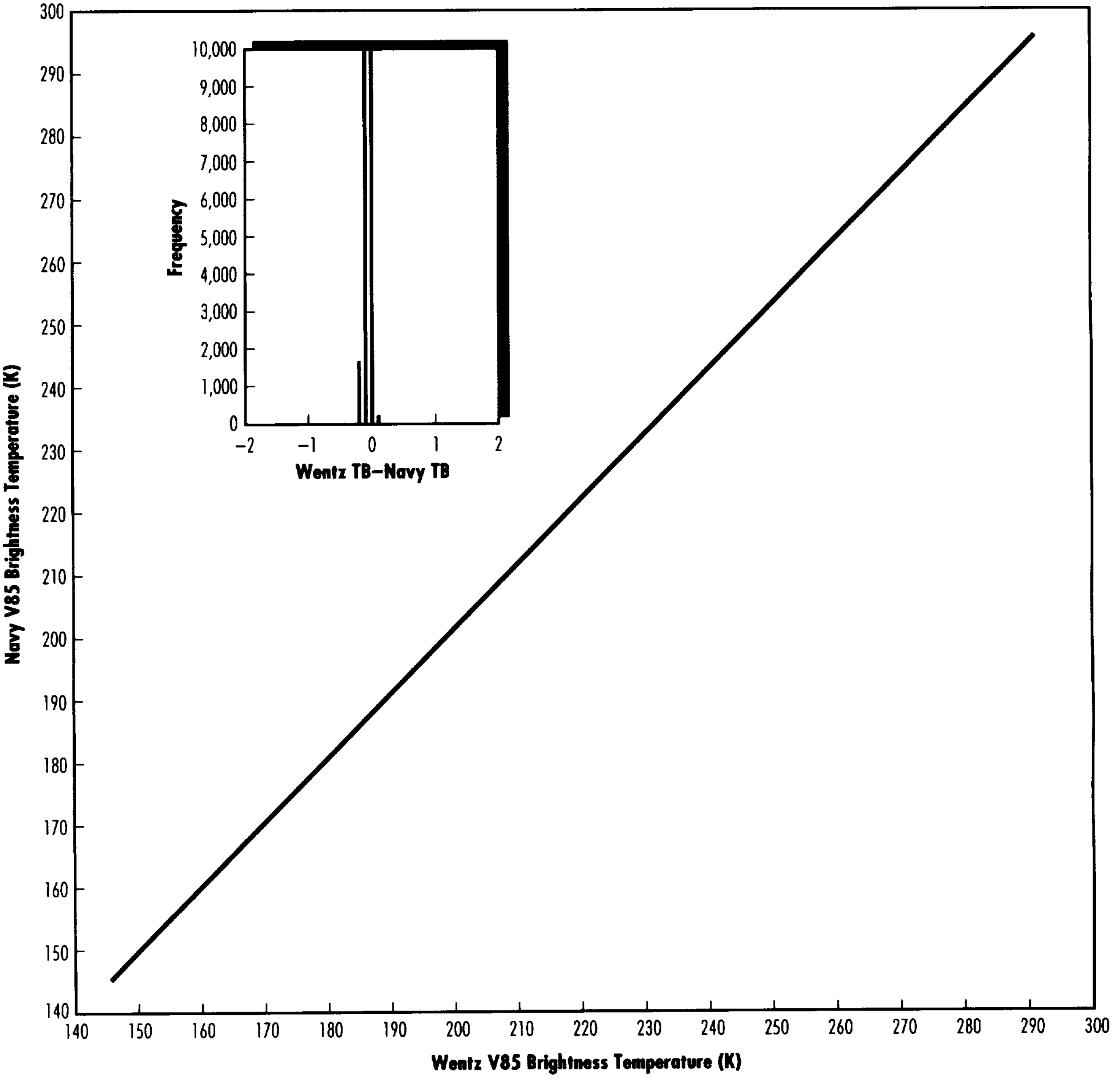

FIGURE 13.—Scatterplot of Wentz versus Navy (Cal/Val) V85 brightness temperatures for August 16, 1987—rev 806 (ascending)—land/ocean data.

data set used to calibrate the algorithm. The calibration data set apparently did not contain a representative sample of high rain-rate events. Thus, the low rain-rate statistics cause the algorithm to be biased towards the lighter rain events.

Goodman, S.J.; LaFontaine, F.J.; Huffman, G.J.; and Adler, R.A. June 1993. An Intercomparison of the Navy Cal/Val and SSM/I Pathfinder Precipitation Algorithms, Shared Processing Network (SPN). Special Sensor Microwave/Imager (SSM/I) Algorithm Symposium. Monterey, CA.

Sponsor: Office of Mission to Planet Earth

University Involvement: University of Wisconsin

■

Global Aerosol Backscatter Experiments

Maurice A. Jarzembski/ES43
205-544-0240

Accurate remote sensing of tropospheric wind profiles from a space-based lidar depends on adequate aerosol backscatter availability. Strength of the atmospheric backscatter determines the signal-to-noise ratio (SNR) of the return signal. The key to the lidar's performance is its sensitivity, the maximization of which requires use of an optimum operating wavelength. Research efforts at MSFC involve assessment of global patterns of backscatter, including both theoretical and experimental studies of atmospheric aerosol scattering properties using data from NASA's Global Backscatter Experiment (GLOBE).

The GLOBE program involves cooperative research efforts among universities, other NASA centers, other government agencies, and international organizations, under the scientific direction of MSFC. Major experimental efforts include a network of CO_2 lidar stations, intensive lidar field campaigns in remote locations, satellite-based aerosol measurements, and laboratory-based calibrations of the various aerosol sensors. These include direct measurements of aerosol scattering properties at selected laser wavelengths and information on aerosol physical, chemical, and optical properties needed to model aerosol scattering properties at other wavelengths where no direct measurements are available. Also, some sensors provide information on aerosol properties in locations where no direct measurements have been obtained. The most important measurement program was the GLOBE backscatter flight survey missions over the Pacific Ocean in fall 1989 (GLOBE I) and spring 1990 (GLOBE II).

Diverse measurements from these field campaigns have been compiled in a centralized GLOBE data base, designed and implemented at MSFC. The data base uses a high-end UNIX workstation, magneto-optical disk mass storage, Ethernet connectivity to MSFC computing resources, Internet connectivity to other GLOBE researchers, advanced data visualization/analysis software, and hierarchical data format (HDF) archival. Detailed intercomparison and quality control of the data sets are being performed.

Case studies for several GLOBE II flights have been accomplished for relationships among various aerosol parameters. Intercomparisons are made with meteorological data from European Center for Medium-Range Weather Forecasting global gridded analyses and geostationary satellite data in an effort to establish the extent of correlation between aerosol backscatter and meteorological variables. Of all the meteorological variables examined, relative and specific humidity exhibit significant correlation with aerosol backscatter. Figure 14 shows time series of correlation between vertical profiles of measured aerosol backscatter mixing ratio and large-scale gridded relative humidity field from ECMWF data for GLOBE II flight 12. The correlation studies indicate two principal modes of statistical behavior, with high correlation between backscatter and relative humidity in maritime air masses, and lower correlation in jet streams near and downstream from large landmasses. Physical, chemical,

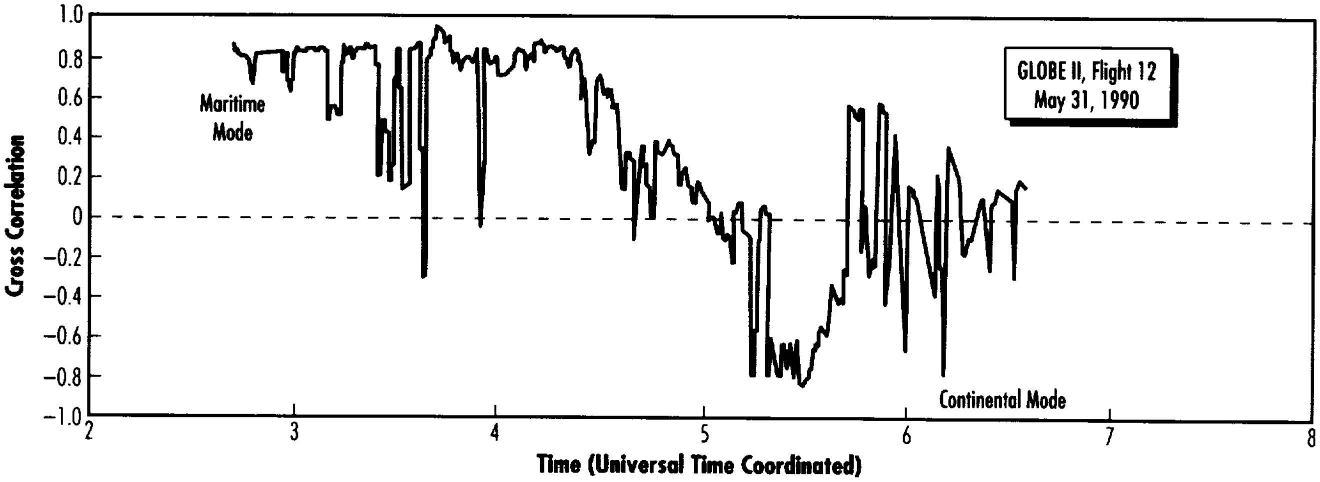

Figure 14.—Correlation of pulsed lidar measurements with relative humidity measurements.

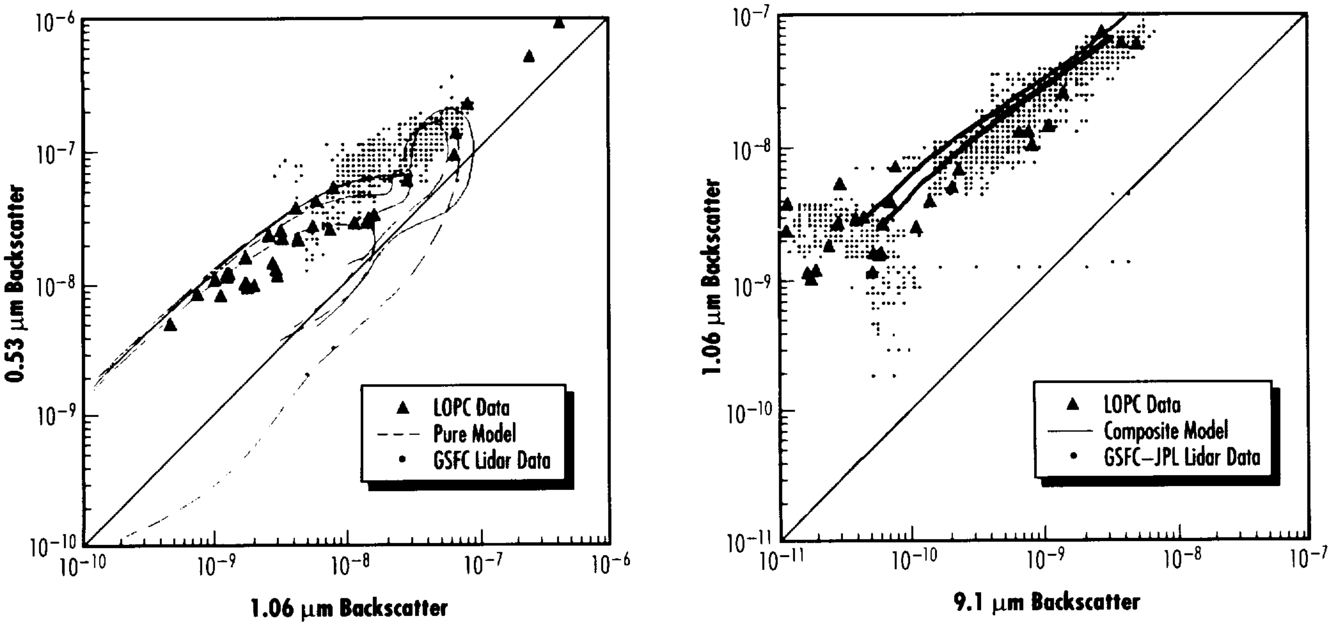

LOPC: Laser Optical Particle Counter GSFC: Goddard Space Flight Center JPL: Jet Propulsion Laboratory

FIGURE 15.—Comparison of pulsed lidar data, microphysics data, and modeled aerosol backscatter.

and optical properties are modeled for major aerosol types and used to estimate typical ranges of aerosol backscatter values for each aerosol type and compared with direct aerosol backscatter measurements. An example is shown in figure 15 as cross-plots of aerosol backscatter coefficients at selected pairs of laser wavelengths. Pulsed lidar measurement values (dots) from flight 12 were obtained between 6.5 and 7.5 km altitude. Backscatter calculations from aerosol microphysical measurements obtained from University of Hawaii Laser Optical Counter (triangles) compare very well with lidar data at various wavelengths. Modeled values (curves) were computed from Mie scattering for typical atmospheric aerosol compositions (sulfuric acid, ammonium sulfate, and dust), using log normal distributions with constant mass concentration of 1.0 μg m^{-3} and geometric mean particle sizes from 0.01 μm (left terminus of curves) to 10 μm (right terminus of curves). Modeled backscatter for various aerosol compositions provide an envelope for the variations in measured data; however, composite aerosol models of a mixture of the various compositions lead to an average backscatter that is in good agreement with measurements. Such intercomparisons between various measurements and modeling provide empirical conversion factors to enable estimation of aerosol backscatter at any required wavelength from direct measurements of aerosol backscatter made at only specific wavelengths. Results are being combined in a preliminary global-scale empirical model of aerosol backscatter properties at a prospective space-based lidar wavelengths.

Bowdle, D.A. 1992. Global Backscatter Experiment (GLOBE) Results: Aerosol Backscatter Wavelength Dependence and Global Distribution. *National Aeronautics and Space Administration Conference Publications* 3158, part 1:57–60. Sixteenth International Laser Radar Conference. Massachusetts Institute of Technology, Cambridge, MA.

Cutten, D.R.; McCaul, E.W., Jr.; Spinhirne, J.D.; Menzies, R.T.; Pueschel, R.; Clarke, A.D.; and Bowdle, D.A. 1993. Comparison of Remotely Measured Multispectral Scattering Parameters for Tropospheric Aerosols. *Technical Digest* 5:403–6. Topical Meeting on Optical Remote Sensing of the Atmosphere. Optical Society of America, Washington, DC.

McCaul, E.W., Jr.; Bowdle, D.A.; Cutten, D.R.; Menzies, R.T.; and Spinhirne, J.D. 1993. Relationships Between Lidar Backscatter and Meteorological Fields. *Technical Digest* 5:407–10. Topical Meeting on Optical Remote Sensing of the Atmosphere. Optical Society of America, Washington, DC.

Sponsor: Office of Mission to Planet Earth

■

Global Atmospheric Modeling

Daniel E. Fitzjarrald/ES42
205–544–1651

There are many pitfalls on the path to producing a predictive capability for the climate. Numerical models offer the best hope for a theoretical description of climate dynamics that could lead to prediction, since they can capture the essential nonlinearities and the myriad of complications. But model calibration and validation, crucial steps in developing any believable theory, remain elusive. It is not enough to validate against the present climate to draw a portrait of the subject, so to speak. Because the subject will not stand still, it is necessary to get all the parts right and bring the subject to life. The real use of predictive capability will not likely be a sort of next-generation climate forecast (who would be in charge of validation, anyway, this generation or the next?), but rather will be used in conducting sensitivity studies and scenarios for different courses of action or for mitigation. All the parts of the simulation must be right in order that the dependence on all the variables can be correct, for it is not known ahead of time which ones will be changed.

In looking at global warming, for example, in response to increased CO_2 or other radiatively active gases, there are many aspects of the atmosphere and ocean system that may change. Many of these changes that are of critical interest involve water substance. Both in estimating the local effects of a given climate change (droughts, etc.) and in predicting the climate change itself, moisture and its transport are indispensable quantities. For example, an increase of temperature from global warming should increase the atmospheric moisture because the air can hold more water vapor. The amplitude of the mid-latitude eddies may therefore increase because of added latent heat release in the storms, or the amplitude may decrease because of increased latent heat transport in the warmer air. The final result may be a combination of these effects, with the increase at smaller scales and the decrease at larger scales. If the relevant parameterizations and model resolution are not adequate, the wrong conclusion may be drawn from model simulations.

Scientists at MSFC are using global atmospheric data to evaluate the performance of the Genesis global atmospheric model, which was developed at the National Center for Atmospheric Research. We are concentrating on the moisture variables; i.e., precipitable water, rainfall, cloud amount and type, etc. The annual and interannual variations in the observed data provide a good testing ground, allowing the response of the model to be evaluated and compared with the present climate. Approximately a decade is available for comparison and analysis, including 13 yr of the Microwave Sounding Unit (MSU) data (tropospheric and stratospheric temperature and rainfall over water). We have made a run of 10 yr at low resolution (15 waves resolved around the globe) using observed sea surface temperatures (SST) and have compared them with MSU-derived temperature and rainfall. Also available for use are two control runs of 10 yr at the same resolution, one with the simple quasi-swamp ocean model and another with prescribed climatological SST. The latter control run allows the intrinsic variations of the model to be compared with the observations, so that the effects of realistic SST forcing can be separated from the intrinsic chaotic variations of the model climate when the SST forcing is the same from year to year. The analysis techniques of these data include comparing the variances and computation of principal components of variation. The position and strength of persistent features such as storm tracks, monsoons, and the Intertropical Convergence Zone (ITCZ) will also be useful in validating the model performance and identifying areas for improvement in moisture parameterizations.

Model resolution will also be varied, within limits, to find a happy medium between improvement of the simulation and manageability of data. Our experience, and that of others, using the prior generation of global climate model was such that increasing the model resolution does not always improve the simulations, that is, make the results look more like the real atmosphere. It has been speculated that these inadequacies were due to the cumulus parameterization, the surface hydrology model, or the tuning of other parameterizations. The surface hydrology, cumulus parameterization, and other parameterizations have been improved in the Genesis model. So, leaving aside some amount of tuning that may be necessary, it is expected that the Genesis simulation will do better at higher resolution. We plan to make at least part of a decade-long run with prescribed SST's, along with a climatological control, at higher resolution (42 waves around the globe).

Sponsor: Office of Mission to Planet Earth

■

Spatial/Temporal Variability of Wind Fields for Design of Remote Sensors

Michael Susko/ES43
205-544-1660

The primary objective of this research project is to report on the spatial and temporal variability of atmospheric flow fields in the troposphere and lower stratosphere for developing design criteria information for remote sensors of satellites. The analysis of the bivariate parameter wind speed differences between the FPS–16 Radar/Jimsphere Wind System and NASA's 50–MHz Radar Wind Profiler will reduce the uncertainties in performance studies of satellites and enhance the validation of the atmospheric and satellite performance studies. This study provides a quality check for satellite winds. Comparison of the flow fields in the troposphere and lower stratosphere of case studies of pairs of Jimsphere balloon releases and Radar Wind Profiler winds during space shuttle launches was performed. The statistics of the mean and standard deviation of the zonal component (u) and meridional component (v) and power spectra density curves show good agreement between the two wind sensors. The standard deviation of the u and v components for shuttle mission STS–37 (five Jimsphere/profiler wind profile data sets) was 1.92 m/s and 1.67 m/s, while for the STS–43 launch (six Jimsphere/profiler wind profile data sets) was 1.39 m/s and 1.44 m/s, respectively. The overall standard deviation was 1.66 m/s for the u component, and 1.55 m/s for the v component, and a standard deviation of 2.27 m/s for the vector wind.

The existing technology for the past three decades (1960's, 1970's, and 1980's) and the present decade (1990's) in measuring winds for the space shuttle launches, has been obtained by the balloon-borne FPS–16 Radar/Jimsphere system. NASA's 50–MHz radar now plays an important role in monitoring winds for substantial profile changes during the day of launch. These comparative data sets were evaluated and their spatial and temporal variability were reported (Susko 1993). The successful interpretation of satellite data depends on a reliable and proven wind sensor.

From NOAA's National Environmental Satellite Data and Information Service (NESDIS) and from the University of Wisconsin's Office of Research and Applications Laboratories, satellite winds obtained by the Geostationary Operational Environmental Satellite (GOES) were assessed. The GOES satellite operational wind measurements from the cloud motions during the space shuttle launches at KSC, FL, of STS–37 and STS–43 on April 5 and August 2, 1991, respectively, have been compared with the FPS–16 Radar/Jimsphere Balloon Systems wind measurements. The statistical results for STS–37 launch winds comparison were as follow: mean, 5.69 m/s; standard deviation, 4.37 m/s; and root mean square, 4.45 m/s. The results for the STS–43 launch wind comparison were: mean 5.91 m/s; standard deviation, 3.15 m/s; and root mean square, 4.41 m/s. For both launches, the overall mean was 5.8 m/s; standard deviation, 3.76 m/s; and root mean square, 4.43 m/s.

The following data analysis of the comparison of the wind components measured by the FPS–16 Radar/Jimsphere Balloon System and NASA's 50–MHz Radar Wind Profiler provides an excellent quality check of the winds provided by the GOES–7 satellite.

A comparison of the u- and v-wind components for the Jimsphere balloon and the Radar Wind Profiler is presented in figures 16 and 17 for STS–43 (Space Shuttle *Atlantis*). The Radar Wind Profiler wind data are computed for a length scale every 150 m, and averaged over 30 m, while the Jimsphere is computed for 30 m. Thus the Jimsphere/Profiler Wind Profile data sets are plotted and compared every 30 m. Figures 16 and 17 illustrate the u and v components comparison of winds aloft during the STS–43 launch. Six Jimsphere/Profiler wind data sets were compared at 0902Z, 1047Z, 1202Z, 1302Z, and 1517Z. The standard deviation for u-wind component differences was 1.39 m/s and 1.45 m/s for the v-wind component. The overall standard deviation for both launches was 1.66 m/s for the vector wind. These data sets provide excellent truth verification during assessment of the GOES–7 satellite data.

The results of satellite wind assessments using the visible infrared spin-scan radiometer atmospheric sounder (VAS) data to assign simultaneous heights and velocities of cloud motion winds CO_2 cloud tracking

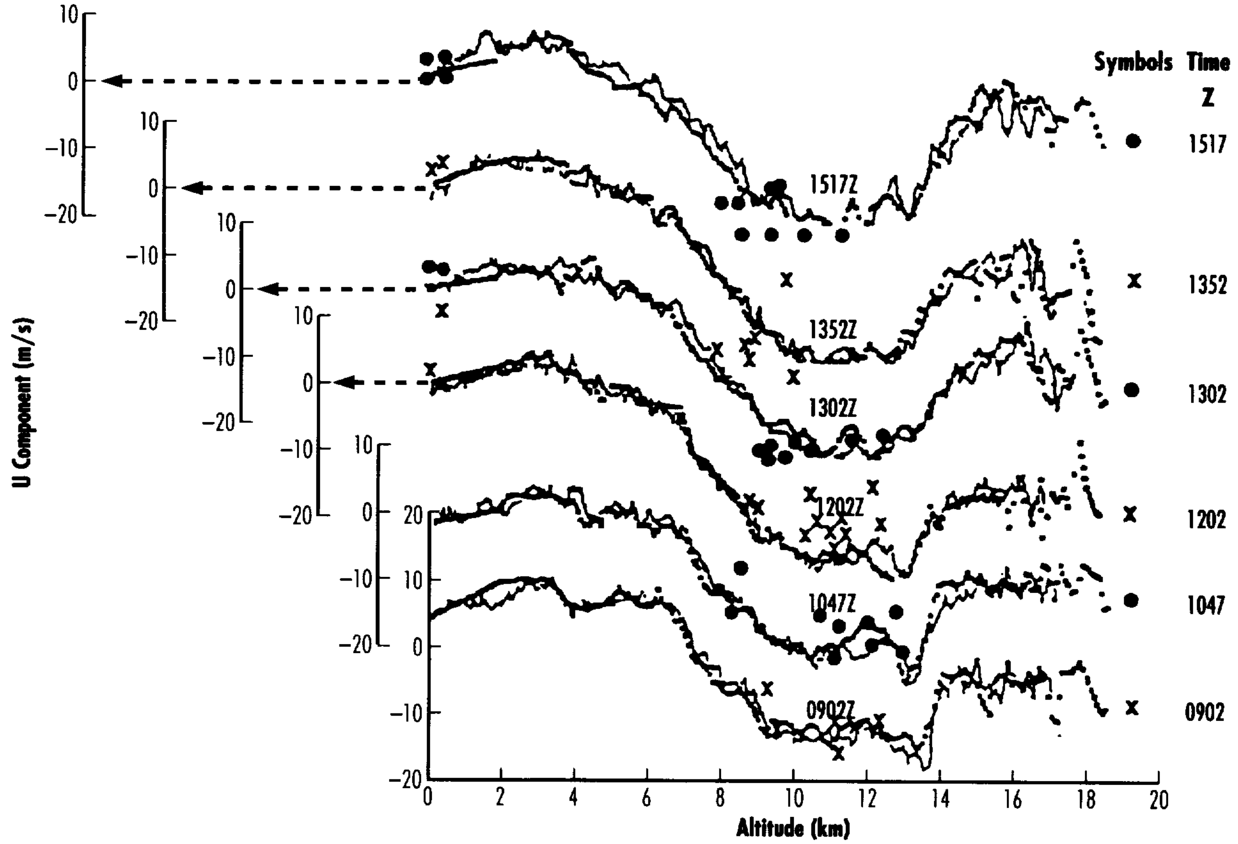

FIGURE 16.—Six u-wind components of the NASA 50-MHz Radar Wind Profiler overlayed on the wind profile of the FPS-16 Radar/Jimsphere measured during the STS-43 launch, August 2, 1991, at KSC, FL.

technique that combines the CO_2 slicing and absorption methods is presented. Tracking clouds at high, middle, and low levels can be accomplished by utilizing time sequences of CO_2 channel images as indicated by Menzel et al. This CO_2 slicing method improves cloud motion vector (CMV) winds determination.

High resolution of wind measurements from satellite imagery provides atmospheric motion through measurement of cloud displacement. If a sequence of cloud images from a geostationary satellite (GOES-7) move with the wind, it is possible to describe the motions of the atmosphere. Figures 16 and 17, with symbols x and o, indicate GOES-7 satellite wind data overlayed on the Jimsphere/Radar Wind Profiler data.

Methods used to derive the "cloud drift" require using good geostationary satellite images of fine geometric fidelity, with time intervals between image of approximately 30 min, the lifetime of the clouds being traced. In order to get a greater density of cloud motion vectors close to the KSC station, they were selected manually. This was done by choosing a target and following it by eye and letting the computer do the vectoring and pressure. This is the procedure used in assessing the CMV. The average distance of wind measurement between the GOES-7 satellite winds and Jimsphere winds was 65 km. The global comparison of satellite/Jimsphere balloon vector

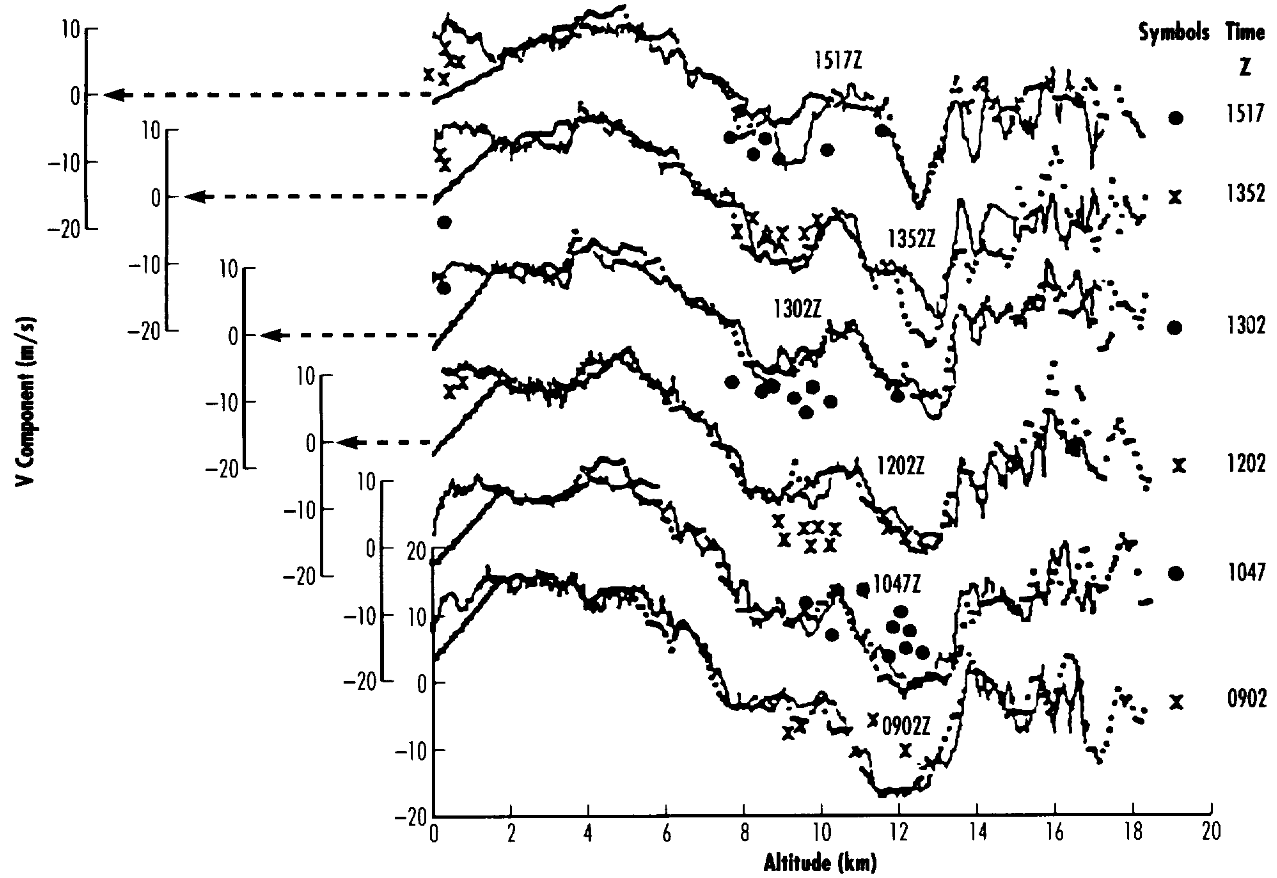

FIGURE 17.—Six v-wind components of the NASA 50-MHz Radar Wind Profiler overlayed on the wind profile of the FPS-16 Radar/Jimsphere measured during the STS-43 launch, August 2, 1991, at KSC, FL.

winds shows a standard deviation of 3.15 m/s for STS-43 and 4.37 m/s for STS-37. The overall standard deviation of the vector wind was 3.76 m/s and a root mean square of 4.43 m/s. It is demonstrated that this unique comparison of the Jimsphere and satellite winds provides excellent ground truth and a frame of reference during testing and validation of satellite data.

Herman, L.D. September 17–19, 1991. The Current Stage of Development of a Method of Producing Cloud Motion Vector at High Latitudes From NOAA Satellites. Proceedings EUM P 10, ISBN 92-9110-0072:21–26. Washington, DC.

Menzel, W.P.; Smith, W.L.; and Stewart, T.R. March 1983. Improved Cloud Motion Wind Vector and Altitude Using VAS. *Journal of Climate and Applied Meteorology* 22:377–84.

Susko, M. January 1993. Comparison of FPS-16 Radar/Jimsphere and NASA's 50 MHz Radar Wind Profiler. American Institute of Aeronautics and Astronautics (AIAA) paper 93-0758.

Sponsor: Office of Space Flight and Applications

University Involvement: University of Wisconsin

■

Earth Observing System Pathfinder Passive Microwave Data Set Production

H. Michael Goodman/ES44
205-544-8006

The Earth Observing System Pathfinder will provide access to large remote-sensing data sets applicable to global climate change research prior to the availability of data from the EOS satellites. The main goal of the Pathfinder program is to make research-quality, long-term global change data sets easily available to the Earth science community. The data sets currently selected are the GOES, the Advanced Very High Resolution Radiometer (AVHRR), Television Infrared Operations Satellite (TIROS) Operational Vertical Sounder (TOVS), the Scanning Multichannel Microwave Radiometer (SMMR), and the Special Sensor Microwave/Imager. The EOS Pathfinder project emphasizes the coincidence of multisatellite observations for global change research. A significant portion of the MSFC Pathfinder project involves the processing of SSM/I data from the Defense Meteorological Satellite Program F8 satellite.

The MSFC component of the Pathfinder project is focused on generating passive microwave antenna temperatures and geophysical products in the satellite projection (commonly referred to as a "swath projection"). The antenna temperature (T_a) data set includes spacecraft and timing information, latitudes and longitudes, calibration data, and surface-type indices. The derived geophysical products have not been fully defined but may include the following global parameters: ocean surface wind speed, columnar liquid water content of clouds, columnar water vapor, rain rate, land surface temperature, land surface type, microwave vegetation indices, and sea ice classification.

The SSM/I Pathfinder project is divided into two stages: benchmark and post-benchmark. The benchmark period extends from August 1987 to November 1988, and uses only data from the DMSP satellite F8 (launched June 19, 1987). The post-benchmark period extends from December 1988 to July 1994, when the Version Zero Earth Observing System Data and Information System (EOSDIS) becomes operational (see *MSFC Research and Technology Operating Report* 1992). The post-benchmark period includes data from DMSP satellites F8, F10 (launched December 1, 1990), and F11 (launched November 28, 1991).

The satellite sensor data for the benchmark period were preprocessed by Dr. Frank Wentz of Remote Sensing Systems. Dr. Wentz performed extensive quality control. The errors he identified—including geolocation and instrument calibration errors, plus others, such as missing, mislocated, or out-of-bound data—will be corrected or flagged by the MSFC Pathfinder processing. The resulting data sets will satisfy the main goal of the Pathfinder project.

SSM/I output data are stored in the hierarchical data format. HDF is a multiobject file format for the transfer of graphical and floating-point data between machines. It was developed by the National Center for Supercomputing Applications (NCSA). The HDF is the standard data format for data distribution in the Version Zero EOSDIS.

After quality control, the Pathfinder data will be archived on the MSFC Version Zero EOSDIS Distributed Active Archive Center (DAAC) optical disk storage device. The products are concurrently listed in the directory for access through the EOSDIS Information Management System. Distribution of the antenna temperatures and the geophysical products is in discrete granules (e.g., 1-mo periods) on 8-mm tape. The benchmark period SSM/I Pathfinder data will be available to the science community through the MSFC DAAC by the end of 1993.

Sponsor: Office of Mission to Planet Earth

Commercial Involvement:
Hughes/STX

■

Four-Dimensional Interactive Analysis Capability

Paul J. Meyer/ES44
205-544-1654

For the past 7 yr, an interactive capability to analyze four-dimensional (4–D) Earth science data sets has been under development. Development of this tool was performed at the Space Science and Engineering Center at the University of Wisconsin-Madison. This effort is nearly complete, and the final product is called Vis5D. The five dimensions the tool handles are the three spatial dimensions, time, and parameters. While developed for Earth science data sets, the tool has been used for other five-dimensional (5–D) data sets, including medical imaging. Capabilities of the tool include isosurface rendering, topography, streamlines, interactive 2–D slicing, and user-defined analysis.

One of the strengths of the tool is the ability to render multiple isosurfaces of the same parameter. In order to support this paradigm, an ability to render semitransparent graphics was necessary. For example, consider the outside of a thunderstorm and some intense rain shaft within the storm. Each may be measured by a cloud liquid water parameter; the outer cloud shell has a relatively low value and the rain shaft has a high value. This low value would be rendered in some specified, user-controlled color as a semitransparent object, while inside the rain shaft would be rendered in a complementary color as opaque. Essentially, one *sees* inside the storm.

The ability to interactively slice the 3–D volume with a color-mapped planar surface has greatly improved understanding as well. This may be done in concert with the isosurfaced rendering. The user may animate this slice in time, and/or may grip the slice and concurrently change the slice orientation. The slices may also be degenerated to simple contour plots in 2–D space.

The latest release of Vis5D provides an ability to place a 3–D probe into the data volume and determine the values of the physical parameters at that location in time and space. Also provided is an ability for the scientists to dynamically incorporate their own analysis function in the software. This allows for the derivation of variables from the current base parameters. This software currently runs on Silicon Graphics, IBM RS6000, and Stardent GS series computers. Support for Sun computers is being explored. It is publicly available via anonymous file transfer protocol (ftp) from:

vis5d.ssec.wisc.edu.

MSFC personnel have added support to ingest the HDF from the National Center for Supercomputing Applications.

Sponsor: Office of Mission to Planet Earth

University Involvement: University of Wisconsin-Madison

■

Evaluation of Thermosphere Density Models

Ronnie J. Suggs/ES44
205–544–7797

Spacecraft designing and mission planning depend heavily on a knowledge of the space environment. One aspect of the space environment continuing to be investigated is the modeling of the upper atmospheric density at orbital altitudes. This region of the atmosphere, called the thermosphere, has been investigated over the years through many NASA programs, resulting in the development of several thermosphere models currently used in the engineering community. It is the purpose of current investigations at MSFC to evaluate several of the major thermosphere models against recent satellite decay-derived density data.

The motivation for the investigations was the availability of recent satellite decay data from a good candidate satellite during a time of high solar activity, as measured by the 10.7-cm radio solar flux. Also, the solar activity level associated with these data was such that it approached values contained in the data bases used in formulating the models. Thermospheric density data obtained from satellite decay are currently the only source of recent density measurements available at orbital altitudes and, thus, provide the only means to evaluate the performance of thermosphere models and to identify systematic errors that may be present during the rise of the current solar cycle. It is known that the models show disagreement among themselves as to the effect of the solar cycle variation on the thermospheric density, especially at high values of solar activity where the models show a diverging trend. Evaluating the models at high solar activity is important because of their use in the aerospace community for predicting satellite decay lifetimes, including the space station reboost and rendezvous strategies during assembly, which are planned to occur during the rise of the next solar cycle. Further motivation is provided by the fact that some solar scientists predict that the next solar cycle may be one of the largest ever recorded (Wilson 1992).

During this past year, analysis was completed comparing four major thermosphere models, three of which are the Jacchia models J70, J71, J77, and the fourth, the MSIS86 model. The J70 model, with the addition of two modifications from the J71 model, makes up the Marshall Engineering Thermosphere (MET) model that has been selected as the baseline model for the space station program. The MET model is also contained in the thermosphere portion of the Global Reference Atmosphere Model 1990 (GRAM–90). The MSIS86 model forms the thermosphere portion of the most recent reference atmosphere, CIRA86.

The models were compared to the densities derived from the decay of the Long Duration Exposure Facility satellite for the rise and peak of the current solar cycle (cycle 22). The density data, which were average orbital values over periods of 1 to 4 d, were used to determine how well the models predicted the known long-term thermosphere variations that are longer than a solar rotation (27 d). Though the focus was on long-term variations such as solar cycle effects and the semiannual variation, some information was obtained on the models' performance in predicting day-to-day density variations. However, due to the sparseness of the LDEF density data set, short-term variations on the order of a day or less were not able to be analyzed.

Thermosphere model systematic errors associated with long-term thermosphere variations often show up in applications as a model bias error when working with time periods of 100 d or less. For longer periods, these errors are seen as time-varying bias errors that greatly affect orbital decay calculations. Analysts often correct for these bias errors in satellite decay work by adjusting the drag coefficient of the spacecraft in their models to agree with current tracking measurements. Analysts, in general, are aware that thermosphere model errors exist, but they are usually not familiar with the physical phenomena responsible for the errors or the degree of bias variability to expect from the thermosphere models. The LDEF analysis was an attempt to quantify the systematic errors present in the models and determine the phenomena responsible for the errors.

An important result found from the analysis was determining the time-varying bias error associated with the variation in density with the solar cycle. A comparison of the LDEF density data with the thermosphere model calculations (fig. 18) shows that the Jacchia models do well at modeling this variation for smoothed 10.7-cm solar flux values greater than 110. On the other hand, the MSIS86 model shows a diverging trend for this solar cycle region culminating to about a 10 percent over prediction in density at the peak of the current solar cycle. For higher values of solar flux that might be expected for very large solar cycles, the trends suggest

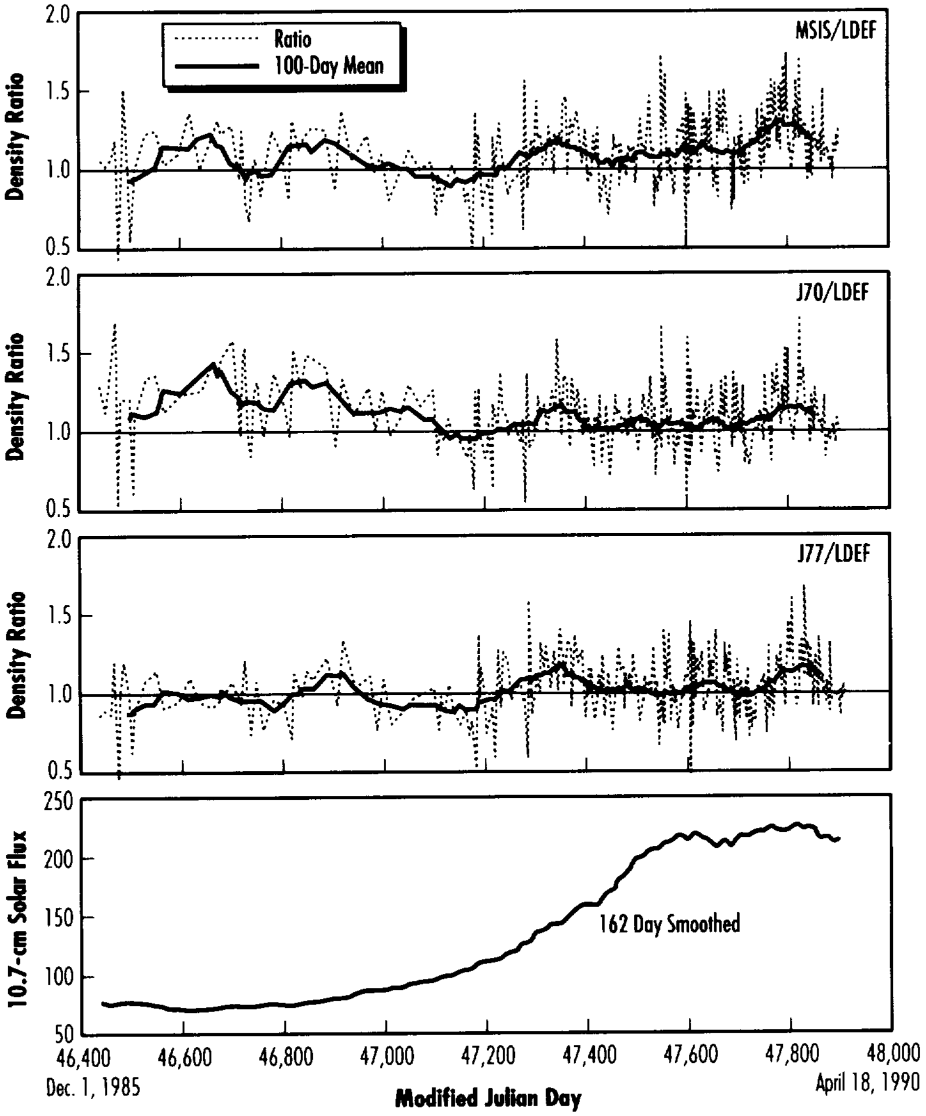

FIGURE 18.—Ratio of average densities calculated from the MSIS and JACCHIA models to the average densities derived from the decay of LDEF. The individual data points are not shown but connected by the dashed line. The bottom panel shows the variation in radio solar flux during the rise of the current solar cycle.

possible bias errors on the order of 20 percent. However, for solar flux values typical at solar minimum, the MSIS86 and J77 models appear to compare well, while the J70 and J71 models perform poorly by overpredicting the density on the order of 20–30 percent. The J77 model seems to do better overall in modeling the solar cycle variation in density.

Even though the mean errors presented in these results appear small, it is the combined errors associated with the different phenomena that results in significant bias errors. Moreover, relatively small bias errors on the order of 10 percent in the models applied over long periods of time translate into large errors in orbit-decay analysis. Also, since the mean error is not simply an offset bias, but varies with time, it becomes difficult to allow for such an error. The results presented here show that work is still needed to improve the characterization of the known long-term thermosphere variations by the models.

Wilson, R.M. 1992. An Early Estimate for the Size of Cycle 23. *Solar Physics* 140:181–93.

Sponsors: Office of Space Flight and Space Station Projects Office

■

Global Climate Monitoring From Satellites

Roy W. Spencer/ES43
205-544-1686

Lower tropospheric and stratospheric temperatures, as well as oceanic rainfall, are being monitored with the Microwave Sounding Units that have been flying on the Television Infrared Operations Satellite (TIROS–N) series operated by NOAA. Data sets of these three parameters are now being produced at daily time resolution and 2.5 degree latitude-longitude spatial resolution. The data sets are of high quality and valuable for a wide variety of weather and climate research. As part of the NASA Pathfinder program, these data are being made available to the climate research community. This will enhance our understanding of climate processes, such as global warming, the effects of rainfall on the atmospheric general circulation, and the effects of ozone depletion on stratospheric temperatures. Monthly data sets are now routinely provided to NOAA's Climate Analysis Center.

In the last year, global tropospheric temperatures have remained below normal due to the June 1991 eruption of Pinatubo volcano in the Philippines. The stratospheric aerosols produced by this volcano reduced the incoming sunlight by about 5 percent and caused the northern hemisphere summer of 1992 to be very cool. As of June 1993, the stratospheric aerosols have mostly cleared out of the stratosphere. During their peak, these aerosols also produced very warm temperatures in the lower stratosphere due to greenhouse trapping of upwelling infrared radiation emitted by the warmer lower atmosphere and surface of the Earth. As of June 1993, the lower stratospheric temperatures have cooled off to nearly record low levels.

Sponsor: Office of Mission to Planet Earth

■

Geophysical Fluid Flow Cell Experiment

Fred W. Leslie/ES42
205-544-1633

The Geophysical Fluid Flow Cell (GFFC) Experiment simulates a wide variety of thermal convection phenomena in spherical geometry. By applying an electric field across a spherical capacitor filled with a dielectric liquid, a body force analogous to gravity is generated around the fluid. The force acts as a buoyant force in that its magnitude is proportional to the local temperature of the fluid and in the radial direction perpendicular to the spherical surface. In this manner, cooler fluid sinks toward the surface of the inner sphere while warmer fluid rises toward the outer sphere. The value of this artificial gravity is proportional to the square of the voltage applied across the sphere and can thus be imposed as desired. With practical voltages, its magnitude is only a fraction of Earth's and so requires a microgravity environment to be significant. The GFFC first flew on Spacelab 3, and has been scheduled for flight aboard the second United States Microgravity Laboratory (USML–2).

Research work is proceeding in computational and experimental geophysical fluid dynamics leading up to the reflight of the GFFC on USML–2. The work is intended to generate fundamental results concerned with nonlinear and chaotic properties of thermal convection and baroclinic waves in terrestrial and planetary atmospheres. The major efforts are focused on thermal convection relevant to Jovian atmospheric dynamics, and on the chaotic behavior of baroclinic waves relevant to the Earth's atmosphere and oceans.

This research has demonstrated, using a quasi-geostrophic convecting channel model, that large scale zonal jets could be generated by convection with vertical shear. This model indicated that high wave-number convection would only occur in a narrow band of parameter space. As the Rayleigh number (Ra) is increased, short wavelength Beta convection rapidly gives way to low wave-number convection. However at unit Prandtl number, such low wave-number cells still tilt and can generate large mean flows. The basic result of wave-number cascade to low values as Ra is increased was verified in a centrifugal convection laboratory experiment where rapid rotation produces a centrifugal buoyancy perpendicular to rotation, yielding an analog to the equitorial annulus.

Numerical models and laboratory experiments show that rigid sidewalls (as present in the GFFC and Earth's oceans) can play a very important role in the dynamics of nonlinear instabilities and waves. Simple experiments with barotropic motion in an annulus showed that separation of the sidewall boundary layer can lead to chaotic motions and strong vortices in the interior of a rotating fluid. In addition, when local separation or instability occurs that is locked topographically to a particular longitude, and when the overall geometry is convected (cyclic), then a zonal teleconnectivity can arise where vortices generated in the instability region can propagate around the annulus and influence the local generation region in various ways. This leads to strong quasi-periodicity and chaos in both numerical simulations and experiments, and may be an important process in the atmosphere and the Antarctic Circumpolar Current.

Why is the large-scale atmospheric motion chaotic? The canonical two-layer Phillips model has been shown to be only weakly chaotic at best. Recent computational simulations of nonlinear baroclinic waves with stress-free meridional barriers suggest that a crucial ingredient is meridional shear that can drastically reduce the critical Froude number for instability. In the oceanic context, rigid (no-slip) meridional walls of the channel model have the counter-intuitive effect of rendering the two-layer model subcritically chaotic. Some special fluid systems like thermohaline convection have been found to be subcritically unstable. This result is important for interpreting ocean eddy generation along coasts by baroclinic instability.

Empirical orthogonal functions (EOF's) were proposed many years ago as a tool for analyzing atmospheric data. Recently they have been used in models to extract self-consistent, low-order dynamical systems from the full equations of atmospheric dynamics. Besides perhaps being useful in building low-order climate models, such methods can yield useful interpretations of the dynamics. However, the pattern recognition algorithms used to find the EOF's have nothing to say dynamically about where they may come from. What is the connection between EOF's and dynamics? This is a major question in atmospheric science. In the baroclinic wave chaos problem, not only has the EOF method been useful in reducing the dimension of the models from over 104 to less than 30, but it has been shown where the EOF's come from a priori. They can be related (by correlation analysis) to the secondary and tertiary linear instabilities of the equilibrated steady baroclinic wave fields. Thus they can be computed a priori. In addition, this research has shown that the long-term baroclinic wave fluxes in chaotic and turbulent regimes can accurately (within a few percent) be determined by finding the unstable fixed points of the model.

The experiments planned for the next flight of the GFFC are expected to further contribute to our understanding of these kinds of processes.

Albaiz, A.; Hart, J.E.; and Leben, R. 1993. Flow Separation and Chaos in a Rotating Annulus. *Computational Fluid Dynamics*, 21 pages, in press.

Brummell, N., and Hart, J.E. 1993. High Rayleigh Number Beta-Convection. *Geophysical and Astrophysical Fluid Dynamics* 85:114.

Mundt, M., and Hart, J.E. June 1993. Secondary Instability, EOF's, and Baroclinic Chaos. To be submitted to the *Journal of Atmospheric Science.*

Sponsor: Office of Mission to Planet Earth

■

The Advanced Microwave Precipitation Radiometer

Robbie E. Hood/ES43
205-544-5407

The Advanced Microwave Precipitation Radiometer (AMPR) and its accompanying data acquisition system fly aboard a NASA ER–2 high-altitude aircraft to collect passive microwave upwelling emissions from the Earth's surface and atmosphere. The instrument is a cross-track scanning, total-power radiometer with four channels centered at 10.7, 19.35, 37.1, and 85.5 GHz. The AMPR utilizes a rotating polarization that varies from a vertical component at 45 degrees to the left of nadir, to equally mixed components at nadir, and finally to a horizontal component at 45 degrees to the right of nadir. The surface resolution of the nadir-viewing footprints ranges in size from 2.8 km for the 10.7 and 19.35 GHz channels, to 1.5 km for the 37.1 GHz channel, and 0.64 km for the 85.5 GHz channel when collected at a high-altitude aircraft height of 20 km.

The AMPR was deployed along with other microwave instrumentation aboard the NASA ER–2 during January and February 1993, as part of the Tropical Ocean Global Atmosphere (TOGA) Coupled Ocean-Atmosphere Response Experiment (COARE). Ground-based operations for the ER–2 were conducted in Townsville, Australia, while flight operations were directed to the western Pacific Ocean region between 20 degrees North and 20 degrees South, bounded by Indonesia on the west and the international date line on the east. TOGA COARE was an international experiment with representatives participating from 15 nations. The overall research objective was to improve our understanding of the relationship between the warm water pool found in this region of the western Pacific and the mean and transient behavior of the global atmosphere system. Specific NASA objectives during this experiment supported both the TOGA COARE research goal and the Tropical Rainfall Measuring Mission (TRMM) as part of the NASA Mission to Planet Earth. AMPR data will be pertinent to TRMM objectives related to studies of tropical oceanic precipitation climatology, vertical structure of precipitation hydrometeors, and physical processes associated with precipitation.

In preparation for TOGA COARE, the AMPR external calibration loads were upgraded to a design similar to the loads used by the DMSP SSM/I in order to improve calibration accuracy. The data acquisition unit, using tape cartridges as a data storage medium, was replaced with a system using flash random access memory (RAM) cards in order to improve flight hardiness and reliability. The ground-based data processing workstation was also upgraded to produce higher resolution color images of AMPR data and speed up post-flight data analysis. The AMPR performed successfully during 15 data collection missions, many of which were at least 8 h in duration. Various types and aspects of oceanic rain systems were sampled. Tropical cyclone Oliver was also studied during developing, maturing, and dissipating stages. These TOGA COARE AMPR data will be reviewed and quality documented during the next year. These data will then be archived at those NASA Earth-Observing System Data and Information System (EOSDIS) Distributed Active Archive Centers (DAAC) that maintain catalogs of passive microwave and TOGA COARE information.

Sponsor: Office of Mission to Planet Earth

■

Multispectral Atmospheric Mapping Sensor

Mark W. James/ES43
205–544–5020

NASA's Multispectral Atmospheric Mapping Sensor (MAMS) is a line scanner with eight visible and three IR channels. (There are actually four IR channels; however, only three are available at any one time on the scanner.) The visible channels range from 0.42 to 1.05 μm, with the IR channels varying from 3.47 to 12.71 μm.

Only three of the IR bands are available during any configuration, and the 6.54- and 3.73-μm bands cannot be used together (table 2). MAMS data are being used to determine atmospheric moisture variability and its importance for cloud formation and storm development at scales not available from satellites. The MAMS instrument is flown aboard NASA's ER–2 high-altitude aircraft where data are recorded on an Exabyte 8-mm tape cartridge.

TABLE 2.—*IR channel information*

Channel	Central Wavelength	Bandwidth (μm) (at 50% response)
9	3.73	3.47–3.86
10	6.54	6.28–6.98
11	11.12	10.55–12.24
12	12.56	12.32–12.71

The baseline system flown in 1985, consisted of a 5-mrad aperture that produced a ground instantaneous field of view (IFOV) of 50 m. With the scan mirror rotation of 12.5 r/s, the noise equivalent change in temperature (NEΔT) ranged from 0.5 to 0.9 K. In 1986, the configuration was changed to improve the NEΔT's down to the 0.3- to 0.5-K range. This resulted from having a larger aperture of 5 mrad that produced a 100-m IFOV at a scan rate of 6.25 r/s. The slower scan speed and larger aperture allowed more radiant energy to fall on the detectors and increased the integration period, improving the NEΔT's of the thermal channels. The scan head or primary optics used by the MAMS spectrometer is also used by other spectrometers such as the Thematic Mapping Sensor (TMS), the Advanced Ocean Color Imager (AOCI), and the MODIS–N Airborne Simulator (MAS). Several changes that directly affect data quality have been made to the scanner system to accommodate the AOCI spectrometer. These changes have improved data quality in all scanner applications. The axe-blade scan mirror was upgraded to a full-face mirror. This change increased the amount of energy falling on the detectors and increased the signal-to-noise ratios in all channels. With the improved dynamic range, the digitization resolution was upgraded from 8 to 10 b for the IR channels. The averaging electronics for the blackbodies were also changed to average over more samples of the blackbodies to reduce the sensitivity of the detectors to noise. With these improvements, sensitivity became less than 0.1 K, with NEΔT less than 0.2 K. Based on current instrument performance, minimal changes are necessary for collection of high-quality data in the future.

When the instrument was taken to the field for deployment, a deficiency in on-site data analysis capabilities for scientific and engineering evaluation of the MAMS data was lacking. The MSFC quick-view system (QVS) was developed to provide a near real-time analysis capability by reading data directly from the data tape after each flight. The QVS consists of off-the-shelf components and custom software running on a personal computer. The MAMS instrument was recently upgraded by NASA's Ames Research Center to allow recording of the data on 8-mm tape cartridges, rather than the larger format 14-track instrumentation tape recorder systems used previously. With this upgrade of the data format, the interface was changed from a single-channel bit and frame synchronization card mounted in the personal computer, to an 8-mm tape drive interfaced to the personal computer by a Small Computer Systems Interface (SCSI). This new data input allows all channels to be entered line-by-line with one pass through the tape. Added flexibility in selection of channels to look at while ingesting data will improve the analysis aspect of the QVS capabilities by providing more data to select from without multiple passes through the tape. The system will utilize the Exabyte tape drive capability of over 500mb/s sustained read rate.

Jedlovec, G.J.; Batson, K.B.; Atkinson, R.J.; Moeller, C.C.; Menzel, W.P.; and James, M.W. 1989. Improved Capabilities of the Multispectral Atmospheric Mapping Sensor (MAMS). NASA Technical Memorandum 100352. (Available from the National Technical Information Society (NTIS) N–20430.) NASA, MSFC, AL.

Jedlovec, G.J.; James, M.W.; Smith, M.R.; and Atkinson, R.J. The MAMS Quick View System–2 (QVS2): A Workstation for NASA Aircraft Scanner Data Evaluation. Preprints: 198–203. Seventh International Conference on Interactive Information and Processing Systems for Meteorology, Hydrology, and Oceanography, American Meteorological Society (AMS). Boston, MA.

Sponsor: Office of Mission to Planet Earth

Multicenter Airborne Coherent Atmospheric Wind Sensor

Jeffry Rothermel/ES43
205-544-1685

Development continues for the Multicenter Airborne Coherent Atmospheric Wind Sensor (MACAWS). The 4-yr project will culminate in 1995, with an airborne scanning pulsed CO_2 Doppler lidar for multidimensional wind and calibrated aerosol backscatter measurement from the NASA DC–8 research aircraft. MACAWS is under joint development by the lidar remote sensing groups of NASA's MSFC and JPL, and NOAA's Wave Propagation Laboratory. MSFC has lead responsibility for overall coordination, science definition, and mission planning. To minimize costs, each organization is sharing major hardware components and subsystems which, in nearly all instances, have been used in previous ground-based or airborne applications.

The principal of operation is similar to that successfully employed by MSFC in previous airborne lidar experiments. In operation, a pulsed lidar beam is generated and precisely directed anywhere within a 64-degree cone using a scanning device mounted on the interior left side of the aircraft.The backscattered, Doppler-shifted radiation is measured to infer the line-of-sight wind velocity, assuming the aerosol scattering particles act as passive wind tracers. By scanning the lidar beam slightly forward and aft during flight (i.e., "co-planar scanning") a field of 2–D wind estimates is obtained within the scan plane. Multiple scan planes, revealing a 3–D view of the velocity and backscatter structure, are obtained by appropriately directing the scanner during flight. Aircraft attitude and speed contributions to the radial velocity measurements are eliminated using information provided by a dedicated inertial navigation system.

Following aircraft integration and check flights, MACAWS will be devoted to a series of specialized field measurements designed to improve understanding of atmospheric dynamic processes over critical scales of motion within the boundary layer and free troposphere. Specifically, MACAWS wind measurements will contribute toward improving parameterization schemes for subgrid scale processes represented within climate and general circulation numerical models. Additionally, measurements with MACAWS will also contribute toward: improved understanding of orographic windstorms, generation of instability along dry lines, evolution of mesoscale circulations in differentially heated boundary layers, interaction of thunderstorms with the environment including generation of new convection by thunderstorm outflows, regional air quality degradation, and land surface processes. The unique measurement capability of MACAWS will contribute to the improvement of predictive capabilities for weather and climate.

Additionally, MACAWS will be applied to reduction of uncertainties in performance of the Laser Atmospheric Wind Sounder (LAWS). LAWS, a spaceborne Doppler lidar for measuring global tropospheric wind fields, is being developed by MSFC. Ground-based lidar studies provide limited insights, thus influencing LAWS performance simulations. MACAWS will be used to duplicate the LAWS measurement perspective, thereby providing unique information not present in ground-based observations. For example, LAWS data will contain a surface return signal useful for calibration, atmospheric extinction estimation, and "ground-truth" velocity estimates. This information can be used to minimize biases in LAWS measurements; airborne studies with MACAWS can provide insight into developing the necessary LAWS algorithms. Other LAWS performance issues that will be addressed are impact of spatial variability on velocity and backscatter sampling, detailed cloud properties, Doppler estimation (particularly near aerosol gradients), and long-term monitoring of natural surfaces that may serve as potential calibration targets for backscatter estimation, as well as for monitoring instrument health. Of course, an airborne lidar system that can simulate the LAWS perspective could be applied to post-launch performance validation studies as well.

Rothermel, J.; Hardesty, R.M.; and Menzies, R.T. March 8–12, 1993. Multicenter Airborne Coherent Atmospheric Wind Sensor. Preprints. Topical Meeting on Optical Remote Sensing of the Atmosphere. Salt Lake City, UT.

Sponsor: Office of Mission to Planet Earth

■

Space Shuttle Lightning Research

Otha H. Vaughan, Jr./ES43
205-544-1648

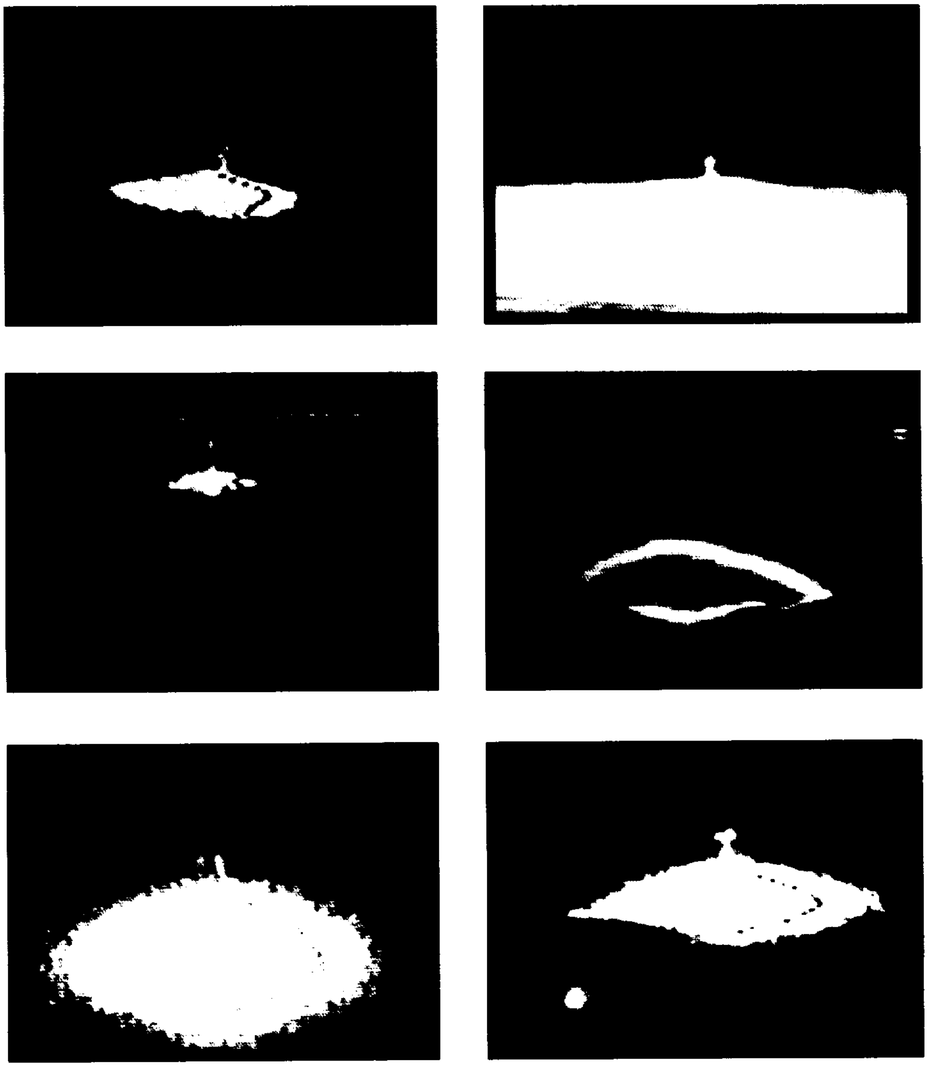

Figure 19.—Various types of vertical lightning as seen by a shuttle payload bay low-light-level TV camera.

The MSFC space shuttle Mesoscale Lightning Experiment (MLE)—flown on earlier shuttle flights and, most recently, on STS-31, -37, -35, -38, -41, -40, and -48—has continued to focus on obtaining additional quantitative measurements of lightning characteristics and created a data base for use in demonstrating observation simulations for future spaceborne lightning mapping systems.

During the earlier shuttle flights, the MLE concentrated on obtaining a video of lightning that was occurring directly below the spacecraft. A considerable amount of data was obtained showing large thunderstorm cells with lightning and frontal complexes, and the large amount of lightning that was occurring within these complexes. During some of the shuttle flights, a new phenomenon was observed by the low-light-level TV cameras as they monitored thunderstorms near the limb of the Earth and its airglow. The phenomenon was a shaft-like discharge moving vertically out of the top of a thunderstorm. It had been observed while conducting the MLE as the shuttle was orbiting over Africa, Australia, South America, and the United States during the nighttime passes over active thunderstorms. At the present time, the cause of this type of lightning discharge is not known.

To date, a total of 17 vertical lightning discharge-type events have been observed using the shuttle low-light-level TV cameras. Figure 19 shows some of the vertical-type discharges that have been observed. These shuttle video observations are to be continued on future flights on a noninterference basis. These data will continue to provide information for use in the development of observation techniques and simulations for future satellite missions, such as the TRMM that is now scheduled to carry the Lightning Imaging Sensor (LIS) being developed at MSFC. This type of research can provide other researchers with a data base for use in understanding terrestrial lightning processes, as well as help in the understanding of lightning processes on other planets. The cloud-to-stratospheric lightning-like discharges, or what may be called vertical lightning, may be more representative of the type of lightning discharges that could be occurring in other planetary atmospheres such as Venus, Jupiter, Saturn, and Neptune.

Vaughan, O.H., Jr.; Blakeslee, R.J.; Boeck, W.L.; Vonnegut, B.; Brook, M.; and McKune, J. July 1992. Picture of the Month: A Cloud to Space Lightning Discharge as Recorded by the Space Shuttle Payload Bay TV Cameras. *Monthly Weather Review* vol. 120, no. 7:1459–61.

Sponsor: Office of Mission to Planet Earth

Aircraft Investigations of Lightning and Thunderstorms

Richard J. Blakeslee/ES43
205-544-1652

In recent years, observations of lightning and thunderstorms from high-altitude U–2 and ER–2 aircraft have furnished data essential for the design and development of satellite-based lightning detectors and have supported investigations of lightning relationships. This research is motivated by the desire to develop an understanding needed for the effective utilization and interpretation of data from the Optical Transient Detector (OTD), the Lightning Imaging Sensor (LIS), the Lightning Mapper Sensor (LMS), and other satellite-based lightning detectors planned for the 1990's and early 2000's.

The emphasis, now, is to quantify the lightning relationships that have been determined. It is hoped that as a result of these kinds of investigations, lightning data alone or in conjunction with other remote sensing techniques will provide quantitative information about such storm characteristics as the occurrence and location of embedded convection, the strengths of updrafts and downdrafts, thermodynamic and electrical energy budgets, precipitation amounts and distributions, and atmospheric chemistry processes. Lightning rates, distribution, and characteristics (i.e., number of strokes per flash, ratio of intracloud to cloud-to-ground lightning, discharge energy, etc.) are all factors that may prove useful in devising quantitative algorithms, and these factors can be studied appropriately with the ER–2.

Lightning instruments have now been integrated on the NASA ER–2 and DC–8 aircraft. This lightning instrumentation detects total storm lightning and differentiates between intracloud and cloud-to-ground discharges. The lightning instruments are also flown with other sensor systems (e.g., infrared, passive microwave, Doppler radar, etc.) to provide new understanding of thunderstorms and precipitation and support detailed satellite simulations of storm measurements through the acquisition and analysis of multiparameter data sets. By developing and maintaining the capability to monitor lightning and thunderstorms with these aircraft, NASA will also be able to provide important ground-truth verifications and calibrations when the OTD, LIS, and other lightning detectors begin operations.

In January and February 1993, science flights were conducted during the international TOGA COARE program to investigate electrical processes of tropical maritime convection and support multisensor precipitation algorithm development. During TOGA COARE, excellent coordination was obtained with aircraft (NASA ER–2 and DC–8, and NOAA P–3's) and ship-based multiparameter observations. Additional lightning coverage was provided by an island-based lightning detection network.

Earlier (July and August 1991), ER–2 science flights were conducted as part of the Convective and Precipitation/Electrification (CaPE) experiment. CaPE provided extensive multiparameter data sets referred to above. More importantly, two of the major scientific goals of this experiment coincide with primary objectives of the ER–2 investigations and NASA's overall lightning program. These goals are: (1) the identification and investigation of the relationships among the co-evolving wind, water, and electrification within the convective cloud; and (2) rainfall estimation. A large number of storm overflights were obtained during CaPE including a number of cases of multiple storm passes. In February and March 1992, the ER–2 participated in the Storm-scale Operations and Research Meteorology-Fronts Experiments Systems Test (STORM–FEST). STORM–FEST provided an opportunity to study wintertime thunderstorms.

Sponsor: Office of Mission to Planet Earth

■

Lightning Imaging Sensor

Hugh J. Christian/ES43
205-544-1649

The Lightning Imaging Sensor (LIS) is currently under development for flight on the TRMM, scheduled for launch in 1997. In addition, an engineering model of the LIS is being assembled, tested, and calibrated for flight. Once qualified, this instrument—the Optical Transient Detector—will be integrated onto a Microlab–1 spacecraft and launched by a Pegasus vehicle in 1994. This will provide a lightning data set 3.5 yr earlier than the TRMM, will be highly complementary to the TRMM, and will demonstrate both the value of global lightning data and the accuracy of LIS-specific scientific algorithms.

The LIS uses an innovative optical design that has been optimized for the unique signal produced by lightning. Lightning is accompanied by the sudden release of electrical energy that is converted into rapid heating in the vicinity of the channel, the generation of a shock wave, and electromagnetic radiation ranging from extremely low-frequency radio waves to x rays. One of the strongest radiation regions is at visible wavelengths, which accounts for almost 1 percent of the total energy released: 100 to 1,000 mW of light. These optical emissions result from the dissociation, excitation, and subsequent recombination of atmospheric constituents that are primarily affected by electron bombardment and the sudden heating of the channel. The heating is so intense that emissions occur primarily at discrete atomic lines, with some continuum at shorter wavelengths. The strongest emission lines are produced by neutral oxygen and nitrogen, and occur in the near infrared, from 7,774 Å to 8,683 Å.

The LIS is a staring imager that is optimized to detect and locate lightning events. It images a scene in much the same manner as a television camera; however, because of the transient nature of lightning, its spectral characteristics, and the difficulties of daytime detection, actual data handling and processing differs vastly from that required by simple images. The heart of the LIS consists of a large mosaic-array, focal-plane assembly, tightly coupled to high-speed processing electronics. This signal processor performs real-time discrimination between lightning events and the background, compressing the total data rate by almost a factor of one million.

As part of the Mission to Planet Earth, LIS and OTD will provide unique data leading to a global climatic lightning data base from which changes in the distribution and frequency of lightning can be studied and related to the physics of the atmosphere that are responsible for these changes. In addition, LIS will contribute toward improving the understanding of the interrelationships between lightning and convective precipitation, clarify the role of lightning in the production and distribution of trace gases, help investigate the mechanisms for electrical coupling of lightning with the ionosphere and magnetosphere, and provide a mechanism for investigating the Earth's global electric circuit by quantifying the electrical variables and determining their relationship to the currents that flow within and near thunderstorms.

Sponsor: Office of Mission to Planet Earth

■

Sensor Development: Lightning Imaging Sensor Calibration

Mark W. James/ES43
205-544-5020

The Earth System Observing Branch of the Earth Science and Applications Division is supporting the development of electro-optical instrumentation for space applications. Under the Earth Observing System (EOS) program, an optical facility is being developed to calibrate the Lightning Imaging Sensor and to measure its performance through the use of realistic simulations. The LIS will image the large-scale distribution of lightning from low-Earth orbit in a 1-nm wide, near-infrared (NIR) wavelength band using a 128- by 128-pixel silicon (Si) charge coupled device (CCD) focal plane array. The sensor is being designed to detect lightning during both low-background (nighttime) and difficult, high-background (daytime) conditions, when the background flux exceeds the signal by many orders of magnitude. The instrument specifications also include a 2-ms frametime and a field of view of approximately 80 by 80 degrees.

The calibration facility is currently supporting two distinct test systems that can be defined as radiometric calibration and lightning scene simulation. Radiometric calibration will be performed on the sensor to verify alignment of the lens assembly to the focal plane, linearity of each pixel, responsitivity of each pixel, and characterization of the narrow-band filter. Uniformity and linearity of each pixel will be accomplished using a large integrating sphere illuminated with a constant light source. The source's intensity will be adjusted by a controlled aperture to ensure constant brightness temperatures. Spectral calibration using the Jones Method of near-field small source will allow a determination of the narrow band filter width using a high-resolution (760–800 nm at 0.1 nm) monochromator. The instrument will be coupled to the monochromator through a fiber-optical bundle with a defocused image to allow entire pixel coverage (fig. 20). The LIS will also be mounted on a two-axis gimbals stage to allow the entire focal plane to be slow scanned. The test will cover approximately 350 to 1,100 nm to ensure coverage of the filter. The alternating current (ac) linearity test is designed to allow the entire system to be tested from end-to-end. The tests up to now are being performed collecting data right off the focal plane and are considered direct current (dc) tests. The real-time event processor (RTEP) will only respond to lightning events that are ac events from the focal plane. The ac linearity test will allow both signal paths to be tested by building upon the fundamental dc linearity test. Also, to ensure that no additional energy will affect the intensity in each pixel by being out-of-band, a test will be performed to verify the out-of-band rejection of the narrow band filter since the pixel's response is somewhat sensitive at or near the filter edges of 150–1,500 nm. This will be accomplished using a board-band monochromator to flood a small integrating sphere with enough energy to allow an indication of a problem in the filter and later using the high-resolution monochromator to characterize, if necessary.

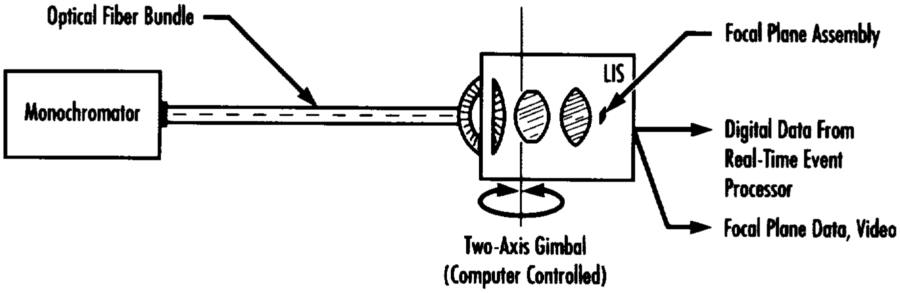

FIGURE 20.—LIS spectral calibration system.

The lightning scene simulator will use a 3-mW NIR diode laser as the source of simulated lightning. Using a mirror scanner for positioning, the laser beam will be pulsed and scanned across a rear projection screen to simulate a dynamic lightning scene. A static background image can also be projected onto the screen and its intensity varied by the use of neutral density filters. A simple combination of plastic field lenses and collimating lens is used to place the lightning scene at the infinite conjugate plane and to obtain wide FOV coverage. The anticipated FOV coverage will be 70 by 70 degrees.

A 486-based compatible computer is being used as the central processor for image capture and control of the laser beam onto the focal plane. High-speed data acquisition modules are being utilized to position the mirror scanner through a windows-based positioning system. The captured frame received from the LIS will be compared against the image map in the computer used to position the laser and adjust the intensity of the beam. The lightning scene simulator is complete and will test the engineering model of the sensor starting in October 1993.

Sponsor: Office of Mission to Planet Earth

■

Advanced Technologies for Geostationary Orbit Remote Sensing

Ronald J. Koczor/ES41
205-544-3078

The Geostationary Earth Observatory will be an important component of NASA's Mission to Planet Earth. It will include several optical instruments to monitor the Earth's environment from the perspective of geostationary orbit and will serve as a complement to NASA's Earth Observing System in low, polar orbit and other Mission to Planet Earth flights.

The geostationary orbit imposes a severe thermal environment on any optical instrument that is on a three-axis-stabilized spacecraft. At the same time, optical resolution requirements are higher in geostationary orbit than in low-Earth orbits (for comparable ground resolution) because of the orbit's farther distance from Earth. The Earth's rotation (and the rotation of the spacecraft over the Earth) allows direct solar flux onto the optical ports of Earth-viewing remote sensors for periods of several hours each day. The higher thermal and optical performance required of instruments in this orbit can take advantage of research presently under way in several new technology areas, including silicon carbide and composite optics and structures, diffractive optics, and chip-scale image motion compensation systems.

Silicon carbide is a serious alternative to beryllium for spaceborne, lightweight telescope and mirror applications. It has excellent thermal properties, significantly lower cost, and simpler, nontoxic fabrication processes. Surface thermal stability of better than 0.25 wave of visible light has been demonstrated over temperature ranges from room temperature to below 90 K. Scientists at MSFC are developing a 0.5-m telescope in which all mirrors and structural elements are made from silicon carbide.

Diffractive optics have a variety of potential applications within spaceborne remote-sensing instruments. While not suitable for the front-end reflective telescopes that are typically used to collect energy in multispectral remote sensors, diffractive optics can be used to create hybrid diffractive/refractive lens elements (resulting in potentially simpler imaging systems), polarization control elements, and antireflection structure surfaces for windows, spectral filters, and detectors. Complex optical elements (having aspheric and high-speed surfaces) can be made physically simpler and with better performance. MSFC also is developing a refractive/diffractive optic for use in lightning sensing from geostationary orbit.

Research is under way to develop these advanced optical technologies to the point where they can be used for the GEO remote-sensing instrument complement to provide unprecedented performance under the severe environment of the GEO.

Koczor, R.J. April 12, 1993. Technology Needs for Geostationary Remote Sensors. Proceedings, *SPIE Conference on Surveillance Technologies and Imaging Components* vol. 1952.

Sponsors: Office of Commercial Programs, Small Business Innovation Research Program; and Office of Mission to Planet Earth, Radiation and Dynamics Branch

Commercial Involvement: SSG, Inc., and Rochester Photonics, Inc.

■

IIII Space Physics

The Mechanisms of Solar Variability—A Study of the Origins of the Variability of the Solar Output

John M. Davis/ES52
205-544-7600

The goal of the Mechanisms of Solar Variability (MSV) program is to improve our understanding of the magnetic connection to solar variability. By following a focused program of theory and observation, with the latter having ground-based, suborbital, and space flight elements, scientists at MSFC expect to achieve a better understanding of this connection. The observational objective is to break the spatial resolution barrier at a few tenths of an arc second and, in doing so, resolve and image for the first time the individual magnetic flux tubes that comprise the solar magnetic field at the photospheric level. The images will contain diagnostics of the vector magnetic field and the plasma velocities and will allow scientists to determine how the individual flux tubes evolve, interact, and coalesce, and how energy is transferred between the surrounding plasma and the magnetic field.

The specific scientific objectives to be addressed by MSV include testing models of coronal heating by determining how the chromosphere and corona are magnetically linked to, and driven by, the photosphere on the scale of individual magnetic flux tubes; providing a quantitiative physical understanding of the Sun's luminosity variation by tightly constraining models of individual photospheric flux tubes; testing the belief that solar flares are releases of an active region's stored magnetic energy; and determining whether active regions disappear by submergence of their magnetic flux, as opposed to diffusion, which is critical to further development of dynamo theory.

These goals may be achieved in a series of steps, each of which is expected to provide incremental advances in the technology and scientific knowledge needed to understand solar variability. The initial step will be to develop a large balloon-borne optical telescope operating in the visible spectral region. A mirror diameter of 1 m will be required to overcome the diffraction limit at the required resolution, and it will be carried to balloon altitudes in excess of 125,000 ft to minimize the atmospheric disturbances—generally referred to as "seeing"—which plague ground-based observations. The telescope will be outfitted with advanced focal plane instrumentation, including high-resolution spectrographs, polarimeters, tunable filters, and large format CCD cameras. This approach allows for interchangeable focal plane instrumentation that is expected to be developed at different institutions, ensuring broad involvement in the program. As a balloon-based observatory, achieving shorter instrument development cycles than are possible with spacecraft programs are expected, thus allowing incorporation of rapidly developing technology into the program.

The balloon telescope will provide data on a rather narrow range of heights in the solar atmosphere from the photosphere, which is the visible surface, to the low chromosphere. This is a result of the rapid increase in temperature of the solar atmosphere with height. At these high temperatures the solar atmosphere radiates energy at wavelengths shorter than the visible, ranging from the ultraviolet to soft x-ray regions. These radiations are absorbed high in the Earth's atmosphere, which is why they are so important to understanding atmospheric chemistry and have to be observed from space. Observations of the hot upper levels of the solar atmosphere will be obtained using suborbital flights on sounding rockets. This approach facilitates the rapid incorporation of new technology into the instrumentation, and the flights can easily be coordinated with the flight of the balloon observatory.

The results from the MSV will indicate the directions for future study, which theoretical models are worth pursuing, and which observations are needed to confirm ideas or to differentiate between competing views. The engineering and scientific experience gained in developing and applying the needed technologies, and for operating and analyzing the scientific data from the meter-class observatory, will form the basis for developing a major space mission (the Advanced Solar Mission) at lower risk and cost than could otherwise be achieved.

MSV is designed to be broadly based and rapidly implemented. Universities and their students will be fully involved in all aspects, from conceptual design, through development and flight, to analysis of the scientific data. The timeline for these activities is consistent with courses of study for advanced degrees. In a wider sense, the images of the immense structures present in the solar atmosphere revealed by scientific observation, have a powerful impact on all who see them, not only because of their inherent beauty, but because they unveil a view of the physical world that is totally unexpected. The fact that the behavior of these structures affects life on Earth provides a readily understandable insight into the importance, and relevance to society, of scientific discovery.

Sponsor: Office of Space Science

■

Solar Magnetic Fields

Gilmer A. Gary/ES52
205-544-7609

The mechanisms that create solar variability must be anchored in the physics of the solar magnetic fields and electric currents since the forces arising from their interaction dominate over all other forces in the solar atmosphere. The magnetic field plays the most important role in determining the Sun's changing behavior and has a direct impact on the Earth's environment. Understanding the physical cause of the UV and x-ray variations in radiation from the solar atmosphere (photosphere, chromosphere, and corona) is important in that radiation produces effects in the Earth's upper atmosphere, thereby producing effects on the Earth. Hence, in solar physics, one major aim is to define the solar magnetic field's topology and evolution in order to understand both the large and small variability of solar radiation. However, the role of the magnetic field is still enigmatic, and careful study is needed. In this effort, MSFC solar scientists have developed unique instrumentation that provides knowledge on the structure of our Sun.

The ground-based MSFC Solar Vector Magnetograph is an internationally recognized instrument for deriving the magnetic structure and electric currents on the Sun. The Vector Magnetograph is a telescope that has a unique focal plane detector. The detector measures the total polarization of the light of a magnetic-sensitive spectral line. Through proper analysis, the polarization measurements yield the magnetic vector field at the photosphere. In connection with this instrumentation, various MSFC solar programs have been undertaken in support of NASA projects and in support of collaborative observations (i.e., *Skylab*, Solar Maximum Mission (SMM), Spacelab, Flares '91, Max '91, Yohkoh, Mechanisms of Solar Variability (MSV)). These solar programs have included: (1) theoretical and observational studies to perform basic research in solar magnetic fields, (2) instrumentation development using new polarimeter techniques, (3) observations with supporting advance data reduction, and (4) programs to predict the probability of major solar flares. The important effort currently is the development of a breadboard instrumentation to test orbital and suborbital flight components of a state-of-the-art vector magnetograph. Various technical details are now being carried out.

Recent accomplishments include: the testing of the complete optical system of a new Experimental Vector Magnetograph (EXVM), installations of electronics in the EXVM CCD camera system and data system, completion of mechanical designs for the EXVM and a conceptual assembly drawing for the EXVM mounted to a stratospheric balloon gondola, analysis of the instrumentation of polarization of the EXVM optics, installation of four 1024- by 1024-CCD chips in the EXVM camera, and testing camera performance. Furthermore, the accomplishments include: testing the EXVM Fabry-Perot filter at the National Solar Observatory (Sacramento Peak Observatory); design and fabrication of the EXVM solar correlation tracker; completion of extensive tests of EXVM polarimeter; completion of optical design and polarization analysis for a balloon-borne 60-cm telescope; study of options for high-density, low-power data storage devices for a balloon EXVM; and a study of a video telemetry system for a balloon EXVM. In basic research, correlations of photospheric motions, magnetic field evolution, and buildup of magnetic shear in two major flare-productive active regions have been studied. The magnetic structure for the June 1991 region has been investigated. Movies of the vector magnetic fields with coaligned H-alpha images for this region that produced five gigantic X-class flares have been developed. Evidence has been produced for changes in the vector magnetic field as a result of solar flares. MSFC scientists have collaborated with the Yohkoh's investigators in understanding the magnetic structures of the Sun.

The mathematical analysis of the extrapolation of the observed magnetic field continues to be an important part of the solar studies. The modern mathematical technique of regularization has been investigated in order to provide a computation tool to allow MSFC scientists to model the structure of the magnetic

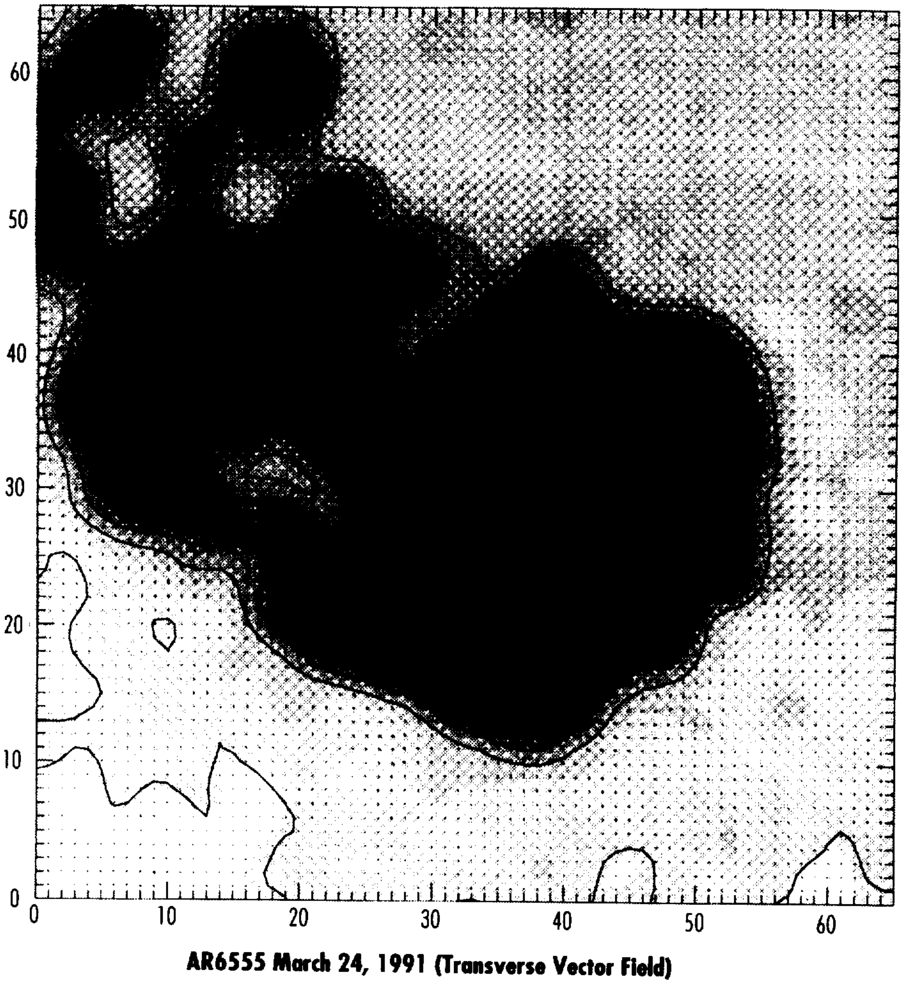

FIGURE 21.—I-intensity contours.

field and the associated electric currents in the solar corona. As part of the physical and mathematical studies of the Sun, MSFC scientists have been invited to participate in various international conferences. MSFC solar scientists continue to collaborate with the international community, participating in a two-way flow of information on all aspects of solar physics.

Research continues on the connection between the magnetic field and solar activity through ground-based observing campaigns and special research projects in the analysis of magnetograph data (fig. 21). Daily observations are being taken and analyzed for Yokhok mission planning and analysis, and for Max '91 campaigns. These important studies will define the NASA orbital and suborbital magnetographs that are needed for the advancement of all of solar science. The EXVM will permit the measurement of solar magnetic fields with the highest accuracy that modern technology and data analysis allow.

Sponsor: Office of Space Science

■

Corona and Solar Wind

Ronald L. Moore/ES52
205-544-7613

The Sun's extended outer atmosphere, the corona, is so hot that it radiates predominantly in x rays and continually explodes out past the planets as the solar wind (fig. 22). The persistent heating that must be present to sustain the hot corona and solar wind is a long-standing premier problem of solar physics. The Sun's coronal luminosity is of the order 1,028 erg/s. X-ray emission of this order or greater, and having the spectral and temporal character of that from the Sun, has been observed to be normal for nearly all stars that, like the Sun, have convective envelopes. From this evidence it is now accepted that a hot corona similar to the solar corona is a common feature of these stars, and the problem of coronal heating has become a focus of solar-stellar astrophysics.

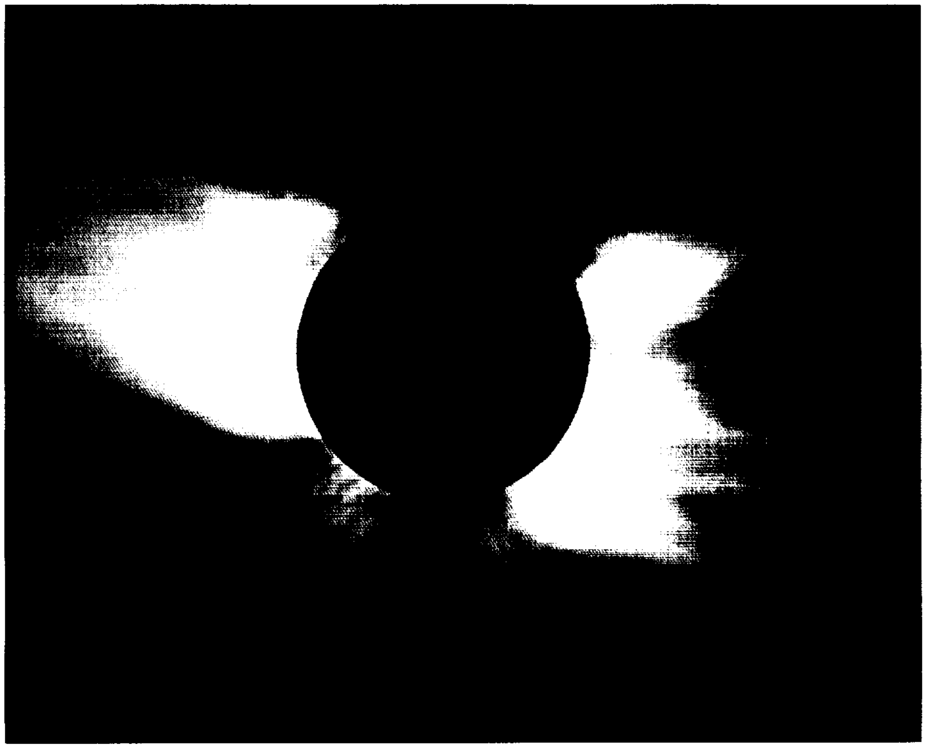

FIGURE 22.—The Sun's corona and solar wind.

The solar corona is permeated by a magnetic field that is rooted in, generated by, and continually changed by the convective envelope. Over much of the surface of the Sun, this magnetic field is in the form of closed loops that confine the coronal plasma. But in some areas, the magnetic field is forced open by the pressure of the hot coronal plasma. From these open-field regions the coronal plasma expands and empties out to fill interplanetary space with the outflowing solar wind. These open-field, relatively empty places in the corona are seen as dark coronal holes in x-ray images of the corona. However, the observed solar wind flow, and much more massive but cooler winds observed from giant stars with convective envelopes, cannot be explained by the coronal gas pressure alone. An additional driver is needed to account for the observed speeds and mass fluxes of the solar and stellar winds. This is another major problem of solar-stellar astrophysics.

During the past year, a group of solar astrophysicists from MSFC, the University of Alabama in Huntsville, and the University of Chicago have continued to make progress on both the coronal heating problem and the solar/stellar wind problem by considering the reflection of Alfven waves in a nonuniform medium, such as in a coronal hole. Their results in the previous few years suggested: (1) that the 106 K temperature in coronal holes is maintained by heating by reflected Alfven waves having periods of about 5 min or longer, and (2) that Alfven waves with periods shorter than about 5 min are not reflected, but propagate on out into the solar wind. This picture requires a dissipation mechanism that works on the reflected Alfven waves much more than on the unreflected ones. During the past year, these scientists have identified a promising mechanism for selectively dissipating the reflected waves, "intermittent magnetic levitation," which is a consequence of the reflection itself.

These researchers have also considered possible generation mechanisms for their proposed Alfven waves in coronal holes. One possibility is the conversion of the vertical (p-mode) oscillations of the Sun's surface (the photosphere) into Alfven waves through interaction of the oscillations with feet of the coronal magnetic field in the upper photosphere and low chromosphere. From a rough estimate, they found that the energy flux of Alfven waves generated in this way could be no more than of order 105 erg/cm^2/s, an order of magnitude less than the flux needed to heat the corona and drive the solar wind. During the past year, they completed and published measurements (from specially tailored observations of the Mg I 4571 A line) of the p-mode energy propagation up through the photosphere. These measurements definitely show that the energy flux in the p-mode oscillations decreases steeply with height in the lower photosphere, to less than 105 erg/cm^2/s in the upper photosphere. This substantiates their previous estimate and conclusion that the p-mode oscillations do not feed enough power into Alfven waves to heat the corona. Thus, they have found some encouragement for their previously published suggestion that microflares low in the magnetic field above the photosphere are the main generators of the required Alfven waves.

The progress of these researchers over the past few years in gaining new understanding of reflection of Alfven waves in open-field regions of stellar atmospheres (coronal holes) led them to propose that the cool massive winds from late-type giant and supergiant stars were driven by such reflection, and that, in the Herzsprung-Russell diagram for these stars, the dividing-line transition from hot x-ray coronas to cool massive winds results from a transition in the topology of the coronal field from mainly closed to mainly open. This suggestion, by itself, offers no explanation for: (1) the 104–105 K temperatures of the cool massive winds, or (2) the transition in the field topology. During the past year, these scientists have found an answer to each of these questions. They proposed that the wind temperature is set by coronal heating by reflected Alfven waves as in solar coronal holes, and that in evolving across the dividing line, the dominant mode of the dynamo generating the magnetic field in these stars changes from being globally organized (as for the field that emerges to form the large solar bipolar sunspot regions) to being local and chaotic (as for the small solar ephemeral bipolar magnetic regions); the reduction in scale of the closed-field bipoles results in nearly all of the field on scales of the stellar radius in the stellar corona becoming open.

Fontenla, J.M.; Rabin, D.; Hathaway, D.H.; and Moore, R.L. 1993. Measurement of p-Mode Energy Propagation in the Quiet Solar Photosphere. *Astrophysics Journal (Ap. J.)* 405:787.

Moore, R.L.; Hammer, R.; Musielak, Z.E.; Suess, S.T.; and An, C.H. 1992. A New Way to Convert Alfven Waves into Heat in Solar Coronal Holes: Intermittent Magnetic Levitation. *Ap. J.* 397:L55.

Rosner, R.; Musielak, Z.E.; Cantaneo, F.; Moore, R.L.; and Suess, S.T. 1993. A Dynamo Explanation for the Disappearance of Coronal X-Ray Emission in Stars With Cool Massive Winds. *Nature*, in press.

Sponsor: Office of Space Science

University Involvement: University of Alabama in Huntsville and University of Chicago

■

Long-Term Solar Activity Predictions

David H. Hathaway/ES52
205–544–7610

The analysis of 250 yr of sunspot observations suggests that solar activity can be represented by a fairly simple mathematical function, with only two or three parameters for each 11-yr sunspot cycle. It has been found, in fact, that each cycle can be characterized by two parameters: the starting time for the cycle and the cycle amplitude. This mathematical function, then, provides a reliable description of the complete cycle. By analyzing the previous 21 sunspot cycles, it has been found that these two parameters can be determined within about 3 yr of the start of the cycle. This, then, gives a reliable prediction of the level of activity for the remaining 5 to 12 yr of the cycle and an estimate for the start of the next cycle.

Solar activity influences the Earth and near-Earth environment in many ways. Over the course of the last 11 yr the total energy output of the Sun varied by about one-tenth of 1 percent. At the same time, the ultraviolet output varied by 3–4 percent and emissions at higher energies had even larger variations. Although the small change in the total output should not alter Earth's climate by any appreciable amount, there is evidence that in the past the variations might have been larger and more influential. There is also evidence that other stars similar to the Sun exhibit larger variations during their cycles. The more substantial changes observed in the ultraviolet output of the Sun influence the formation of ozone in the stratosphere, while the more energetic emissions influence the Earth's uppermost atmosphere, at spacecraft altitudes.

Monitoring and predicting solar activity over the course of the solar cycle is important for the space program because it provides useful information for determining the orbital decay of satellites and space-based platforms such as a space station. A good determination of solar cycle variations is also useful for understanding the changes seen in the Earth's climate and stratospheric chemistry. A better understanding of how the Sun produces these variations should lead to a better understanding of how other stars behave, as well. Unfortunately, there are no good predictive theories for how the solar cycle works. However, looking back at previous behavior may show what patterns persist from cycle to cycle.

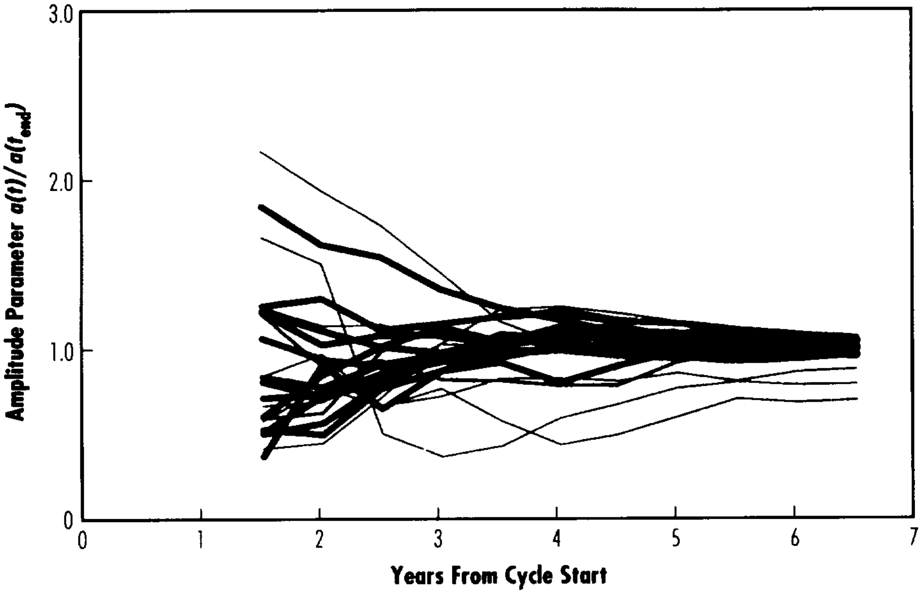

FIGURE 23.—Solar cycle amplitude determinations.

Sunspot observations associated with the Swiss Federal Observatory in Zurich extend back to the mid-18th century. Although the early observations are somewhat unreliable, this data set does provide a long, continuous record of the number of sunspots present on the Sun. Detailed daily observations of sunspots were started at the Greenwich Observatory in 1874. Observations of other indicators of solar activity—such as radio flux, x-ray flux, and magnetic flux—were started much more recently and only cover four to five solar cycles, at best. While these newer data contain much more information about the Sun, the sunspot number data give a better picture of the solar cycle and of cycle-to-cycle variations.

Scientists at MSFC analyzed the Zurich data in the form of monthly averages of the daily sunspot number counts from 1749 to 1993. Although the average cycle is 11 yr in length, individual cycles are anywhere from 8 to 15 yr long. In addition, the amplitudes of the cycles vary by factors of four or more. In spite of these variations from cycle to cycle, several characteristics were found that were similar. For example, the rate at which the sunspot numbers increase from the time of sunspot minimum is well represented by a function that increases as the cube of the time in months from minimum. Similarly, the rate at which the sunspot numbers decrease from the time of sunspot maximum is well represented by a function that decreases exponentially with time. A single function was devised that combines these two different behaviors, starting with a function containing four parameters loosely characterized as: starting time, amplitude, time from minimum to maximum, and ratio of rise time to decay time. It was found that the last of these parameters was unchanged from cycle to cycle. It was also found that the time interval from minimum to maximum is related to the amplitude of the cycle. Big cycles reach maximum quickly, while small cycles take longer. By employing this relationship between rise time and amplitude in the function itself, scientists were left with a function containing only two parameters: starting time and amplitude.

Fitting this function to the sunspot number data for each cycle showed that the function could fit the data to within the variations given by the daily measurements. It was also found that the values determined for the parameters for each cycle were well determined within 3 yr of the start of the cycle. Within months of the start of a solar cycle, the starting date can be determined. When trying to determine the amplitude parameter, it was found that it converges to a constant value within about 3 yr. This is often before reaching the maximum of the cycle. With both parameters determined this early in the cycle, a prediction can then be made of how the activity will vary over the remaining 5 to 12 yr of the cycle. In figure 23, the amplitude parameter that is determined at different times during each cycle is compared to its value determined at the end of the cycle. The ratio of these two numbers is plotted for each of the last 21 cycles as functions of the time from the start of the cycle. For the first eight cycles, the sunspot data were less reliable because of missing data. These cycles are represented by the thin lines.

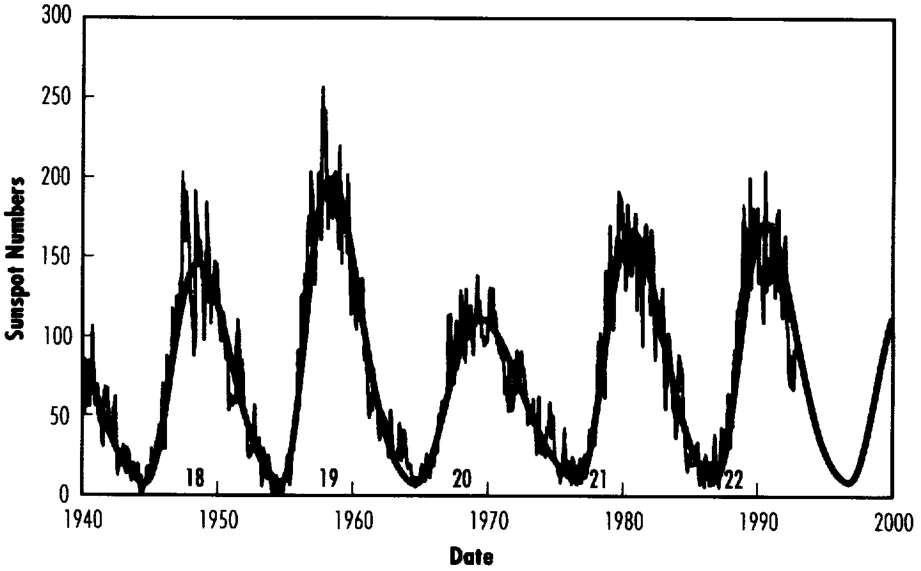

FIGURE 24.—Sunspot numbers, 1940–2000.

The later, more reliable data are represented by the thick lines. This shows that if we take the parameters determined early in each cycle, we can produce the function that represents the final form of that cycle.

As an added bonus, it was also found that the time for the start of the next cycle is related to the rise time of the present cycle. This allows the prediction to be extended into the start of the next cycle. Figure 24 shows the sunspot number data for the last five cycles along with the functions that were fit through the data. Figure 24 also includes predictions for the activity level for the rest of this cycle and the start of the next. The monthly sunspot numbers are shown with the thin jagged line. Our fit through the data is shown with the thick smooth line. The goodness of fit between the data and our function extends to all of the earlier cycles. Only the last five have been plotted so that details are more visible.

Future research will analyze the other available measures of solar activity to see if this function works as well with them. We also intend to search for patterns in the variations of the parameters to see if future cycles can be predicted from the past cycles. While this research does not provide a better understanding of how the solar cycle works, it does provide a tool for predicting future activity and it characterizes the cycle in a way that allows for better comparison with future theories of the solar cycle.

Hathaway, D.H.; Wilson, R.M.; and Reichmann, E.J. 1993. The Shape of the Solar Cycle. *Solar Physics*, in press.

Sponsor: Office of Space Science

■

The Effect of Solar Wind Changes on the Heliospheric Termination Shock

Steven T. Suess/ES52
205-544-7611

Several spacecraft are now exploring the outer reaches of the solar system. These include *Voyagers* 1 and 2, *Pioneers* 10 and 11, and, presently, *Ulysses*. New discoveries continue to be made, with the most recent being the detection of the presence of the boundary between the solar wind and the local interstellar medium—the heliopause (Gurnett et al. 1993). The heliopause is reported to lie near 120 astronomical units (AU) from the Sun. Inside the heliopause, there is a standing shock wave in the solar wind that is quasi-spherical and centered on the Sun. The distance to this shock—the "heliospheric termination shock"—is 60 to 100 AU, well within the reach of the *Voyager* spacecraft within the next few years. Planning for the encounter with the termination shock is well under way, using models of the shape of the shock and how it responds to changes in the solar wind.

The solar wind is highly time dependent, with the dynamic pressure often changing by an order of magnitude over a few days. Over a solar rotation of 27 d, there are quasi-periodic changes in the solar wind associated with the structure of the corona. Taken together, these changes will drive the termination shock inward and outward over several AU on time scales of days to years.

An analysis of the response of the termination shock distance to solar wind fluctuations has recently been made to understand how the shock motion would affect observations of the shock made during its encounter with a spacecraft (Suess 1993). This analysis depends on the speed the shock moves, on the speed of the spacecraft, and on the thickness of the shock. Typical spacecraft speeds are in the vicinity of 5 AU/yr, whereas the shock could reasonably be expected to move several AU/mo, so that the shock may move very quickly in comparison to a spacecraft. There is a great deal of data on the thickness of collisionless shocks, all of which suggests that the shock is very thin by spacecraft standards. That is, given the relative speed of the shock and spacecraft just mentioned, the shock will pass over the spacecraft in a few minutes.

The conclusion is that the termination shock is very agile in comparison to a spacecraft and would pass over a spacecraft very quickly. This makes it difficult to base an observation program on first detecting the shock and then adapting experiment procedures to conditions in the shock. However, the agility of the shock also provides a way to still construct an observing program that would be able to collect a comprehensive set of information on the shock. The reason for this is that solar wind fluctuations occur continuously, driving the shock both inward and outward, with the consequence that once the shock is first encountered by a spacecraft, it will very likely be encountered several more times. A simple calculation demonstrates this result (fig. 25). The top panel of figure 25 shows synthetic, but representative data for how the solar wind dynamic pressure changes over a year's time, along with the solar wind speed in the second panel. The third panel shows the resulting shock speed, calculated using a plausible set of assumptions. The bottom panel shows the distance to the

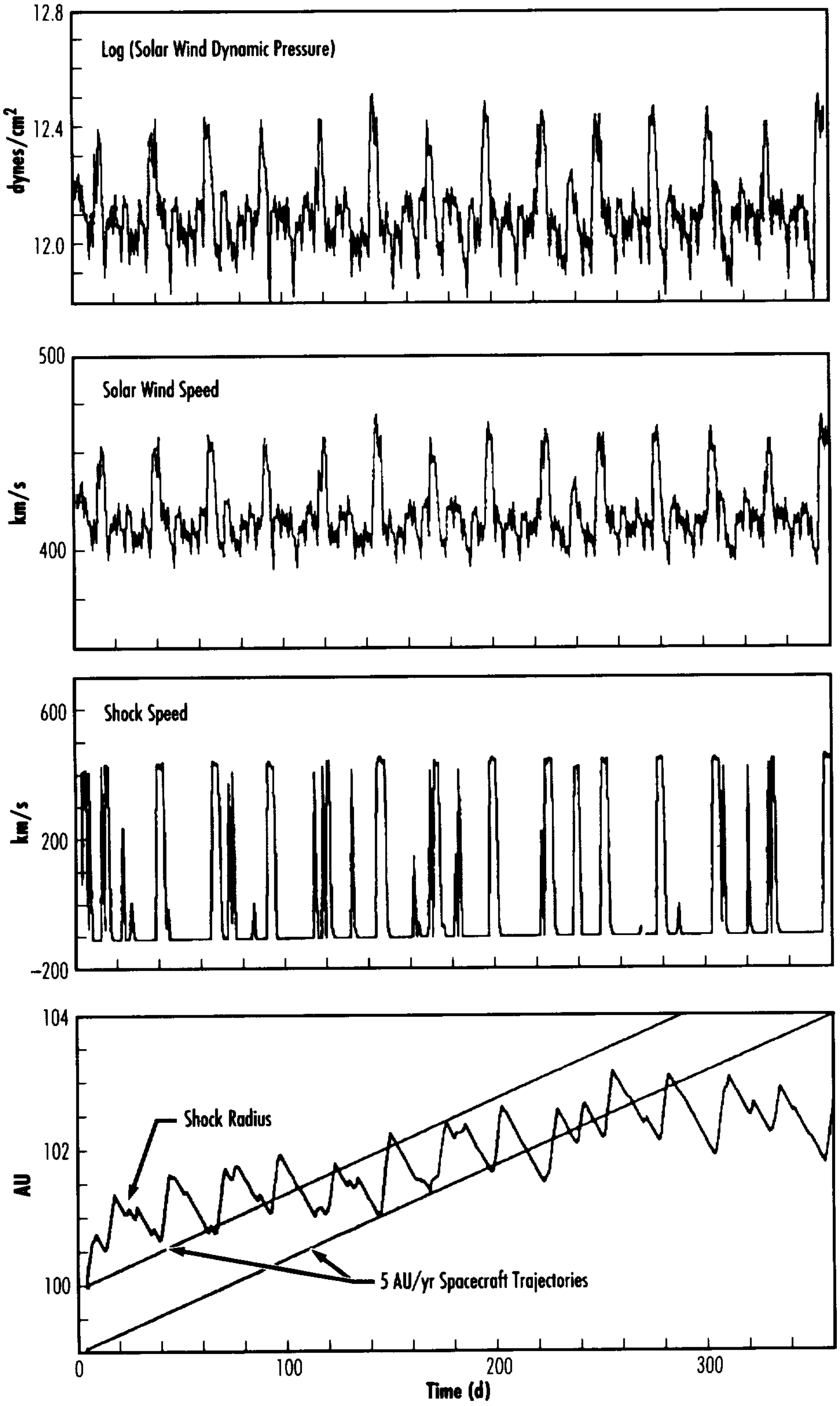

FIGURE 25.—Simulated variation of solar wind and termination shock properties for a period of 1 yr.

termination shock over the same year's time. Overlaid onto this bottom panel are two trajectories for spacecraft moving at 5 AU/yr. It is seen that both spacecraft would encounter the shock several times.

Because shock motion depends on solar wind properties, which are measured on *Voyager* spacecraft, it will probably also be possible to make a definite prediction of the timing for the second and subsequent termination shock encounters once the shock is first encountered. This, then provides a concrete basis for planning an observational program to measure the properties of the termination shock, based on knowledge of the solar wind from in situ measurements and timing of the first shock encounter.

A final point is that fluctuations in the solar wind are only weakly correlated from one location to another. That is, dynamic pressure fluctuations in one direction from the Sun are not necessarily the same as in another direction. This is particularly true around solar sunspot maximum, when solar flares and coronal transients are ejecting mass into the solar wind several times a day. Consequently, the shock, which might otherwise be quasi-spherical, may be driven outward at one location at the same time it is being driven inwards elsewhere. This would lead to a bumpy termination shock. The known amplitude of solar wind dynamic pressure fluctuations leads to the suggestion that the bumps on the termination shock might have an amplitude of 10 percent of the total distance to the shock. This is shown schematically in figure 26, which is intended to reinforce the suggestion that the termination shock is not a smooth surface.

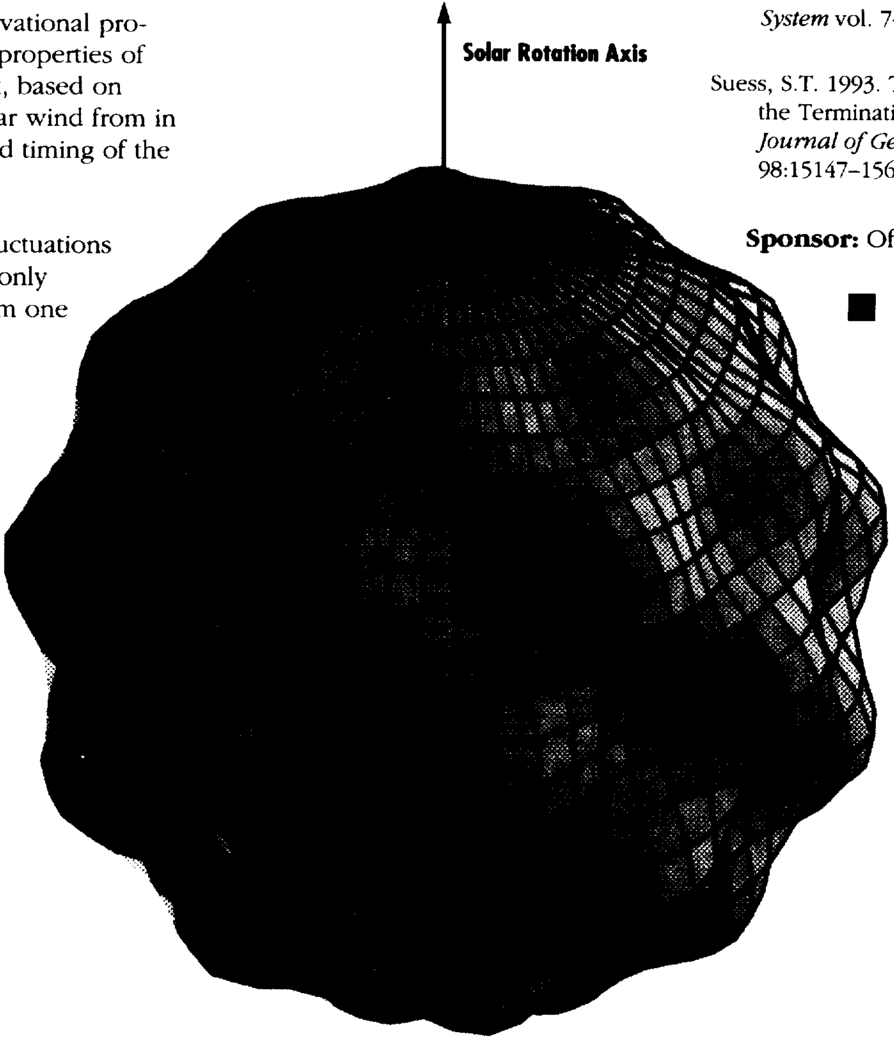

FIGURE 26.—Representation of the termination shock for a spatially and temporally varying solar wind. In this case, the shock is continually being bumped outward in quasi-random directions.

Gurnett, D.A.; Kurth, W.S.; Kaiser, M.L.; Desch, M.D.; and Farrell, W.M. 1993. The 1992–93 Heliospheric Radio Emission Event. *Earth Observing System* vol. 74, no. 16:241.

Suess, S.T. 1993. Temporal Variations in the Termination Shock Distance. *Journal of Geophysical Research* 98:15147–156.

Sponsor: Office of Space Science

Understanding the Quiet Solar Transition Region—The Source of Solar Ultraviolet Radiation

James F. Dowdy, Jr./ES52
205-544-7604

The quiet Sun is all of the solar atmosphere that is not showing enhanced activity or depressed emission, which is most of the Sun for most of the time. For a long time, this condition was thought to be produced by a relatively simple background, steady-state solar atmosphere. The Sun's transition region is a temperature region between 10^4 and 10^6 K, producing most of the solar ultraviolet radiation that impinges on the Earth, providing the main energy input to the upper terrestrial atmosphere and, thereby, having a major influence on such phenomena as atmospheric ozone.

Most of the Sun's ultraviolet radiation comes from the transition region of the quiet Sun, which we know is mostly confined to a layer that is 2,000-km thick. It was tempting to imagine the transition region as a thin layer with a steep temperature gradient giving rise to strong heat conduction downward from the overlying hot corona. It was not until UV telescopes on NASA-sponsored spacecraft began to take observations with improved spatial resolution that the inadequacy of describing the transition region as a simple steady-state layer began to be seen. Despite the realization by many that small-scale, variable processes were playing a role in the basic physics of the transition region, the notion persisted that these small transient events were simply perturbations on a background steady-state atmosphere.

The goal of this research is to take a careful, detailed look at the available data to establish the importance of the small-scale, variable component of the quiet solar transition region. It has been found to be variable everywhere, all of the time, on all measured spatial scales and, therefore, cannot be the result of a simple large-scale, steady-state layer. This research has also helped to establish that the small-scale, variable structure in the solar ultraviolet is related to the small-scale magnetic field. The importance of this result for understanding the solar atmosphere is that it changes the energy budget for the coronal heating mechanism, one of the outstanding problems of solar physics, because the back-heating of the steady-state models was thought to be the dominant energy drain on the corona. The importance of this result for the terrestrial atmosphere is that it begins to provide a better understanding of the source of solar UV radiation.

The UV data being examined were taken by instruments on the Apollo Telescope Mount (ATM) on *Skylab* in 1973. Data from the Harvard Extreme Ultraviolet Spectroheliometer covered the 300 to 1,300 Å wavelength range. Ironically, very little data from this wavelength range have been taken since that time, making these the latest data available for addressing, in particular, the hotter transition region, which is between 10^5 and 10^6 K. Furthermore, the development of data analysis techniques and more powerful computers since the initial analysis of the *Skylab* data was done, has provided many new ways to get a better understanding of the Sun.

Is the quiet solar transition region variable on small scales? Specifically, does it vary too much to be explained by a steady-state model? Figure 27 shows examples of the types of variability that are observed. Feature A is a bright and relatively long-lived event. The event is 1.7 times brighter in raster 6 than its mean brightness during a 9-raster sequence from which these samples are taken. Feature B gives rise to an event of even greater maximum-to-minimum contrast (approximately 2.7) that peaks sharply in time at raster 6. Several high-contrast events can be seen to occur in composite feature C, which is always brighter than average, but bright feature D changes relatively little during the time sequence. Thus, there is no obvious preference for high-contrast events to occur in brighter areas. If instrumental fluctuations are removed, then the data still show that the quiet solar transition region varies from 10 to 30 percent of the mean intensity in all pixels, with no measurable correlation with intensity. For example, feature E is not usually prominent, yet it achieves high contrast (approximately 2.1) during two separate brightenings. Such brightenings cannot be explained by a simple steady-state model.

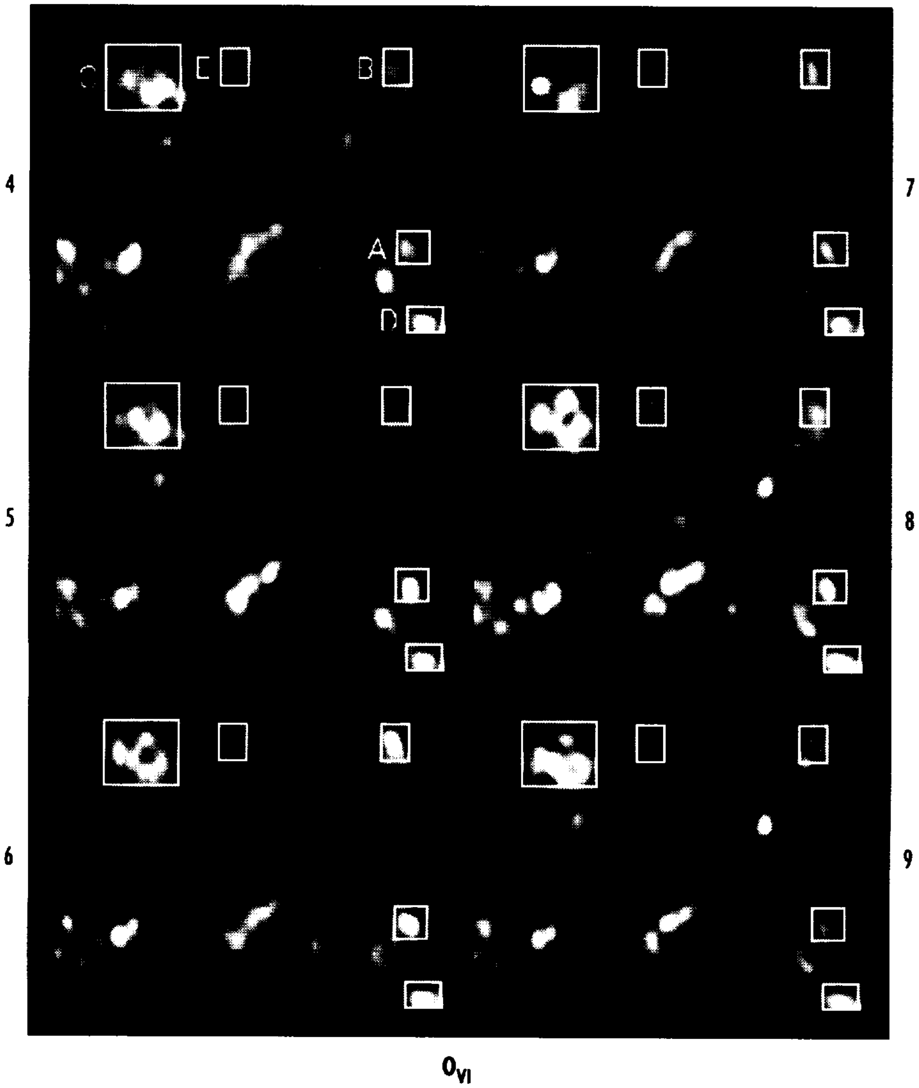

FIGURE 27.—Variability of the O_{VI} 1032 Å EUV emission line illustrated by six consecutive rasters spanning 33 min (each raster taken 5.5 min apart). The width of these rasters is approximately 0.08 times the Sun's diameter. The boxed and labeled features are discussed in the text.

The relationship between the transition region and the small-scale magnetic field also undermines the notion of a steady, back-heated transition region. Figure 28 shows a grey-scaled image of the transition region at 3.5×10^6 K, with superimposed contours of the magnetic field with solid lines indicating positive polarity and dashed lines negative polarity. The basic unit of magnetic structure on the Sun is a loop. A loop shows up on a magnetogram as a pair of adjacent patches of positive and negative polarity. If ultraviolet emission is produced in such a loop, then a bright feature will be seen on the boundary between the two adjacent patches of opposite polarity. Figure 28 shows several such features enclosed in boxes. These features imply loops that are typically 3,000 to 7,000 km in length. The spatial variation in brightness and its association with the small-scale magnetic field argues against a spatially homogeneous and steady transition region.

The analysis of this data has only begun. The Harvard data set includes spectra correlated with images like those shown here. These spectra are now available, and the analysis software has been developed to allow a

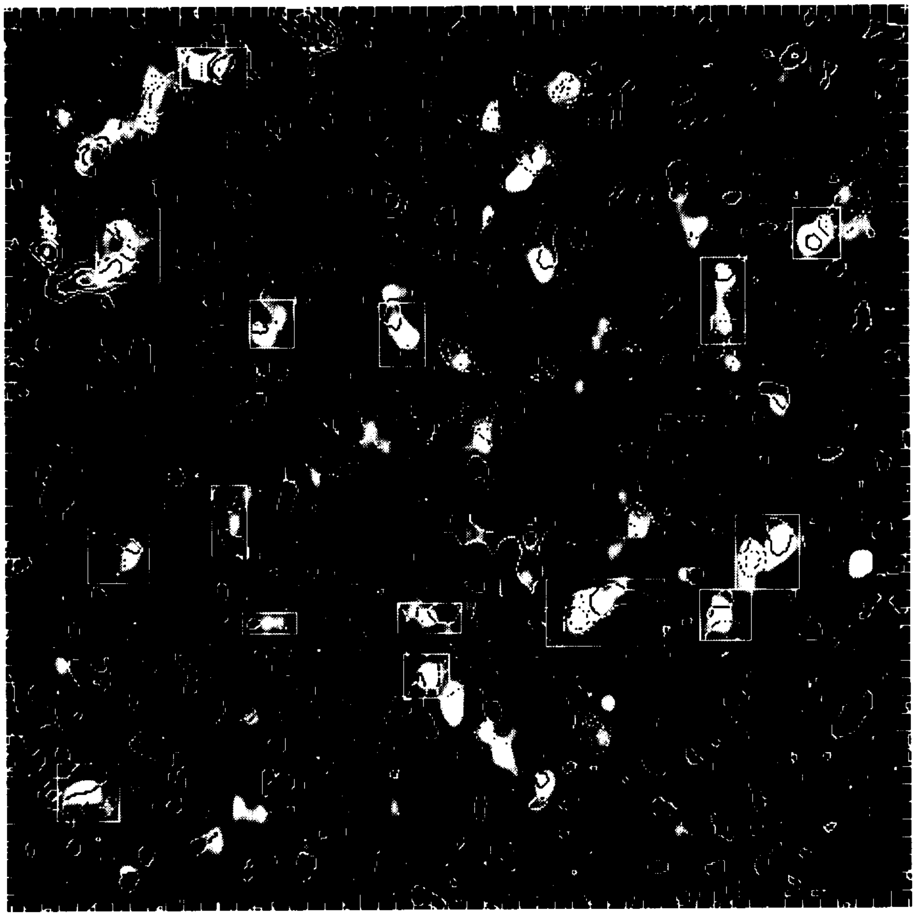

FIGURE 28.—An EUV spectroheliogram of the quiet Sun taken in the O_{VI} 1032 Å EUV emission line with contours of the underlying magnetic field. The width of this raster is approximately 0.16 times the Sun's diameter. The boxed features are discussed in the text.

detailed look at the physical processes occuring at interesting sites like those in figures 27 and 28. The most promising aspect of this work is that it will provide much more stringent constraints on models of the quiet solar transition region.

Dowdy, J.R., Jr. 1992. Observational Evidence for Hotter Transition Region Loops Within the Supergranular Network. *Ap. J.* 411:406.

Mariska, J.T., and Dowdy, J.F., Jr. 1992. Solar Doppler-Shift Measurements in the Ne VII 465 Å Emission Line. *Ap. J.* 401:754.

Rabin, D., and Dowdy, J.R., Jr. 1992. Pervasive Variability in the Quiet Solar Transition Region. *Ap. J.* 398:665.

Sponsor: Office of Space Science, Solar Science Branch

■

Substorm-Generated Impulsive Plasma Flows

Thomas E. Moore/ES53
205-544-7633

The Dynamics Explorer Retarding Ion Mass Spectrometer (DE–1/RIMS) data set has recently been searched for evidence of impulsive plasma flows expected to accompany substorm collapses of the nightside geomagnetic field. The probability of observing such events is low because their duration is only several minutes per day and the Dynamics Explorer spacecraft spends only a small fraction of its time in locations that are potentially affected. A few examples of these impulsive plasma flows have nevertheless been found, in part because the region of space affected is larger than expected. The nature of the flows observed supports an earlier inference from electric field measurements but indicates that the exact behavior of the magnetic field is quite different from that expected. The results provide additional information about how substorms occur and illustrate a new mechanism for accelerating terrestrial plasma into the magnetosphere.

The essence of a substorm is the abrupt collapse of the magnetic field on the nightside of the Earth from a highly stretched state toward a more nearly dipolar configuration, with an associated release of potential energy stored in the initially stretched field. Such dipolarization events are generally accompanied by the detachment of a large volume of the stretched field region, which is then carried off downstream by the solar wind in the form of an independent magnetic structure called a "plasmoid." Associated with the collapse, the polar aurora brightens and expands poleward dramatically, defining the expansion phase of the auroral substorm. An isolated substorm dipolarization event occurs in 1 to 2 min, with the auroral expansion continuing for a period of up to an hour. When substorms recur frequently enough that they become difficult to distinguish, we speak of a full-fledged "magnetic storm," which produces a characteristic reduction of the ground-level geomagnetic field, owing to a global-scale current that encircles the Earth, known as the "ring current."

Substorm-related flow bursts have been found in the DE–1/RIMS data set during orbits like that schematically illustrated in figure 29. As DE–1 moved equatorward across field lines that intercept the Earth's surface near 60 degrees latitude, large headwind flows were seen in all ion species sampled, exceeding 50 km/s, or more than 10 times the speed of the spacecraft. The flows were so strong that the heavier ion species energies as seen in the spacecraft frame were briefly beyond the energy range of the RIMS instrument. These flows evolved in time or space into crosswinds away from the Earth, along the local magnetic field. The variation of the measured velocities for three ion species is shown in figure 30. The time scale over which the event was observed was approximately 1–2 min, in agreement with other observations of strong substorm plasma flows, but the motion of the spacecraft during the measurement precludes a purely temporal interpretation.

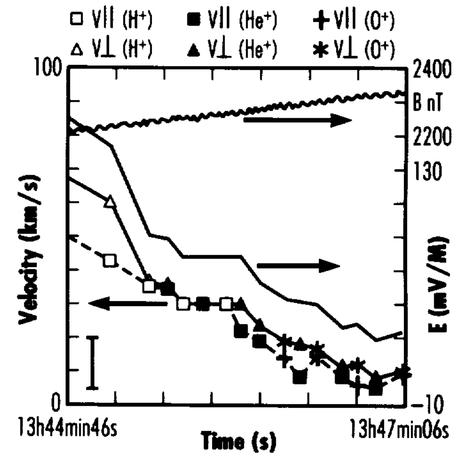

Figure 30.—Plasma flow velocities during an impulsive substorm flow event. Also shown is the magnitude of the measured magnetic field and inferred electric field.

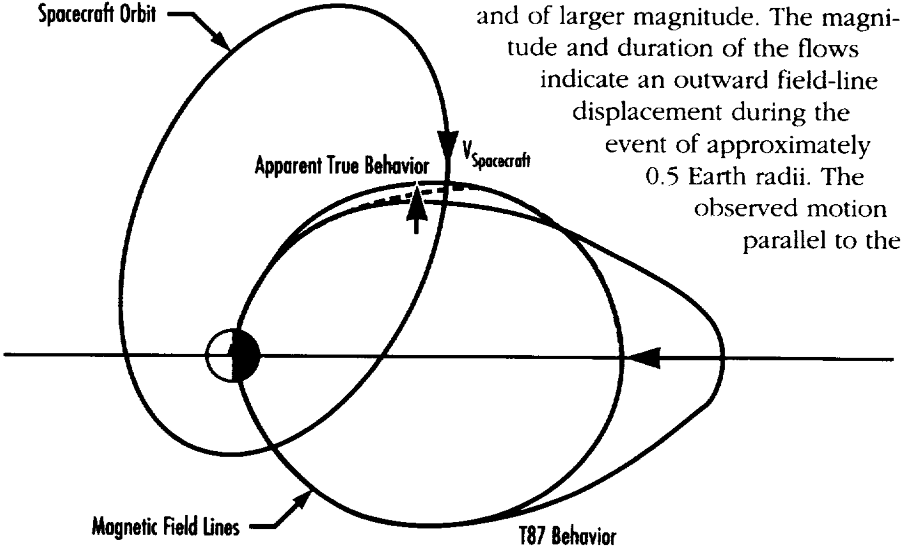

Figure 29.—Geometry and interpretation of DE observations of impulsive substorm plasma flows.

A basic theorem of magnetohydrodynamics (due to H. Alfven) states that the plasma along a magnetic field line must move as a unit with that field line during the magnetic field changes. The naive expectation, based upon the behavior of empirical models of the disturbed geomagnetic field (Delcourt et al. 1991), was that plasma flows during a collapse would be inward toward the Earth and/or equatorial plane. The change of field-line shape would then be as illustrated in the lower half of figure 29. The observed flows are in the direction exactly opposite to that and of larger magnitude. The magnitude and duration of the flows indicate an outward field-line displacement during the event of approximately 0.5 Earth radii. The observed motion parallel to the local magnetic field can be understood to result from centrifugal effects of the motions driven by the changing magnetic field.

These results force a reevaluation of expectations of the geomagnetic field behavior during substorms. In fact, they corroborate an earlier observation of electric fields from which an outward substorm motion was inferred (Aggson et al. 1977). The upper half of figure 29 shows how field lines could move in a way consistent with observations, expanding at high latitudes as they collapse inward at low latitudes. The actual behavior is determined by the global distribution of electrical currents within the plasma medium of the magnetosphere. Motion such as we observe is consistent with magnetic field lines that are in tension owing to a current in the tail, rather than being inflated by a current system within the inner magnetosphere.

The results are consistent with the overall dipolarization of the geomagnetic field known to occur during substorms, if the field line shape when stretched is as shown in the upper half of figure 29. The intense impulsive flows of all species of low-energy ionospheric ions severely disturb this high extension of the ionosphere at the observation points, accelerating the ions to many times their normal thermal energies and freeing them from gravitational equilibrium. The resulting strong plasma flows are a significant mechanism for accelerating low-energy plasma into the low-latitude magnetosphere.

Aggson, T.L., and Heppner, J.P. 1977. Observations of Large Transient Magnetospheric Electric Fields. *Journal of Geophysical Research* 82:5155.

Delcourt, D.C., and Sauvaud, J.A. 1991. Generation of Energic Proton Shells During Substorms. *Journal of Geophysical Research* 96:1585.

Liu, C.; Perez, J.D.; Moore, T.E.; and Chappell, C.R. 1993. Low Energy Particle Signature of Substorm Dipolarization. *Geophysical Research Letters*, submitted for publication.

Sponsor: Office of Space Science

■

Mass Spectrometer Resolution Enhancement Using an Electrostatic Lens

Thomas E. Moore/ES53
205–544–7633

Modern space plasma ion mass spectrometry seeks measurement of the density, temperature, and flow for each ion species sampled, as well as identification of anisotropies and other abnormal features in the species velocity distributions, under low Mach number conditions where particle arrival directions span the entire sky. To do this at time resolution commensurate with the phenomena being observed (often a fraction of a second) is a feat that essentially requires the simultaneous operation of an ensemble of identical instruments, arranged so that their several fields of view form a fan and sweep out the full sky during each spin of a spacecraft. The design of a compact and lightweight instrument meeting this requirement has required significant compromise in specifications for mass resolution, owing to the impossibility of implementing conventional magnetic focusing techniques in such a geometry. Through the use of an electrostatic immersion lens, a technique has been developed for achieving sharp mass spectral resolution in this design. This technique is being incorporated into an existing design for flight on upcoming sounding rocket flights.

The design process begins with a digital CAD description of a proposed instrument mechanical layout. A finite-element mesh is adapted to the design, on which Laplace's equation is solved for the electric potential distribution within the instrument. Similarly, the magnetic field intensity and direction are determined and incorporated into a complete description of the controlling fields. This permits the calculation of trajectories of charged particles traveling through the device, usually termed "ray tracing." The transmission properties of the proposed design can thus be determined, and iterations of the design can be performed with the objective of optimizing itsdesirable characteristics.

Electric potentials are generally used to select the energy/charge of particles passed through the analyzer to a detector. Spaceborne mass analysis has, in contrast, been performed by deflection of the particles in a magnetic field. Designs capable of resolving elements with adjacent mass numbers have been based upon focusing 90-degree deflection magnetic sector geometries using permanent magnets (Moore 1977). Such designs form a sharply resolved mass spectrum by bringing initially divergent particles together along a focal plane. Achievement of such focusing places significant constraints on the overall geometry of an instrument, which are incompatible with clustering multiple sectors in a cylindrically symmetric arrangement.

In order to overcome this problem, a hybrid design has been adopted in which an electrostatic lens is used in conjunction with a simple toroidal permanent magnet design (in place of a special magnetic geometry) to achieve the desired convergence of initially divergent rays. The design provides for focal length adjustment of the lens by simply varying the potential applied to one of the lens elements. In contrast, the standard magnetic sector designs must be set for optimal focus by means of mechanical adjustments. Figure 31 shows the analyzer design in a cross-section view. The upper half is an energy/angle analyzer based upon the conventional hemispherical analyzer or "top hat" with a 90-degree deflection (Pollock et al. 1987). The lower half of the analyzer is a toroidal yokeless permanent magnet design consisting of wedge-shaped magnetized elements separated by air gaps through which the particles are deflected (Lynch 1992). The magnetic field is oriented azimuthally around the cylindrical symmetry axis in a sense so as to deflect positively charged ions radially inward.

Particles within the energy and angular passbands of the hemispherical analyzer are passed on to the magnetic analyzer. Between the exit of the former and the entrance to the latter, they encounter the new element of this design, an electrostatic immersion lens. In figure 31 the immersion lens is absent, and the ion rays exhibit significant angular dispersion exiting from the energy analyzer, which grows larger as they traverse the magnetic analyzer, resulting in poor separation of the ion species at the detector plane located at the bottom of the figure.

In figure 32 the immersion lens has been added and activated. The lens has been biased in such a way that the rays are nearly focused by the

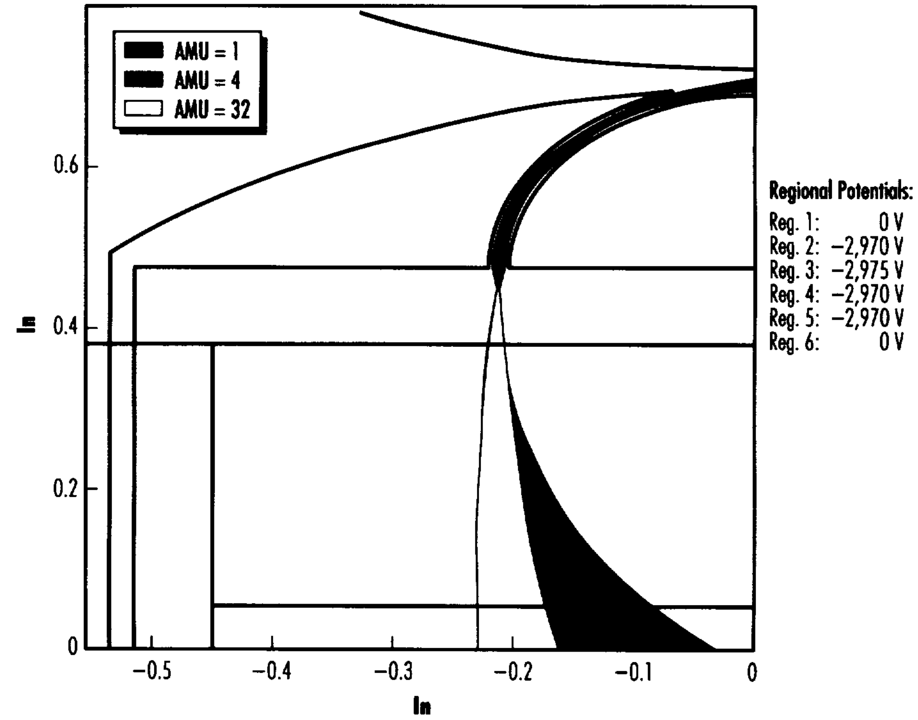

FIGURE 31.—Atomic mass units (AMU's) 1,4,32, with no lens, particle ray traces.

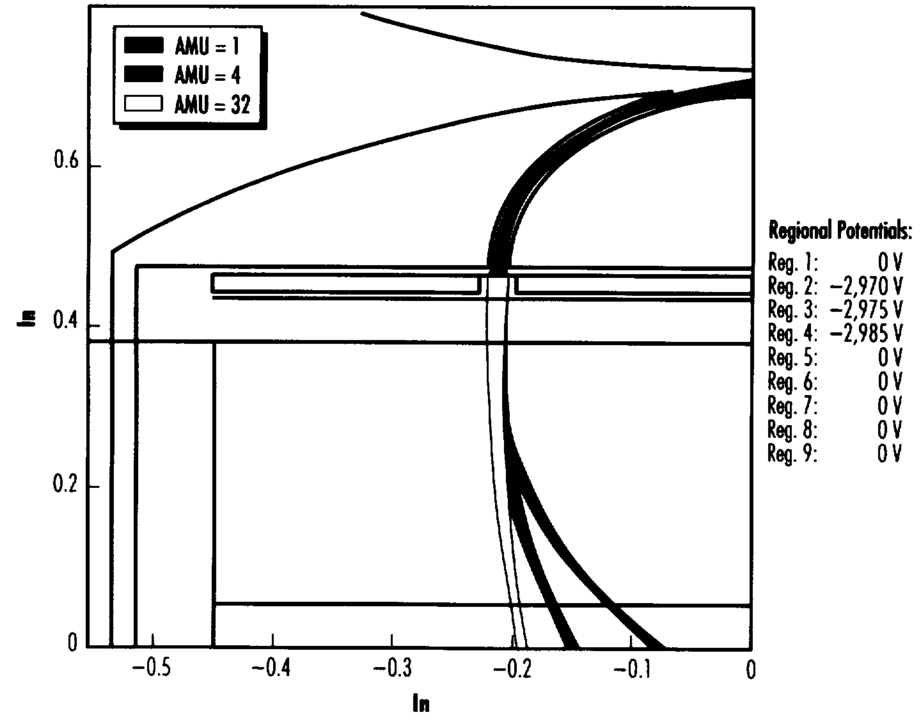

FIGURE 32.—AMU 1,4,32, with lens, particle ray traces.

time they arrive at the detector plane. The bundle widths for each species are reduced significantly, and this translates into a capability to separate much more closely spaced masses than in the case without the lens. An irreducible (with this design) blurring of the bundles remains because of the finite range of energies being passed by the energy analyzer. Reduction of this residual bundle width could produce even greater improvements in mass resolution, especially at larger masses where total deflection, and therefore mass dispersion, are weaker.

The improvement in mass resolution already realized by this technique is significant for future instrument designs and well worth the modest added complexity. It will permit accurate analysis of the plasma composition at very high time resolution in situations where the plasma is not cold or dense enough to be monitored with a single aperture, conventional mass spectrometer.

Lynch, K.A. 1992. Fine Structure of Auroral Particle Acceleration. Dissertation, University of New Hampshire. Durham, NH.

Moore, T.E. 1977. Spectrograph Suitable for the Mass and Energy Analysis of Space Plasmas Over the Energy Range 0.1–10 keV. *Review of Scientific Instrumentation* 48:221.

Pollock, C.J. 1987. Rocket-Borne-Low-Energy Ion Measurements in Space. Dissertation, University of New Hampshire. Durham, NH.

Sponsor: Office of Space Science

University Involvement: Auburn University

Application of Focusing Electrostatic Mirrors to a Spaceborne Ion Mass Spectrometer

---

Craig J. Pollock/ES53
205-544-7638

Several years ago, a report was given on the concept of a focusing electrostatic mirror for use in charged par-ticle spectrometers in space (*Research and Technology 1989: Annual Report of the Marshall Space Flight Center*, NASA TM–100369). Such mirrors offer the potential for large apertures and concomitant increases in sensitivity in instruments that have traditionally been characterized by small apertures. Large enhancements in sensitivity resulting from the application of this technology will lead to new discoveries when instruments using it are deployed into the near-Earth space environment. This report describes the application of focusing electrostatic mirrors, in combination with retarding potential analyzers (RPA), in the MSFC Thermal Ion Dynamics Experiment (TIDE), which has been developed to fly on the Polar spacecraft, part of the International Solar Terrestrial Physics Program. A unique feature of this combination is the ability to electrostatically control the instrument sensitivity, using uplinked instrument commanding or onboard microprocessor algorithms. The result is a much more flexible and capable instrument offering a very large sensitivity and an automatic gain control (AGC) function that provides a large increase in dynamic range.

Figure 33 shows a computer model cross section of one of seven identical sectors in the TIDE instrument. This figure demonstrates the result of end-to-end computerized electrostatic ray tracing of ion paths through the TIDE instrument. Such ray tracing was used extensively in various phases of instrument development. Particles enter from the right within the collimated field of view and are selected based on energy per charge by the combined action of the focusing mirror and the RPA. The mirror/RPA system rejects particles that are outside a prescribed energy bandpass. More energetic particles are not reflected toward the RPA, but pass through the mirror and are lost. Less energetic particles are electrostatically rejected by the RPA and not permitted to enter the time of flight (TOF) mass analysis chamber below.

Since the mirror is not oriented perpendicular to the incoming ion flight path, mirror voltages less than the incoming ion energy per charge are sufficient to reflect the ion toward the RPA. For an idealized flat 45-degree orientation, a mirror voltage of 0.5 E/q is sufficient to reflect ions toward the RPA. An applied RPA voltage larger than E/q, however, is sufficient to reject particles from the RPA. For this idealized case, then, and for the applied mirror voltage (V_M) equal to the applied RPA voltage ($V_R=V_M$), ions are selected in the energy range between V_R and $2V_R$. As another example, if V_M is only 75 percent as large as V_R, ($V_R=4\ V_M/3$) then, again for the idealized case of a flat mirror oriented at 45 degrees to the incoming

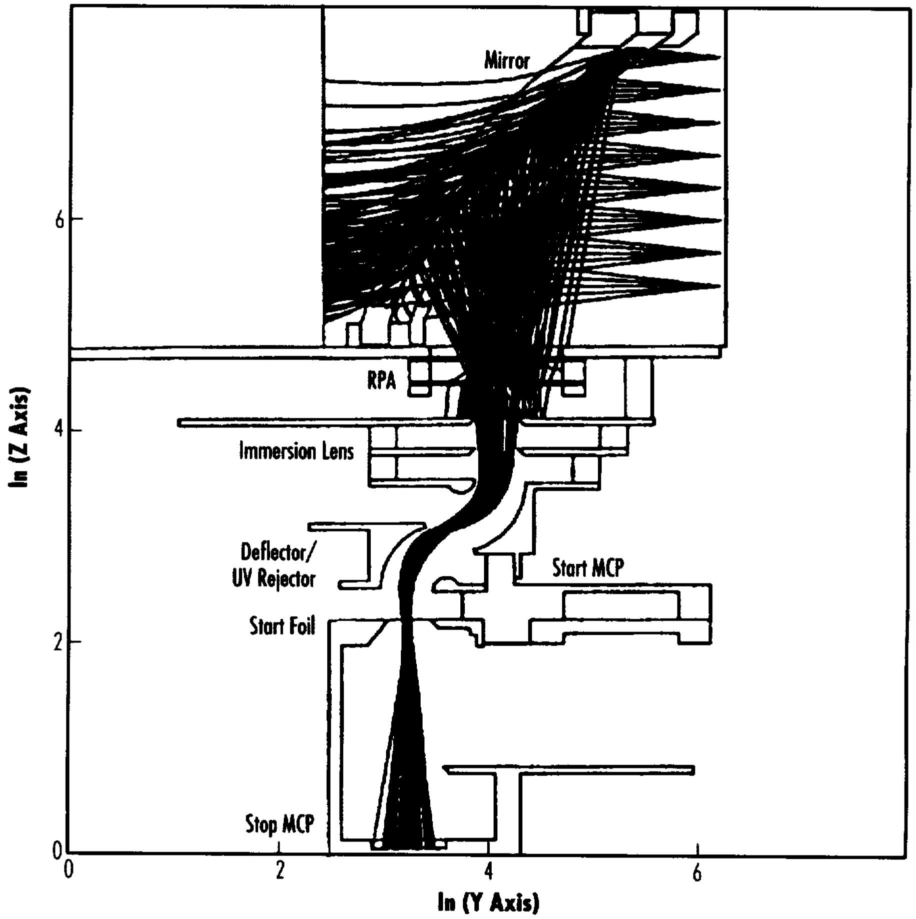

FIGURE 33.—TIDE flight version particle ray traces.

ion flight path, ions are selected in the energy range between V_R and 1.5 V_R. By varying the ratio of the mirror voltage to the RPA voltage, the width of the energy bandpass can be controlled.

We have recently performed extensive calibration measurements on the flight version of the TIDE instrument, prior to delivery to the Polar spacecraft contractor for integration and test. This calibration was performed in the MSFC Low Energy Ion Facility (LEIF) in 1993. An example of the calibration data, illustrating the AGC function of the mirror/RPA system, is shown in figure 34. Here, the energy/angle response of one of the seven TIDE sectors to an incident 25 eV/q monodirectional ion beam is shown. The instrument count rate is contoured as a function of sector look direction along the vertical axis and the applied V_{RPA} and V_M along the horizontal axes. In the top panel of figure 34, the value of V_M is fixed equal to the value of V_{RPA}, whereas in the bottom panel, V_M is only 60 percent of V_{RPA}. The effect of the more limited energy bandpass is clearly illustrated in this figure. For the V_M=V_{RPA} case, the energy bandpass extends from near V_{RPA}=10 V to V_{RPA}=25 V, while for the V_M=0.6 V_{RPA} case, significant transmission doesn't occur until V_{RPA} is approximately equal to 17 V and the upper end of the bandpass remains near 25 V.

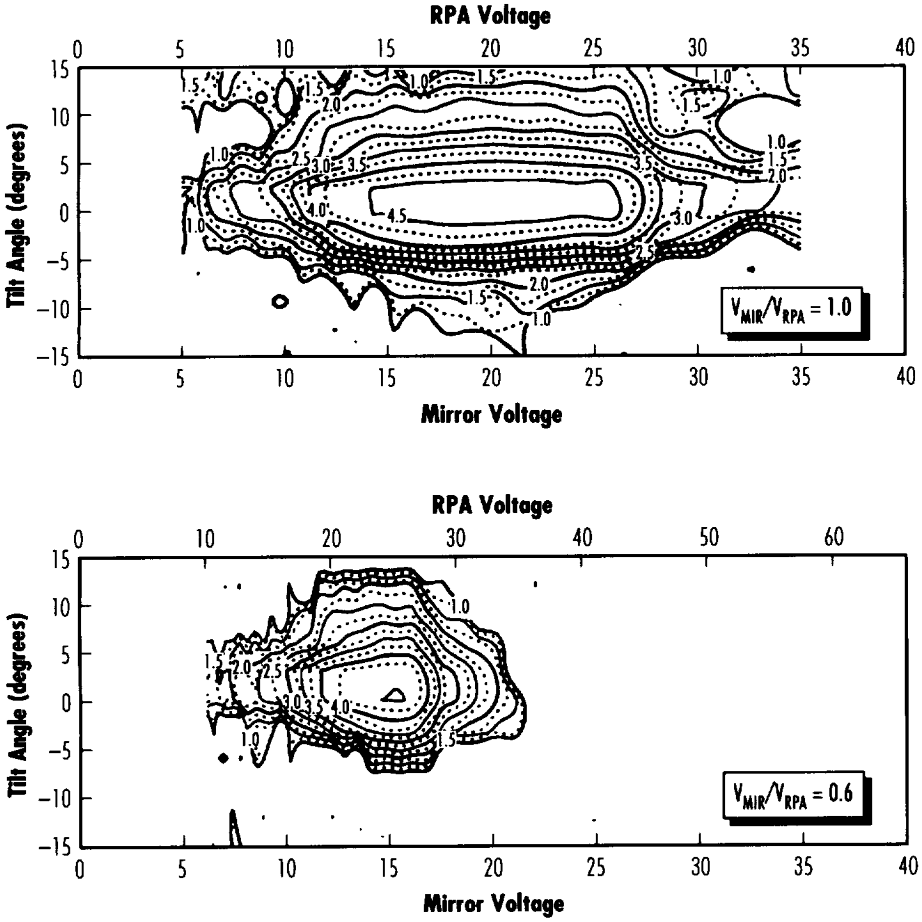

FIGURE 34.—TIDE count rate (Hz).

With careful calibration of instrument energy bandpass as a function of both V_M and V_{RPA}, which has been conducted, the sensitivity of the instrument may be reliably and quantitatively varied by more than 3 orders of magnitude.

The concept, described previously, of a focusing electrostatic mirror has been incorporated into an ion mass spectrometer for flight on a polar orbiting scientific satellite. The increased sensitivity resulting from this technology will result in new discoveries relevant to the nature of the near-Earth plasma environment. The mirror/RPA combination used in this spectrometer yields differential energy measurements and allows for the ability to quantitatively adjust the width of the energy bandpass and the instrument sensitivity on orbit, through voltage power supply control. Thus, an AGC capability has been achieved that will significantly enhance the scientific value of the data returned from the TIDE instrument.

Sponsor: Office of Space Science

■

The Ionosphere as an Alpha Particle Source

Barbara L. Giles/ES53
205-544-7637

Thomas E. Moore/ES53
205-544-7633

At one time, it was thought that the solar wind was the principal source of the plasma particles populating the Earth's magnetosphere. However, subsequent studies have confirmed the presence of energized ions from the Earth's own ionosphere to be present throughout the magnetosphere. This has turned the debate from whether the ionosphere contributes significantly at all, to a question of relative contribution. To what degree are the ionospheric and solar wind sources able to supply the magnetospheric plasma content?

Because the solar wind and the thermal plasma escaping from the ionosphere have the same major compositional element, singly ionized hydrogen (H^+), it is difficult to unambiguously determine which is the source of these particles. There is an abundant amount of O^+ in the ionosphere, but little in the solar wind so that the presence of O^+ is viewed as an accepted indicator of an ionospheric contribution. Similarly, because alpha particles make up on average 4.0 percent of the solar wind plasma, the presence of doubly ionized helium (He^{++}) (alpha particles) in the absence of He^+ has been used as a signature of a solar wind contribution. However, the application of these indicators is not straightforward. Magnetospheric plasma does contain He^{++} (although less than expected from a solar wind source) and it contains appreciable quantities of He^+. Does this suggest that the magnetosphere is dominated by ionospheric ions with a weak mixture of solar wind particles even when alpha particles are detected? The ionosphere can generate higher charge-state ions, such as He^{++} or other M/z=2 ions through charge exchange interactions through direct ionization by auroral electrons. The real implication here is that the mere presence of He^{++} cannot be considered as an indicator of one source or the other.

The RIMS experiment on the DE–1 satellite resulted from a major effort to thoroughly characterize the inner magnetosphere's low-energy plasma component by measuring ions ranging from 0 to 50 eV. The RIMS effort has, in its lifetime, revealed previously unobserved ionospheric plasma sources to the magnetosphere, and provides good observational evidence concerning the relative contributions of the internal and external sources to magnetospheric plasma content.

Recent work investigated RIMS ion pitch angle measurements with respect to geomagnetic disturbance level, invariant latitude, magnetic local time, and altitude for M/z=2 ions that are believed to be alpha particles. Included are outflow events in the auroral zone, polar cap, and cusp, separated into altitude regions below and above 3 Earth radii. In addition to a customary division into beam, conic, and upwelling distributions, the high-latitude observations fall into three categories corresponding to ion bulk speeds that are: (1) less than, (2) comparable to, or (3) faster than that of the spacecraft. This separation, along with the altitude partition, serves to identify conditions under which these ionospheric source ions are gravitationally bound and when they are more energetic and able to escape to the outer magnetosphere.

Figure 35 shows low altitude (≤ 3.0 Earth radii) invariant latitude versus magnetic local time (MLT) occurrence probabilities (2.5 degrees by 1 h bins) for He^{++} field-aligned outflow distributions. The scale at the side of this plot represents the occurrence

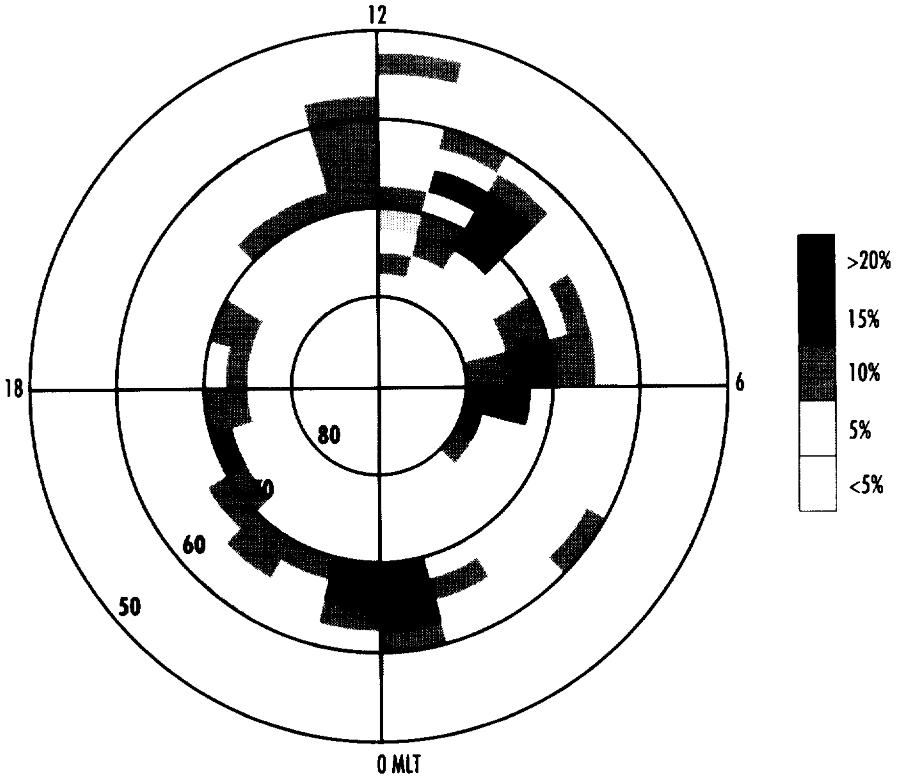

FIGURE 35.—He^{++} field-aligned outflow occurrences.

probability as a percentage—the number of samples fitting the distribution criteria divided by the total number of samples. These field-aligned outflows occur with 10–20 percent probability in an oval pattern that covers nearly all local times and appears to be roughly coincident with the auroral oval. There is an expansion of this oval to lower latitudes at higher geomagnetic activity levels and evidence of an increase in maximum probabilities. Bulk velocity calculations have determined that these measurements represent outflows of sufficient velocity to escape Earth's gravitational potential. From this, it is suggested that the auroral oval as a whole appears to be a consistent source of alpha particles with sufficient velocity to populate outer magnetosphere regions.

Chappell, C.R.; Moore, T.E.; and Waite, J.H., Jr. 1987. The Ionosphere as a Fully Adequate Source of Plasma for the Earth's Magnetosphere. *Journal of Geophysical Research* 92:5896.

Giles, B.L.; Chappell, C.R.; Moore, T.E.; Comfort, R.H.; and Waite, J.H., Jr. 1993. Statistical Survey of Pitch Angle Distributions in Core(0–50 eV) Ions from Dynamics Explorer-1: Outflow in the Auroral Zone, Polar Cap, and Cusp. Submitted to the *Journal of Geophysical Research*.

Moore, T.E. 1991. Origins of Magnetospheric Plasma. *Review of Geophysics* 1039.

Sponsor: Office of Space Science

■

Two-Dimensional Motion of Oxygen Ions in Earth's High-Latitude Ionosphere

Michael O. Chandler/ES53
205-544-7645

Thomas E. Moore/ES53
205-544-7633

The high-latitude regions of Earth's ionosphere and magnetosphere are sites of interplay between influences of the Sun and Earth. This interplay results in very dynamic behavior of the ions that reside in or traverse these regions. The motions of these ions are studied in detail in an effort to understand where they originated (their source), where they ultimately go to (their sink), and how they affect or are affected by the region through which they travel.

Recent studies of the major ion species H^+, He^+, and O^+ that are present at high latitudes have shown complex patterns of motion. These motions have revealed new sources and sinks for these ions and have suggested ways in which they may influence the overall behavior of Earth's plasma environment. In particular, O^+ is known to move upward from the cusp and auroral ionosphere in large quantities. In addition, O^+ has been observed at high altitudes over the polar ionosphere. Thus it is clear that at least some of the up-flowing O^+ reaches escape velocity, with respect to Earth's gravitational field, and is free to traverse the magnetosphere under the influence of electric and magnetic fields only. However, is it true that all of this outwardly moving O^+ escapes or does some portion—that which does not possess escape energy—return to the ionosphere? If so, where does it return and how does it influence the plasma that already resides there?

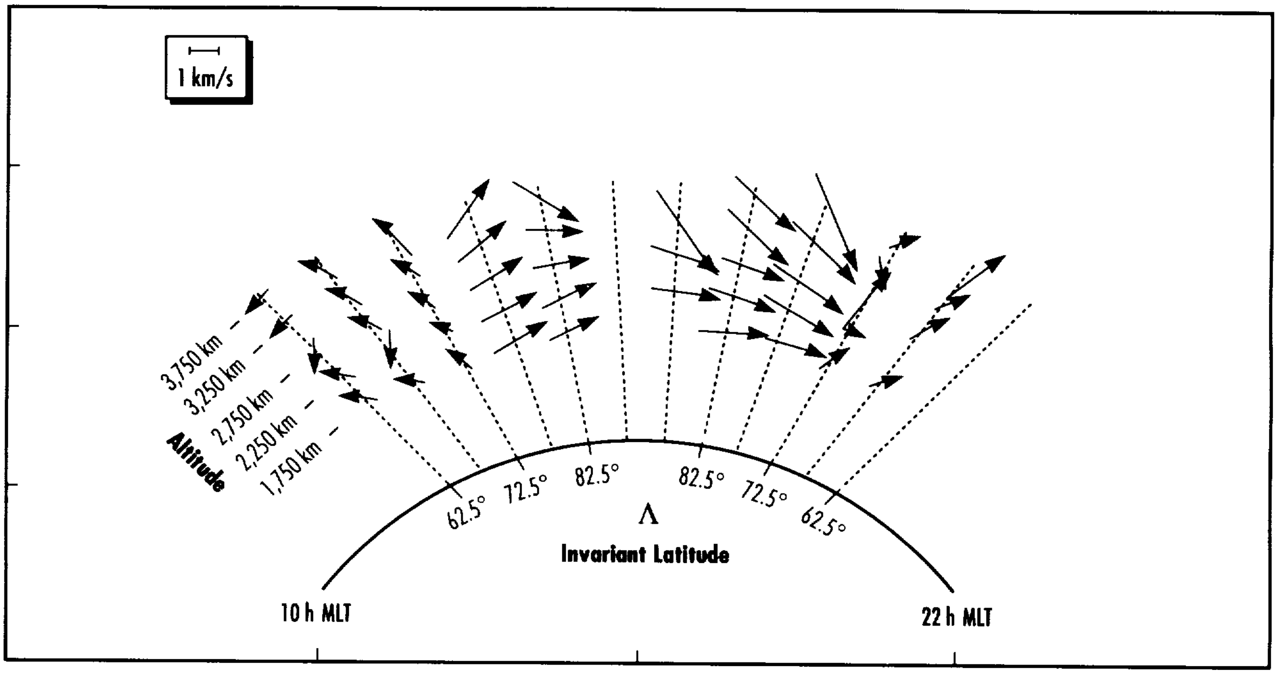

FIGURE 36.—Two-dimensional O^+ velocity field in the polar ionosphere/magnetosphere.

These questions are being addressed through the statistical analysis of more than 4 yr of observations of O^+ (as well as H^+ and He^+) by the RIMS, which was on board the DE–1 satellite. Although the DE–1 satellite has ceased operations, the wealth of data that it produced is still providing new and exciting information on the behavior of the lowest energy ions within the magnetosphere. By statistical analysis it has been possible to put together a 2–D picture of the motion of O^+ from its sources in the cusp and auroral ionospheres, anti-sunward across the polar cap (fig. 36). The motion of O^+ along magnetic field lines (the dotted lines in fig. 36) was derived from the RIMS data, while the motion perpendicular to the magnetic field (which results from electric fields present in the ionosphere) was taken from averages derived by a separate instrument. Combining these two velocity fields gives the average motion in two dimensions, as shown. The upward motion is readily apparent from the dayside cusp/auroral zone (62.5 degrees<Λ<77.5 degrees). Coupled with the anti-sunward motion for Λ>72.5 degrees the result is a poleward transport of O^+. But notice that as the ions move more poleward, the velocity turns downward at the higher altitudes before becoming predominantly upward on the nightside (Λ <72.5 degrees) in what corresponds again to the auroral zone. These downward velocities in the polar cap are indicative of the ions that were accelerated out of the dayside ionosphere with insufficient energy (or upward speed) to escape gravity and, thus, ultimately fell back into the ionosphere. The apparent ballistic trajectories hinted at by the velocity vectors result from the horizontal transport of the ions, under the influence of electric fields, which occurs simultaneously with the upward and downward motions. Further analysis of this type can be used to determine how much O^+ escapes the ionosphere and how much returns under different geophysical conditions. Expanding this type of analysis to higher altitudes—beyond the 4,000-km limit set in this study—will show where the escaping O^+ ultimately goes.

The goal of this type of research is to provide a clear understanding of the nature of the near-Earth plasma environment—how it evolves, how it interacts with the interplanetary environment, how it affects the Earth—to improve the understanding of the total Earth-space system. The search for answers to questions regarding the fundamental workings of nature is the heart of scientific inquiry, and scientific inquiry is an integral part of NASA.

Sponsor: Office of Space Science

■

A Cleft Ion Fountain Model

Dennis L. Gallagher/ES53
205-544-7587

In recent years, the ionosphere has become recognized as a major source of plasma in the magnetosphere (Chappell et al. 1987). The dominant sources of outflowing plasma are at high latitudes in the auroral zone and in the polar cap. One of these sources has been found in the dayside ionosphere in the vicinity of the northern magnetic cusp and is referred to as the cleft ion fountain. The cleft ion fountain is estimated to supply over 10^{24} hydrogen and oxygen ions per second, as well as lower fluxes of helium, nitrogen, and molecular ions.

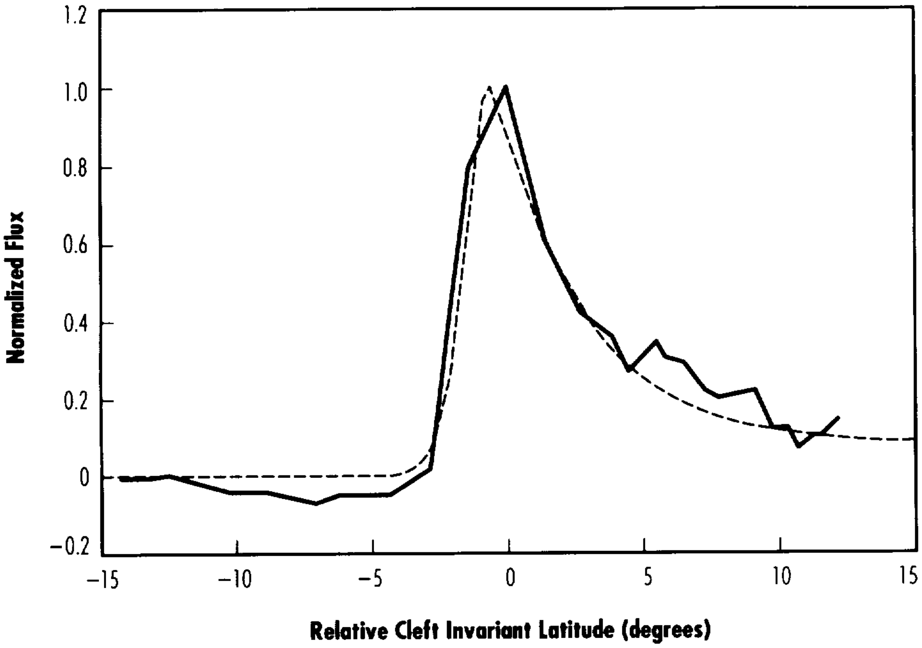

FIGURE 37.—Typical latitude profile of O+ flux in the cleft ion fountain. North magnetic pole is to the right.

These ions are thought to be energized perpendicular to the magnetic field at a relatively low altitude and then driven outward by the magnetic mirror force. At 2 Earth radii, the outflowing ions are found to be flowing up magnetic field lines with mass-dependent velocities; i.e., lighter ions move with greater upward velocities. As the ions move upward, they are convected anti-sunward by an electric field imposed on the polar cap by the motion of the solar wind through the Earth's magnetic field. Due to their slower upward velocities, heavier ions are convected more strongly anti-sunward than are the lighter ions. The resulting anti-sunward "spray," or spatial dispersion of ions from the cleft region of the polar cap, is the origin of the name "cleft ion fountain."

An understanding of the cleft ion fountain has developed from a number of point measurements and through the computer simulation of ions flowing out of the ionosphere through convective and accelerating electric fields. Although a relatively clear picture of the properties and dynamics of cleft ion outflow has been developed, the global structure, interrelationship to other polar cap and magnetospheric processes, and the responses to changing geophysical conditions remain to be understood. Due to recent advances in imaging instrument design, it has become possible to remotely observe magnetospheric structures like the cleft ion fountain on a global scale. Whether imaging in scattered light from the Sun or low-energy neutral atoms, instrument design depends upon estimates of the luminocities of the source plasmas.

Recent efforts have focused on the development of a model of the cleft ion fountain that may be efficiently used in computer simulations of global images of this ionospheric plasma source. The goal of this modeling is to obtain an analytical, continuous global description of outflowing oxygen flux and perhaps density as a function of position over the polar cap. The modeling is based on RIMS measurements of the cleft fountain from the DE–1 spacecraft and on kinetic simulations of outflowing ion trajectories. Although kinetic simulations could be directly used to predict ion flux as a function of position, the intensive computational requirements make this alternative impractical.

A typical latitudinal profile of cleft oxygen ion outflow is shown in figure 37. In this figure, upflowing oxygen flux is plotted (solid line) against invariant latitude relative to the latitude of the peak in the flux at about 73 degrees. Flux is normalized to the peak flux of about 2×10^8 per cm^2/s. The flux is also normalized using a factor of $(R/2)^3$ to compensate for the relatively small variation in spacecraft radial distance (R) during this polar cap pass. Relative latitude is shown increasing toward the northern pole to the right. As shown, the low latitude boundary of the cleft ion fountain is usually sharp, with a more slowly falling profile at high latitudes. The dotted line in the figure represents an analytical approximation to the observed flux profile.

By using observations from many orbital passes like that shown in figure 37, the local time profile of the cleft ion fountain has been obtained on a statistical basis. On average and during conditions of low geophysical activity, the cleft ion fountain is approximately 2-h wide in magnetic local time and centered at prenoon local times. For the purpose of this model development, the local time profile is assumed to be Gaussian with a width of 2 h in local time and centered at noon.

Outflowing oxygen trajectories are taken from Lockwood et al. (1983). The trajectories are for a perpendicular electric field strength of 35 mV/m at 90 degrees latitude and no parallel electric field. In their figure 6, oxygen trajectories are shown for initial ionospheric parallel energies ranging from 1 to 20 eV. Although not strictly correct, these trajectories are taken to generally represent the paths that oxygen ions would take when rotated to the latitude where the outflow occurs. In this way it becomes possible to relate outflow from a given latitude and at a given initial energy to the polar cap locations where those outflowing ions can be observed.

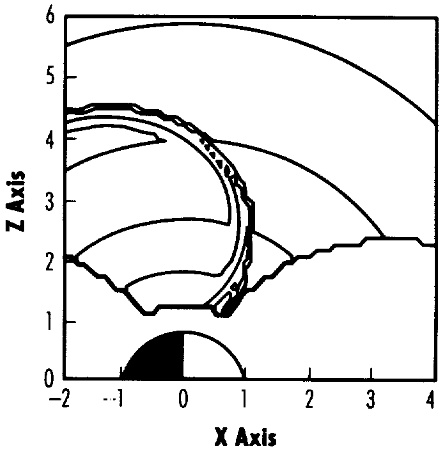

FIGURE 38.—Logarithmic contours of O^+ flux and polar wind.

Observed low altitude fluxes, energies, and densities can be mapped to the locations of interest once the originating ionospheric locations for various initial energy oxygen ions are determined. This mapping requires that the influence of the diverging magnetic field, convective electric potential, and spatial energy dispersion of these quantities be taken into account. This is performed incrementally over the spectrum of initial ion energies in order to assemble an approximate picture of what would be observed in particle velocity phase space at arbitrary locations over the polar cap. Figure 38 is an example of the early work in developing this model of the cleft ion fountain. The figure shows contours of oxygen flux superimposed on the polar wind over the polar cap, for a source limited in latitude and initial energy. Solar magnetic coordinates are used in the figure. When complete, the modeling of the cleft ion fountain will provide an analytical description of fountain characteristics that can be used to simulate plasma imager observations over the polar cap and, thereby, contribute to imager design and mission planning.

Chappell, C.R.; Moore, T.E.; and Waite, J.H., Jr. 1987. The Ionosphere as a Fully Adequate Source of Plasma for the Earth's Magnetosphere. *Journal of Geophysical Research* 92:5896–910.

Lockwood, M.; Chandler, M.O.; Horwitz, J.L.; Waite, J.H. Jr.; Moore, T.E.; and Chappell, C.R. 1985. The Cleft Ion Fountain. *Journal of Geophysical Research* 90:9736–48.

Sponsor: Office of Space Science

■

Minor Ion Contributions to the Ionosphere and Magnetosphere

Paul D. Craven/ES53
205-544-7639

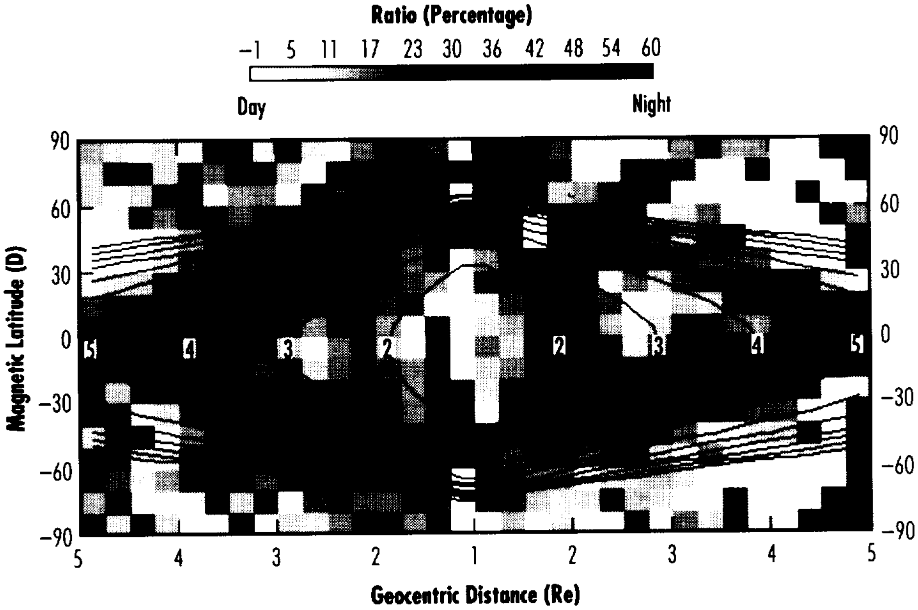

Figure 39.—Average N^+/O^+ ratio for all conditions.

Reported observations of singly ionized nitrogen (N^+) from both rockets and satellites have covered the last 30 yr. Measurements in the ionosphere from satellites started in 1958 with *Sputnik* 3 (Chandra et al. 1970). The reported measurements of N^+ range in altitude from 140 km to several Earth radii. Most of the early measurements are in the ionosphere below 1,000 km. Interest in the ion composition in the outer ionosphere and magnetosphere started with the measurements of O^+ and He^+ reported by Shelley et al., in 1972. Subsequent measurements of ion composition in the magnetosphere resulted in the discovery of low-energy N^+ and doubly ionized nitrogen (N^{++}) by Chappell et al., in 1982. The ambient conditions (i.e., local time, solar activity, geomagnetic activity, and season), over which all these measurements (covering the ionosphere and magnetosphere) were made, cover a wide range. The reported N^+ number densities range from a low of 0.001 percent to more than 100 percent of the O^+ number density. The great range relative to O^+ is due to the large range in the locations and ambient conditions of the measurements.

When this study was started, the challenge was to concentrate on and model the plasmaspheric N^+ and to compare the model with the measurements to determine how well the plasmaspheric processes are understood. In order to do this, the major ions (those with the highest density, H^+, He^+, and O^+) had to be included because ionic nitrogen interacts with all of them in some way. The objective is to compare the predictions of computerized physical models that fully simulate the plasmasphere/ionosphere with the data to confirm our understanding of ionospheric/plasmaspheric processes and ionosphere/plasmasphere interactions, or determine where the weaknesses are. The physical model used is the Field Line Interhemispheric Plasma model that contains all the necessary ion-neutral and ion-ion interactions, photochemistry, and diffusion processes (Richards and Torr 1985).

Relatively little has been done with N^+ even though it is the second most abundant ion in the ionosphere at the F_2 peak (O^+ is the most abundant), and ionospheric/plasmaspheric models show it to be a constant companion of O^+. Because N^+ has a mass near that of O^+, it should follow the O^+, but with a lower density. Its concentration relative to O^+ can be used as a test of the importance of transport relative to chemical production and loss effects. Further out in the magnetotail, the contribution of heavy ions other than oxygen to the total density is something of an unknown. Until relatively recently, few of the high-altitude (above the topside ionosphere) instruments have been capable of separating low energy N^+ and O^+ and because of this, some of the O^+ that has been reported may contain some N^+. This study relies heavily on measurements made with RIMS on the DE–1 satellite. These observations were taken from 1981 though 1984 and cover altitudes from about 600 km to about 24,250 km. This instrument is capable of separating the nitrogen and oxygen ions.

Figure 39 shows a global view of the ratio of N^+ to O^+ as a percentage, in grey-scale format, averaged over all seasons, geomagnetic and solar conditions, and 12 h in local time. The dayside and nightside are juxtaposed at the center. Dayside local time is on the left and night on the right. The geocentric altitudes run to the left and right from the center.

Dipole field lines centered on the Earth and corresponding to McIlwain L values of 2 to 11 are shown as the solid lines with those for 2 to 5 labeled. The darkest grey scale represents ratios that are greater than or equal to 60 percent, while the white areas represent no data. One of the most apparent features in this plot is the fact that on the dayside, the ratio is largest between geomagnetic field lines that represent the outer plasmasphere and the equatorward side of the auroral zone. On the nightside, the ratio is greatest in the southern hemisphere in the equatorward region of the outer plasmasphere. The nightside auroral zone field lines (the outermost of the field lines shown) have a reduced amount of N^+ relative to the day side. The data in this figure indicate that the ratio is generally greater than 30 percent in the regions just mentioned. In the inner plasmasphere the ratio is roughly 10 to 30 percent, with a peak around 2 Re geocentric distance on the night side between ±60 degrees geomagnetic latitude.

Overall it is shown that, on average, N^+ is present practically everywhere in the magnetosphere and, in general, its density is a significant fraction of the O^+ density. Studies presently in progress that compare the measurements with the physical model will indicate how well we understand all the processes that affect the terrestrial ions including their production, loss, and transport. The studies will also indicate how well we understand the physical processes that govern the interactions between different regions of Earth-space, in particular the thermosphere, ionosphere, and magnetosphere. An understanding of these regions and the processes that take place in them, particularly the interactions between different constituents and the connections between different regions, is an important part of understanding the Earth's total environment and changes to it.

Chandra, S.; Troy, B.E.; Donely, J.L., Jr.; and Bourdeux, R.E. 1970. *OGO 4 Observations of Ion Composition and Temperatures in the Topside Ionosphere.* NASA/Goddard Space Flight Center Document No. X–615–70–1.

Chappell, C.R.; Olsen, R.C.; Green, J.L.; Johnson, J.F.E.; and Waite, J.H., Jr. 1982. The Discovery of Nitrogen Ions in the Earth's Magnetosphere. *Geophysical Research Letters* 9:937.

Richards, P.G., and Torr, D.G. 1985. Seasonal, Diurnal, and Solar Cyclical Variations of the Limiting H^+ Flux in the Earth's Topside Ionosphere. *Journal of Geophysical Research* 91:5261.

Shelly, E.G., Johnson, R.G., and Sharp, R.D. 1972. Satellite Observations of Energetic Heavy Ions During a Geomagnetic Storm. *Journal of Geophysical Research* 77:6104.

Sponsor: Office of Space Science

■

The Tethered Satellite System–1 Research on Orbital Plasma Electrodynamics Investigation

Nobie H. Stone/ES53
205–544–7642

In 1985, the MSFC Research on Orbital Plasma Electrodynamics (ROPE) investigation was selected for the first TSS mission. ROPE flew on TSS–1 in August 1992 (Stone 1992, and Dobrowolny and Stone 1993). The investigation consisted of two banks of instruments to measure the characteristics and distributions of charged particles around the tethered Italian Space Agency-built satellite—one bank mounted on the satellite's surface and the other on the end of the satellite's fixed boom (Stone et al. 1993). Three Soft Particle Energy Spectrometers (SPES) were mounted on the satellite's surface—one at the equator, one at 45 degrees, and one on the spin axis. It was intended that these body-mounted sensors, in conjunction with satellite spin, map the distribution of electron flux to the satellite's surface. The boom-mounted sensor package consisted of two SPES—one facing the satellite and the other facing radially away—and one Differential Ion Flux Probe (DIFP) facing the satellite (fig. 40). The purpose of the boom-mounted sensors was to measure the ion and electron flux into and out of the plasma sheath surrounding the satellite.

The objective of the ROPE investigation was to study the complex phenomena and processes expected to exist around a satellite traveling at mesothermal speeds (supersonic with respect to the ions and neutrals, but highly subsonic for electrons), that is highly biased and extracts electrons from the ionospheric plasma. For example, it was expected that for tether lengths greater than 10 km, the satellite would become biased to a potential of several kilovolts. In this case, measurements from the ROPE sensors would provide a unique opportunity to investigate the resulting high-voltage plasma sheath, the way in which current would flow through the sheath to the satellite, how this current would be distributed and affected by the geomagnetic field, and the magnitude of such a current as a function of the ambient ionospheric parameters and the magnitude of the voltage developed across the tether. The ionization of neutral gas within the sheath and the effect of ionization on the tether current could also be investigated.

The prime ROPE objectives could not be met because the system deployed to only 256 m, rather than the planned 20 km. However, in spite of this, the ROPE investigation had several accomplishments and will contribute to the understanding of the physics of short electrodynamic tethers in space.

The instrument design and its operation and control were validated. The two types of sensors, DIFP and SPES, both performed as expected. The floating supply, which controls the potential of the boom-mounted sensor package, exhibited a minor problem in its low-potential range. This problem, which resulted from a mismatch between the measurement and commanding rates in the feedback loop, is easily corrected.

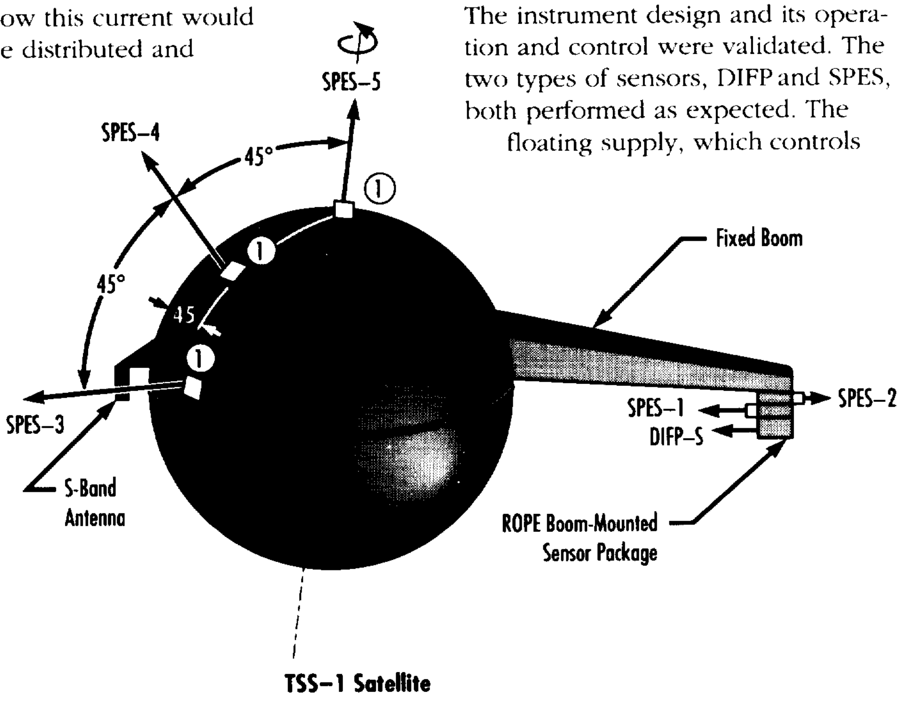

FIGURE 40.—ROPE sensor location.

In addition, the data obtained by ROPE indicate several interesting events in the behavior of the tether at low voltages and short deployments. For example, it was determined that the charge carriers for the tether current are suprathermal electrons in the 40 to 50 eV energy range—not the thermal electrons (0.1 eV range) as had been expected.

This conclusion was arrived at from two approaches. First, the flux density of the suprathermal electrons detected by the SPES–3 sensor on the surface of the satellite (fig. 41(a)) was integrated over the area of the satellite's surface to arrive at a total electron flux to the satellite (Winningham et al. 1992). If these electrons were the charge carriers, the total electron flux should be in accord with the measured tether current. This was found to be the case. Secondly, these data represent an event where the satellite potential increased over a period of time (fig. 41(c)). As the satellite's potential increased, the energy and current density of the thermal electrons also increased (fig. 41(b)). If these electrons were the current carriers, the total tether current should have also increased—but the current did not respond to the increased thermal electron flux and, in fact, decreased slightly. This is interpreted to mean

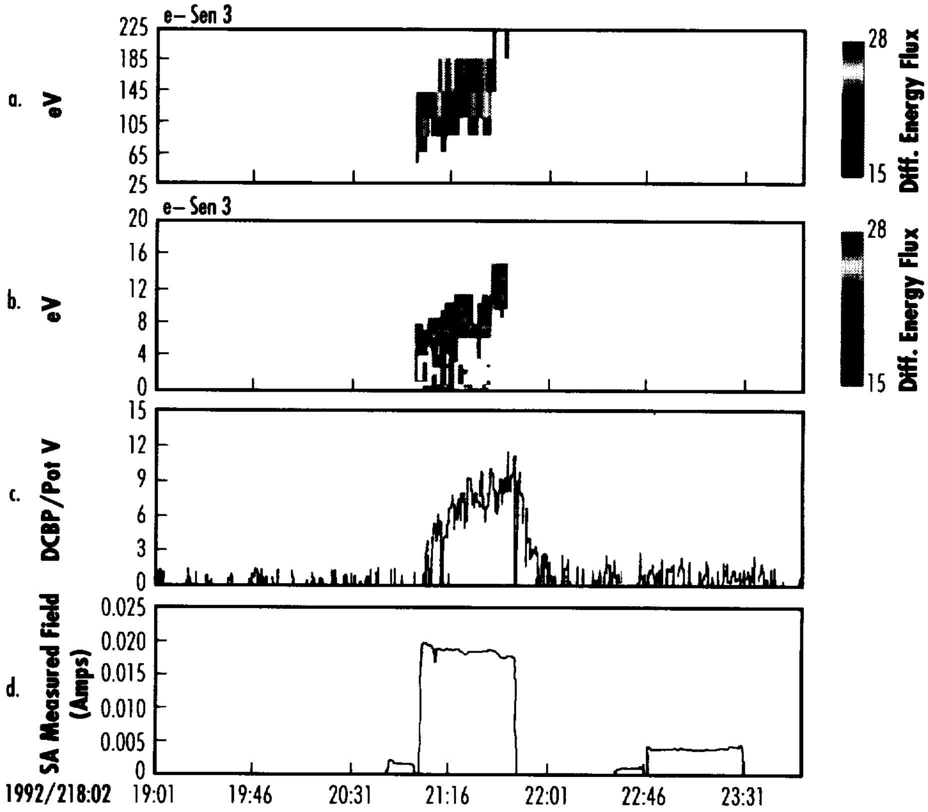

FIGURE 41.—(a) Suprathermal particles measured by SPES–3, (b) thermal particles measured by SPES–3, (c) satellite potential, and (d) tether current.

that the bulk of the current is carried by the suprathermal electrons (fig. 41(a)), and that the slight increase in flux due to the enhanced number of thermal electrons being collected was insignificant (Wright et al. 1992).

If the conclusion that the current is carried by suprathermal electrons rather than thermal electrons is correct, it will carry some interesting implications. For example, thermal electrons exist in the natural geoplasma environment. But the 40 to 50 eV electrons do not. They must be created somewhere, and the best theory is that the orbiter, with its cloud of water and other gaseous emissions, is involved. The next step will be to identify the appropriate ionization and charge-transport processes that could account for suprathermal electronics, created at the orbiter, being observed at the satellite 256 m away.

Dobrowolny, M., and Stone, N.H. 1993. A Technical Overview of TSS–1: The First Tethered Satellite System Mission. In press, *Nuovo Cimento.*

Stone, N.H. 1992. An Early Assessment of the TSS–1 Mission. Invited paper, *EOS Transactions,* American Geophysical Union (AGU) 73 (42), 424.

Stone, N.H.; Wright, K.H., Jr.; Winningham, J.D.; Biard, J.; and Gurgiolo, C. 1993. A Technical Description of the TSS–1 ROPE Investigation. In press, *Nuovo Cimento.*

Winningham, J.D.; Baird, J.; Stone, N.H.; and Wright, K.H., Jr. Tethered Satellite Current Collection System—How Well Do We Understand It? *EOS Transactions,* AGU 73 (42), 422.

Wright, K.H., Jr.; Stone, N.H.; Winningham, J.D.; and Samir, U. 1992. Preliminary Observations of the ROPE Experiment During the First Tethered Satellite Mission. *EOS Transactions,* AGU 73 (42), 424.

Sponsor: Office of Space Science

University Involvement: University of Alabama in Huntsville

■

Application of Automated Data Acquisition to the Low-Energy Ion Facility

Victoria N. Coffey/ES53
205-544-7635

The MSFC Magnetospheric Physics Branch laboratory focuses on the development and testing of low-energy ion mass spectrometers and electron detectors. The new generation of detectors requires large volumes of data-taking, which led toward the efforts of automating the testing and data-collecting sequences. This report describes the application of the automated laboratory toward a recent intense test and calibration that was done for the TIDE to be flown for the Global Geospace Science (GGS) Mission.

The automation of the LEIF is based on a Macintosh IIfx™ multi-tasking computer and the LabView™ software and hardware from National Instrument. This software is a graphical, object-oriented language that allows the development of a virtual instrument (VI) that can define a measurement of an instrument or emulate an instrument. These VI's, in turn, can become a subprocess to a larger VI or procedure.

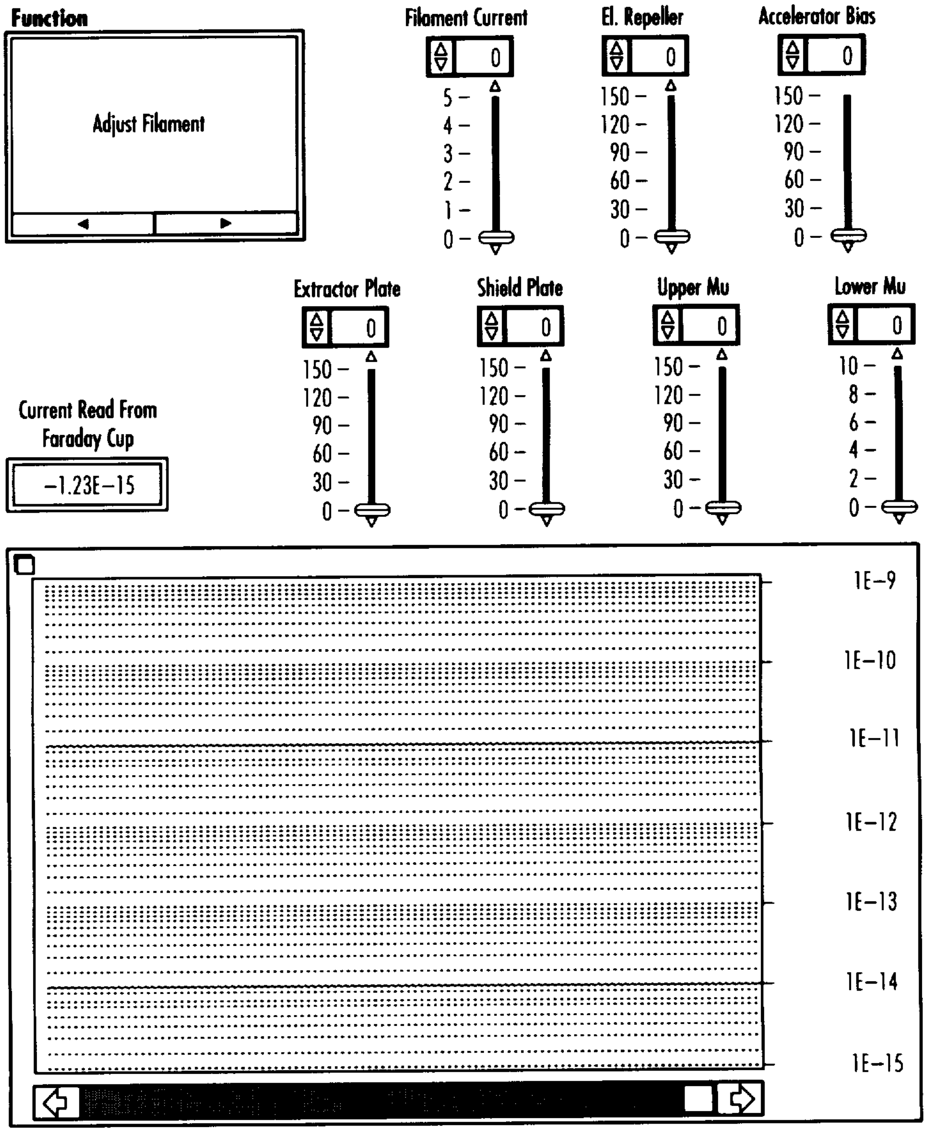

Function: Adjust Filament

Filament Current: 0

El. Repeller: 0

Accelerator Bias: 0

Extractor Plate: 0

Shield Plate: 0

Upper Mu: 0

Lower Mu: 0

Current Read From Faraday Cup: -1.23E-15

Figure 42.—Ion source front panel.

There are several types of instrument devices and controllers in the LEIF lab to be interfaced with the LabView™ software and hardware for the basic "handshaking" requirement. VI's were developed to control the 12-ion-source power supplies, the motion of the two-axis instrument fixture, the motion of a Faraday cup, an electrometer that measures the current from the Faraday cup, a pulse height analyzer, a chamber pressure controller, and so forth. The interfaces used were eighter digital, analog, or the general purpose interface bus (GPIB).

For example, the ion source in the laboratory is controlled by 12 separate power supplies that are used to optimize the particle beam. Manually, it was not easy to tune the source for a particulate beam energy and was time consuming to obtain low-energy particle beams due to the sensitivity of the source to even small voltage changes to the source elements. After interfacing LabView™ and the computer with the power supplies, the particle beams were easier and quicker to obtain with small controlled voltage changes (40 mV). As shown in figure 42, the controls of the ion source are listed across the top on the front panel. To obtain a desired particle energy, the filament current is slowly brought up to the nominal value. Then the non-varying power supplies are set to their values: an electron repeller, the anode potential, and the five magnetic coils (not shown in the figure). The shield plate, extractor plate, and upper and lower mu metals are then slowly swept while watching the output of the electrometer measuring the current from the Faraday cup. The current to the Faraday cup is plotted as a function of time to view the response of the beam to the settings.

After the basic handshaking VI's were developed, they could be built into larger VI's that make up control-and-data-taking sequences. A front panel and partial code of a VI that was used to test TIDE is shown in figure 43. The left side of the front panel shows the control parameters that have to be typed in by the user before starting the program. The right side of the front panel shows the output data parameters that are being obtained in real time from the different devices during the test. The bottom figure contains the inner loop of the VI. The script to this VI is listed below:

```
Do i=  1, Number of data uploads
       to instrument
   1.  Move Faraday cup into
       beam path, read electrome-
       ter, move out cup, write
       electrometer current to com-
       puter screen and to file.
   2.  Read particle energy of ion
       source and write to file.
   Do i=  Minimum azimuth angle,
          maximum azimuth angle
      1.  Move rotation axis to next
          angle input.
      2.  Write angle to computer
          screen and to file.
      Do i=  Minimum polar angle, maxi-
             mum polar angle
         1.  Move rotation axis to next
             angle input.
         2.  Write current angle to com-
             puter screen and to file.
         3.  Move Faraday cup into
             beam path, command power
             supply sweep for retarding
             potential curve, plot to
             screen, and then print.
         4.  Inquire over Ethernet line to
             a UNIX machine to verify
             status of data upload to
             instument.
      enddo
   enddo
enddo
```

The development of this automated system has resulted in significant increases in the efficiency and value of the LEIF laboratory. It would not have been possible to meet the stringent requirements of the TIDE testing and calibration without the use of this automation system for such lengthy tests. It has proven to be versatile for new applications, and procedures are easy to implement with the hardware boards and the modular, icon-based software. In the future, more work will be done on completely automating the ion source.

Sponsor: Marshall Space Flight Center Director's Discretionary Fund

■

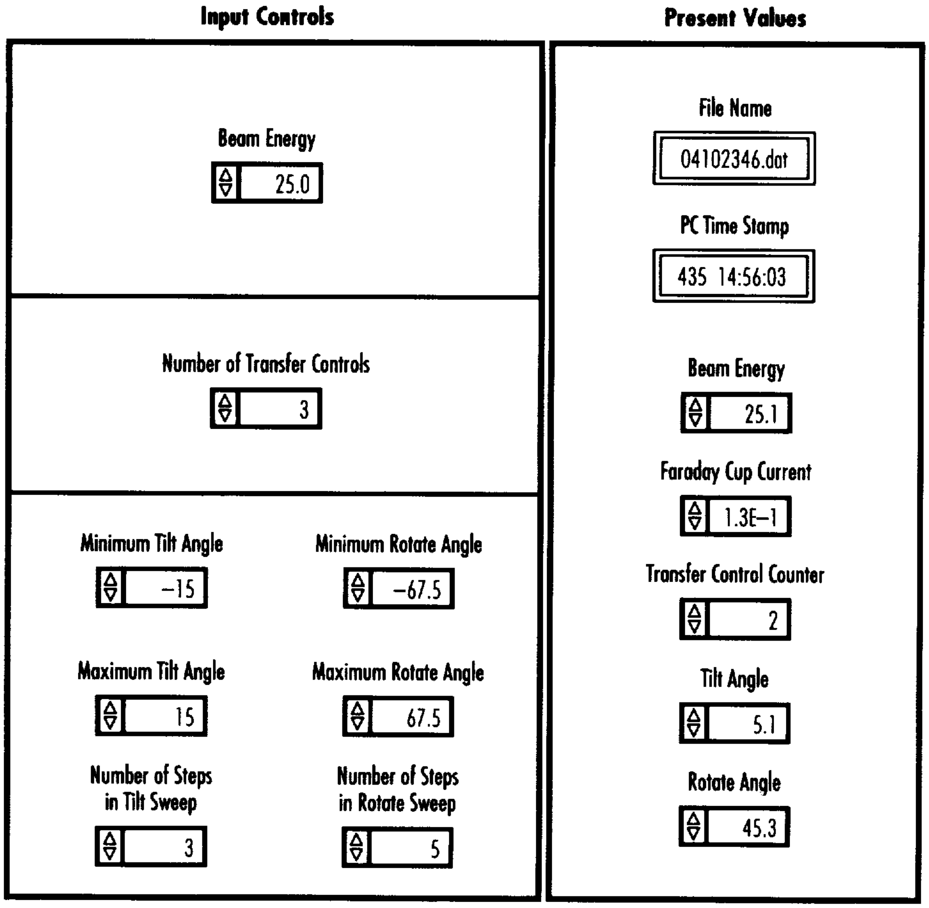

Input Controls

Beam Energy
25.0

Number of Transfer Controls
3

Minimum Tilt Angle
-15

Minimum Rotate Angle
-67.5

Maximum Tilt Angle
15

Maximum Rotate Angle
67.5

Number of Steps in Tilt Sweep
3

Number of Steps in Rotate Sweep
5

Present Values

File Name
04102346.dat

PC Time Stamp
435 14:56:03

Beam Energy
25.1

Faraday Cup Current
1.3E-1

Transfer Control Counter
2

Tilt Angle
5.1

Rotate Angle
45.3

FIGURE 43.—Ion source front panel of VI.

Enhanced Capabilities of an Electrostatic Deflection and Collimation System

Nelson G. Martinez/ES53
205-544-7653

The description of the lower ionosphere populations of multiple ion plasma streams differing in flow direction is fundamental to the understanding of the mechanisms of the ionosphere/atmosphere coupling. After the launching of the first artificial satellite in the late 1950's, there have been many efforts to design scientific instrumentation capable of characterizing the lower ionosphere ion plasma. In that regard, the Differential Ion Flux (DIF) Probe (Stone et al. 1985) has proven to be highly successful after having been flown on two sounding rocket and three space shuttle missions. One of the most important reasons for this achievement is the design of an Electrostatic Deflection and Collimation System (EDCS) as part of the DIF sensor head. This article briefly describes modifications to the EDCS design by using ray tracing simulation and miniaturization technology and the future application of these improvements to a new generation of space instruments.

The main feature of the EDCS is an electro-optical system consisting of a set of 45-degree beveled slits. Each side of the slits becomes an electrode with a shape of an inverted isosceles triangle, being plated thoroughly with copper and with the two slanted sides electrically insulated from each other. Each of these sides has an applied voltage swept through a range from 0 to ±15 V,

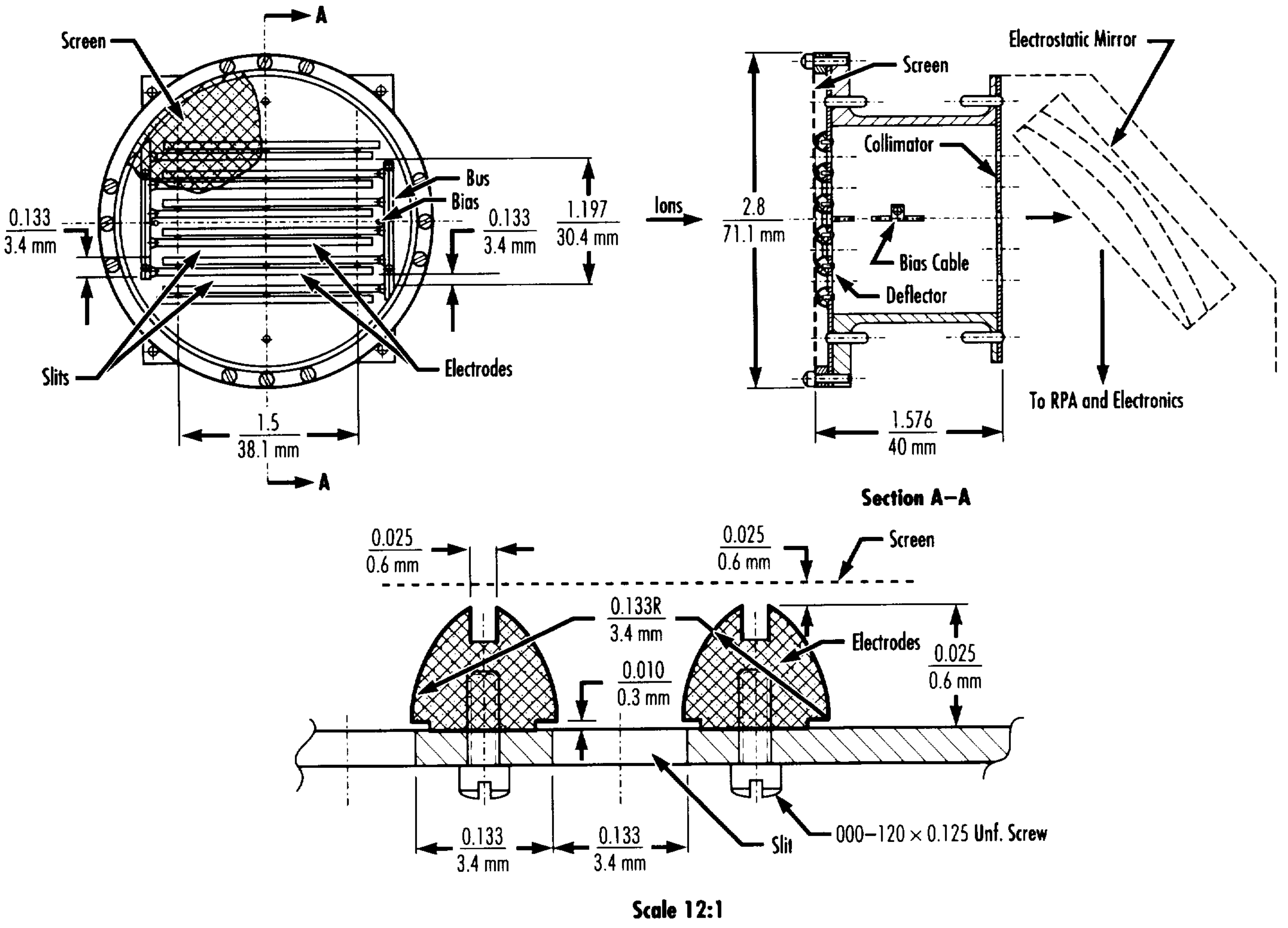

Figure 44.—Cross sections of EDCS on DIF.

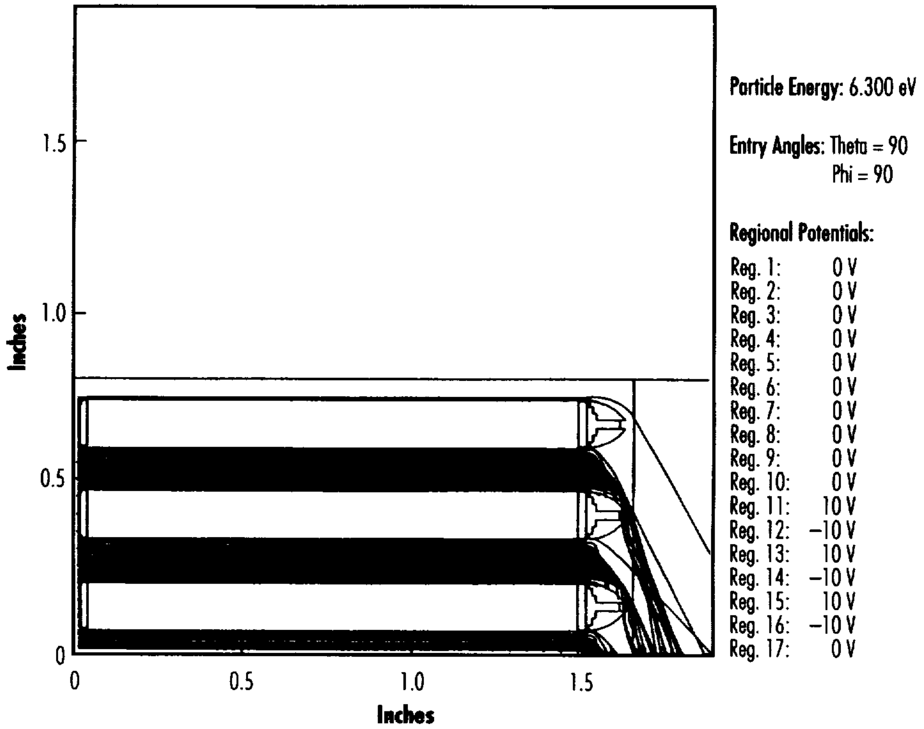

FIGURE 45.—CRIMS deflectors particle ray tracers.

respectively, in a 400-ms period. The interelectrode electric field makes it possible to increase the polar angle resolution from 5 degrees with simple slits, to about 60 degrees, allowing the increase of sensitivity distinctive to the DIF probe.

The application of a computer simulation using a 2–D ray tracing program was the first step needed to improve the EDCS. The performance of several electrode cross sections was computer simulated. The results range from poor sensitivity with electrodes consisting of two parallel plates, to a better sensitivity by using plates with the triangular shape, as in the DIF, to a much better performance with electrodes of pentagonal contour. The simulations lead to semicircular electrodes with a radial electric field configuration and eventually to the cross sections shown in figure 44.

Although the electrode cross section seems relatively simple, the design requires highly miniaturized components that must be capable of withstanding the severe launch environment typical of the sounding rockets payloads. The electrodes shown in figure 44 are constructed from Noryl™, a commercially available plastic with good machining properties, by cutting the profile using a specially designed mill cutter. The electrodes' external conducting surfaces are made by vacuum deposition.

The modified EDCS will be integrated into the prototype of the Cometary Rendezvous Ion Mass Spectrometer (CRIMS) instrument. This instrument has been thoroughly tested in the Low Energy Ion Facility; consequently, the results of testing the modified version can be fully assessed by comparison with the existing data. The CRIMS modification is shown in figure 45. Five sets of slits, each flanked by a set of electrodes, make up the new instrument aperture. Each slit is 3.4 by 44.5 mm, providing a total aperture area of 7.5 cm^2. The electrode set covers the 3.4 mm interslit space and is permanently fastened to the aluminum substrate. The bias voltage is supplied via two buses with spring contacts running along the electrodes' lateral sides.

Space plasma instrumentation fitted with the larger apertures permitted by the new electrode design will allow a better description of the densely populated multiple plasma ions streams typical in the lower terrestrial ionosphere.

Stone, N.H.; Lewter, B.J.; Chisholm, W.L.; and Wright, K.H. October 1985. Instrument for Differential Ion Flux Vector Measurements on Spacelab 2. *Review of Scientific Instrumentation* 56(10).

Sponsor: Office of Space Science

Infrared Spectroscopy of the Earth's Upper Atmosphere and Planetary Atmospheres

Mian M. Abbas/ES55
205-544-7680

Infrared thermal emission observations from ground-based, airborne, and spacecraft platforms provide a powerful tool for studies of the thermal structure and constituent distributions of the atmospheres of the Earth and the planets. Many atmospheric gases exhibit vibrational-rotational transitions in the 10–3,000 cm^{-1} spectral region, which may be observed with high sensitivity and high spectral resolution spectrometers. The observed spectrum of the Earth's atmosphere, for example, includes spectral features of the trace gases CO_2, H_2O, HO_2, H_2O_2, OH, N_2O, NO, NO_2, HNO_3, N_2O_5, ClO, $ClONO_2$, HF, HCl, and HCN. A synthetic infrared spectrum of Saturn's moon Titan, calculated for a model atmosphere with a limb tangent viewing geometry, exhibits some very prominent features of a number of trace gases in Titan's atmosphere (fig. 46). A detailed analysis of the observed infrared spectra provides information about the temperature and gas concentration profiles, and physical and chemical processes in the atmospheres.

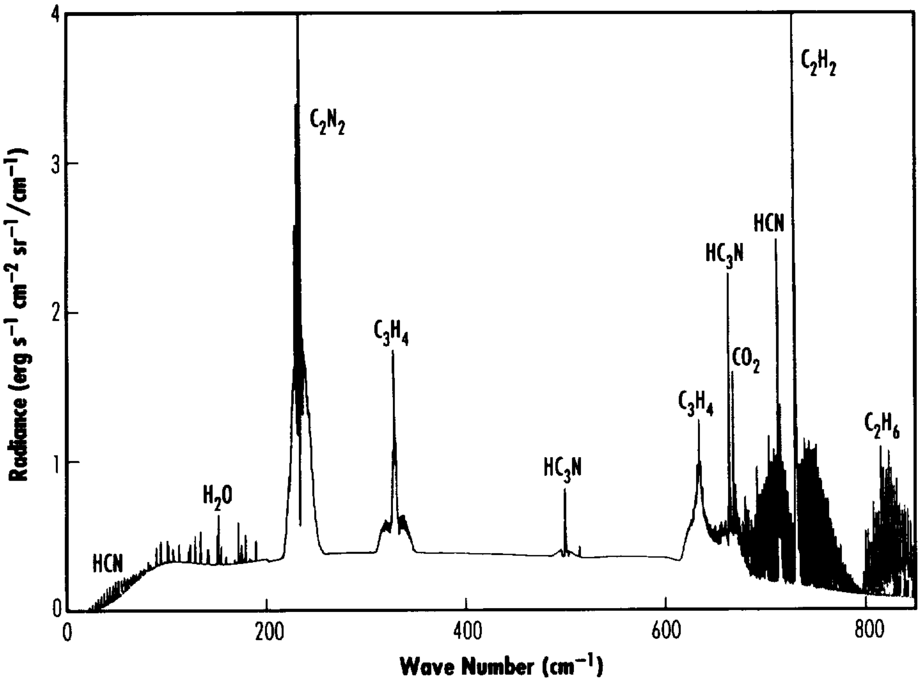

Figure 46.—Titan synthetic limb tangent spectrum $\Delta v = 0.5$ cm^{-1}.

Infrared radiative transfer models and spectral inversion techniques for studies of the thermal structure and constituent distributions of the Earth and planetary atmospheres have been developed at MSFC. The three main focus areas concentrated on during 1992 are described in this article.

The first focus area was development of rapid inversion techniques for accurate retrieval of thermal structure and gas concentration profiles from infrared observations with instruments with a finite field of view. An analysis of a large amount of data obtained from spacecraft measurements becomes a very time-consuming process when the instrumental and physical processes in the atmosphere are fully accounted for in order to minimize the retrieval errors.

The second focus area was development of infrared radiative transfer models and inversion techniques for studies of Saturn and Titan, in support of the Composite Infrared Spectrometer (CIRS) on the *Cassini* orbiter mission. Preliminary studies of radiative transfer models and suitable methods for analysis of synthetic data generated for the two sources to be observed with the CIRS instrument are in progress.

Thirdly, radiative transfer models have been developed for calculation of planetary-averaged broadband thermal emission flux of Uranus and Neptune, with the atmospheric temperature profiles determined from the *Voyager* data. These calculations provide a basis for comparison with the Kuiper Airborne Observatory (KAO) observations of the two sources in order to develop infrared photometric standards for in-flight calibration of the Infrared Space Observatory (ISO) Photopolarimeter Instrument (ISOPHOT). KAO flux observations of Uranus and Neptune made on March 7, March 16, and July 17, 1992, are found to be in agreement with the model flux calculations to within the uncertainty in the model temperature profiles.

Sponsors: Office of Space Science and Marshall Space Flight Center Director's Discretionary Fund

■

Imaging the Auroral Oval at Vacuum Ultraviolet Wavelengths

Jerry K. Owens/ES55
205-544-7678

The emissions of light known as auroras result from the collisions between energetic particles (such as protons and electrons) and atmospheric gases in the lower thermosphere (altitudes between approximately 100 and 150 km). These are solar wind particles that are swept up by the Earth's magnetic field and accelerated by the various electromagnetic processes operative within the magnetosphere. Large fluxes of these particles (equivalent to 100-million kW during the almost daily events known as magnetic substorms) are channeled down into the atmosphere at high latitudes. The auroras occur around a magnetic field line footprint corresponding roughly to a geomagnetic latitude of 70 degrees, but are displaced to lower latitudes at local midnight. The band of emissions thus formed around the geomagnetic poles is known as the auroral oval. The energetic particle collisions produce emissions throughout the spectrum from the vacuum ultraviolet to the infrared but, to date, almost all of the work has been done in the visible wavelengths observable from the ground. The observations have also been restricted to nightside aurora due to the severe limitations imposed by the bright scattered sunlight on the dayside of the Earth.

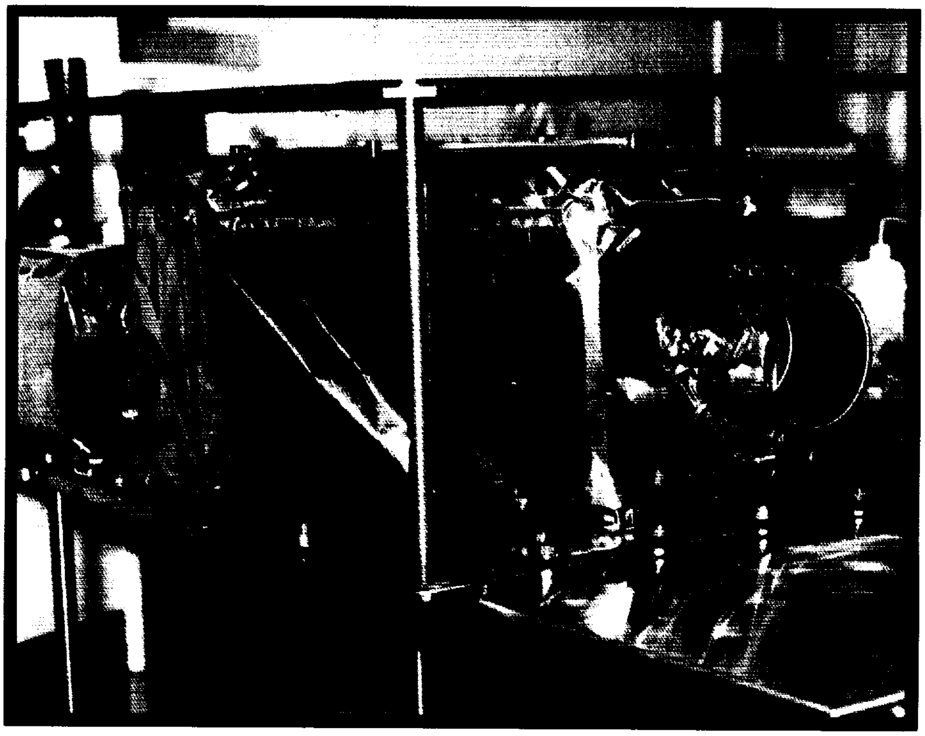
FIGURE 47.—The UVI in a clean room in the Space Science Laboratory.

The Ultraviolet Imager (UVI) (fig. 47) was constructed and delivered in July 1993 for integration as part of the Polar spacecraft of the GGS program. The Polar spacecraft is scheduled to be launched in 1994 into a highly eccentric orbit (9×2 Earth radii). This orbit will allow the UVI to view the entire auroral oval for approximately 9 h per orbit, and it will be able to perform studies at higher spatial resolution of smaller regions for the remaining 9 h. Operating in the vacuum ultraviolet, UVI can provide information on both the sunlit and dark auroras, vastly increasing the scope and value of the data for global studies that are now needed. Using images from UVI acquired in different spectral bands, researchers will be able to determine the characteristic energy of the particles incident on the atmosphere as well as the total energy deposited (Germany et al. 1990). Since the instrument is an imager, the spatial and temporal morphology of the aurora will also be studied. Since images of the auroral oval obtained from space provide spatial/temporal information that maps back to different regions of the magnetosphere, the UVI will also provide a frame of reference that will allow auroral features to be related to events monitored in remote regions of the Earth's magnetosphere.

The UVI comprises a fast optical system (f/2.8) with good image quality over its full 8-degree field of view, a passively cooled intensified CCD focal plane detector that represents an evolution of systems developed by this research group for other programs, and a set of narrow bandpass interference filters. To make quantitative measurements in the 120- to 220-nm wavelength region, new filters had to be developed (Zukic et al. 1990a and 1990b) with bandpasses as narrow as 5 nm (fig. 48), which is a major advance in filter technology over previously attainable bandpasses in this spectral

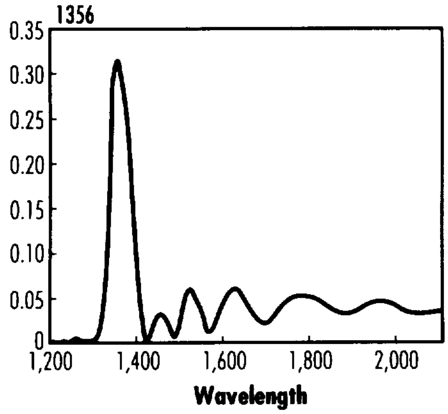

FIGURE 48.—An example of the wavelength response of a narrow bandpass vacuum ultraviolet filter developed for the UVI.

region. Thus, UVI represents technological advances in the state of the art in optics, detectors, and vacuum ultraviolet filters.

Germany, G.A.; Torr, M.R.; Richards, P.G.; and Torr, D.G. 1990. The Dependence of Modeled OI 1356 and N_2 Lyman Birge Hopfield Auroral Emissions on the Neutral Atmosphere. *Journal of Geophysical Research* 95:7725.

Zukic, M.; Torr, D.G.; Spann, J.F.; and Torr, M.R. 1990a. Vacuum Ultraviolet Thin Films. 1: Optical Constants of BaF_2 , CaF_2 , LaF_3 , MgF_2 , Al_2O_3, HfO_2 , and SiO_2 Thin Films. *Applied Optics* 29:4284.

Zukic, M.D.; Torr, D.G.; Spann, J.F.; and Torr, M.R. 1990b. Vacuum Ultraviolet Thin Films. 2: Vacuum Ultraviolet All-Dielectric Narrowband Filters. *Applied Optics* 29:4293.

Sponsor: Office of Space Science

■

Spectroscopy of the Mesosphere and Thermosphere From the Space Shuttle

Jerry K. Owens/ES55
205-544-7678

Spectroscopy is a powerful means for remote sensing of the composition and temperature of the atmosphere, and these measurements allow a determination of the physical and chemical processes occurring in the region of the atmosphere being observed. The mesosphere (about 60 to 100 km) and thermosphere (100 km to approximately 500 km) are regions that have extensive emission spectra in the UV, visible, and NIR spectral regions. Much of the spectroscopy of this region of the atmosphere has been done from the ground, where it is limited to nighttime observations of visible wavelengths, or by small instruments flown on sounding rockets or satellites, which have covered limited portions of the wavelength range at any one time. The mesosphere/lower thermosphere (MLT) region (about 60 to 150 km) is too low for direct measurements from satellites and too high to use high-altitude aircraft or balloons. Measurements of this region have, until now, been limited to occasional sounding rocket flights. Thus, the term "ignorosphere" has often been used in connection with this region. Remote sensing techniques are now being developed for the study of the MLT region.

The Imaging Spectrometric Observatory (ISO) flew on the first mission of the Atmospheric Laboratory for Applications and Science (ATLAS–1). This was a Spacelab mission that was launched on March 24, 1992, and landed April 2, 1992. From the space shuttle, the ISO was able to measure, for the first time, the emission spectrum of the mesosphere, thermosphere, and ionosphere under both sunlit and dark conditions over a broad wavelength range (30 to 830 nm).

The ISO is an array of five state-of-the-art imaging spectrometers, each of which has an intensified CCD focal plane detector that allows 10's of nm of spectral information to be acquired simultaneously, while acquiring spatial information along the length of the spectrometers' slits. As a result, ISO was able to measure emissions from almost all the species of interest in mesosphere and thermosphere.

Among the most interesting and important topics in the study of the MLT region is the chemistry of ozone. The production of ozone in the mesosphere is the result of a chemical reaction involving atomic oxygen, molecular oxygen, and a third body resulting in the creation of ozone and leaving the third body unchanged. Thus, the concentrations of atomic and molecular oxygen must be determined, which makes the study of oxygen emissions and chemistry necessary. Owens et al. (1993) have begun a study of these emissions and the associated chemistry using data obtained by ISO on the ATLAS–1 mission. The dominant destruction mechanism for ozone in the mesosphere is chemical reaction with atomic hydrogen, which produces molecular oxygen and vibrationally excited hydroxyl radicals. Destruction of hydroxyl then occurs by reaction with atomic oxygen to form molecular oxygen and atomic hydrogen, so there is a naturally occurring catalytic destruction of ozone by atomic hydrogen. As shown in figure 49, ISO measured hydroxyl (OH) at night, as well as the oxygen emissions needed to study oxygen chemistry.

Because of its importance in the destruction of ozone, it is also very desirable to measure hydroxyl in the daytime. However, bright dayglow emissions, such as the first positive system of molecular nitrogen, obscure the hydroxyl emissions seen at night. ISO made the first measurements from orbit of electronically excited hydroxyl in the dayglow (Morgan et al. 1993), which emits light of wavelengths around 309 nm. This unique measurement of the altitude profile of hydroxyl in the dayglow required very careful design, construction, and execution of the instrument, the observation technique, and the analysis technique to extract this weak emission from the bright scattered-light background of the dayglow.

Another electronically excited molecular emission resulting primarily from resonance fluorescence scattering of sunlight is the first negative system of ionized molecular nitrogen. The peak concentration of ionized molecular nitrogen is in the thermosphere at an altitude of about 160 km. The photochemical scheme for this species has been the subject of much debate over the past decade, and a test of the model has been problematic due to the intense scattered sunlight background against which the measurements must be made. Since a determination of the relative populations of vibrational levels higher than two require information on vibrational progressions that cannot be observed from the ground, the high-quality measurements made by ISO on the ATLAS–1 mission (Torr et al. 1993) provide the first information on this issue.

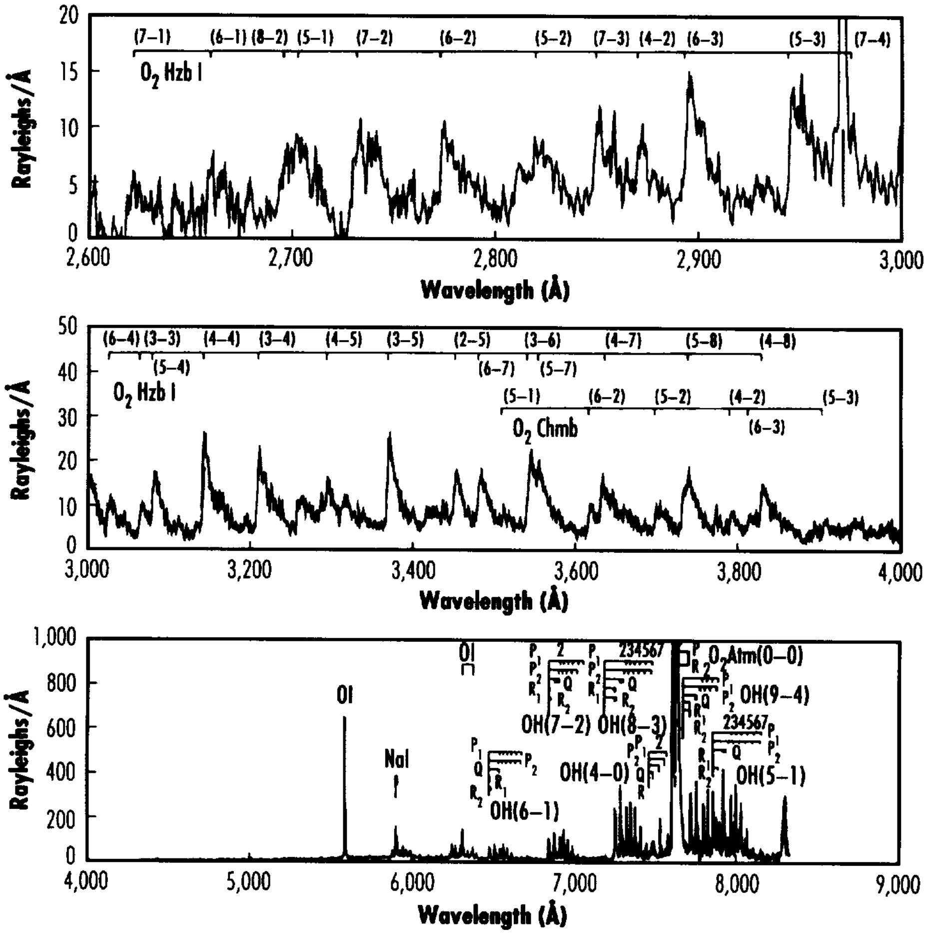

FIGURE 49.—Spectrum of mesospheric nightglow over New Guinea measured by the ISO on ATLAS–1 at about GMT 18:05 on day 88, 1992, at an altitude of approximately 80 km.

Morgan, M.F.; Torr, D.G.; and Torr, M.R. 1993. Preliminary Measurements of Mesospheric OH $X^2\Pi$ by ISO on ATLAS–1. *Geophysical Research Letters* 20:511–14.

Owens, J.K.; Torr, D.G.; Torr, M.R.; Chang, T.; Fennelly, J.A.; Richards, P.G.; Morgan, M.F.; Baldridge, T.W.; Fellows, C.W.; Dougani, H.; Swift, W.; Tejada, A.; Orme, T.; Germany, G.A.; and Yung, S. 1993. Mesospheric Nightglow Spectral Survey Taken by the ISO Spectral Spatial Imager on ATLAS–1. *Geophysical Research Letters* 20:515–18.

Torr, M.R.; Torr, D.G.; Chang, T.; Richards, P.G.; Baldridge, T.W.; Owens, J.K.; Dougani, H.; Fellows, C.; Swift, W.; Yung, S.; and Hladky, J. 1993. The First Negative Bands of N_2^+ in the Dayglow from the ATLAS–1 Shuttle Mission. *Geophysical Research Letters* 20:523–26.

Sponsor: Office of Space Science

Burst and Transient Source Experiment Observations of Gamma-Ray Bursts

Gerald J. Fishman/ES66
205-544-7691

In spite of two decades of study, the origin of gamma-ray bursts remains an enigma. The bursts last from a few milliseconds to several hundred seconds, often exhibiting complex temporal structure on many timescales. Their spectra are nonthermal, with almost all of the luminosity in the low-energy gamma-ray band. No unambiguous counterparts have been found at any other wavelength. Some gamma-ray burst emission has been seen at photon energies above 2 GeV.

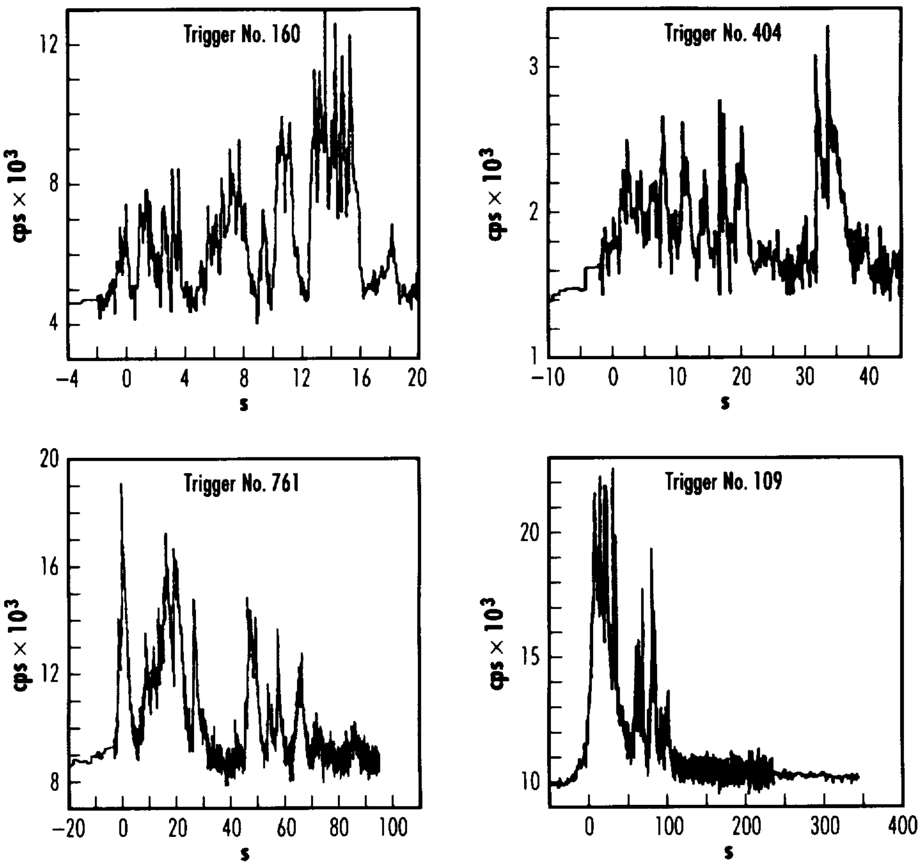

FIGURE 51.—Examples of four intense gamma-ray bursts observed by BATSE.

The Burst and Transient Source Experiment was designed primarily to investigate gamma-ray bursts, with unprecedented sensitivity. BATSE is one of four instruments on the Compton Gamma Ray Observatory (CGRO), launched into Earth orbit by the space shuttle on April 5, 1991. BATSE consists of eight detector modules, placed at the corners of the CGRO spacecraft. The CGRO is in a circular orbit, with an inclination of 28.5 degrees. The initial altitude was 450 km, and decreased to approximately 350 km by June 5, 1993. Burst triggering is disabled whenever the spacecraft passes through the South Atlantic Anomaly (SAA), and whenever the spacecraft is within one of several high-latitude regions identified as having a high probability of triggers caused by particle precipitation. On April 19, 1991, the burst trigger was enabled, and BATSE began to record gamma-ray bursts at a rate of about 0.8/d. An early and quite unexpected finding was that the distribution of burst sources is isotropic (fig. 50), but there is a deficiency of weak sources, presumably at larger distances (Meegan et al. 1992). No known galactic population has such a distribution, leading to speculation that the sources either reside in a previously unknown very large galactic corona or they are at cosmological distances.

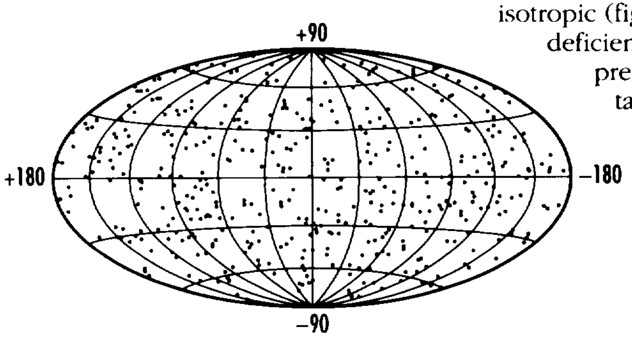

FIGURE 50.—The celestial distribution of 447 gamma-ray bursts.

The first catalog of gamma-ray bursts observed with BATSE has recently been submitted for publication (Fishman et al. 1993). This catalog contains the 260 bursts that satisfied the onboard trigger criteria from April 21, 1991, until March 5, 1992. Figure 51, from the burst catalog illustrates the extremely complex temporal structure found in some gamma-ray bursts.

Meegan, C.A.; Fishman, G.J.; Wilson, R.B.; Pacicsas, W.S.; Pendleton, G.N.; Horack, J.M.; Brock, M.N.; and Kouveliotou, C. 1992. *Nature* 355:143.

Sponsor: Office of Space Science

■

X-Ray Astronomy Research

Brian D. Ramsey/ES65
205-544-7743

Martin C. Weisskopf/ES01
205-544-7740

The laboratory work of the x-ray astronomy group has focused primarily on the development of new detectors for x-ray astronomy. Three instruments are currently under development, all based on variants of the gas-filled proportional counter. The first of these is a large-area imaging proportional counter that is flown on a high-altitude balloon as part of a collaboration with Harvard College Observatory and serves as a test-bed for new techniques developed in-house to improve energy resolution, spatial resolution, and background rejection. These techniques include advanced body materials for lower instrument background, special gas mixtures (Penning mixtures) to improve energy resolution, fluorescence gating to reduce background, and lately, the use of microstrip technology to provide high-uniformity electrode readout and fine electrode structure for enhanced performance. This latter technology is being developed both in-house to investigate and develop new readout techniques, and out-of-house for the production of a large-area flight version, currently scheduled for delivery in 1993.

A second instrument under development is a hard x-ray imaging polarimeter. This device utilizes an intensified CCD camera to image the photoelectron tracks produced by x-rays interacting in the detector gas. The imaging is made possible through the development of a special kind of gas counter—an optical avalanche chamber—that produces extremely large quantities of light photons ($>10^7$) under x-ray irradiation. Analysis of the initial ejection direction of the photoelectron permits a measure of the polarization of the incident x-ray photon. A large-area (30 by 30 cm) flight version is currently under construction for flight on a high-altitude balloon in 1994–95.

The third instrument under development is a hybrid detector that combines a sodium iodide/cesium iodide phoswich detector with an optical avalanche chamber. The chamber is optically coupled to the front of the phoswich and provides response at low energies, while the sodium iodide takes over at energies where the gas becomes transparent. Both sections of the hybrid are read out by a common set of photomultiplier tubes under the phoswich. The net result is a broad band instrument with high sensitivity for hard x-ray imaging from 25 to 600 keV. This instrument, also a collaboration with Harvard College Observatory, is scheduled for flight in 1995.

The group continues the development program in hard x-ray optics and has recently x-ray tested a Kirkpatrick-Baez mirror assembly fabricated from high-quality silicon wafers. The intention is to increase the high energy response of this assembly through the in-house application of multilayer technology and software has been developed to aid in defining the necessary coating materials, thicknesses, and number of layers.

The MSFC x-ray astronomy group is continuing to collaborate on the Stellar X-Ray Polarimeter experiment, scheduled to fly aboard the Spectrum-X-Gamma spacecraft in 1995. Monte Carlo simulations have been performed that detail the instrument's sensitivity for various cosmic sources of interest. These simulations have recently been used to predict, for example, the effects of changes in the composition of the detector fill gases.

Under the auspices of the MSFC Center Director's Discretionary Fund, the group has built four microwave receivers, together with associated optics and electronics, to measure the magnitude of the Sunyaev-Zel'dovich effect. This effect, a spectral distortion of the primordial background radiation, offers a powerful probe of the cosmic distance scale and provides a measure of the size and age of the universe. The

C-2.

instrument under development combines recent advances in microwave technology with existing interferometers and provides a novel approach to an exceptionally difficult measurement. The first observations are scheduled for 1993 at the Owens Valley interferometric telescope array.

The group built an x-ray detector system to test the replicated optics currently under fabrication by the optics group at MSFC. The detector has better than 500 μ spatial resolution at 8 keV, which corresponds to 20 arc seconds for the replicated optic's focal length. The tests, conducted by the X-ray Astronomy Branch, were scheduled to be completed in 1993. This work has led to the development of a very large set of software tools that have widespread application in, for example, the design of x-ray optics or the design and evaluation of x-ray instrumentation.

Austin, R.A., and Ramsey, B.D. 1993. Optical Imaging Chamber for X-ray Astronomy. *Optical Engineering* vol. 32, no. 8.

Ramsey, B.D. 1992. The Microstrip Proportional Counter. *SPIE 1743: 96–103.*

Ramsey, B.D.; Austin, R.A.; Minamitani, T.; Weisskopf, M.C.; Lum, K.H.S.; and Manadhar, R.P. 1993. A Hybrid Gas Detector for Hard X-ray Astronomy. *SPIE* 2006, in press.

Sponsor: Office of Space Science

University Involvement: Harvard University

■

The Observation of Direct Electron-Positron Pairs by Relativistic Heavy Ions in Nuclear Emulsion

James H. Derrickson/ES64
205–544–7698

The direct Coulomb electron-positron pairs produced along the tracks of heavy ions in nuclear emulsion have been the subject of recent theoretical and experimental studies. The European Center for Nuclear Research (CERN) exposures of emulsion plates to oxygen ions at 60 and 200 GeV/n and sulfur ions at 200 GeV/n have been analyzed to yield the direct-pair cross section, energy, and emission angle distributions. The measurements at 200 GeV/n compare well with recent theoretical calculations, when corrected for the background due to the chance association of two knock-on (KO) electrons. This was the dominant background source that satisfied the microscope scanning criteria for a "candidate" direct electron-positron pair event. The 200 GeV/n oxygen data, which are the least contaminated by the KO electron background (approximately 15 percent), that are presented in figures 52 and 53 show the total direct-pair energy distribution and pair-member emission angle distribution, respectively. The broken line is the theoretical prediction without the KO electron contamination and is based solely on the total oxygen ion path length scanned. In the near future, the KO electron contamination will be included in the Monte Carlo simulation of the energy and emission angle distributions for all the pair data sets. Because the chance KO–KO electron background is not a serious problem for the 200 GeV/n oxygen case, the direct-pair energy distribution and the pair-member emission angle distribution satisfactorily match the theoretical

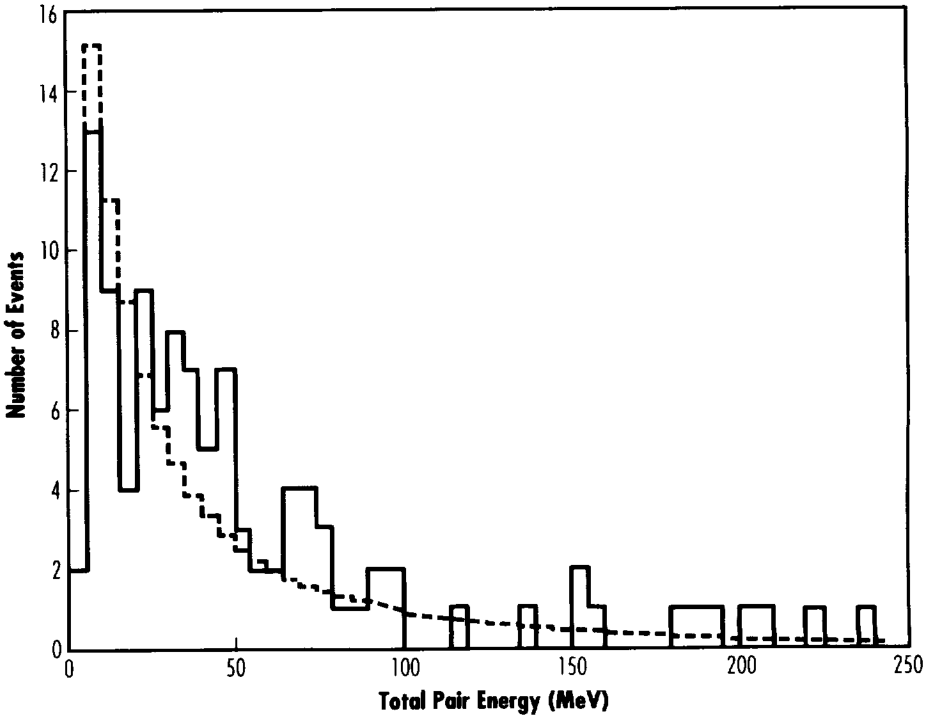

FIGURE 52.—Comparison of the measured direct pair energy distribution with theory (broken line) for oxygen ions at 200 GeVn.

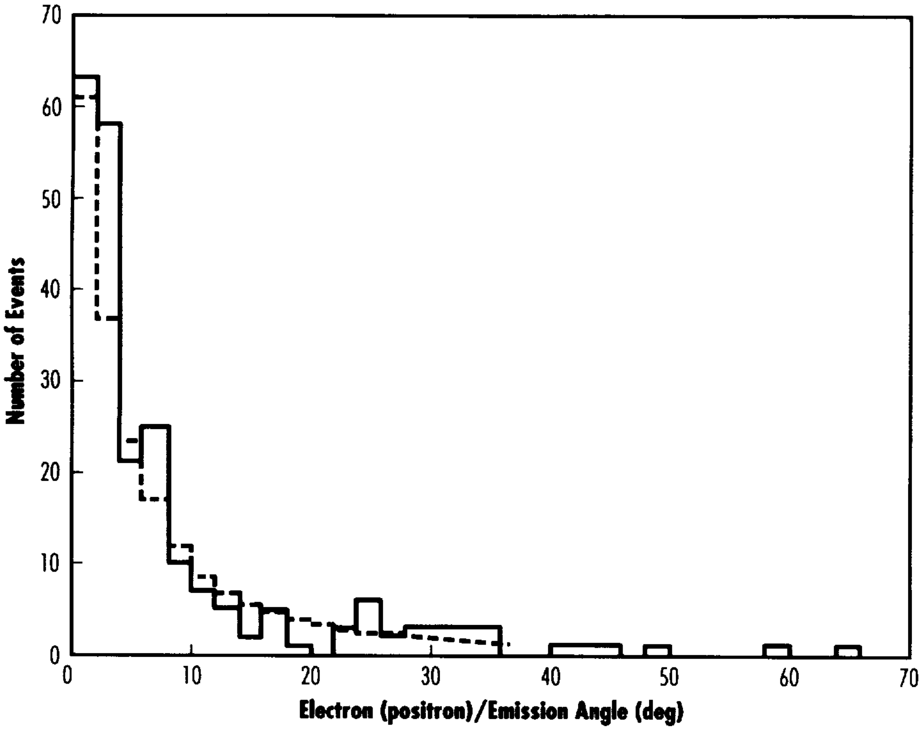

FIGURE 53.—Comparison of the measured emission angle distribution for the pair members with theory (broken line) for oxygen ions at 200 GeVn.

TABLE 3.— *Measurements and theoretical calculation of the interation mean free path for producing direct pairs from oxygen ions at 200 GeV/n where the total pair energy is greater than 4 and 10 MeV. The length of oxygen ion track scanned was 565 cm*

Projectile	Energy (GeV/n)	Mean Interaction Path (cm)	
		(E_{pair} 4 MeV)	(E_{pair} 10 MeV)
0^{16}	200	5.00 ± 0.05	5.80 ± 0.60
0^{16}	200	5.0	6.2

calculations. The measured and theoretical direct pair yield for 200 GeV/n oxygen is listed in table 3 for two pair energy thresholds, 4 and 10 MeV. The theoretical pair yield includes the chance double-KO electron background.

An objective of this study has been to evaluate the possibility of measuring the primary energy of extremely relativistic cosmic rays ($E>10^{13}$ eV/n) utilizing the direct-pair method. A detector for measuring the direct pairs along the tracks of heavy cosmic ray ions has been proposed by the Japanese-American Cooperative Emulsion Experiment (JACEE) collaboration. This collaboration includes scientists from MSFC, and from the United States, Japanese, and Polish universities. The JACEE "pair-meter" consists of a multilayer stack of thin (50–200 μm) lead plates, low-density spacers (thickness to be determined), emulsion plates (50 μm), and CR39 tracking layers. The detector is designed to produce more direct pairs per mass thickness. For cosmic ray energies above 10^{13} eV/n, the direct pairs will be emitted predominately in the forward direction and will be preferentially detected in the emulsion layers. A Monte Carlo simulation of the pair-meter is in progress to evaluate its practical energy resolution. The pair-meter will be part of the target of a large area emulsion chamber to be flown on a long duration balloon flight in Antarctica in the 1993–94 austral summer season. The data collected on this JACEE balloon flight and the simulation will be used to assess the performance of the pair-meter.

Asakimori, K. et al. 1993. Twenty-third International Cosmic Ray Conference (ICRC), Calgary, Canada.

Derrickson, J. et al. 1993. Twenty-third ICRC, Calgary, Canada, 1992. Submitted to *Physical Review A*.

Eby, P.B. 1991. *Physical Review A* 43:2258. 1992. Submitted to *Nuclear Instruments and Methods*, Sec. B.

Sponsors: Office of Space Science and Marshall Space Flight Center Director's Discretionary Fund.

■

Cosmic Ray Proton Spectrum Changes at 4×10^{13} Electronvolts

Thomas A. Parnell/ES64
205-544-7690

The cosmic-ray group at MSFC performs balloon-borne experiments to study the composition, energy spectra, and interactions of cosmic ray nuclei above 10^{12} eV (1 TeV). This research is performed with colleagues in the United States, Japan, and Poland, who form the JACEE collaboration that has flown 11 experiments since 1979. These instruments consist of large passive detector assemblies (emulsion chambers). Because of the steep energy spectra of cosmic rays (approximately proportional to $E^{-2.7}$), the investigation of cosmic rays above 1 TeV requires large exposure factors (area × solid angle × time). The JACEE balloon-borne experiments have achieved nearly 1.0 m^2/sr/h above 38 km in 11 balloon flights from the United States, Japan, Australia, and the Antarctic. The typical emulsion chamber is 0.8 m^2 in area, approximately 20-cm thick, and contains 600 kg of material. It includes multiple layers of photographic emulsion, acrylic plates, x-ray film, passive nuclear track detectors (CR39), and lead plates.

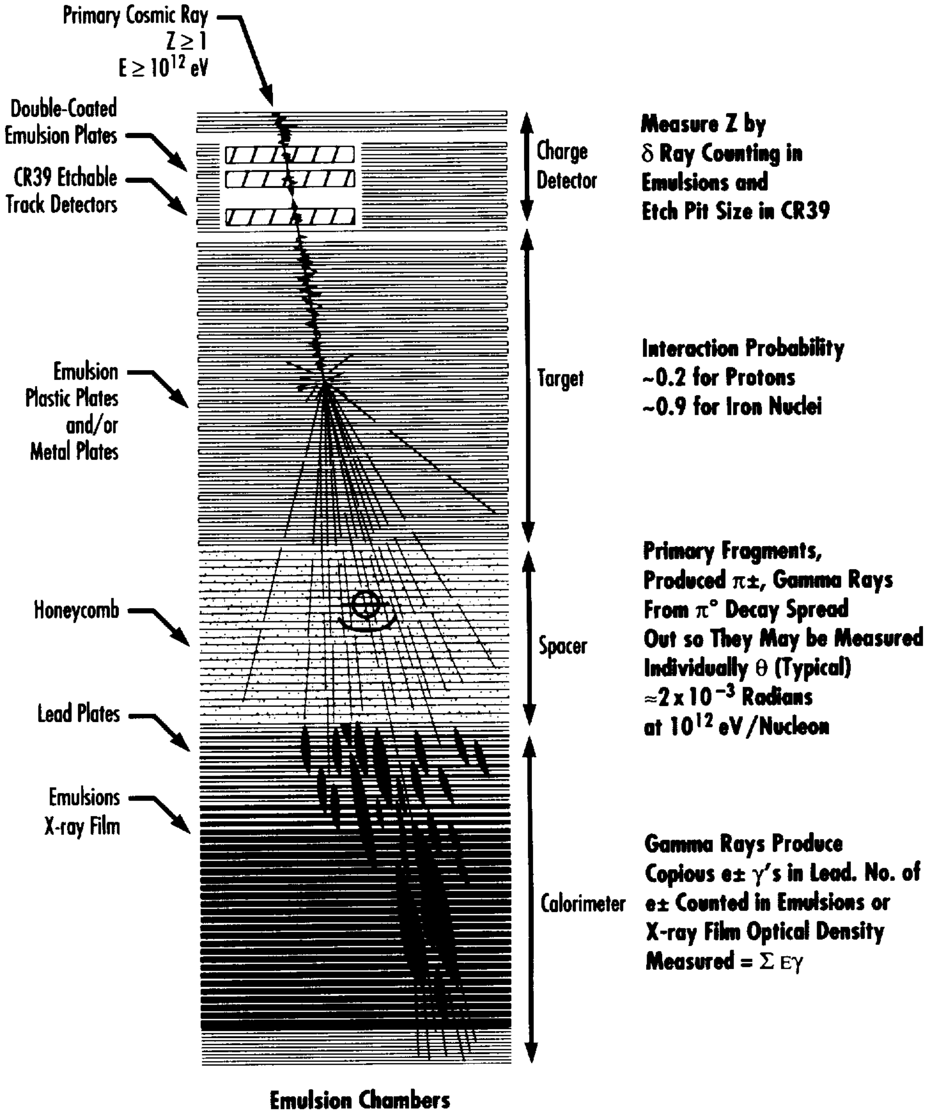

FIGURE 54.—A schematic of an emulsion chamber of the type flown by the JACEE collaboration.

Following the flights, the photographic materials and other passive track detectors are developed and, after initial analysis of the x-ray film with microdensitometers at MSFC, are divided among the collaborators for microscope measurements of particle tracks in the emulsions and other passive detectors. The analysis determines the atomic number of each incident nucleus (above a threshold of approximately 10^{12} eV), the energy it deposits in the chamber following a nuclear interaction, and the characteristics of the mesons and other particles produced in the interaction. Approximately 1,000 nuclei from hydrogen (H) through iron (Fe) have been analyzed. The JACEE group has produced the highest energy direct data on the composition and spectra, extending by a factor 10 in energy above other experiments. It has been known from cosmic ray air shower experiments (large arrays of detectors on the ground), that the cosmic-ray spectrum extends to ~10^{20} eV, but the spectrum has a bend (intensity decrease) around 3×10^{15} eV. This bend has been speculated to be due to either the end of confinement of cosmic ray nuclei by the weak galactic magnetic fields, or due to the inability of the processes that accelerate cosmic rays to push them to higher energies, or perhaps contributions from both. These uncertainties have motivated measurements of the composition and spectra of cosmic rays to increasingly higher energies.

The JACEE collaboration has for the first time produced data that show a clear spectral bend for an individual

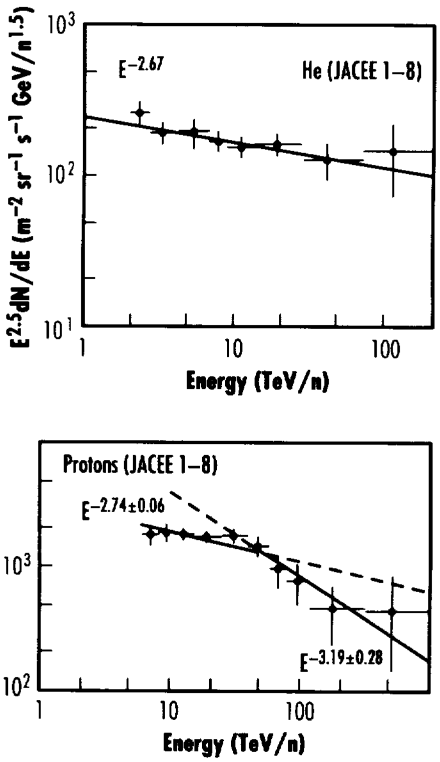

Figure 55.—Comparison of (a) helium and (b) proton spectrum from JACEE experiments.

element, the H nucleus (fig. 54). This surprisingly sharp bend occurs at approximately 4×10^{13} eV (40 TeV). An additional surprise is that the helium spectrum (fig. 55) shows no evidence of change to beyond 40 TeV. If the spectral bend in the air shower experiments is due to the end of galactic confinement or acceleration, the protons should bend around 100 TeV, with ion nuclei bending at around 260 TeV ($\sim 3 \times 10^{15}$ eV).

The JACEE observation of the proton spectral bend is unambiguous in the data, but its implication is uncertain. The JACEE collaboration plans further experiments with larger chambers and longer duration balloon flights. Further measurement and exposures approximately 30 times that already achieved would extend the composition and spectra data above 10^{15} eV and would confirm the acceleration processes and the galactic containment models.

Asakimori, K. et al. 1993. Twenty-third ICRC. Calgary, Canada.

Parnell et al. 1989. *Advances in Space Research* vol. 9, no. 12:45–54.

Sponsor: Office of Space Science

■

Discovery of X-Ray Nova Persei 1992 (GRO J0422+32) With the Burst and Transient Source Experiment

B. Alan Harmon/ES66
205-544-4924

In August 1992, a very bright x-ray nova (GRO J0422+32) appeared in the constellation of Perseus. It was discovered about 3 d into its outburst, using the BATSE on the CGRO. Large occultation steps were observed in the raw data, and also intense flickering of the source caused frequent triggering of the instrument into the burst mode. The intensity of GRO J0422+32 was monitored with the Earth occultation technique. (A description of the method applied to BATSE can found in *Research and Technology 1992.*) The integrated daily flux between 20 and 300 showed the source rising in intensity to its primary maximum in about 5 to 6 d, which then decayed exponentially with a characteristic time of 41 d. At its peak, the source was about 3 times brighter than the brightest persistent hard x-ray sources in the sky—the Crab Nebula and Cygnus X-1. In December 1992, about 120 d after the initial outburst, a second maximum appeared in the GRO light curve, followed by a decrease in intensity at the same rate observed after the primary maximum (fig. 56). The source was no longer visible to BATSE after April 1993.

The light curve of GRO J0422+32 is typical in shape (fast rise, exponential decay, secondary maximum) of x-ray novae because they resemble the optical light curves of classical novae. The objects that produce the outbursts are thought to consist of

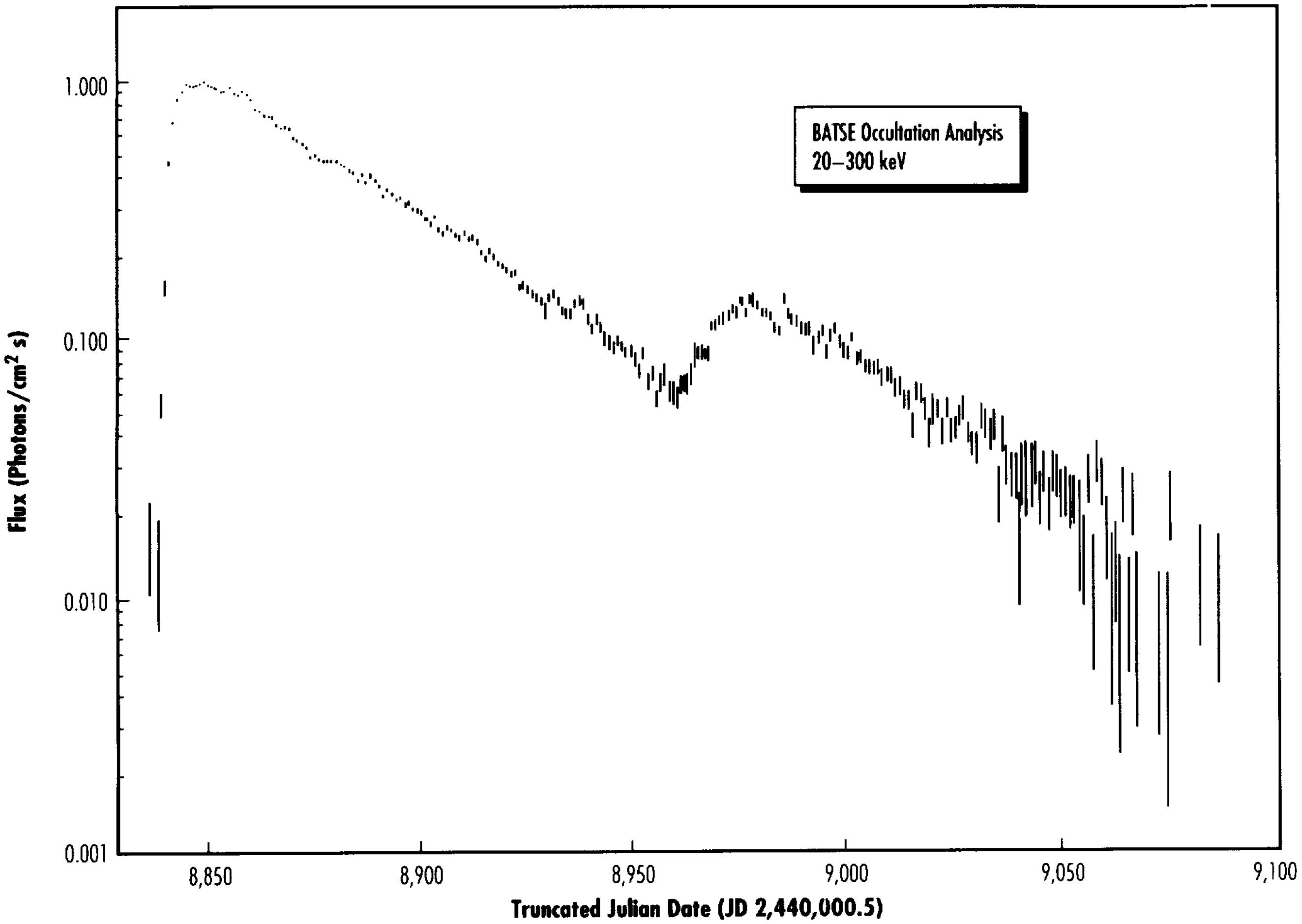

FIGURE 56.—Hard x-ray light curve for GRO J0422+32.

two stars (a binary system), one of which is a normal hydrogen/helium-burning star and the other a compact object, which can be a neutron star or black hole. The cause of the outbursts is not well understood, but suggested explanations involve either a large mass transfer from the normal star or perhaps an accretion disk instability (Chan et al. 1993). Both scenarios result in a sudden increase in matter accreted onto the compact object.

All-sky monitoring in recent years by several spacecraft such as Ginga, Granat, and now the CGRO, has added to our knowledge of x-ray novae in binary systems. Specifically, the spectral and temporal characteristics that are considered indicators of potential black holes have been identified in x-ray novae. One characteristic is a bimodal spectral behavior, where, at times, the source spectrum is dominated by a hard power law component in the x-ray regime (few keV to 100 keV, spectral index approximately −2), usually steepening in the gamma-ray regime (fig. 57). At other times the spectrum is dominated by a very soft, blackbody component in the 1–10 keV energy band. Another characteristic is flickering in x-rays on short timescales (milliseconds to seconds) that appears as low-frequency noise in a power density spectrum. The flickering and very hard spectrum above 20 keV were both observed in the outburst of GRO J0422+32. The soft component below 10 keV, however, if present, is outside the energy range of the BATSE instrument.

The spectral behavior of the x-ray novae can vary from source to source. The spectrum of GRO J0422+32 can be described reasonably well with an optically thin bremsstrahlung model or a Comptonization model. Except

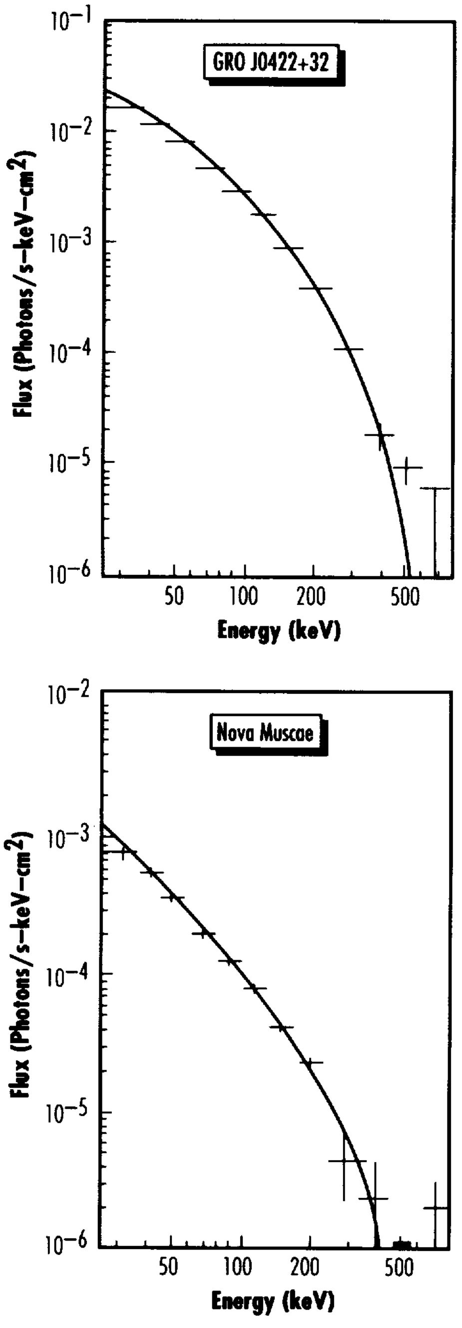

FIGURE 57.—Photon spectra of two x-ray novae: GRO J0422+32 and Nova Muscae.

for a softening of the spectrum near the primary maximum, the spectrum was extremely stable in shape during the long decay period and showed no strong changes in the spectrum during the onset and decay of the December secondary maximum (Paciesas 1993). This is in contrast to GRS 1124–68 (X-ray Nova Muscae 1991) where BATSE detected a distinct hardening of the spectrum during a secondary maximum in the light curve of this source 150 to 200 d after the initial outburst in January 1991 (Paciesas 1993).

The spectral and temporal characteristics observed by BATSE represent clues, although not proof, that the compact object in the GRO J0422+32 system may be a black hole. More observations of x-ray novae, both in the hard x-ray/gamma-ray regime, and at other wavelengths, are needed.

Chan, W.A.; Livio, M.; Gehrels, N. 1993. The Secondary Maxima in Black Hole X-ray Nova Light Curves: Clues Toward a Complete Picture. *Ap. J.* 408:L5.

Paciesas, W.S. et al. February 1993. BATSE Observations of Black-Hole X-ray Binaries. Presentation at Integral Workshop, Les Diablerets, Switzerland.

Stinson, H., ed. *Research and Technology Report 1992: Annual Report of the Marshall Space Flight Center*, NASA TM–103599, p. 29.

Sponsor: Office of Space Science

■

Infrared Space Astronomy and Space Research

Charles M. Telesco/ES63
205–544–7723

In 1993, infrared (IR) astronomy at MSFC has focused on three research areas: (1) scientific and technical participation in the European Space Agency's (ESA's) Infrared Space Observatory (ISO) program, (2) the extensive observation of star-forming regions in other galaxies and of protoplanetary disks around other stars using the previously developed MSFC mid-IR camera, and (3) the development of a new advanced IR camera for astronomical and shuttle-related observations.

The MSFC IR astronomy program has continued to contribute to the development of the ISOPHOT, an IR spectrophotometer that will be one of the four IR instruments to be flown aboard ESA's ISO, scheduled for launch in 1995 (fig. 58). ISO will be the next major IR space experiment and the only one scheduled to be launched this decade. Negotiations between NASA and ESA are nearing completion, which will make NASA a full partner in ISO.

The MSFC ISO responsibilities have included the definition and coordination of a broad range of astronomical observations to be carried out by the international ISOPHOT team of scientists during their guaranteed observing time. Those planned observations include the search for the illusive substellar brown dwarfs and the determination of the energy output of some of the most distant galaxies in the universe. A major MSFC task is to establish the set of celestial objects that will serve as far-IR photometric standards for ISOPHOT during the mission. This task has required that MSFC astronomers carry out an extensive program of airborne and ground-based IR observations using the NASA Infrared Telescope Facility (IRTF)

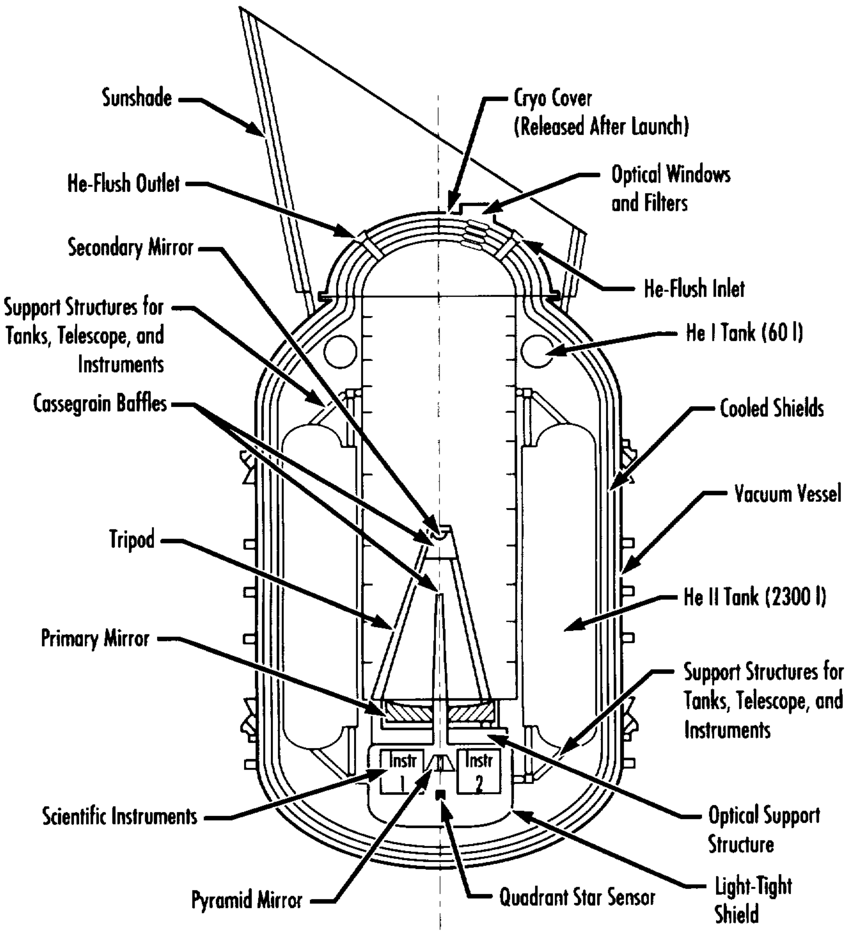

ISO Payload Module

FIGURE 58.—The ISO, to be launched in 1995.

on Mauna Kea, HI, and the NASA Kuiper Airborne Observatory to determine the spectral energy distributions of potential candidates. In early 1993, extensive theoretical analysis and modeling of the data obtained so far indicated for the first time that selected asteroids will be suitable primary photometric standards for ISO.

The MSFC mid-IR camera, with 20 extremely sensitive bolometer detectors, has been operational since 1985. This camera has permitted a broad range of astronomical observations at major observatories, including the only extensive program to map regions of star formation in other galaxies. Analysis of these unique IR images has led to a recognition of the causes of extremely intense episodes of star formation in the cores of many galaxies. In collaboration with BATSE scientists at MSFC, the first mid-IR detection of a transient gamma-ray source, GRO J0422+32, was made with the MSFC IR array at the NASA IRTF. These long-wavelength observations will constrain the structure of the outer region of the accretion disk which may surround a black hole and emit the gamma radiation.

This year the MSFC mid-IR camera extended the discovery, made with the same camera at the IRTF, of the "silicate feature" from a protoplanetary disk. This broad spectral feature in the mid-IR is a signature of silicate dust grains, and is an important diagnostic of particle sizes and evolutionary histories. The detection of this feature around the star Beta Pictoris is opening the way to a better understanding of the evolution of disks that may be in the process of forming planets. As part of a broad survey of stars like Beta Pictoris, the silicate feature has recently been discovered around another star, 51 Ophiuci, which demonstrates that the silicate feature may be ubiquitous enough to permit statistical analyses of the feature in the context of evolution of planetary systems.

Significant progress has been made in the development of an advanced, high-speed mid-IR camera and spectrometer. This cryogenically cooled detector system, which will be an extremely versatile instrument using a state-of-the-art arsenic-doped silicon detector array containing 10,000 pixels, will permit rapid imaging with very high spatial resolution, as well as multiresolution spectroscopy. In addition to its use for astronomical observations, this new camera will provide ground-based imaging of the orbiting space shuttle in order to better understand the environment of the shuttle during its missions. The system fabrication is nearing completion, with the first field operation scheduled at the IRTF in 1993.

Hawarden, T.G.; Cummings, R.O.; Telesco, C.M.; and Thronson, H.A. 1992. Optimized Radiative Cooling of Infrared Space Telescopes and Applications to Possible Missions. *Space Science Review* 61:113–44.

Telesco, C.M.; Dressel, L.L.; and Wolstencroft, R.D. 1993. The Genesis of Starbursts and Infrared Emission in the Centers of Galaxies. *Ap. J.*

Telesco, C.M.; Pina, R.; Fajardo, S.; Fishman, G.; Kouveliotou, C.; and Van Paradijs, J. 1992. GRO J0422+32. International Astronomical Union (IAU), circular no. 5613.

Sponsor: Office of Space Science

■

Microgravity Science and Applications

Electromagnetic Field Effects in Semiconductor Crystal Growth

Martin P. Volz/ES75
205-544-5078

The quality of all bulk-grown crystals depends on mass and heat transfer processes present in the crystal growth system. In particular, gravity-driven convective flows in the melt affect the uniformity of the grown semiconductor and the distribution of defects and impurities. In most instances, the force of gravity has proven to be detrimental to the quality of the grown crystals, and thus there have been numerous studies of semiconductor materials in low-gravity environments. The purpose of this investigation is to examine the effects that an additional force has on gravity-driven fluid flow processes. This additional force is the Lorentz force and is the result of combined electric and magnetic fields.

Work has begun on developing a growth cell that can accommodate large current densities and that will be placed in a transverse electromagnet. Current research efforts are focused on examining the criteria for the onset of thermal instability as a function of electric, magnetic, and gravitational field strength in electrically conducting liquids. Also, the possibility of using externally applied electromagnetic fields to influence fluid motion in the melt, the rate of solid phase accrual, and the shape of the solid/liquid interface is being assessed. Indium antimonide (In-Sb) and gallium indium antimonide (Ga-In-Sb) are the semiconductor alloys that are being used in the initial studies.

Sponsor: Marshall Space Flight Center Director's Discretionary Fund

Real-Time X-Ray Microscopy of Solidification Processes

Peter A. Curreri/ES75
205-544-7763

Physical processes that occur at, or near, interphase boundaries during solidification or other phase transformations, play a major role in the determination of many of the technologically important properties of solids. In this advanced technology development program, MSFC will develop a high-resolution x-ray microscope to view, in situ and in real time, interfacial processes in metallic systems either during freezing or solid-solid transformations. The X-Ray Transmission Microscope (XTM) will operate in the hard x-ray range (10 to 100 keV) and achieve magnification through projection.

To date, interfacial morphologies and particle-interface interactions in the respective metallic, optically opaque systems have been deduced from postprocess metallographic analyses of specimens. Thus, little information is obtained about the detailed dynamics of the processes. These investigations have been considerably augmented by real-time observations of transparent materials; yet, since some of the interfacial and transport properties of these materials differ greatly from those of metals and semiconductors, the results are not necessarily representative of these opaque systems.

The XTM to be developed will achieve magnification through projection. Figure 59 schematically indicates the major components of the system and their placement. A metal sample (thickness on the order of 1 mm) is contained in a specially

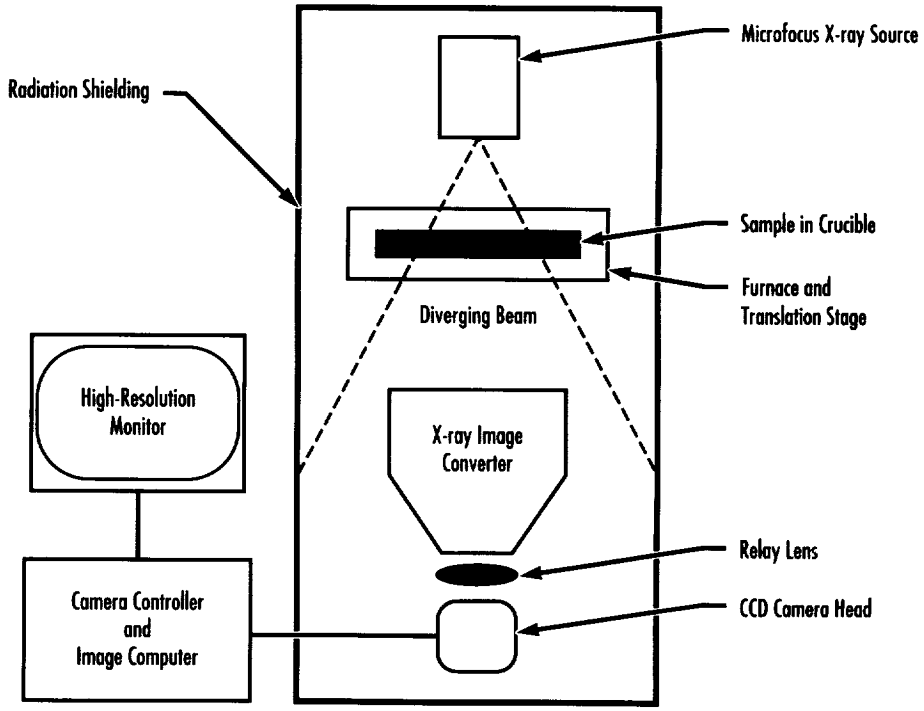

FIGURE 59.—Schematic of XTM prototype showing configuration of the various components.

designed, high-transmittance crucible. A high-temperature furnace on a translation stage imposes a temperature gradient onto the sample. The solid-liquid interface is positioned in proximity to the focal spot of a microfocus x-ray source. The diverging x-ray beam permeates the sample and the resulting shadow falls on an x-ray image converter. The resulting visible image is converted to a digital image by a CCD camera and stored in a computer. This image is displayed on a high-resolution monitor, either in real time or after further processing (contrast enhancement, filtering, etc.). Hard copies of the images are obtained either photographically from the high-resolution monitor or, with some loss of quality, from a video printer.

NASA's Materials Science and Applications Division (MSAD) currently supports a large number of research projects that are concerned with gravity-induced phenomena in materials processing. These include the influences of convection and sedimentation on solute distributions, interface morphologies, particle-interface interactions, segregation, droplet formation, and coalescence.

In opaque materials, the interpretation of solidification phenomena has been restricted to metallurgical or radiographic analysis after solidification. Thus, little information is obtained about the detailed dynamics of the processes. This shortcoming impedes fundamental research and important technology developments, since the phenomena that occur at interphase boundaries during solidification determine many of the important properties of solids. Similar impediments arise in studies of solid-solid processes.

Sponsor: Office of Life and Microgravity Sciences and Applications

University Involvement: University of Alabama in Huntsville

■

The Effects of Temperature on Tetragonal Lysozyme Face Growth Rates

Marc L. Pusey/ES76
205–544–7823

Protein crystals are typically grown by methods that involve an uncontrolled increase in the concentrations of both the protein molecule and the agent(s) used to precipitate it from solution. Recently, however, the use of temperature as a more controllable means of effecting nucleation and controlling the crystal growth process has attracted attention. However, what is not known is precisely how protein crystal growth rates change with temperature or any of the other variables that may be employed. Scientists at the biophysics laboratory at MSFC have initiated a long-term study of these parameters.

Because protein crystal growth is typically a slow process (maximum growth rates of approximately 10^{-2} μm/s), detailed studies of the face growth rates required that a microscopy system be devised that

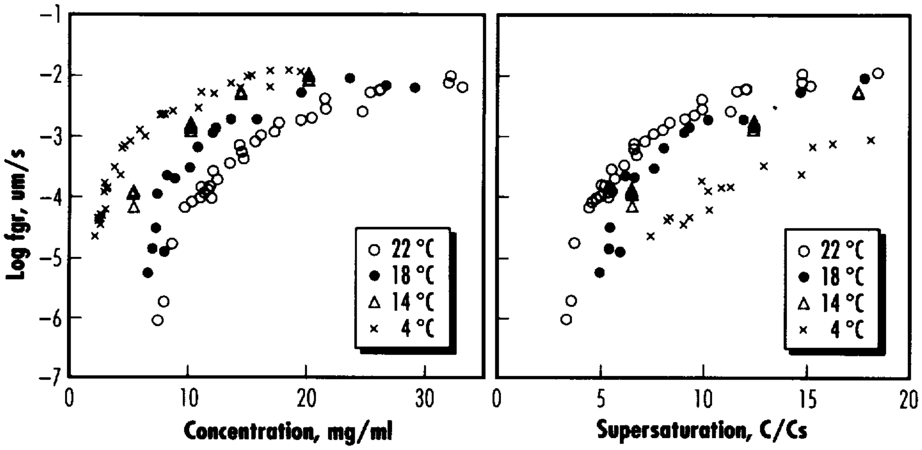

FIGURE 60.—Effects of temperature on the (110) face growth rate (fgr) of tetragonal lysozyme at pH 4.0, 5% sodium chloride (NaCl).

allowed us to follow multiple crystal growth rates during one experimental run. We have recently completed such an apparatus (Pusey 1993) and have been successfully using it for the past year. The system consists of a horizontally mounted video microscope, with the growth cell being a thermostatted block that hangs down into the microscope's focal plane. The thermostatted block is mounted on a pair of computer-controlled translation stages to adjust its position in the vertical and transverse planes (x and y axes). The microscope system is also mounted on a translation stage that is used for focus control. Positions of crystals to be measured are preloaded into the controlling PC. Measurement consists of the system focusing on each crystal in turn and measuring the distance across the parallel faces of interest.

Figure 60 shows the results of 110 face-growth rates obtained from tetragonal lysozyme as a function of temperature. The left panel shows the data plotted as a function of absolute protein concentration. As expected, lower temperatures required lower protein concentrations to achieve equivalent growthrates. Note, however, that at about 20 mg/mL, the growth rates become essentially independent of temperature and only become a function of the protein concentration. Thus, control of growth rates by temperatures can only be achieved at low-protein concentrations.

The right panel shows the same data except that they are plotted using a supersaturation ratio axis. In this case note that the positions of the lines have been reversed. We have found that for tetragonal lysozyme conditions that result in a reduction of the proteins, saturation concentrations also result in a shift of this plot to the right; i.e., higher relative supersaturations are required to achieve equivalent face-growth rates when one goes to conditions that give lower solubilities. Whether this is a general rule for proteins, or even other forms of lysozyme, remains to be determined.

Pusey, M.L. 1993. A Computer Controlled Microscopy System for Following Protein Crystal Face Growth. *Review of Scientific Instruments*, in press.

Sponsor: Office of Life and Microgravity Sciences and Applications

■

Kinetics of Diffusional Droplet Growth in a Liquid/Liquid Two-Phase System

Barbara R. Facemire/ES74
205-544-7810

The objectives of this work are:
(1) to improve understanding of the influence of diffusional droplet coarsening, or Ostwald ripening, on phase-separation processes and microstructure evolution; (2) to ascertain the effect of gravity on this coarsening; and (3) to perform modeling studies to serve as predictive tools. A transparent metal model system, succinonitrile/water (SCN/H_2O), allows direct observation of the phase-separation events of interest. The SCN/H_2O system has an isopycnic point (temperature where the densities of the two fluid phases are equal) near 42 °C and offers the opportunity to perform experiments on the ground where gravity-driven sedimentation and buoyancy can be greatly reduced. Using holography to record the entire test-cell volume at selected times during the coarsening process makes it possible to obtain data on droplet size distributions for a large number of droplets at any given point during the coarsening process. The holograms serve as an archive "storing the experiment" at specific instances in time.

A quench experiment was performed in a narrow path-length test cell. The path length of the cell was 100 µm (fig. 61). (The large number of droplets produced in a quench and the requirements of the holographic technique dictate the narrow cell so that the sample will be transparent.) Due to the test-cell geometry and the method of quenching, the droplets nucleated on or near one wall and were attached there for the duration

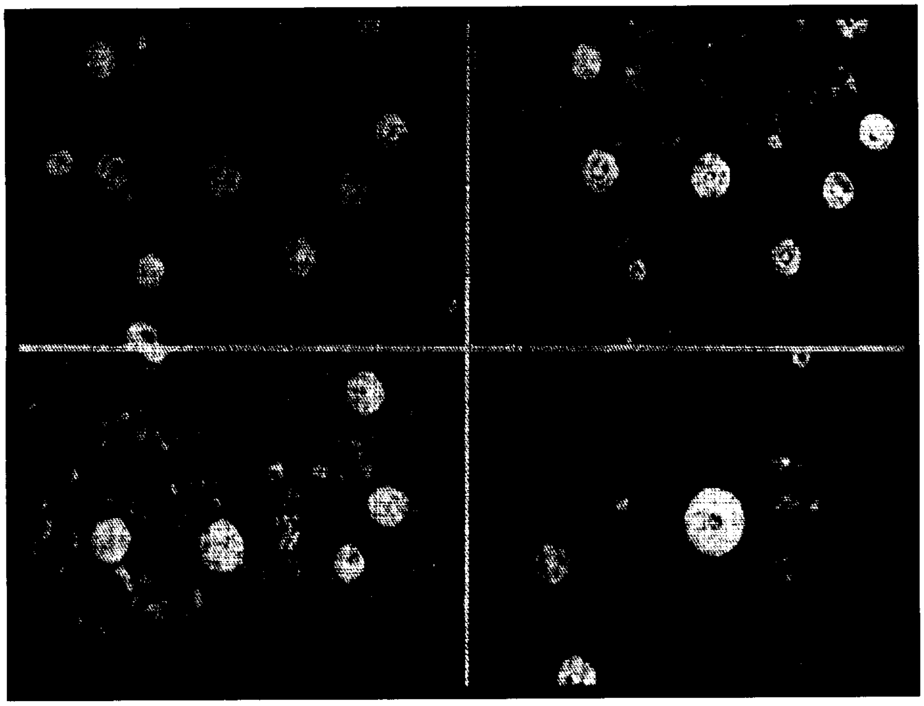

FIGURE 61.—This series of photographs, spanning an experiment time of about 4 mo, shows diffusional growth of droplets in a 100 μm path-length test cell. The smaller succinonitrile-rich droplets lose mass through diffusion to the larger droplets. Droplet number decreases with time as $t^{-3/4}$ and the average droplet radius increases as $t^{1/4}$.

of the experiment. This situation further reduced any possibility of gravity-induced droplet movement. The 152 holograms taken during the experiment follow the ripening process for 1×10^7 seconds (approximately 4 mo). Preliminary analyses of this experiment are currently being prepared for publication. For tractability, these results are based on measurements of droplet size distributions for about 5 percent of the volume available for study in each of the 14 selected holograms. Results indicate the number of droplets of discrete phase decrease with time according to $N(t)=At^{-0.733}$ and that the average droplet radius increases with time according to $R(t)=Bt^{0.247}$. These results are in excellent agreement with the scaling laws accompanying ripening of 3–D droplets located on a 2–D substrate. This result agrees with mixed dimensionality scaling predictions from the literature and match well the geometry of the experiment. The literature also reveals agreement with mixed dimensionality in modeling the development of thin films of semiconductor materials.

Most modeling schemes are based on global averages; however, the local environment around any given droplet can significantly influence the resulting microstructure in that location. An estimate of the field surrounding each droplet based on a monopole approximation, while accurately predicting the scaling laws, does not perform as well in predicting individual droplet lifetimes (R versus t). A dipolar approximation correction to the monopole calculation better models local effects.

This experiment, while designed to reduce the influence of gravity, is not entirely free of gravity's effects. As droplets grow and shrink, concentration gradients (and thus density gradients) form, which can lead to gravity-driven convective flows. Additionally, most materials of commercial or technical interest are not quenched to an isopycnic point. One goal of this investigation is to design a flight experiment to perform a similar study in microgravity far from the isopycnic temperature. The diffusional process is slow, and long times are required to obtain data from quench experiments. This suggests that quench experiments would be best performed on the space station or a retrievable satellite. For Spacelab missions, an experiment consisting of tethered droplets is under consideration that will require the deployment of nl droplets. Such small volumes are required for a measurable change in diameter to occur within the time limitations of a Spacelab mission. During the past year, several methods of deploying nl droplets have been evaluated. These technologies were developed for biological applications, such as cell injection, and appear promising for droplet formation. Methods of isolating these droplets from the injection volume are under investigation.

Fradkov, V.E.; Mani, S.; and Glicksman, M.E. November 1993. Mixed Dimensional Coarsening of 3–D Droplets by 2–D Diffusion. To be presented at Materials Research Society meeting, Boston, MA.

Frazier, D.O., and Facemire, B.R. 1989. Non-Ideality Near the Monotectic Composition of a Miscibility-Gap Type System: Succinonitrile-Water. *Thermochimica Acta* 145:301–29.

Frazier, D.O.; Facemire, B.R.; Loo, B.H.; Burns, D.; and Thiessen, D.B. 1990. Solidification Behavior of Impurity-Doped Succinonitrile Solutions in High-Surface Area, Low-Bulk Volume Containers. *Journal of Crystal Growth* 106:101–15.

Rogers, J.R.; Downey, J.P.; Witherow, W.K.; Facemire, B.R.; Frazier, D.O.; Fradkov, V.E.; Mani, S.; and Glicksman, M.E. A Study of Diffusive Droplet Growth in a Narrow Test Cell Using Holography. To be submitted to *J. Colloid Interface Sci.*

Rogers, J.R.; Downey, J.P.; Witherow, W.K.; Facemire, B.R.; Frazier, D.O.; Fradkov, E.V.; Mani, S.; and Glicksman, M.E. July 1993. A Study of Diffusional Growth in a Liquid-Liquid Miscibility-Gap System Using Holographic Techniques. A poster presentation at the Gordon Conference.

Rogers, J.R. et al. October 1993. A Study of Diffusional Growth in a Liquid-Liquid Miscibility-Gap System Using Holographic Techniques. To be presented at the 45th Southeast Regional Meeting of the American Chemical Society, Johnson City, TN.

Rogers, J.R. et al. September 1993. Diffusional Growth of Succinonitrile-Rich Droplets on a 2–D Surface in a Succinonitrile-Water Miscibility Gap System. To be presented at the 7th Annual Alabama Materials Research Conference, Normal, AL.

Sponsor: Office of Life and Microgravity Sciences and Applications

■

Separation of Large DNA Molecules in Free Fluids

Percy H. Rhodes/ES76
205–544–7807

The current challenge for biological separation processes is the isolation of the intact DNA molecule from individual eukaryotic chromosomes. The process of mapping and sequencing the entire human genome requires the separation by electrophoresis of large (long-chained) DNA molecules and their fragments. Since the total sequence is essentially in a three-billion-base "message," it is of vital importance to execute the separations involved with great speed.

Electrophoretic separation is enhanced in low gravity by virtue of the absence of thermal convection (Rhodes and Snyder 1982). On Earth, DNA molecules up to a few megabase pairs are currently being separated using gel electrophoresis. The gel structure is sufficiently rigid to overcome the detrimental effects of gravity-induced thermal convection. However, this process is tedious and requires runs that take about a week to complete (Smith et al. 1987). By processing in low gravity and using a free fluid, the time required for separation can be reduced many orders of magnitude. A significant problem in processing large DNA molecules in a free fluid, however, is that all molecules migrate at the same speed, regardless of their length (Oliverd et al. 1964). Some way must be found to orient these molecules and make their migration velocity a function of their length in order to achieve separation.

The objective of this research is to investigate the orientation in free fluid of long-chained DNA molecules in the presence of high-strength electric fields (in excess of 100 V/cm). The goals are to quantitatively determine the relationship between electrophoretic mobility, the applied field strength, and the length of the individual linear DNA molecules subject to imposed electric fields. This research will determine if electrophoretic separation of DNA in a free fluid is possible and, thus, access the potential of space-based separation of large DNA molecules.

Grossman, P.D., and Soane, D.S. 1990. Orientation Effects on the Electrophoretic Mobility of Rod-Shaped Molecules in Free Solution. *Analytical Chemistry* 62.

Oliverd, B.M.; Baine, P.; and Davidson, N. 1964. Electrophoresis of Nucleic Acids. *Biopolymers* 2:245–57.

Rhodes, P.H., and Synder, R.S. 1982. The Effect of Small Temperature Gradients and Flow in a Continuous Flow Electrophoresis Chamber. *Materials Processing in Reduced Gravity Environment of Space.*'Elsevier Science Pub. Co.

Smith, C.L.; Matsumoto, T.; Niwa, O.; Kico, S.; Fan, J.D.; Yanagida, M.; and Cantor, C.R. 1987. *Nucleic Acids Research* 15:4481–89.

Sponsor: Office of Life and Microgravity Sciences and Applications

■

Highly Rarefied Solids in Microgravity: Toward the Limits for a Solid With Zero Volume and Infinite Surface Area

David A. Noever/ES76
205-544-7783

Since the discovery of aerogels in the 1980's, many investigators have speculated on gravity limits to producing new varieties of highly porous materials. In biology and chemistry, such large porosity can aid otherwise impossible enzymatic and catalytic aims. The mathematical ideal (called Menger's Sponge) is a solid with infinite surface area and zero volume—in essence, a new kind of matter (a gelled aerosol) much akin to frozen smoke. If realizable, an essential feature of such a remarkable object would be its highly textured or spongelike (fractal) properties. This roughness on all scales gives its mesh of intertwined fibers many unusual features: large catalytic activity; low sound and heat conductance; and, most spectacularly, an equivalent surface tension in a solid. Such fluid-like surface tension allows the solid to pass reversibly through tiny orifices while recovering its original shape. On Earth, however, large single blocks of such low-density materials collapse, compress, or sag under their own weight into condensed pancakes.

On recent KC–135 flights, we sought to demonstrate a key component of producing higher surface area fractals. Flight paths were selected to give a range of gravity (g) levels: 0.01 g (low), 0.16 g (lunar), 0.33 g (Martian), 1 g (Earth), and 1.8 g (high). Results, using the model material of hydrophobic silica, indicated that stable agglomeration of such tenuous, taffy-like fibers can increase markedly in reduced gravity (fig. 62). As measured by fractal dimension, effective surface area and roughness increased by 40 percent in low gravity. This finding supports the conclusion that relieving internal weight stresses on delicate aggregates can enhance their overall size (by 2 orders of magnitude) and internal surface area (fig. 63).

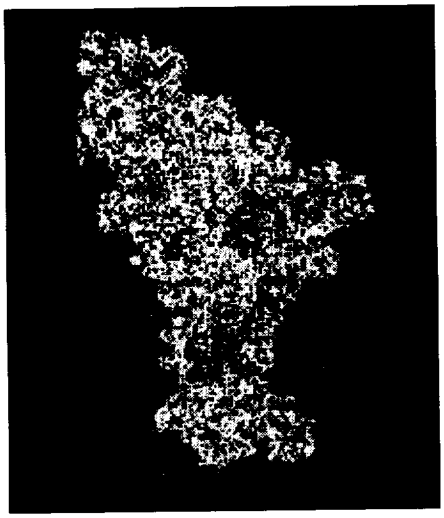

Figure 62.—Cross-sectional view of low-gravity solid produced in a highly rarefied form.

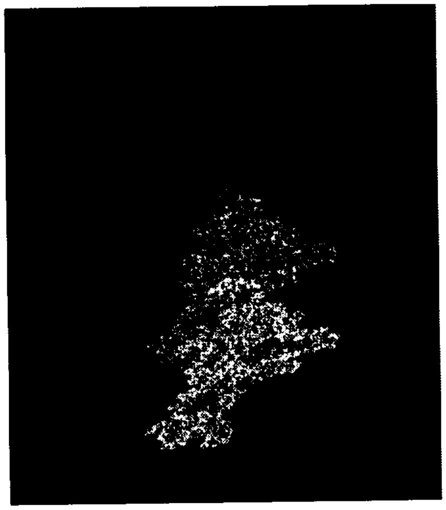

Figure 63.—Three-dimensional cutaway of highly rarefied silica solid produced in low gravity.

That such aggregates can damp heat and sound makes them the highest rated insulators ever produced. Their large surface area makes them uniquely reactive for catalysis and enzymatic uses. In principle, their density can be reduced to less than 10^{-4} parts of solids and hence their intertwined matrix can exist as a solid that weighs less than air. The fluid-like surface tension of the material has yet to be practically applied, but offers one explanation for how ball lightning and glow discharges can distort around (and seemingly through) solid objects while retaining their essential volume and globular shape. For other model materials, future flights will investigate further the highly textured and fractal nature of low-gravity assembly.

A detailed mathematical analysis of fractal fibers has been undertaken including predictions for their enhanced reactivity, sound and heat damping, surface tension, and prospects for achieving solid densities less than air. The evidence accumulated on the last flight would indicate quantitatively that microgravity offers a stable prospective environment for producing unique examples of such frozen smoke.

Noever, D.A., and Nikora,V.I. 1993. *Physics Review Letters*, submitted for publication.

Sponsor: Marshall Space Flight Center Director's Discretionary Fund

■

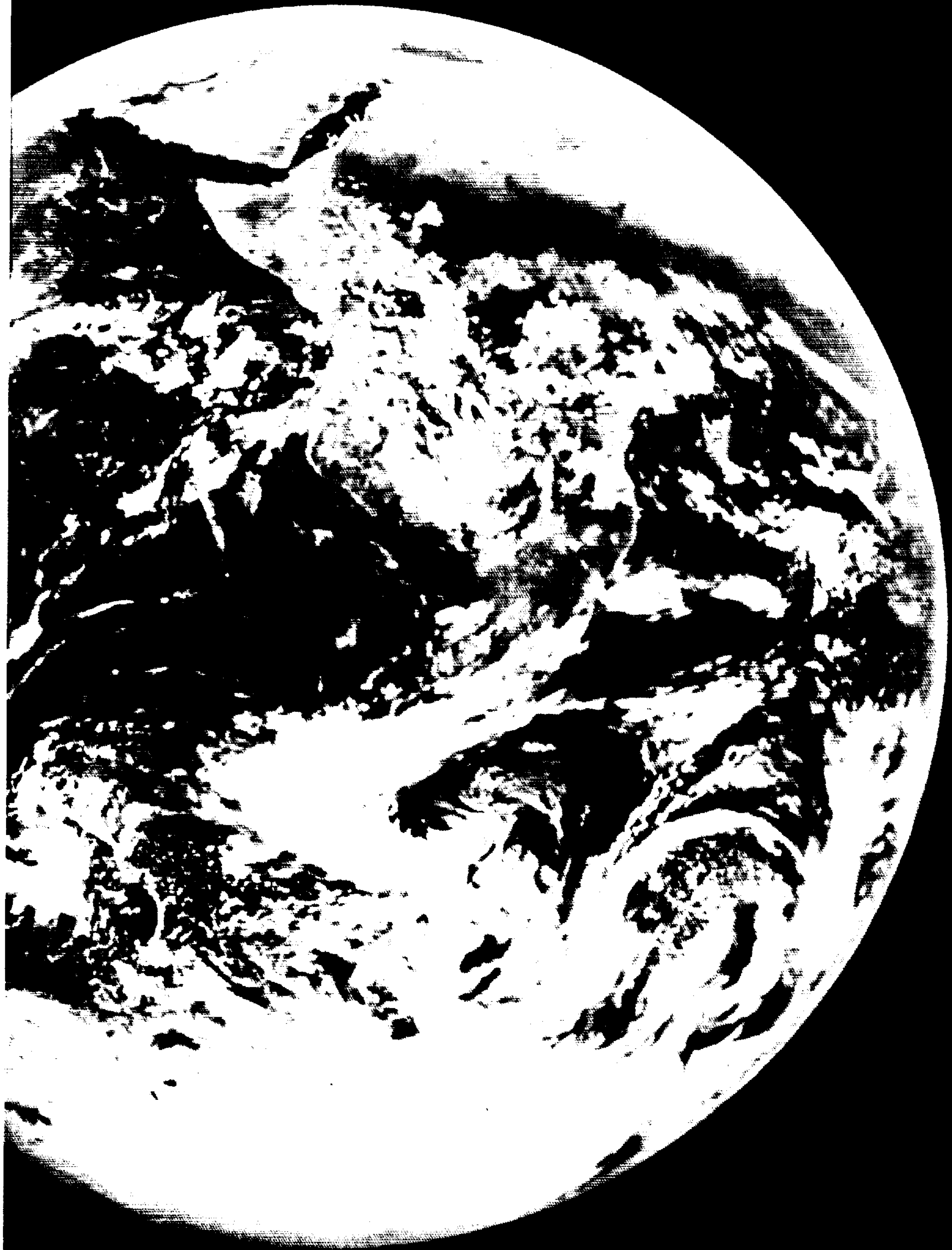

Technology Programs

The achievements of *Skylab* and Spacelab give us all a shared source of pride. The steps taken in these programs provide the United States with experience bases that are like "foundation stones" upon which our Nation's space efforts will continue to be built. Just as the research and technology efforts of the sixties were the foundation that enabled our successes in both *Skylab* and Spacelab, the scientific results and the new technology developed from these programs form additional building blocks that both enable the future development of space programs and, through application of new science and technology, improve the quality of life on Earth for the benefit of all.

It has been very exciting to be associated with such programs, and more exciting yet to imagine the potential benefits that new science and technology developments will bring to the people of our country and the world. It is this Nation's innovative spirit that has put America at the forefront of the technological revolution and made it the world leader in space.

As always, we at MSFC are dedicated to leading the development of new technologies that will keep our country both the leader in space and in applying newly gained information for the benefit of all Earth's people. In this section are representative selections describing current activities in the areas of propulsion, materials and processes, structures and dynamics, automated systems, space systems, and avionics. With the continued development of such technologies and insightful applications, the next two decades will yield programs, products, and applications as exciting as those just experienced.

Gabriel R. Wallace, Director
Research and Technology Office

Avionics

Mass Data Storage Unit

Scott L. Bridge/EB35
205-544-8572

A contract for a solid-state recorder (SSR) project was started in March 1991. The objective of this project is to advance technology to improve the availability of space shuttle main engine (SSME) performance data acquired during launch and to enhance the data storage capabilities of NASA for monitoring engine data in high-vibration environments. Technology used previously does not support the data storage requirements of future engine health and performance monitoring systems and does not support operation in a harsh environment near the SSME. Unlike a magnetic tape recorder, an SSR is ideal for space flight applications because it incorporates no moving parts.

MSFC has required the SSR developed under this program to be an all-digital unit in order to interface more readily with differing systems on various projects. A widely used Military Standard 1553B data bus has been incorporated into the design to control the recorder, and an additional 1553B bus in the SSR receives data from an engine health monitoring system or another source. Hardware design, fabrication, and integration of the microprocessor board, electrical backplane, built-in test function, power supply, and all memory modules have been completed for a prototype SSR. Fairchild Space Company designed a rugged multichip module proven in the Air Force F15 fighter program. Each module has 50 one-Mb memory devices. Design and fabrication of the memory controller and the input/output interface circuit boards have been completed, and testing of the prototype engineering model was completed August 1993.

A solid-state technology study report has been delivered to NASA, and a preliminary design review of the project was successfully completed in April 1992. Although the memory capacity of the prototype is 800 Mb (large enough to fully test and verify the desired design for a space-qualified unit), the selected architecture is readily expandable to 10 Gb. The prototype has a standard RS–422 data interface, a Military Standard 1553 data bus, and a high-speed channel input and output. Users will be able to play back data faster because the SSR, unlike magnetic tape recorders, has the capability to play back and record data simultaneously.

Sponsor: Office of Advanced Concepts and Technology

Commercial Involvement: Fairchild Space and Defense Co.

■

Modular Software for Engine Control

Charles L. Cozelos/EB42
205-544-3730

The purpose of this project is to develop a viable approach, using Ada™ computer language, to rocket engine control software and software tools that allow the incorporation of technology developments in sensors, actuators, connectors, communications (i.e., optical bus), and engine control health monitoring techniques. Also, the project will allow insertion of emerging technologies in the computer and electronics fields. This design will permit a delta software verification and elimination of the periodic end-to-end verification of the SSME, which usually requires 5 or 6 mo of labor-intensive effort. The design will support flexible and modular interfaces.

IBM was selected as the implementing contractor. In February 1993, at the formal kick-off meeting, the Software Management Plan and Development Plan were reviewed. In June 1993, a software architecture review was completed. The architecture approach was accepted, and IBM was given authorization to proceed.

Sponsor: Office of Advanced Concepts and Technology

Commercial Involvement: IBM

■

Monitoring and Diagnosing the Environmental Control and Life Support System

Amy N. Cardno/EB43
205-544-3039

Brandon S. Dewberry/EB43
205-544-4247

The Environmental Control and Life Support System (ECLSS) Advanced Automation Project (AAP) is in its fifth year of developing an intelligent system to monitor and diagnose the space station ECLSS. Model-based diagnosis is the technology chosen by this project to provide fault detection and diagnosis of the ECLSS (fig. 64). The model-based reasoning algorithm requires a model of the system. It then analyzes this model and automatically detects and diagnoses faults. For monitoring the system, a graphical user interface is provided that consists of a schematic of the system and critical sensor information.

The model consists of complex structural and behavioral relationships of the subsystem's components. Faults are detected by noting discrepancies between subsystem and model sensor values. A fault candidate list is generated by fault diagnosis procedures. Various operations are performed on the fault candidate list, including model inversion, to remove suspected components from the candidate list. A candidate list of one component is declared to be the faulty component.

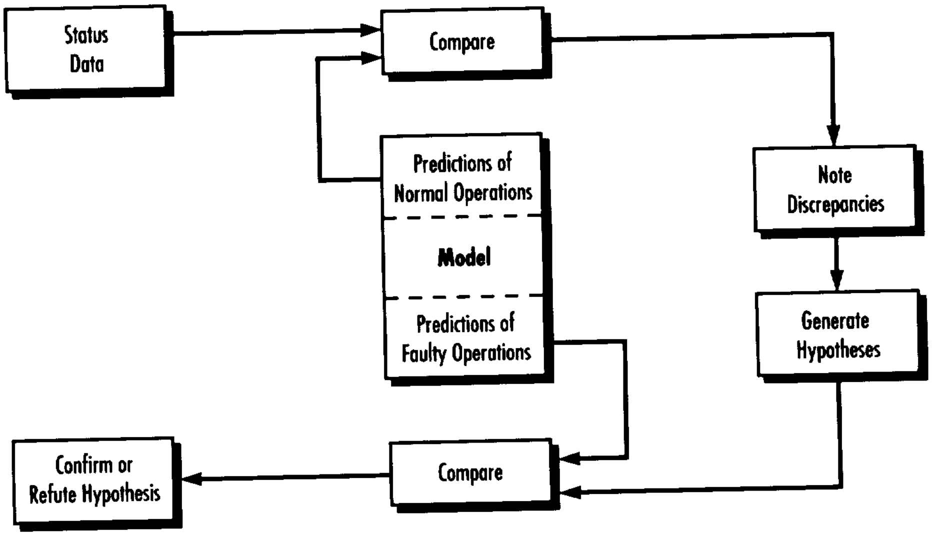

FIGURE 64.—ECLSS AAP logic flow.

The ECLSS AAP is targeting the technology toward the space station ground support centers. This past year, the ECLSS AAP has worked closely with JSC's Space Station Control Center Complex to provide this technology. Currently, models of the carbon dioxide removal assembly and the temperature and humidity control system have been developed and are ready to be assessed by the control center engineers.

Sponsor: Space Station Engineering

■

Solid-State Coherent Doppler Lidar

Michael J. Kavaya/EB54
205-544-8453

Most of the scientific measurements made by NASA involve remote sensing. The use of lasers for remote sensing is often the optimum approach and sometimes the only technique for certain measurements. Light detection and ranging (lidar) will likely progress to become as useful and beneficial as microwave radio detection and ranging (radar) has proven to be. Coherent Doppler lidar is a subset of lidar that simultaneously provides high sensitivity—leading to large signal-to-noise ratios—and the ability to record and utilize the spectral position and shape of the returning light, and the light's polarization properties, as well as the light's intensity. In addition to target range, reflectance, depolarization, vibration spectrum, and other measurements, coherent Doppler lidar can measure the velocity of the target that scattered the detected light. This is due to the wavelength shift (Doppler shift) experienced by the reflected light arising from the relative motion between the lidar and the target. When the target is either air molecules or aerosol particles floating in the air, the lidar measures the wind velocity. These two targets have sufficient reflectance only for the short wavelengths produced by lasers (versus microwave radar wavelengths).

Potential applications of this wind velocity profiling capability include wind profiling for shuttle and rocket launches, shuttle landings, advanced warning to airline pilots of dangerous wind shear and microbursts, pollution research and source identification, improved targeting for military ordnance and parachuted personnel and supplies, and automobile speed monitoring. The most exciting application of the wind profiling capability is the concept of global measurements of wind throughout the troposphere from an Earth-orbiting lidar (fig. 65). As stated in the NASA report referenced below, "knowledge of the global wind field is widely recognized as fundamental to advancing our understanding and prediction of the total Earth system," and "the increased use of global wind vector fields in numerical prediction models offers perhaps the greatest potential for increased accuracy in operational forecasts."

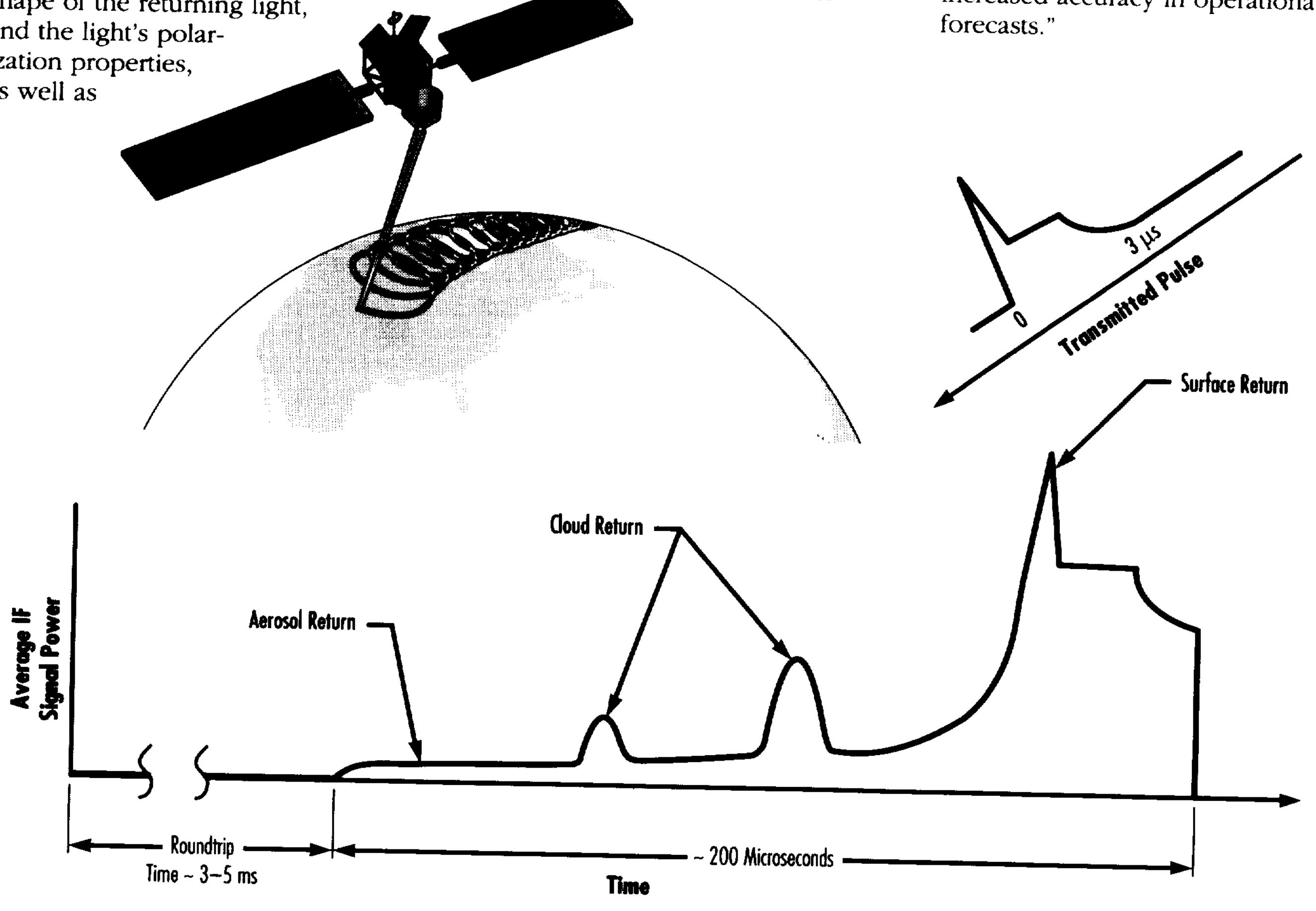

FIGURE 65.—Laser Atmospheric Wind Sounder.

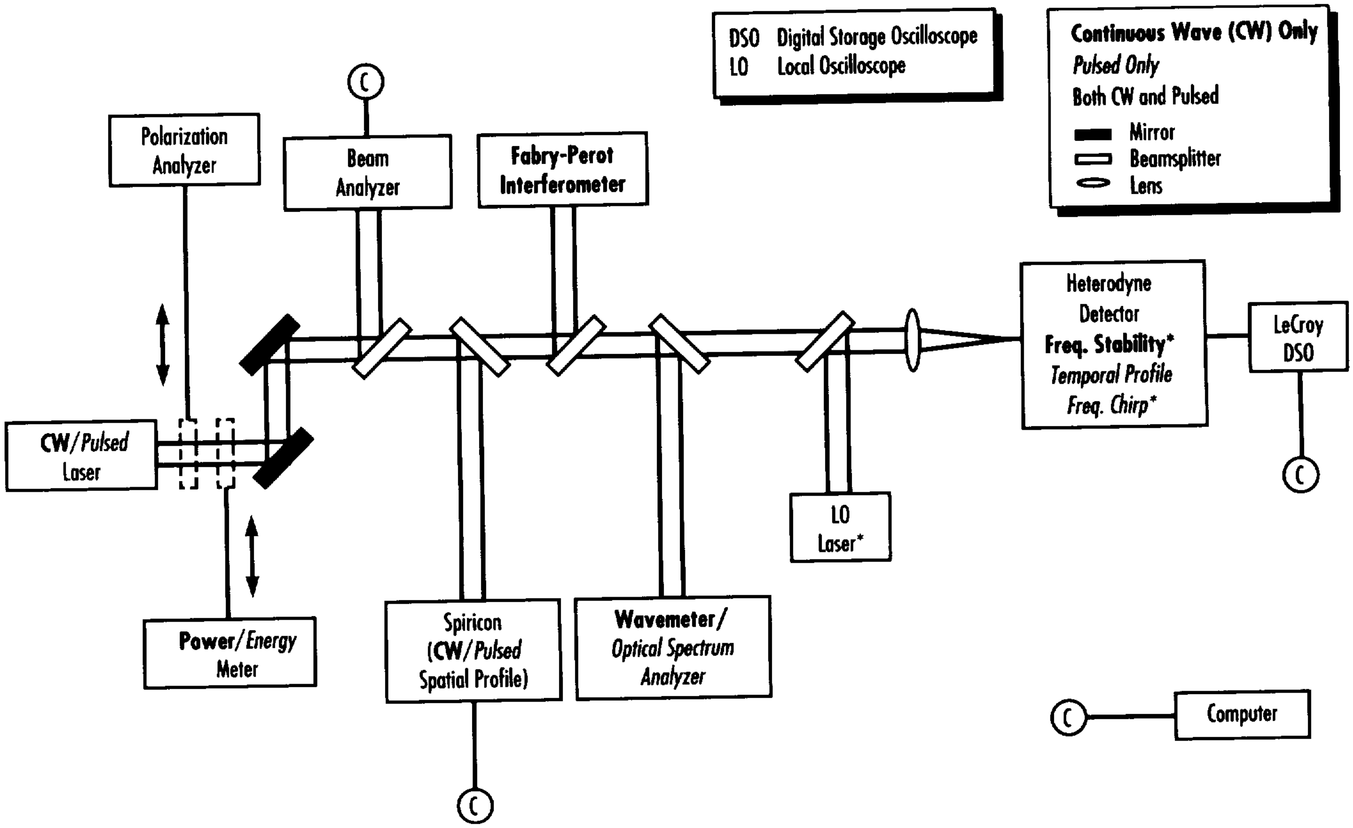

FIGURE 66.—Laser characterization facility.

The "heart" of all lidar systems is the laser. Solid-state lasers are an emerging technology with tremendous potential to eliminate consumables and to improve the compactness and lifetime of lidar systems. These qualities are all particularly desirable for space missions. The goals of this program are to develop a laser transmitter and receiver for an eyesafe solid-state coherent Doppler lidar system satisfying the mission requirements of an Earth-orbiting wind profiler, to develop facilities to test candidate lasers and receivers for performance and suitability, to develop a solid-state coherent Doppler lidar test-bed, to demonstrate laser and receiver performance in the test-bed, to develop a lidar calibration range, and to apply the developed technologies to other missions.

This effort is part of a multi-Center program to develop the technology and knowledge to enable many highly desired and long awaited laser remote sensing missions. During this first year, MSFC has defined preliminary mission requirements for the laser and receiver; communicated these requirements to Langley Research Center (LaRC), where the solid-state lasers and one type of lidar receiver are being developed; teamed with JPL in the development of a different type of lidar receiver; contracted with TRW to more thoroughly define the mission requirements for the lidar system; and begun development of a solid-state laser characterization facility at MSFC (fig. 66).

The laser characterization facility will be used to test and characterize candidate lasers developed by LaRC and others. The information learned will be shared with the laser developers to allow efficient and optimum development paths, and will be used at MSFC to permit interpretation of laser performance in a coherent Doppler lidar system. In future years, MSFC plans to develop a companion detector characterization facility, a lidar test-bed facility, a lidar target calibration facility, and a lidar calibration range.

Curran, R.J., Chair. January 1987. Earth Observing System Instrument Panel Report for the Laser Atmospheric Wind Sounder (LAWS), vol. IIg.

Sponsor: Office of Advanced Concepts and Technology

Commercial Involvement: TRW

■

Space Station Module Power Management and Distribution Automated Subsystem

Bryan K. Walls/EB72
205-544-3311

Norma Dugal-Whitehead/EB72
205-544-3304

The space station module power management and distribution system breadboard is a test-bed demonstrating advanced automation techniques based on a space station module electrical distribution system. By appropriately distributing computing power from the switch-gear in the power system up to a central workstation, the system can react immediately to guarantee safety, while still effectively coordinating actions on a system-wide basis. PMAD functions such as scheduling/rescheduling, fault detection and isolation, creation of load-shedding lists, and display of system status are handled by independent autonomous agents—separate programs that work together to get the job done. A human operator, working with the user interface and its associated planner, acts as another autonomous agent and is smoothly inte- grated into the whole system. This high level of integration and capability makes the SSM/PMAD system breadboard a world-class example of cutting-edge automation techniques.

The approaches and techniques proved in the SSM/PMAD system are now being integrated into the electrical power system console software for the JSC Consolidated Control Center. Developed in cooperation with the LeRC, as well as controllers at KSC, an EPS console using these technologies is expected to enable better, less expensive operations than current techniques.

The SSM/PMAD system is an outgrowth of work begun back in the late 1970's. In recognition of the high cost of personnel required to operate *Skylab*, the MSFC Astrionics Laboratory began looking at techniques to automate power systems. In 1987, funding became available to take what had already been learned and to push the state of the art in breadboard modeling of the electrical power system in the habitation and laboratory modules of the space station. Two contracts for the effort were awarded to the Martin Marietta Corporation, through whom the current SSM/PMAD system has been developed.

The power distribution system in the breadboard consists of two 120–V dc buses. They are configured radially, with power flowing from power distribution control units (PDCU's) on each bus into three load centers. Each load center is powered by each bus so that redundant switching within a load center is possible. The lowest level of switches function as both remotely-controlled switches and as circuit breakers. Besides opening due to high current like normal circuit breakers, these remote power controllers (RPC's) are also capable of opening due to a high current over time (I^2t), under low voltage, or high temperature. Each RPC also has a built-in current sensor.

In each load center and PDCU is a lowest level processor (LLP). The LLP monitors the switches and administers the local portions of the master schedule. It opens or closes switches according to the schedule, monitors switch currents to make sure they are within scheduled limits, and sheds loads that are not. In case of a fault, the LLP will handle redundant switching, if necessary, and can shed loads, starting with the least important loads, by using its load-shed list.

The other segments of control and protection in the SSM/PMAD system are called autonomous agents. Currently these agents consist of Maestro that creates and maintains the master schedule from activities created by the user; the front end load enabler schedule (FELES) that divides the master schedule up into a form usable by each LLP; the Load Priority List Management System that creates the load-shed lists for each LLP; the fault recovery and management expert system (FRAMES) that monitors and actively diagnoses faults in the system, notifying Maestro of the results so rescheduling can occur; knowledge and negotiation tool (KANT), a planner that allows a human user to interact with the system as an agent; and the user interface that apprises the user of the system state. These systems all work together through the knowledge management and design (KNOMAD) tool.

This highly integrated autonomous system is a prototype for future space missions that require low-cost operation of complex systems. The RPC's and LLP's will have to be designed into the systems to take full advantage of the possible benefits, but significant savings are possible by using just those techniques that apply for the system at hand. Current work on the SSM/PMAD breadboard is focused on applying the techniques that have been developed into the EPS console of JSC's Consolidated Control Center, which will operate both the space station and shuttle.

Sponsor: Office of Advanced Concepts and Technology

Commercial Involvement: Martin Marietta Corporation; Synbiotics, Inc.; and Micon Engineering

University Involvement: University of Alabama in Huntsville, University of Central Florida, Florida Institute of Technology, and University of Tennessee Space Institute

■

Materials and Manufacturing Processes

Hybrid Capacitive-Inductive Microsensor Arrays for Evaluating the Integrity of Thermal Barrier Coatings

Samuel S. Russell/EH13
205-544-4411

Shakeel S. Razvi/CQ05
205-544-7377

The consistency of thermal coatings on turbine blades and other gas turbine components is important in the prevention of oxidation, corrosion, and erosion of these components. This SBIR effort seeks the simultaneous detection of coating bond, porosity, and thickness through hybrid electrical test methods. A novel hybrid sensor array was designed and built using thin film technologies that fuse the capacitive and inductive sensing methodologies into a single sensor design. The sensors were sputtered on dielectric substrates and may be miniaturized for application. The design was optimized by using a finite element model of the electrical response due to anomalies in thermal protective coatings.

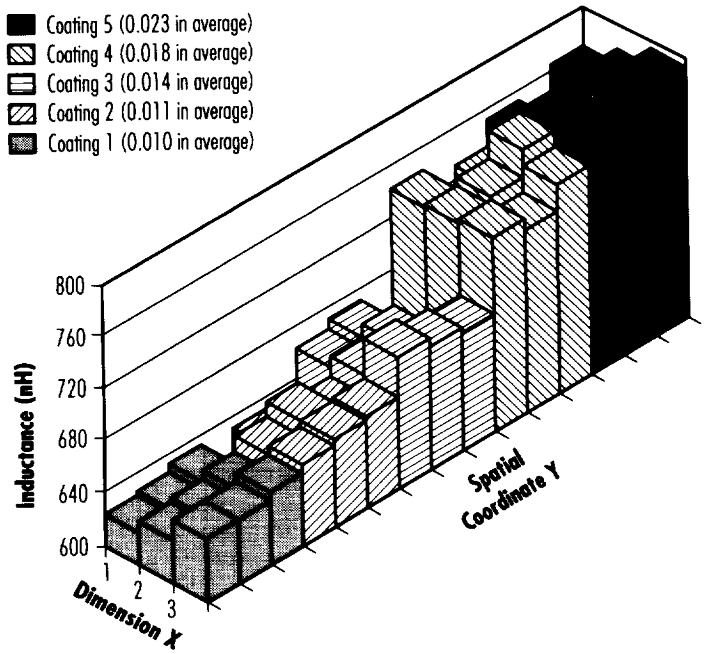

FIGURE 67.—Three-dimensional column chart showing inductance measured over coatings varying in thickness between 0.025–0.050 in.

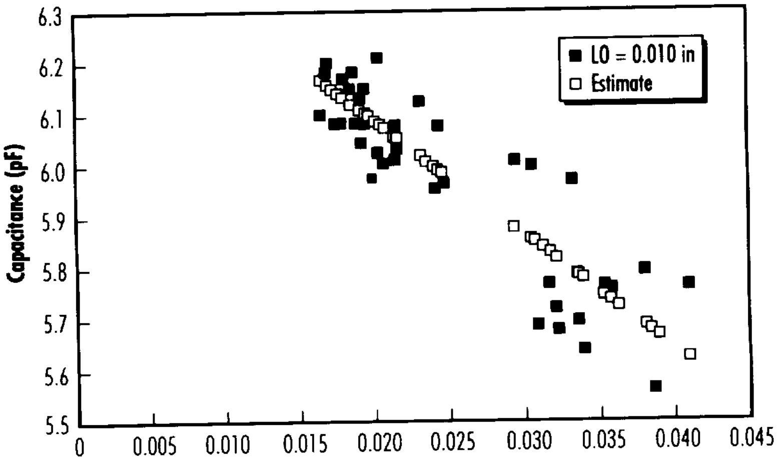

FIGURE 68.—Measured capacitance plotted against thickness/permittivity of thermal barrier coatings at locations shown above. Sensor lift-off (LO)=0.010 in.

A series of tests were conducted to optimize the use of this sensor with standard eddy current instrumentation over a frequency range of 100 Hz to 10 MHz. Inconel plates were coated with zirconium oxide, 8 percent yttrium oxide, of differing thicknesses and porosities to simulate coating variations on high-temperature turbomachinery. Figures 67 and 68 show changes in the inductance and capacitance of the sensor elements plotted against different coating thicknesses and permittivities. Experiments revealed that the sensor is sensitive to changes in coating thickness of 0.001 in or smaller and porosities on the order of 5 percent.

Further development of these sensors and sensor arrays, and their subsequent integration into an automated inspection system for thermal barrier coating characterization, is under consideration. An SBIR Phase II contract for this effort is anticipated.

Sponsor: Office of Advanced Concepts and Technology, Small Business Innovation Research Program

Formability Study of Aerospace Aluminum Alloys

George E. Wertz/EH15
205–544–2663

The space station module walls are being fabricated of 2219 aluminum. Early tests performed to evaluate the performance of 2219–T87 versus 5456–H116 aluminum relative to micrometeoroid and orbital debris impact damage were inconclusive, in that no significant difference was measured from hypervelocity impact tests. Therefore, the aluminum alloy 2219–T87 was selected for the module walls based on other criteria. In order to gain a better understanding of the relationship between hypervelocity impact damage and different alloys of aluminum, additional studies were initiated incorporating hypervelocity penetration mechanics models. These models use material forming-limit data to help establish the material fracture criteria.

The technique used to investigate the forming-limits of materials involves biaxial punch stretch testing of sheet metal specimens clamped securely between two die plates at the periphery. In this test, the strains in a specimen vary over the stretched dome from a strain state near plane strain near the flange to one approximating balanced biaxial tension at the pole. The use of lubrication makes the strain ratio at fracture more biaxial as the flow localization and failure occur near the flange when poorly lubricated and at the pole when good lubrication is utilized. The strain paths and failure strains are measured through the prior application of grids onto the test specimens.

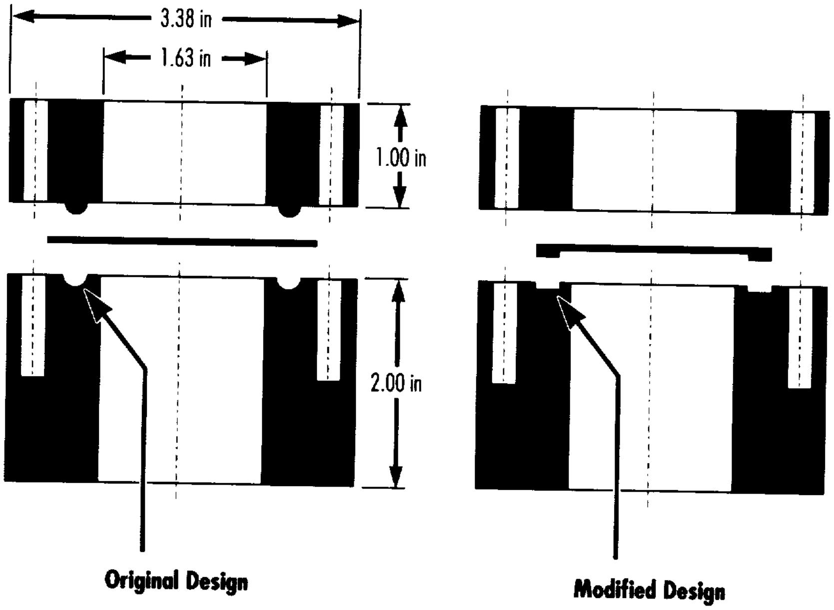

Figure 69.—Formability test fixture.

The specimens are photographically printed with a circle-grid pattern using a photosensitive-resist method. The circle diameter is important in measuring the deformations accurately and must be small in relation to the strain gradient in the specimen. Once the material is deformed, the original circles will appear elliptical near the fracture point. The percent change in shape on the long side is major strain (always positive and larger than the original circle) and the percent change on the short side is minor strain (can be either larger or smaller and, therefore, positive or negative).

The material under examination is made to thin over a range of strain ratios to its failure point. Failure is defined as the appearance of localized thinning or necking, and not necessarily final separation of the material. These failure/nonfailure data can be represented graphically as forming-limit diagrams against which forming strains can be compared. This forming-limit diagram plots the two principal surface strains in the sheet over those combinations of strain where thinning occurs. Any combination of the two surface strains falling below the forming-limit curve is considered acceptable. Any combination falling above it will produce a failure.

The attached experimental data have been obtained for aluminum alloys 2219–T87 and 5456–H116 using a standard technique, but with a modified test fixture. Since the alloys under investigation are tempered for ultimate strength, the standard holder caused premature failure at the hold-down bead. In order to prevent this premature failure, the fixture (fig. 69) was prepared along with appropriate material specimens. Successful tests are being performed using this modified test fixture. The experimental data for 2219–T87 and 5456–H116 are plotted as a forming-limit diagram (fig. 70) for indicating a material's forming strain. At any single point on the material, the forming strain equals the metal's

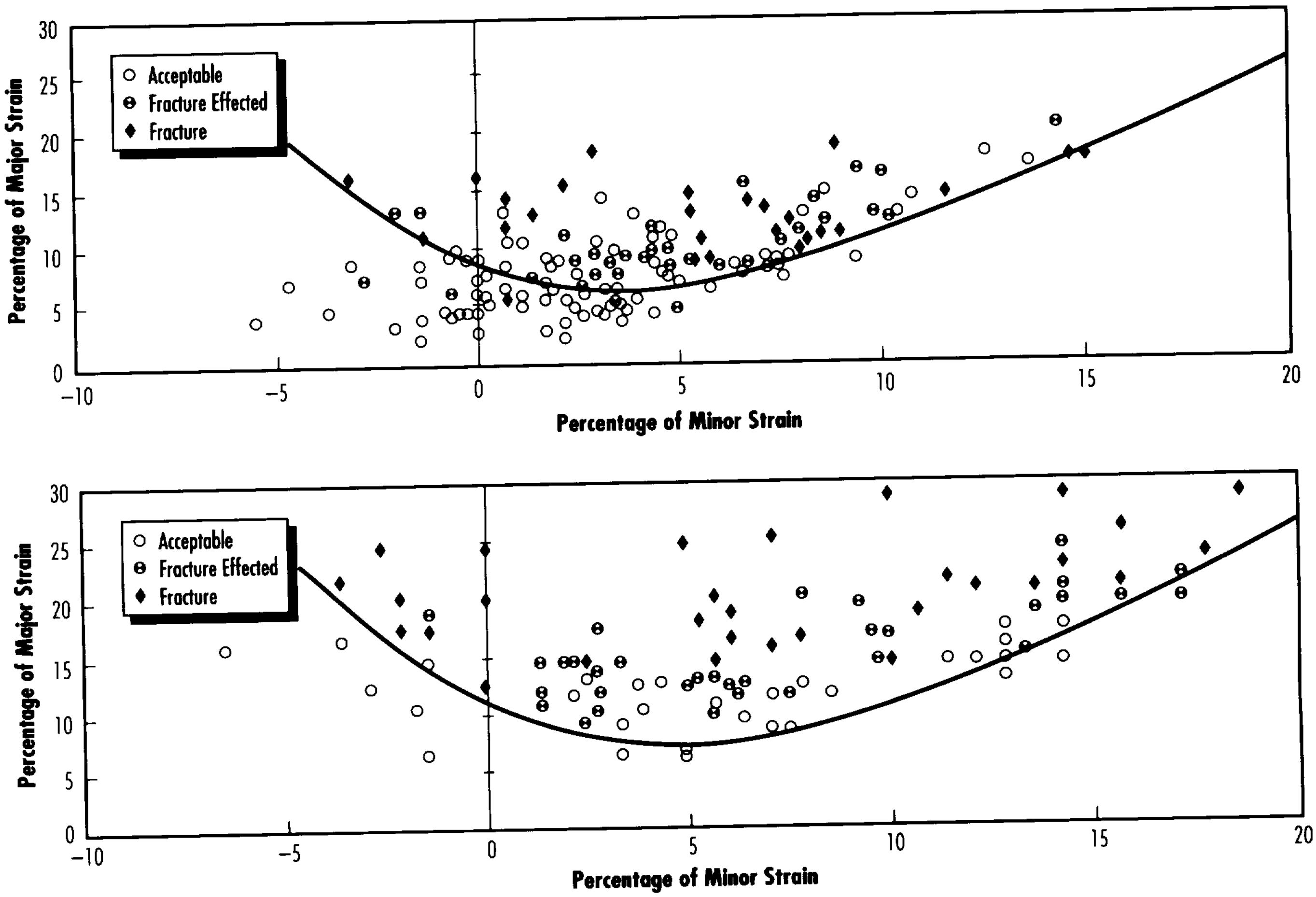

FIGURE 70.—Forming limit curve 2219-T87 (top) and forming limit curve 5456-H116 (bottom).

ultimate capacity to be worked or deformed. This point is said to be the metal's forming limits. Exceeding this limit will tear the material.

The concept of this forming-limit diagram is useful in predicting when given strains in a material will produce failure. Forming-limit data may characterize the potential performance of aluminum alloys proposed as space station module wall materials. These strain-based failure criteria will be imposed in the development of hydrocodes to simulate the deformation processes of hypervelocity impacts from micrometeoroids and orbital debris on space structures.

Sponsor: Space Station Projects Office

■

Long Duration Exposure Facility Experiments and Space Environment Effects on Materials Studies

Miria M. Finckenor/EH15
205-544-9244

Roger C. Linton/EH15
205-544-2526

Ann F. Whitaker/EH41
205-544-2510

The Long Duration Exposure Facility data base of space environmental effects on materials continues to provide valuable information for designing long-term mission spacecraft. The three LDEF experiments currently being analyzed are the Solar Array Material Passive LDEF Experiment A0171, the Atomic Oxygen Stimulated Outgassing Experiment A0034, and the Thermal Control Surfaces Experiment S0069. Materials being evaluated include polymers, metals, composites, thermal control coatings, dielectric films, and solar cells.

Experiment A0171 passively exposed a variety of materials to the ram (leading edge) environment of atomic oxygen, ultraviolet radiation, thermal vacuum, and meteoroid/orbital debris impact. Atomic oxygen attack of bulk metals is being evaluated through various techniques, including ellipsometry, changes in optical properties, and electron scanning analysis (ESCA). Effects of the space environment on polymeric material performance are also being studied. Analysis includes differential scanning calorimetry, differential thermal analysis, and thermogravimetric analysis on polymeric flight and control samples.

Experiment A0034 consisted of two modules, exposing selected thermal control materials to LDEF leading and trailing edge conditions. Current studies include laboratory exposure testing of thermal control coatings, including selected flight samples, to determine specific effects and influences of atomic oxygen and ultraviolet radiation. Optical witness samples are being evaluated for deposition of outgassing products, with results correlated to the performance of the adjacent coating.

Experiment S0069 studies have included remeasuring optical properties of flight samples to study the effect of long-term ground storage. Fourier Transform Infrared (FTIR) measurements of the surfaces of flight samples are being analyzed. Trend analysis based on spectral band dependence is in progress and will be completed for presentation at the LDEF Third Post-Retrieval Symposium in November 1993.

MSFC, in cooperation with the University of Alabama in Huntsville, the Alabama Space Grant Consortium, and the Society for Manufacturing and Process Engineering (SAMPE), held the LDEF Materials Results for Spacecraft Applications Conference on October 27–28, 1993. More than 250 attendees toured the MSFC facilities and heard presentations on the spacecraft environment, atomic oxygen erosion and ultraviolet radiation damage, composites and other structural materials, thermal control materials, and optical materials, as well as plenary sessions on future space exploration.

Sponsor: Office of Advanced Concepts and Technology

University Involvement: University of Alabama in Huntsville

■

Novel Material Concepts for Spacecraft Debris

Angela M. Nolen/EH15
205-544-9245

James M. Zwiener/EH15
205-544-2528

The design and operation of spacecraft must give serious consideration to the space debris environment and its effect on mission performance. Hypervelocity impacts by orbital debris particles can cause severe damage to vital spacecraft systems and components, resulting in component degradation, catastrophic structural failure, or injury to crew members. Conventional dual-plate aluminum bumper/pressure wall shields, originally developed to provide spacecraft protection against the natural micrometeoroid hazard, will result in significant weight penalties when designed to protect spacecraft against a continuously increasing orbital debris environment. More efficient orbital debris shield designs are urgently needed to provide improved protection and lower weight for future spacecraft missions. Improvements in analytical modeling capability are also required to allow for more cost-effective design and evaluation of advanced material concepts for a wide range of impact conditions.

Technology Development Association, Inc. (TDA) has addressed these issues this year in a Phase I SBIR program. The primary objective of this program is the development of novel fabric material concepts that offer lightweight and improved debris protection compared with the conventional dual-plate aluminum shielding. The debris shielding concepts identified by TDA as a result of the Phase I program include a multilayer, functionally gradient fabric and a 3-D flexible sandwich core fabric geometry. These concepts are unique in that they combine the beneficial shield material properties and geometry in order to achieve the desired functionality, while offering improved weight and volume efficiency. These concepts also provide the ability to tailor the constituent materials and geometry in order to provide protection against a wide range of debris impact conditions (i.e., projectile density, size, and impact velocity). A significant feature of the program is the development of a numerical analysis model for the design, evaluation, and optimization of flexible fabric materials or debris shield applications. The analysis model resulting from the Phase I research effort has established the engineering design guidelines and techniques for developing optimal fabric material systems that provide improved spacecraft protection for a wide range of particle sizes, impact angles, and velocities.

This research program offers significant benefits for future spacecraft that must be designed to operate in an orbital debris environment. The Phase I program has laid the necessary groundwork for further development and experimentation in Phase II. Several candidate functionally gradient fabric material configurations, as well as a 3-D sandwich core fabric concept, have been recommended for further development and evaluation.

Sponsor: Office of Advanced Concepts and Technology, Small Business Innovation Research Program

Commercial Involvement: Technology Development Association, Inc.

■

Approximation Techniques to Determine the Increase in Surface Area Due to Surface Roughness

David L. Edwards/EH15
205-544-4081

The soluble core of future large solid rocket motors may utilize a conductive/waterproof barrier to form the initial propellant surface. Techniques for applying the conductive/waterproof barrier to the soluble core are brush, spray, and molded applications. The increased surface area created by some of these applications may have a potentially adverse effect on the initial pressure spike during ignition of the solid rocket motor. This technique provides a method to approximate the increase in surface area due to surface roughness.

Three samples—identified as brush, spray, and molded—are measured using a Dektak II surface profiler. This instrument utilizes a stylus that measures surface structure over a preset length. Figure 71 shows the scans obtained from the Dektak II. Although these scans indicate a random surface roughness, approximations can be made to make the roughness a periodic function. The approximations utilized were the triangular wave approximation (TWA), conic section wave approximation (CSWA), and the rectangular wave approximation (RWA). The investigator must examine the scans and approximate the average amplitude and period of the funtion. These values will be used in the TWA, CSWA, and RWA approximation techniques.

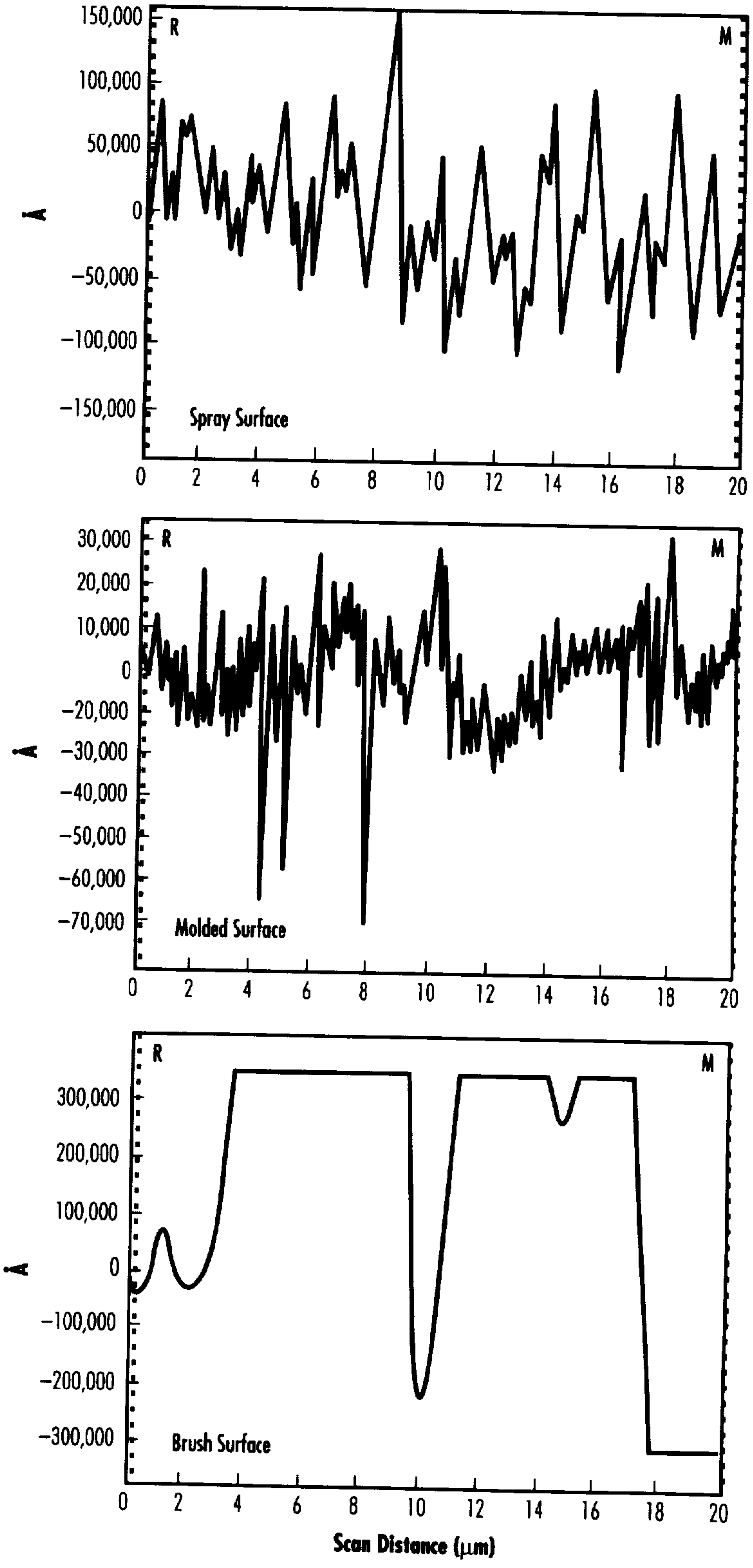

FIGURE 71.—Dektak II scan of spray, molded, and brush surfaces.

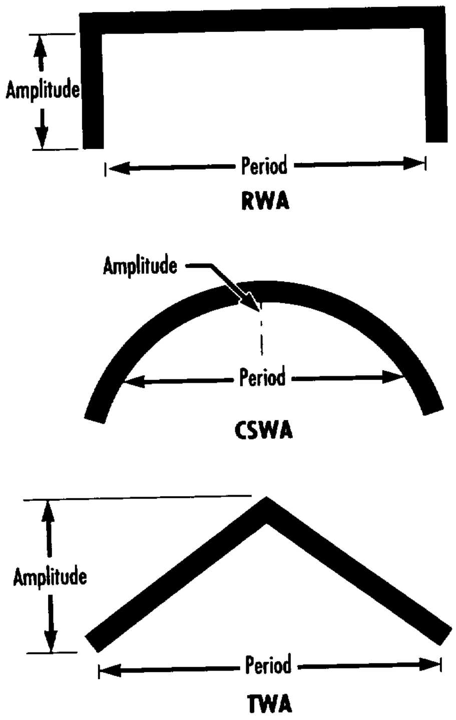

FIGURE 72.—Wave approximation techniques.

TABLE 4.—*Percentage increase in surface area for coatings*

Coating	TWA	CSWA	RWA
Spray	0.009999%	0.045500%	1.97%
Molded	0.005625%	0.001295%	1.48%
Brush	2.164700%	2.870000%	24.22%

Figure 72 shows the various wave approximation techniques used in this work. The TWA utilizes the Pythagorean theorem given by $\ell = (x^2 + y^2)^{1/2}$ for the increased length over one-half of the period in one direction. Multiplying $\ell \times \ell$ to get an area, then comparing to a perfectly flat surface, will yield a change in surface area.

The CSWA technique uses the period as the chord of a circle and the amplitude as the distance from the center of the chord to the circle. Using these values, the arc length (ℓ) can be determined. As with the TWA, the area $\ell \times \ell$ is calculated and compared to a flat surface to determine the change in surface area. The RWA uses the period as one side of a rectangle and the amplitude as the other side. The equation for determining the length (ℓ) is: $\ell = 2$ (amplitude)+period. Once ℓ has been determined, the area can be calculated as in the TWA and CSWA, then compared to a flat surface to determine the change in surface area.

Application of this technique for the soluble core coatings shows that the molded coating application is the smoothest surface, with the spray coating providing a slightly rougher surface. The brush coating is 2 and 3 orders of magnitude rougher than the spray and molded coatings, respectively. Table 4 summarizes the percentage increase in surface area for the various coatings using these techniques.

Sponsor: Office of Space Systems Development

■

Optical Effects Facility

Roger C. Linton/EH15
205-544-2526

Molecular film contamination deposited on and degrading the performance of critical optical surfaces, whether in space or in ground-based testing, can be sensitive to the effects of repressurization, atmospheric exposure, and subsequent depressurization (when required). Therefore, for the most accurate analysis of the effects of contamination deposited in a vacuum on optical surfaces, measurements of the thickness and the optical effects should be performed in situ, that is, in the environment in which it will be used. The in situ contamination effects facility in the MSFC Materials and Processes Laboratory provides this capability for optical witness samples exposed in vacuum to heated materials with actively monitored data from temperature-controlled quartz crystal microbalances (TQCM's) and four vacuum ultraviolet (UV) wavelength optical signal detectors. This facility is providing data for candidate space materials, relating the optical effects of deposited contamination on optical witness samples as a function of time, source material temperature, and witness sample temperature; correlating the measured thickness growth in real time with TQCM's; and analyzing the evolved molecular species with a residual gas analyzer (RGA). Three solar-blind photomultiplier detectors positioned at specular and forward- and back-scattering angles from the optical collectors provide a measure of the bidirectional reflectance distribution function (BRDF) from molecularly contaminated optics at vacuum UV wavelengths. For purposes of normalization of signal, the intensity of the krypton microwave-excited resonance lamp used as the illumination source is monitored by a fourth detector at the vacuum chamber entrance aperture. The principal emission of this krypton source includes the characteristic krypton resonance lines at 116.5 and 123.6 nm.

This facility provides a more comprehensive investigation of the effects of contamination on optical surfaces by experimentally relating the observed optical degradation to molecular contamination growth kinetics for correlation with analytical modeling. Recent testing with candidate silicone seal materials (SSF) and Hysol™ adhesive have indicated a significant difference in effects dependent on the inherent optical constants of the optical witness samples.

Sponsor: Office of Advanced Concepts and Technology

University Involvement: University of Alabama in Huntsville

■

Beam Processing of NARloy-Z for Improved Microstructure, Properties, and Life Enhancement of Main Combustion Chamber Liner

Biliyar N. Bhat/EH23
205-544-2596

Efforts are under way to improve the space shuttle main engine life of the main combustion chamber (MCC). The MCC life is limited by the life of its liner, currently made from a copper (Cu)-based alloy, wrought NARloy-Z (Cu, 3 weight percent silver (Ag), 0.5 weight percent zirconium (Zr)), which is degraded in the engine operating environment. The microstructure is changed with grain boundary precipitations and migration of vacancies to grain boundaries, forming voids that often result in grain boundary separation. These microstructural changes result in lower mechanical properties, especially lower ductility at operating temperatures (~550 °C). This has led to formation of cracks in the MCC liner. Additionally, vacuum plasma spraying (VPS) of NARloy-Z has been used to form MCC liners as a low-cost alternative to the current process. Unfortunately, VPS NARloy-Z also tends to have a nonuniform microstructure containing voids and grain boundary precipitates similar to the degraded wrought NARloy-Z. The present research effort is directed toward restoration of NARloy-Z microstructure through beam processing that will enhance the life of the liner. This process is applicable to both wrought (degraded) and VPS MCC liners and is expected to produce microstructure, mechanical, and thermal properties equivalent to or better than conventional wrought NARloy-Z.

Initially, the feasibility of beam processing was demonstrated with VPS NARloy-Z specimens that had nonuniform microstructures containing cavities, voids, and grain boundary precipitates similar to the microstructure of the SSME MCC liner after hot firing. Both electron and laser beams were used for the feasibility study, which consisted of glazing the surface of NARloy-Z to a depth of 0.25 to 1.25 mm and examining the microstructure optically and in a scanning electron microscope. The glazed areas showed a very uniform distribution of fine precipitates throughout the matrix (fig. 73). The grain size was much finer, which enhances mechanical properties, especially ductility. No grain boundary precipitation was observed. Cavities and voids were eliminated. Both laser and electron beam glazing produced similar, uniform microstructures in the wrought alloy. Due to inherent rapid melting and solidification that occur during glazing, solid solubility of the solute atoms Ag and Zr in the matrix is extended and, hence, hardness and strength of the alloy are improved. A mechanical property data base is being generated for the laser-glazed NARloy-Z. A patent application has also been made on this process.

FIGURE 73.—Optical (a) and scanning electron (b) micro graphs of VPS NARloy-Z showing dramatic miersstructural improvement in a laser-glazed surface (LGS).

It is planned to use the beam processes to enhance the life of the SSME MCC liner. This is a joint program with Rockwell International, Rocketdyne Division, with participation from three universities: the University of Illinois, Urbana-Champaign (U of I); Pennsylvania State University (Penn State); and the University of Tennessee Space Institute (UTSI). The preliminary laser glazing work was done at U of I. Laser glazing of NARloy-Z test specimens is being done at Penn State; these specimens will be used to generate a mechanical property data base. Electron beam glazing and material characterization are being done in-house by Dr. J. Singh, a senior National Research Council Fellow working in the Materials and Processes Laboratory. UTSI will assist in developing laser glazing parameters for the SSME MCC liner.

In summary, laser and electron beam processing has been used successfully to restore and improve NARloy-Z microstructure. These processes look promising for enhancing the life of the SSME MCC liner. Periodic laser glazing of the hot wall of the wrought NARloy-Z liner will restore the original microstructure, prevent crack formation, and, hence, could extend the life of the liner indefinitely.

Sponsors: Office of Advanced Concepts and Technology, and Office of Space Flight

Commercial Involvement: Rocketdyne, A Division of Rockwell International

University Involvement: University of Illinois, Pennsylvania State University, and University of Tennessee Space Institute

■

Vacuum Welding and Brazing for Space Applications

Richard M. Poorman/EH25
205-544-1986

Interest in vacuum welding at MSFC is related to development of space welding fabrication and repair capabilities. Expanding these welding and brazing capabilities is essential to meet NASA's space exploration goals. The primary developments described here are oriented to processes and materials.

Initial welding and brazing experiments by MSFC were done on *Skylab* in 1973. These were electron beam (EB) welds on aluminum, stainless steel, and tantalum. The braze joints were on stainless steel tube couplings. All experiments were successful and pointed to the fact that gravity has only a minor effect on welding or brazing such joints. Surface tension drives the metal flow. The presence or absence of a vacuum may dictate the process to be used in space welding.

The current effort has been directed at gas tungsten arc welding (GTAW). This includes welding in both vacuum and one-atmosphere environments. The GTAW process, operated in a one-atmosphere environment, is well established. However, GTAW welding in a vacuum will require development work.

A welding arc requires the presence of ionized material within the arc to carry the welding current. A vacuum welding technique has been developed in which argon gas is supplied through a hollow electrode. Welding torches and electrode designs have been developed for vacuum welding. With these tools, numerous vacuum welds and weld overlays have been made in vacuum chambers at MSFC.

The vacuum welds show some unique characteristics. Fluidity and wetting action of the weld pool are greatly enhanced. Welding pools of Inconel 718™ and Incoloy 903™ are noted for their sluggish flow and lack of wetting. However, weld pools of these alloys in a vacuum are very fluid and blend smoothly at the weld's liquid/solid surface. This enhances the performance of the weld. Pool fluidity and blend of weld nugget are very desirable weld characteristics that reduce the notch effects and stress risers in the weld zone. Cracking is also a common problem in weld overlays of Inconel 903™ on Inconel 718™. Vacuum weld tests have shown less tendency to form cracks than conventional welding processes in atmosphere.

Extensive weld studies of GTAW at various gravity levels have been conducted. Both automated and manual welds were made in low-gravity aboard a KC–135 aircraft. All were made in a gaseous environment of one atmosphere. The gravity level does not produce any unexpected changes. Minor changes in microstructure were observed. Materials welded were aluminum, 304L and 347 stainless steel, and Inconel 718™. No significant mechanical properties changes have been associated with gravity levels (fig. 74).

FIGURE 74.—Manual welding in low gravity on the KC–135 aircraft.

Processes other than GTAW are also being evaluated for space welding applications. They include plasma arc, gas metal arc, and electron beam.

Poorman, R.M. June 1991. Vacuum Vapor Deposition—A Spinoff of Space Welding Development. NASA TM–103542.

Russell, C.K.; Poorman, R.M.; Jones, C.S.; and Nunes, A.C. III. October 21–24, 1991. Considerations of Metal Joining Processes for Space Fabrication, Construction, and Repair. SAMPE 23d International Technical Conference.

United States Patent 5,149,932—Arc/Gas Electrode—September 22, 1992. Inventors: Richard M. Poorman and Jack Weeks.

Sponsors: Office of Advanced Concepts and Technology, and Office of Space Flight

■

Forming of Aluminum-Lithium and High Aspect Ratio Orthogrid Panels

Benny F. Graham/EH25
205-544-4808

Recent advances in aluminum-lithium alloys have made them more attractive for potential use in cryogenic tank applications. As a result, advanced forming and manufacturing methods need to be developed in order to use these alloys effectively.

In the past, methods used to shape lightweight stiffened structural components made from aluminum have been "bump" forming on a hydraulic press brake and high-temperature restraint ("age") forming. With strength-to-weight ratios becoming increasingly more critical, complex lightweight rib-stiffened structural forms of this alloy, such as orthogrid panels, will require advances in forming techniques in order to ensure both structural integrity and cost-effective producibility. Preliminary results from "roll" forming orthogrid test panels at MSFC are promising. More development is needed to quantify results and evaluate factors such as curvature and radial surface conformity and stiffening rib aspect ratios. In order to meet dimensional requirements, age forming also will likely be part of the final processing sequence.

Forming development on orthogrid panels at MSFC began by machining and forming these panels to the external tank (ET) radius (fig. 75) by both "bump" and "roll" forming methods. Aluminum alloy 2219 was used in order to compare both processes with a well-known alloy. Results showed incremental "coining" on the stiffening ribs for the bump-formed panel and continuous "coining" on the stiffening ribs on the roll-formed panel. A third panel with varying rib aspect ratios was roll formed using a protective cover plate on the stiffening ribs and showed almost no "coining" on the ribs. A fourth panel with higher stiffening rib aspect ratios was roll formed without a protective cover sheet and produced rib buckling on the higher rib aspect ratios. These third and fourth panels also established an aspect ratio forming limit. All of the panels revealed some curvature variations. A fifth panel made from aluminum-lithium alloy 2195 was machined at MSFC and roll formed using a protective cover plate on the stiffening ribs. This prototype test panel showed negligible "coining" on the ribs and an improvement in anticlastic curvature (fig. 75). Further investigations seek to establish age-forming characteristics and identify the most effective processes to achieve acceptable panels for cryogenic tankage and other applications.

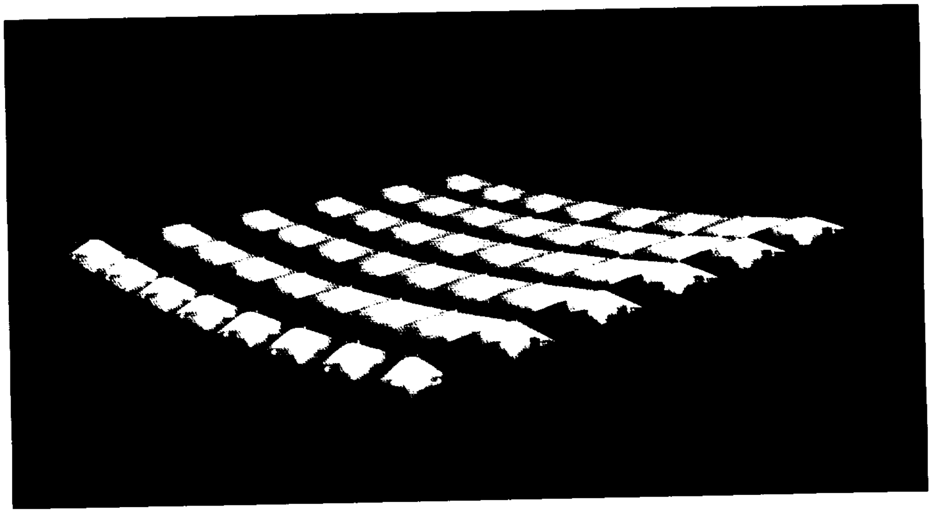

FIGURE 75.—Prototype aluminum-lithium alloy 2195 roll-formed panel.

Sponsors: Office of Space Flight, and Office of Space Systems Development

■

New Weld Controller Nearing Completion, and Welding Pendant Incorporates New Technologies

Kirby G. Lawless/EH25
205-544-2821

Computer-controlled variable polarity plasma arc (VPPA) welding has been used in the production of the space shuttle ET since 1983. This welding system provides control of the critical welding parameters, in addition to providing historical documentation of programmed and actual welding parameters for all welds.

A new welding control computer has been defined as a UNIX-based controller able to integrate various sensor processing and multiple axes of motion. It is projected that the first major integration efforts for this controller will include vision sensor processing, automated wire positioning, and weld model calculations based on sensor feedback. Two versions of the advanced weld controller have recently been accepted through factory delivery testing.

Incorporating some of the newest off-the-shelf technologies, the new weld pendant, developed at MSFC, has been designed to be robust, flexible, and tied to accepted industry standards. The pendant control hardware is made up of local operating network (LON) neuron chips, which are each programmable microprocessors with built-in support for many communication and data acquisitions. Because the chip is programmable, less demand will be placed on the weld controller processor for handling operator interface. In addition, a programmable gas plasma display is being incorporated for flexible use as a text or graphics screen. These displays were originally targeted at the military for jet fighter cockpit displays, and are durable and robust enough for the factory environment. The result is a pendant that can be configured to accommodate emerging process control technologies, without long development periods. Incorporation of the new controller into ET production welding is targeted for fiscal year 1995.

Sponsor: Office of Space Flight

■

Thermal Spray Forming of Refractory Sample Ampoule Cartridges for Single Crystal Growth Space Furnaces

Frank R. Zimmerman/EH25
205-544-4958

Richard M. Poorman/EH25
205-544-1986

A thermal spray process is being used to build up refractory metals and ceramics into a containment cartridge for high-temperature, single-crystal semiconductor growth experiments. This process uses high-energy plasma inside a low-pressure (100–200 torr) inert environment to apply layers of material onto a removable mandrel. A variety of materials are being characterized and evaluated against a demanding set of requirements, including high service temperature (up to 1,600 °C), oxidation resistance, and resistance to liquid metal attack. Techniques to spray form refractory metals (tungsten, molybdenum, niobium, tantalum) and ceramics (alumina, boron nitride) are being developed in the plasma spray cell at MSFC.

NASA's Crystal Growth Furnace (CGF) has flown on the USML–1 Spacelab mission to conduct single-crystal growth work on a variety of semiconductor materials. These semiconductor crystals (gallium arsenide (Ga-As), cadmium zinc telluride (Cd-An-Te), mercurous zinc telluride (Hg-Zn-Te), mercurous cadmium telluride (Hg-Cd-Te)) are grown in quartz ampoules surrounded by insulation, thermocouples, and other instrumentation. The entire experiment is contained within a sample ampoule cartridge (SAC) (fig. 76) that facilitates handling and installation into the furnace. The SAC also functions as a containment system, which is required to protect the flight crew from the highly toxic materials used in these crystal growth experiments. If the ampoule containing the crystal growth material should rupture, these cartridges provide a necessary level of containment. The containment requirement is complicated by the fact that most of these crystal growth compounds are known to aggressively attack most common structural metals at furnace operating temperatures.

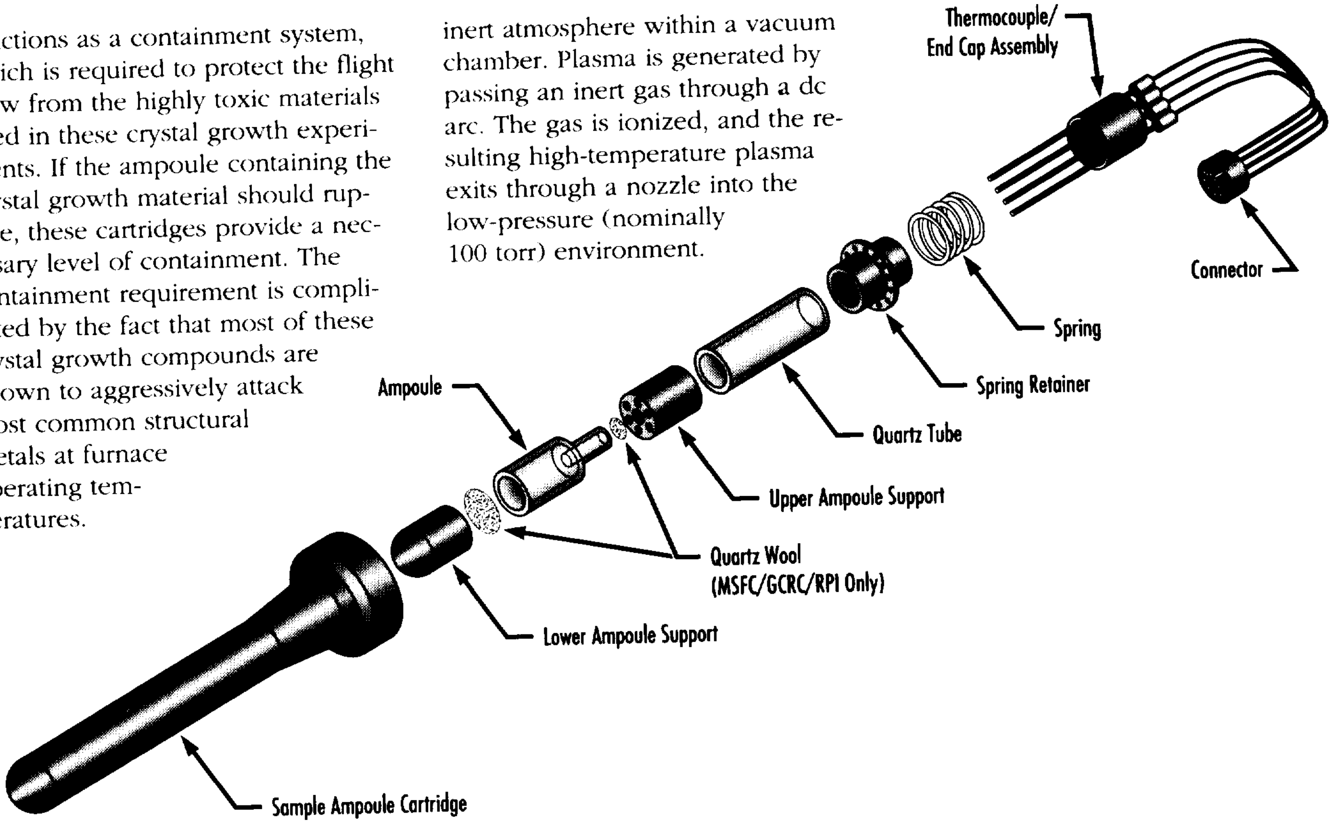

FIGURE 76.—CGF cartridge exploded view.

Currently, these cartridges are made of materials that are attacked at a rate that will not fully penetrate the cartridge within the duration of the experiment. For experiments of longer duration, a more chemically resistant material is required to ensure that no breach in the containment will occur. Regardless of the material used, the current manufacturing sequence is labor intensive, dependent upon product availability, and contains several fabrication steps and joining processes.

To address these issues of chemical inertness and manufacturing, MSFC's Materials and Processes Laboratory has undertaken an effort to form the SAC using the vacuum plasma spray process. VPS is a thermal spray process conducted in a low-pressure, inert atmosphere within a vacuum chamber. Plasma is generated by passing an inert gas through a dc arc. The gas is ionized, and the resulting high-temperature plasma exits through a nozzle into the low-pressure (nominally 100 torr) environment.

The material to be deposited is injected into the plasma plume as a fine powder, heated, and accelerated toward the substrate to be coated. To form containment cartridges, a combination of materials will be deposited in layers on a removable mandrel. During VPS forming, the mandrel functions as a male mold, with the outer contour of the mandrel forming the inside contour of the sprayed deposit.

The service temperature of these cartridges will range from 1,100 to 1,600 °C. Several refractory metals and ceramics are being considered to accommodate these high temperatures. The metals (tungsten (W), niobium (Nb), molybdenum (Mo), and tantalum (Ta)) provide structural strength and toughness for these thin wall structures 0.64 to 0.76 mm. Ceramic (alumina, boron nitride, silica) coatings will be used to protect the metal from high-temperature oxidation and liquid semiconductor attack, if needed.

The fabrication sequence to form these cartridges will incorporate up to three layers of material in a monolithic structure. Each of these layers will be deposited on a removable mandrel using the VPS process (fig. 77). The first layer sprayed will form the inside surface of the cartridge. Its function is to contain the liquid crystal growth material should the ampoule rupture. Ceramics such as alumina and boron nitride are inert to many of the semiconductor materials used in these experiments. While providing excellent chemical

FIGURE 77.—Vacuum plasma spray deposition of refractory material onto removable mandrel.

resistance, ceramics are too brittle to have sufficient handling strength in the thickness range of interest. A second layer of refractory metal will be sprayed to provide bulk structural strength to the thin wall cartridge for room-temperature handling and high-temperature operation. The third layer is an oxidation-resistant material (probably ceramic) to protect the underlying refractory metal from high-temperature oxidation. Several full-sized test articles have been spray formed with multiple layers. Metallographic examination verified the proper thickness of each layer and the microstructure of each material. Leak- and burst-testing were also performed to qualify the VPS process parameters.

The VPS forming process allows the selection of materials based on their desirable properties. Consequently, each sample ampoule cartridge can be designed for a specific application and set of requirements, with few restrictions imposed by the manufacturing process.

Sponsors: Payload Projects Office, MSFC; and Microgravity Science and Applications Division, NASA Headquarters

■

New Direction in Phthalocyanine Pigments

Diep V. Trinh/EH32
205-544-6797

Phthalocyanines have been used as pigments in coatings and related applications for many years. These pigments are some of the most stable organic pigments known. The phthalo blue and green pigments have been shown to be UV stable and thermally stable to over 400 °C. These phthalocyanines are both a semiconductor and photoconductor, exhibiting catalytic activity and photostabilization capability of polymers. Many metal-free and metallic phthalocyanine derivatives have been prepared. The new classes of phthalocyanine pigments could be used as coatings on NASA spacecraft material such as glass to decrease the optical degradation from UV light and as a coating on solar cells to increase lifetime and efficiency.

The synthesis of the single-ringed phthalocyanine based on 1,2 didodecyloxy-4,5 dicyanobenzene (fig. 78) and bisphthalocyanine based upon a naphthalene core, have been completed. These compounds have been purified. The characterization of the single-ring and double-ring compound by UV/visible, Fourier transform infrared, nuclear magnetic resonance (NMR), x-ray diffraction, and mass spectroscopy were completed. The successful synthesis of the key 1,8-naphthalene intermediate compound (fig. 79) led to a new and unique class of phthalocyanine. The first example of its type and the first amine/imine tautomer to be isolated is 1,8-napthalene. The proton and carbon-13 NMR's illustrate that this compound does not tautomerize rapidly on an NMR time scale as has been proposed previously in literature.

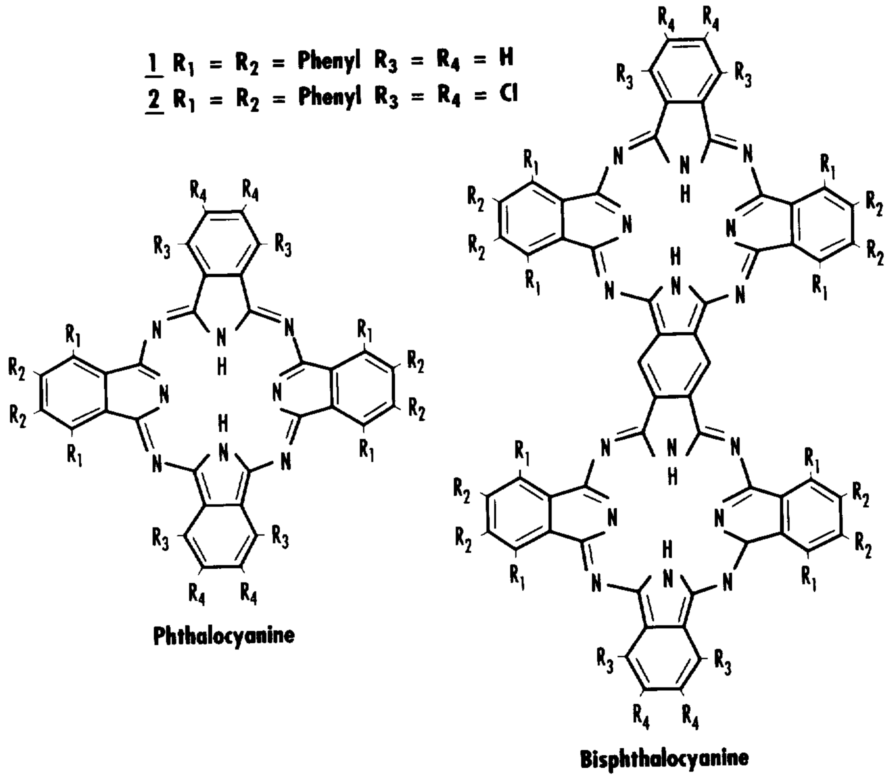

FIGURE 78.—Phthalocyanine and bisphthalocyanine.

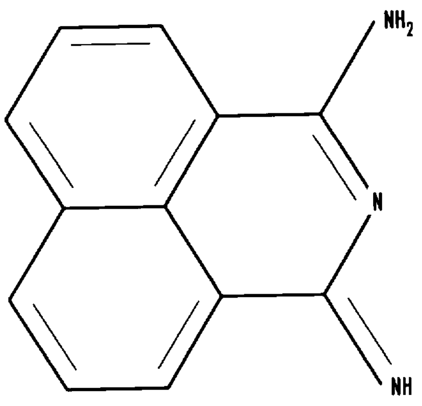

FIGURE 79.—Compound 1,8-naphthalene.

The isolation of a green, stable new compound based upon 1,8-naphthalene is the first of its type to be synthesized. It represents a new series of chemicals that may possess unique catalytic, conductive, or photochemical properties.

The work on these structures represents several breakthroughs and firsts. The integral use of molecular modeling, including quantum mechanics with synthesis, has proven that the combination is the best approach to technological advancement in this area. Barriers, table targets, and interpreted results were found that would not have been possible without molecular modeling or synthetic results.

The evaluation of phthalocyanine for protecting plastic (in this case, polystyrene) from UV damage has been conducted. Samples of polystyrene with no inhibitor, 3-percent phthalo blue (commercial) and 3-percent phthalo green (commercial), respectively, were prepared. These will serve as standards for comparison with the newly synthesized pigments. The sample and reference material have been tested for tensile strength, gloss, color, and change within the IR spectra after exposure to UV light. The polymer undergoes photodegradation by photopolymerization and cross-linking without oxygen. The newly synthesized pigments decreased the photopolymerization process of polystyrene approximately 66 percent.

Sponsor: Marshall Space Flight Center Director's Discretionary Fund

Environmental Replacement Technology: Aqueous Cleaners, Primers, and Adhesives for SRM Cases

M. Louise Semmel/EH33
205-544-3650

The production of ozone depleting substances, such as chlorinated solvents routinely present in cleaners, primers, and adhesives used in the manufacture of solid rocket motors, will become severely limited in 1995. This will have a significant impact unless suitable replacement materials are identified, characterized, and put into use in the near term. Part of the effort of the MSFC Solid Propulsion Integrity Program (SPIP) has been to identify, characterize, and help implement replacement materials for the shuttle redesigned solid rocket motor case/insulation bondline, which utilizes a Kevlar™-filled ethylene propylene diene monomer (EPDM) rubber bonded to steel.

Two candidate replacement cleaners, an aqueous-based primer and an aqueous-based adhesive for Kevlar™-filled EPDM, were chosen for study. Peel and tensile button tests were conducted to determine bond properties of a vulcanized EPDM/steel bond utilizing these aqueous-based materials and to assess the sensitivity of the bondline strength to hydrocarbon contamination relative to current solvent-based materials.

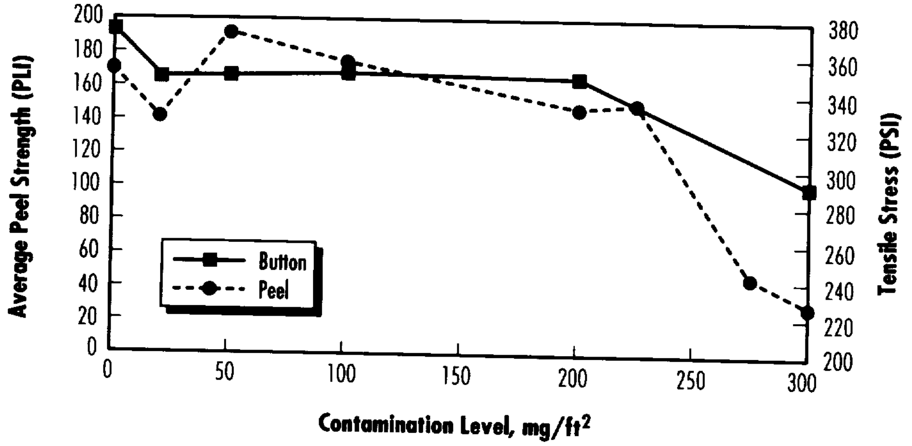

Figure 80.—Bond sensitivity to contamination.

To assess the selected aqueous-based cleaners, test panels coated with hydrocarbon grease were spray-cleaned with Brulin 815™ or Turco 3878 LFNC™ or were exposed to a standard vapor degreaser with 1,1,1 trichloroethane. All panels received surface inspection and were then primed and adhesive-coated with either the solvent-based system or the aqueous-based system. Both the surface analysis and the bond test data show that the aqueous-based cleaners performed equally well in removing hydrocarbon grease from the steel surface.

The bond sensitivity to contamination was assessed by recontaminating clean panels with HD–2 grease, a common hydrocarbon grease, to known levels. While the aqueous-based primer/adhesive system is not as tolerant of hydrocarbon contamination as the solvent-based system, it showed no bondline degradation below 200 mg/ft^2 (fig. 80).

Although many factors will affect the decision of a solvent-based cleaner replacement, the Turco 3878 LFNC™ and Brulin 815™ are both effective on hydrocarbon grease. The new aqueous-based primer/adhesive system recommended for bonding EPDM to steel performs as well as the solvent-based system in producing a bond that is tolerant to grease contamination levels up to 200 mg/ft^2.

Sponsor: Solid Propulsion Integrity Program, Office of Space Systems Development

Commercial Involvement: Science Applications International Corporation

■

Development of an Advanced Solid Propellant Simulant

M. Louise Semmel/EH33
205-544-3650

Typically, inert propellants have been developed for very limited use and are not representative of live propellant overall. Because the solid rocket motor (SRM) manufacturers have the facilities to mix, cast, and test live solid propellants, there seemed to be no real need to invest in the development of an inert propellant that simulated live propellant for a variety of purposes. However, for the past few years, the SPIP has been working to improve the reliability of solid rocket motors through a series of efforts focusing on solid motor design and fabrication. Some members of the SPIP team do not have the facilities to handle live propellants; also, development efforts are, by necessity, more limited and more costly with a live propellant than with an inert material. For these reasons, the SPIP bondlines task team began development of an inert propellant that would satisfy the team's multiple requirements.

The approach taken in the development of the advanced inert propellant was to substitute ammonium sulfate (AS) for the oxidizer; all other ingredients would remain the same at typical concentrations. The AS concentration in the advanced inert propellant is within 10 percent of the ammonium perchlorate (AP) concentration typically used in hydroxy-terminated polybutadiene (HTPB) propellants and provides a much more realistic relationship between the binder and filler.

This approach also allowed the use of bonding agents, such as HX-752™ and Tepanol™, which have typically not been used in inert formulations because they do not react with fillers (NaCl, sand, etc.). These bonding agents greatly increase the propellant strength by bonding the AP and the polymer matrix together and preventing early dewetting of the solid particles. The resulting inert propellant produces the same type of bond reinforcement and mechanical properties behavior as is seen in live propellant.

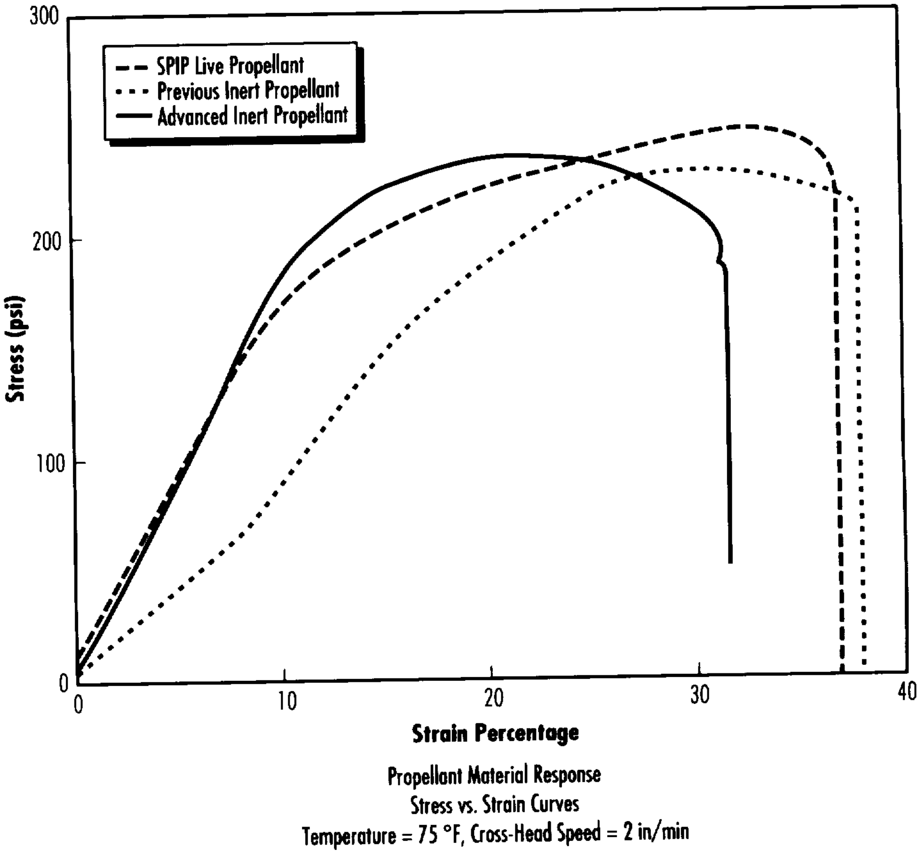

FIGURE 81.—Live-inert propellant comparison.

The high level of AS made initial mixes of the advanced inert propellant difficult to process. It was speculated that the density change of the AS versus AP and the particle shape significantly changed the packing fraction of the solids. This required that the coarse-to-fine AS ratio be modified to optimize the packing fraction and achieve acceptable processing.

With the process modifications, the advanced inert propellant processes well and typically has an end-of-mix viscosity of 5 kP. Joint Army, Navy, NASA, and Air Force (JANNAF)-type C dogbone samples were tested over a temperature range from 0 to 120 °F and compared to the data collected for a previous inert and a live propellant being used in the SPIP program. The 75 °F data are shown in figure 81.

The modulus behavior and the coefficient of thermal expansion indicate that the advanced inert propellant simulates live propellant over a wide temperature range. Based on these data, it was shown that the advanced inert propellant exhibited properties similar to those of live propellant, and that the AS/HX–752™ reaction produced solids bonding similar to that of AP/HX–752™.

Evaluations of the insulation/liner/inert propellant bondlines were performed using a conical bond-in-tension (C–BIT) specimen. The results indicate that the bondlines present in the samples cast with the advanced inert propellant provided bondlines with strength very similar to that of the live propellant. Failure modes were 100-percent cohesive in propellant.

The data indicate that the advanced inert propellant can effectively represent live HTPB propellant with respect to mechanical, rheological, and bondline properties. This propellant simulant is an ideal substitute for testing in laboratories that are not equipped to work with live propellants, while generating useful data directly applicable to current solid propellant programs. It also provides the solid propulsion community with a safer, lower cost alternative to live propellant for shipping, training, and technique development.

Sponsor: Solid Propulsion Integrity Program, Office of Space Systems Development

Commercial Involvement: Science Applications International Corporation

■

Carbon Phenolic Ablative Materials Test Methodology

Cindy G. Upton/EH34
205–544–5755

To improve the reproducibility, reliability, and uniformity of SRM nozzles, a NASA-sponsored SPIP has established an industry advisory committee to improve test methodology for carbon phenolic materials, including constituents, prepreg, and cured materials. The industry advisory committee is a voluntary group that is represented by domestic aerospace material suppliers, fabricators, design organizations, and testing agencies. The committee has met biannually since 1988 to improve the performance of American-manufactured SRM nozzles.

An example of one of the committee's activities is the selection of new and improved acceptance tests for cured phenolic materials. Ablative components for the space shuttle SRM's are manufactured from tape-wrapped phenolic resin preimpregnated carbonized rayon cloth (prepreg). The parts are then cured at elevated temperature and pressure. Tag ends of each ablative component of the nozzle and exit cone of each solid rocket motor are removed for testing. The results of these tag-end tests are one of the criteria governing whether each part will be accepted or rejected for use in flight motors.

The acceptance tests were initially selected to discriminate between parts that had or had not received adequate processing and to detect deviations from the historical data base that might indicate an out-of-experience performance of the part during firing. These tests are: residual volatiles, compressive strength, resin content, and specific gravity. All of these tests were initially selected over 10 yr ago. Since then, much more has been learned about the behavior of carbon phenolic materials in their use environment.

Several types of anomalous behavior have been observed both in flight and in static motor parts that had passed all acceptance criteria. Furthermore, there has not been a trend in acceptance test data that would suggest that there was a difference between anomalous and nominal performing parts. Figures 82 and 83 show the relationship between two acceptance tests presently employed for parts (cowl and outer boot ring, respectively) that performed satisfactorily, and those that exhibited wedgeout—an anomalous and potentially dangerous behavior. Clearly, there is no relationship between the data and the performance.

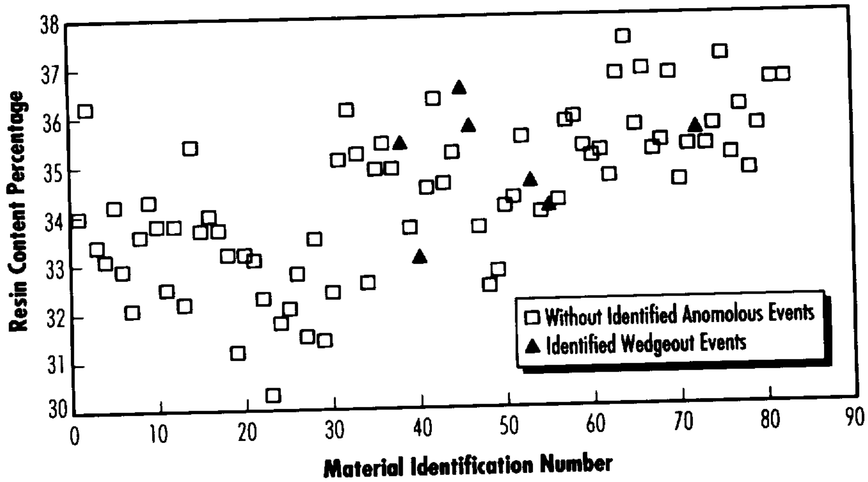

FIGURE 82.—SRM/RSRM cowl resin content (mean values).

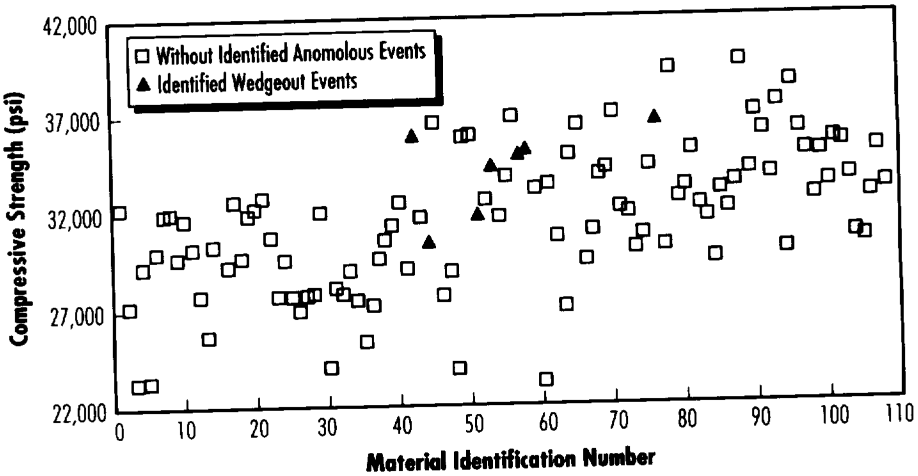

FIGURE 83.—SRM/RSRM outer boot ring compressive strength (mean values).

This, along with similar observations made between acceptance test data from all 4 tests, and 5 of the 10 historically worst performing parts in the redesigned solid rocket motor (RSRM), indicated that presently employed acceptance tests were not completely adequate for prediction of performance.

At this time, there is general agreement in the rocket nozzle community that existing acceptance tests for cured carbon phenolic composites are of limited value. This SPIP industry advisory committee has initiated a process that will result in the recommendation of additional and alternative cured composite acceptance tests for SRM programs.

Sponsor: Office of Space Flight

■

Torch-Produced Diamond Films

Floyd E. Roberts III/EH34
205-544-1967

Continuous films of diamond offer a number of outstanding material properties with practical application in aerospace systems. Diamond boasts the highest hardness and the highest room-temperature thermal conductivity of any known material. Diamond also possesses a small coefficient of thermal expansion and a low coefficient of friction. Diamond films have applications in areas such as impact-resistant surfaces, turbine blade edge coatings, cooling tube surface coatings, and combustion chamber linings.

This year, MSFC has initiated an atomic force microscope (AFM) study of torch-produced diamond crystals. The diamond films grown in the designed experiment are undergoing surface structural analysis on the AFM. This work is being done in parallel with the chemical dynamics simulation run on the two-dimensional kinetics (TDK) program. This program is commonly used in the analysis of exhaust plume gas phase constituents for rocket nozzles. MSFC is using a simulation run of the program for gas phase analysis of the deposition structure. The surface structures noted on the surface of samples will be compared with the preferred surface displayed by the possible constituents identified by the chemical kinetics program. Figure 84 shows a 2- by 2-µ section at a Z magnification of 50 Å of a diamond crystal surface from the AFM. MSFC is working to extend this analysis to the bulk of samples. The program is adding an air table to the microscope

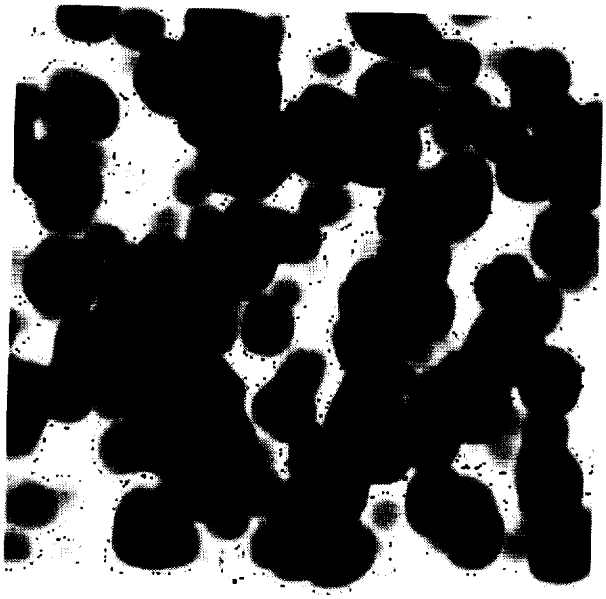

FIGURE 84.—Atomic force microscope image of 100 diamond crystal 2- by 2-μ at Z magnification of 50 Å.

setup to achieve atomic level surface imaging. The ongoing work is focused on a series of designed experiments that will fine-tune some of the developments of the past year. The project work, done in conjunction with Rocketdyne, is continuing and is structured around optimization of related alternate processing avenues. This work will comprise the bulk of the final project phase.

The technology developed in this program has already seen use in other programs at MSFC. The Pyrolaser System Software developed to monitor the changing emissivity and temperature of a growing diamond film, has been accepted into NASA's Computer Software Management and Information Center (COSMIC®) distribution program. The pyrolaser package is an operating system for the pyrolaser pyrometer. Temperature and emissivity measurements may be either collected as if the pyrometer were being operated in the manual mode, or data may be collected on real-time stripcharts and stored in spreadsheet format for posttest analysis. A shell is supplied to allow macros, which are test-specific, to be easily added to the system. (The program is available through COSMIC®.) The space station group is also using software developed in the MSFC diamond lab to test components of the CO_2 environmental air recycling system test loop. The software has been transferred to this group and required only cosmetic change before being used in the space station CO_2 recycling component test setup.

Sponsors: Office of Space Flight, and Marshall Space Flight Center Director's Discretionary Fund

Commercial Involvement: Rocketdyne, A Division of Rockwell International

■

Development of Low Thermal Conductivity PAN-Based Fibers for SRM Nozzle Applications

Raymond G. Clinton/EH34
205-544-2682

In late 1989, the Materials and Processes Laboratory initiated a research program to develop and evaluate low thermal conductivity (LTC) polyacrylonitrile (PAN)-based carbon fibers as potential replacements for rayon-based carbon fibers traditionally used as reinforcement in carbon cloth phenolic ablative nozzle material applications.

A PAN fiber replacement offers supplier stability, multiple domestic sources, and a greater resistance to the characteristic rayon-based carbon phenolic pore pressure-driven failure modes, based upon laboratory and subscale SRM test results to date. The disadvantages of PAN, including high thermal conductivity, increased weight, and lower resistance to delamination are being addressed in the subject program.

Results from Phase I of the LTC PAN fiber development effort have been reported elsewhere (Clinton et al. 1990). A second series of forty-pound charge (FPC) motor tests was defined, based on the results of Phase I tests of both the FPC subscale SRM and the MSFC nozzle insulation test motor (NITM–2) subscale SRM, plus industry input from the SPIP PAN development workshop in which a drop-in rayon replacement was voted as top priority. The background, approach, and materials descriptions for the Phase II series are provided in *Research and Technology 1992* (Clinton 1992).

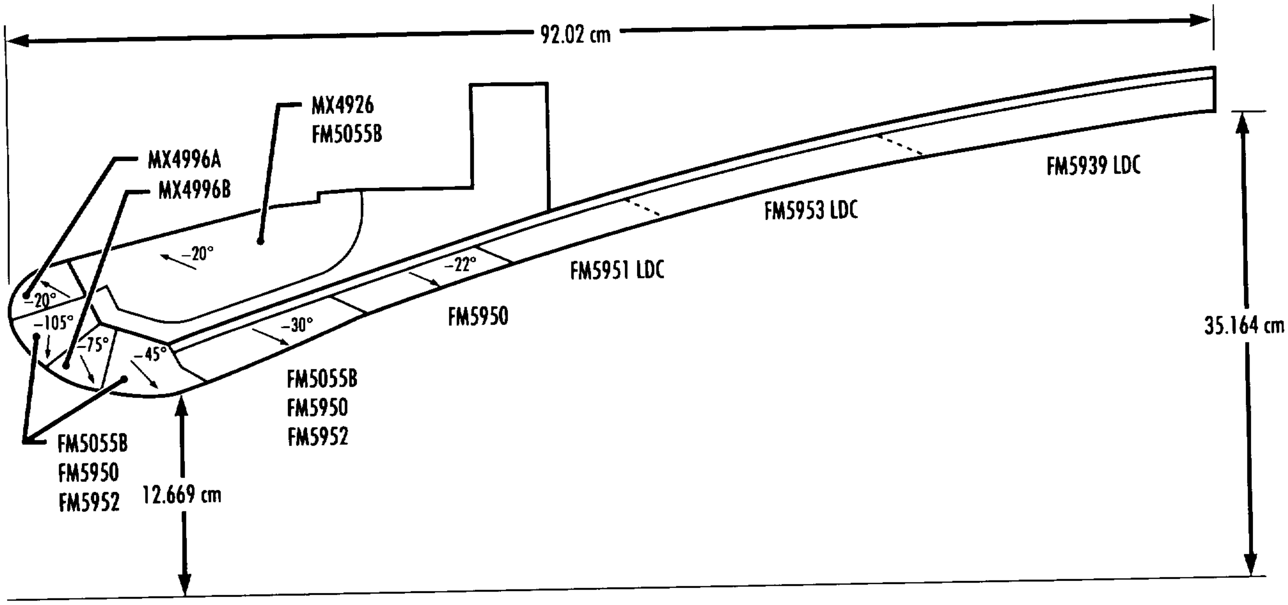

FIGURE 85.—Cross-sectional view of SPIP–3 MNASA nozzle.

The primary objective was to generate char- and erosion-performance data on candidate PAN-based ablative materials in an SRM environment for evaluation and downselection of rayon replacement materials for scale-up to modified-NASA (MNASA) subscale SRM tests and subsequent process optimization. These performance results from the Phase II test series are provided in table 5. Secondary objectives relating to this project included the evaluation of fiber/fabric heat treatment effects, a performance comparison of spun- versus continuous-fiber reinforcements, evaluation of resin system effects, and evaluation of tow size/weave effects. A complete discussion of the analysis of the results in the above categories is beyond the scope of this summary, but has been reported by Emery and Hill (1992).

Rationale for downselection of materials to be tested in the SPIP–3 MNASA motor fell into two categories: performance factors and programmatic issues. Using the thermal performance data from FPC tests, erosion rate and total heat affected depth were component-specific weighted for performance evaluation. The PAN thermal performance was compared by component with an expected range for rayon-based ablatives established with FM5055B as baseline. Post-fire conditions, which were cause for rejection, were excessive cross-ply expansion and wedge-out. Post-fire conditions that served as tie-breakers were pocketing in the 90-degree section and plylift. Programmatic criteria were cost, product availability, processability of prepreg, and PAN precursor source (foreign or domestic). Based upon these factors and criteria, the SPIP team selected the Hercules LFP–2 and Amoco 25 fibers, with B.P. Chemicals/Ironsides 91LD™ phenolic resin to be tested in both standard and low-density formulations. Product codes for these materials are the following: FM5950 (LFP–2/91LD); FM5952 (Amoco 25/91LD); FM5951LDC (LFP–2/91LD); FM5953LDC (Amoco 25/91LD).

Placement of these materials within the SPIP–3 MNASA nozzle, which utilized a replacement MNASA nozzle design, is shown in figure 85. The approach was to enable both standard density LTC PAN candidates to be compared to each other and to a "control" or baseline rayon-based ablative material (FM5055B was selected), in the same environment. This was accomplished by bonding

TABLE 5.—*Erosion rate and heat affected depth results from Phase II FPC motor tests*

Material	45° Erosion Depth		45° Affected Depth		Nose (45°)	Approach	Throat	Forward Exit	Aft Exit
	Rating[1] Percent	Miles/s	Rating[1] Percent	Inch					
MX4933	76	4.8	161	0.82	[illegible]	119	85	127	144
MX4934	87	5.5	153	0.78	113	120	[illegible]	127	140
T300/91LD	89	5.6	129	0.66	105	[illegible]	[illegible]	113	129
MX4904	[illegible]	5.7	143	0.73	111	117	[illegible]	122	132
VCX 14/P39	[illegible]	5.8	137	0.70	[illegible]	115	[illegible]	119	128
Amoco 23/P39	[illegible]	5.8	135	0.69	[illegible]	114	[illegible]	118	126
MX4963	[illegible]	6.0	137	0.70	112	116	[illegible]	120	129
Avcarb B2/91LD	[illegible]	6.2	[illegible]	0.52	[illegible]	[illegible]	[illegible]	[illegible]	[illegible]
FM5796	[illegible]	6.3	122	0.62	109	111	[illegible]	113	118
FM5055B	100	6.3	100	0.51	100	100	[illegible]	100	100
MX4952	[illegible]	6.7	149	0.76	123	128	[illegible]	132	140
LFP-2/91LD	[illegible]	6.8	114	0.58	[illegible]	111	[illegible]	112	113
MX4926	[illegible]	6.8	116	0.59	111	112	[illegible]	113	114
Amoco 25/91LD	[illegible]	6.9	[illegible]	0.55	[illegible]	[illegible]	[illegible]	[illegible]	[illegible]
BASF/(91LD)	113	7.1	[illegible]	0.46	104	[illegible]	111	99	[illegible]
LFP-2/P39	114	7.2	118	0.60	116	116	114	116	117
AS4/P39	117	7.4	[illegible]	0.52	111	[illegible]	116	105	105
BASF-2/SC1008	119	7.5	137	0.70	126	128	121	130	133
Amoco 23/91LD	121	7.6	118	0.60	120	120	121	119	119
MX4972	122	7.7	131	0.67	126	127	123	127	129
LFP-2/SC1008	124	7.8	[illegible]	0.55	118	116	122	114	127
FM5014	125	7.9	112	0.57	120	119	124	117	115
Avcarb B2/SC1008	125	7.9	116	0.59	121	119	124	120	118
Amoco 23/SC1008	129	8.1	[illegible]	0.56	121	120	127	118	114
BASF-1/SC1008	130	8.2	122	0.62	127	126	129	125	124
LFP-1/SC1008	137	8.6	112	0.57	127	125	135	122	117
Avcarb B2S/91LD	137	8.6	114	0.58	128	126	135	123	118
Avcarb GS/91LD	152	9.6	[illegible]	0.51	131	126	147	121	[illegible]
Avcarb G/SC1008	154	9.7	[illegible]	0.55	136	131	149	126	117
Avcarb G/91LD	156	9.8	[illegible]	0.54	136	131	151	126	116

[1] Ratings based on FM5055 control; 100% = FM5055B performance/black boxes indicate ±10% tolerance band about FM5055B performance.

equal sections of the three materials to form a single ring for the forward inlet, throat, and forward exit cone. As it was impractical to reconstruct an aft exit cone by bonding full-length axial sections, low-density materials were incorporated in the form of circumferentially continuous sections (fig. 85). The FM5939LDC material is the rayon-based material selected for use in a replacement nozzle and will serve as the low-density baseline for comparison in as much as this can be accomplished considering the variation in environment within the aft exit cone.

The SPIP–3 MNASA motor was tested at MSFC in September 1993. Performance results from this test will be provided in the 1994 annual report.

Clinton, R.G., Jr.; Pinoli, P.C.; and Canfield, A.R. October 1990. Development of Low Thermal Conductivity PAN-Based Fibers for Solid Rocket Nozzle Application. JANNAF Rocket Nozzle Subcommittee Meeting, Pasadena, CA.

Clinton, R.G., Jr. 1992. Development of Low Thermal Conductivity PAN-Based Fibers for SRM Nozzle Applications. *Research and Technology 1992: Annual Report of the Marshall Space Flight Center*, NASA TM–103559.

Emery, E.A., and Hill, K.H. December 1992. PAN Material Performance Evaluation. JANNAF Rocket Nozzle Subcommittee Meeting, Lockheed Missiles and Space Company, Sunnyvale, CA. CPIA Publication 592.

Sponsor: Office of Space Systems Development

■

Enhanced Aerospace Insulation Systems

Edwin A. Weaver/EH35
205–544–3466

Historically, the external tank program has relied on the commercial urethane market for its foam insulation systems. However, with more than 99 percent of the urethane market dedicated to less demanding applications (construction, furniture, etc.), commercial systems suppliers are typically not motivated to develop materials to specifically meet stringent ET design requirements. This—along with the fact that foam system suppliers tend to change their raw materials or processing methods to address the needs of their bulk market to match competitors and/or comply with changing Environmental Protection Agency (EPA) and Occupational Safety and Health Act (OSHA) regulations—results in uncertain continued availability of ET thermal protection system (TPS) materials. Over the life of the ET program, this uncertainty has been demonstrated by over 10 uncontrollable changes to TPS materials, resulting in costly requalification programs and potential loss of sole-source suppliers.

To address this lack of visibility and control of ET TPS materials, NASA decided, in 1987, to establish a laboratory capable of formulating TPS materials specific to ET requirements. This laboratory is now operational, and the primary focus is the development of TPS systems that are foamed with "environmentally friendly" blowing agents. All currently used ET foam insulations are foamed or "blown," with chlorofluorocarbon (CFC) 11. With the advance of the Rowland-Molina theory in the 1970's, scientists began to believe that CFC's had a detrimental effect on the Earth's stratospheric ozone layer. Subsequently, an international agreement—the Montreal Protocol—was ratified to phase out the use of CFC's. The phaseout of CFC's in the ET program is scheduled for completion in 1996. Hydrofluorocarbon (HCFC) 141b with greatly reduced ozone depletion potential (ODP) will be implemented as the blowing agent for TPS materials, but this second generation blowing agent will also be regulated and eventually banned, currently scheduled for the year 2002.

The focus of the MSFC TPS Materials Research Laboratory is to evaluate and develop a data base for third generation blowing agents with no ODP. In the evaluations, the compatibility and solubility of potential blowing agents with isocyanate and polyol foam components is tested, the effect of the foaming reaction is quantified, and, if necessary, compensated for by change in blowing agent and/or catalyst levels; in the final stages of the evaluation the mechanical and physical properties of foams produced with the third generation blowing agents are tested. To date, several materials have been investigated as third generation blowing agents. These include fluorinated ethers, fluorinated hydrocarbons, perfluorinated pentane, gaseous hydroflourocarbons, and water that reacts with the isocyanate component to produce carbon dioxide gas that acts as a foaming agent.

Sponsor: Office of Space Flight

Commercial Involvement: Martin Marietta Corporation

■

Fiber Placement: New Technology for Automated Composite Manufacturing

John H. Vickers/EH35
205-544-3581

Automated fiber placement is a manufacturing process used for producing complex composite structures. It represents a significant advancement in the state of the art for automated composite manufacturing. Fiber placement capability was established at the MSFC Productivity Enhancement Complex in 1992, in collaboration with the Thiokol Corporation.

Fiber placement was developed as a distinct solution to problems inherent in other automated composite manufacturing systems. This equipment provides unique capabilities to build composite parts in complex 3–D shapes with concave and other asymmetrical configurations.

A project in the Center Director's Discretionary Fund program is the use of fiber placement capabilities to investigate a fully automated composite processing method for fabrication of an optimally designed optical bench. The primary justification for selection of these materials is the ability to maintain precise focal length without thermal control or active focusing systems; coefficients of thermal expansion of zero can be obtained. While structures are successfully fabricated for this application, they are manufactured as one-of-a-kind and primarily by hand. The fiber placement process will supplant the considerable manual element of this fabrication process, thereby increasing repeatability and improving analysis and correlation of resultant data.

Sponsors: Marshall Space Flight Center Director's Discretionary Fund, Payload Projects Office, Space Shuttle Projects Office, and Office of Advanced Concepts and Technology, Technology Utilization Office

Commercial Involvement: Thiokol Corporation

■

Environmentally Friendly Sprayable Ablator for the Solid Rocket Booster

Carl N. Lester/EH35
205-544-4804

Progress has been made in the continuing effort to develop and qualify an environmentally friendly replacement for the ablator currently used for the space shuttle SRB's—Marshall sprayable ablator-2(MSA–2). The MSA–2 ablator performs well, but will be phased out because of impending environmental regulations due to its chlorinated hydrocarbon solvent system. Two environmentally friendly candidate systems to replace MSA–2 include MSA–3—a third-generation, water-based ablator—and United Space Boosters, Inc. (USBI) Sprayable Insulator (USI), which has recently gained prominence after emerging from a USBI independent research and development (IR&D) project as a viable replacement candidate. The goal is to have a qualified replacement for MSA–2 in production by 1996.

MSA–3 predecessors—MSA–1 and MSA–2—were first flown on the SRB's in November 1981 and March 1989, respectively. MSA–2 provided a more flexible resin system that improved flight performance and could be sprayed more thickly without cracking, which expanded the application of the ablator to new areas of the SRB.

MSA–3 consists of water-dispersible resin, surfactant, defoamer, thixotropic agent (Bentonite), and fillers such as ground cork, glass fibers, and glass spheres (fig. 86). It is robotically sprayed on a painted aluminum target located on a rotating turntable. After curing, the ablator is top-coated with a moisture-resistant paint to help maintain its strength and integrity. A high-temperature cure provides the quickest processing timeline, although an ambient cure is being investigated.

Preliminary thermal characterization has been accomplished, as has sensitivity testing to study the production tolerances for mixing, applying, curing, and repairing the material on an actual flight structure. After completion of the development phase, the material will be ready for qualification and transition into the production spray cells, where final validation will occur.

USI is another innovative ablative concept that employs an epoxy resin with ground cork and glass fillers in a solventless, convergent spray process. Features of this process include on-demand availability and ambient-cure capability. This technology has been transferred to the MSFC Productivity Enhancement Complex Sprayable Ablator Research Cell, where it is being developed along with MSA–3 as a candidate replacement for MSA–2. Prior to implementation, a decision will be made as to which of the materials (MSA–3 or USI) is transitioned to production, based on such factors as cost-effectiveness and robustness of process.

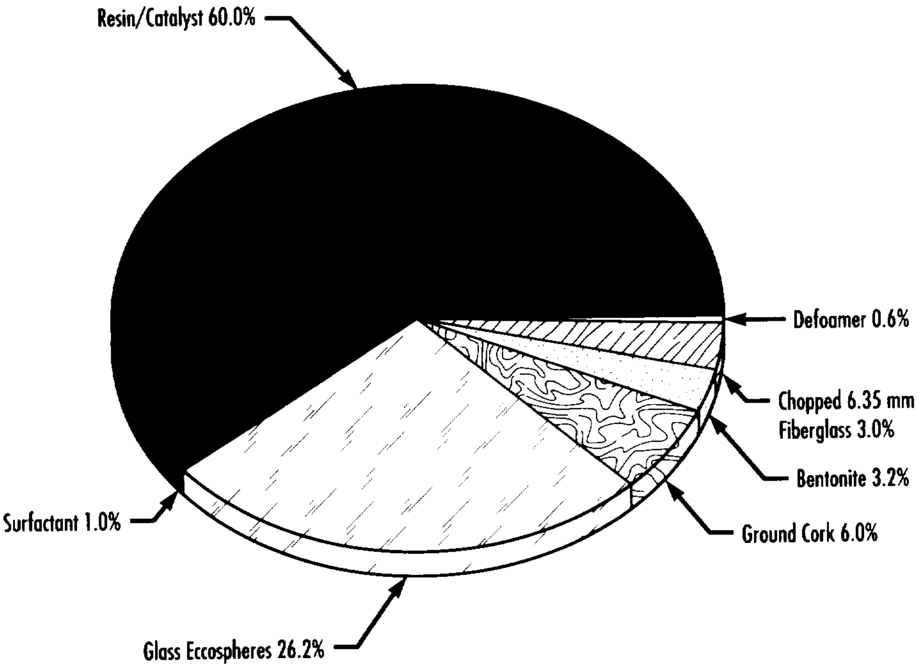

Figure 86.—Typical composition of cured MSA–3 in weight percentage.

The Air Force was sufficiently impressed with these materials to participate in a joint effort to qualify an MSA–2 replacement material for the Titan IV rocket payload fairings. Currently under way, this effort will attempt to utilize as much of the SRB development and qualification work as possible.

In developing MSA–3 and USI, the Productivity Enhancement Complex at MSFC is fulfilling its mission as one of the nation's preeminent research centers. Considering the impending environmental regulations, the implementation of a compliant replacement for MSA–2 is of critical importance to the space shuttle program. These environmentally friendly materials will be available for other launch programs as well, as evidenced by the Air Force Titan IV application, and will reaffirm NASA's commitment to the ecology of our planet.

Sponsors: Solid Rocket Booster Project Office, and Office of Space Flight

■

Mission Operations

Virtual Reality Applications Program

Joseph P. Hale II/EO23
205-544-2193

The objectives of MSFC's Virtual Reality (VR) Applications Program are to develop, validate, and utilize VR as a human factors design and operations analysis tool, and to assess and evaluate VR as a tool in other applications (e.g., training, operations development, mission support, teleoperations planning, etc.). The long-term goals of this technology program are to enable specialized human factors analyses earlier in the hardware and operations development process, and to develop more effective training and mission support systems.

The capability to perform specialized human factors analyses earlier in the hardware and operations development process is required to better refine and validate requirements during the requirements definition phase. This leads to a more efficient design process where perturbations caused by late-occurring requirements changes are minimized. A validated set of VR analytical tools must be developed to enable a more efficient process for the design and development of space systems and operations. Similarly, training and mission support systems must exploit state-of-the-art computer-based technologies to maximize training effectiveness and enhance mission support.

The approach of the VR Applications Program is to develop and validate appropriate virtual environments and associated object kinematic and behavioral attributes for specific classes of applications. These application-specific environments and associated simulations will be validated, where possible, through empirical comparisons with existing, accepted tools and methodologies. These validated VR analytical tools will then be available for use in the design and development of space systems and operations, and in training and missions support systems.

The MSFC VR systems reside in the Computer Applications and Virtual Environments (CAVE) Laboratory in building 4610. System components consist of VPL Research, Inc., Eyephones (Model 1 and LX), DataGloves™, and software (Swivel 3–D, Body Electric, and ISAAC); Polhemus Isotrak and Fastrak spatial tracking systems; two Macintosh IIfx computers; and two Silicon Graphics, Inc., graphics computers (4–D/310VGX and 4–D/320VGXB). Figure 87 shows a user donning the specialized VR gear. Figure 88 shows a fully outfitted VR user. Two single-person configurations are possible. These are the Eyephone Model 1 (stereo views) with one DataGlove™ and the Eyephone LX (stereo views) with one or two DataGloves™ (i.e., both right and left hands, simultaneously). A two-person configuration is possible and consists of both Eyephones (monocular views) with one DataGlove™ associated with the Eyephone Model 1, and up to two DataGloves™ associated with the Eyephone LX. In the two-person configuration, both participants are in the same Virtual World (VW) simultaneously and each is able to see and interact with the computer-generated image of the other.

FIGURE 87.—User donning the specialized VR gear.

Several VR development activities are under way at MSFC and with JSC. EXOS, Inc., is under a Phase II SBIR contract to develop a Sensing and Force-Reflecting Exoskeleton (SAFiRE) for the hand. This device will provide force-reflecting feedback to the fingers and hand as the user touches and grasps virtual objects. Tomorrowtools, under a Phase I SBIR contract, is developing a 30-sensor spatial tracking system. Using ultrasonics to determine the location of each of the sensors and infrared to transmit data to the base units, this system will provide an untethered method to track up to 30 body points and other objects simultaneously. This will be particularly useful in dynamic work envelope analyses. In-house work is under way to broadcast the video signals to the Eyephones, removing the video cable to the user that is now required. Integration of the two latter activities' products will free the user from existing input/output (I/O) cables.

MSFC is cooperating with JSC in their efforts to develop a long distance two-person capability using their in-house-developed VR system. Long distance capability would allow two people to simultaneously see and

FIGURE 88.—Fully outfitted VR user.

interact with the computer-generated image of the other in the same VW, with one person at JSC and the other at MSFC. Basic capabilities have already been demonstrated. As VR technology evolves, this virtual link between, and eventually among, the NASA centers may provide both major foreseeable and unanticipated benefits.

Human factors issues and considerations in hardware and operations development present a large class of potential VR applications. VR technologies and techniques currently provide some limited macroergonomic and microergonomic analytical tools for consideration of operational, viewing, and reach envelope requirements, in both one-gravity (Earth) and microgravity (space) environments. Macroergonomics analyses for the topological design of work areas can consider what one is able to see from a variety of eye reference points. These analyses can also include operationally driven components such as translation paths among the various worksites. Combined with scaleable user anthropometry attributes, microergonomics analyses for the spatial layout of workstations can consider what one is able to see from a variety of eye reference points and what one is able to touch from a variety of shoulder and seat reference points and/or foot restraint locations, using a range of virtual anthropometric sizes.

Many analyses that use Fomecor™ mockups (full-scale "cardboard" mockups), the KC–135 (plane that provides approximately 30 s of weightlessness during each cycle of parabolic flight), or the Neutral Buoyancy Simulator (underwater facility for simulating weightlessness), are candidates for VR. It is not that VR would completely replace these other technologies and techniques, but rather will add another tool to the analytical tool kit.

In some instances, VR might be considered for use in an analysis that would have otherwise not been undertaken. Resources (time, people, materials, etc.) required for a "standard" simulation or mockup analysis may be greater than the expected return. In this case, VR, due to its relatively low utilization costs, would surpass the cost/benefit ratio threshold and enable an analysis that would have otherwise been foregone. Similarly, VR can enhance and enable more effective utilization of standard simulation and mockup analyses. By preceding these analyses with preliminary VR analyses, both the hardware and operations can be refined so that the return from the standard analyses is increased. This is accomplished by either reducing the magnitude or number of standard analyses and improving the fidelity of those analyses with a more mature design. Because the VW's are nothing more than computer files, design changes can be done more quickly and, subsequently, more candidate configurations can be analyzed than are currently possible with existing standard human factor tools (e.g., Fomecor™ mockups).

Several VR applications validation studies are under way at MSFC. The selected applications are those that can utilize existing VR technology and capabilities. Before VR can be used with confidence in a particular application, it must be validated for that class of application. For that reason, a specific validation study has been proposed for classes of applications. The validation approach is to compare the results from the VR analyses or applications with a specific past or present analysis, design, and/or actual flight experience.

Early applications utilizing the VR system currently in place at MSFC fall primarily into viewing analyses (including visualization of spatial layouts) and reach-envelope analyses. A VR validation study is under way to develop, assess, and validate VR as a macroergonomics analysis tool for the topological design of work areas. Two existing control rooms and their corresponding virtual counterparts will be used to collect subjects' qualitative and quantitative judgments on a variety of measures. The MSFC Spacelab Payload Operations Control Center (POCC) and the Data Control Room (DCR) have been selected, based on their apparent separation on a variety of continua (e.g., large/small, spacious/cramped, aesthetically well/poorly designed, etc.). A corresponding Virtual POCC (VPOCC) and Virtual DCR (VDCR) have been developed that contain the basic elements (e.g., tables, monitors, printers, communication panels, etc.) and spatial layout of their real-world counterparts.

Forty-eight subjects (24 males and 24 females) will participate in a within-subjects design study. Overall independent variables (IV's) include World (Real/Virtual) and Design (Good/Poor), with Gender as a blocking variable. "Nested" within the Design variable, the subjects will either estimate the range to items (Range Estimation) or choose (forced) which of a pair of objects is closer (Relative Range). The Range Estimation IV's are item (Object/Surface) and the item's range from the observer (Near/Far). The Relative Range IV's are Field of View (FOV) (Same/Different; i.e., whether or not the subject can see both objects simultaneously in the same FOV), and the objects' range from the observer (Close/Away). Adjective-pair Likert scales, range estimation, relative range forced choice, and elapsed time to answer range questions will be collected as dependent variables (DV's).

The MSFC VR capability has already been utilized in a couple of activities. Both primarily involved immersive visualization of architectural spaces. One supported the recent move of the CAVE Laboratory into its new quarters. Two different laboratory layouts were developed and modeled in Swivel 3–D. Several of the lab staff then "entered" the virtual laboratories and evaluated the configurations as both users and visitors. Layouts were modified near real time and reevaluated. Based upon these evaluations, one modified layout was chosen and implemented.

In a second activity, support was provided to the 30-percent design review of the space station Payload Control Area (PCA). The PCA will be the payload operations control room, analogous to the Spacelab POCC. Several configurations of the console floor plan layout, large video screens, and public viewing area were modeled in Swivel 3–D. Designers, management, and the Public Affairs Office (PAO) utilized the system to immersively visualize the options. PAO evaluated the view from the public viewing area at various raised floor heights and performed a preliminary camera viewing analysis, "flying" to various possible camera locations to inspect the composition of the possible camera FOV's. The ability to pan and tilt and change "lenses" (i.e., narrow to wide-angle FOV's) in real time was especially useful.

Sponsors: Space Station Projects Office; Marshall Space Flight Center Director's Discretionary Fund; Office of Advanced Concepts and Technology, Small Business Innovation Research Program; Summer Faculty Fellowship Program; Historically Black Colleges and Universities; Engineering Technology Base (Institutional)

Commercial Involvement: EXOS, Inc., and Tomorrowtools

■

A Dynamic Human-Computer Interface Prototyping Environment With Embedded Evaluation Capability

Joseph P. Hale II/EO23
205-544-2193

Many of the activities and functions at MSFC and, for that matter, throughout the agency, take place via a computer interface. Commercially available applications (e.g., word processors and spreadsheets) come with their own human-computer interfaces (HCI's). However, since much of the work at MSFC is done with specialized and prototype systems and processes, unique HCI's must be developed and tailored to specific applications or environments. Figure 89 shows a user at a workstation with an HCI. In many cases, the HCI's must be developed either prior to the completion of a fully functioning target system or process, or isolated from the existing system/process. In both instances, the HCI requirements must be developed without the benefit of interacting with the target system or process. At MSFC, these include the HCI's at the test stands and laboratories, on the various Huntsville Operations Support Center (HOSC) and POCC consoles, on the Spacelab Payload and General Support Computer (PGSC), and, soon, on the space station Payload Operations Integration Center (POIC) consoles and onboard payload workstations.


FIGURE 89.—User of a workstation with an HCI.

With the advent of today's advanced graphical user interfaces (e.g., icons, pop-up menus, virtual control and display panels, etc.), the user's ability to monitor and control systems and processes can be greatly enhanced through proper attention to the "look-and-feel" of the HCI. Thus, the process to develop the HCI requirements and specifications has gained increased importance. Ideally, this process should employ an iterative "test-and-revise" methodology where the design requirements are developed and extensively refined before design implementation, minimizing costly (e.g., money and time) rework of requirements or design that can occur during later phases. Software development problems usually occur during requirements specification, and it is here that elaborate feedback loops are needed, though seldom provided (Budde et al. 1991).

Prototyping is a methodology based on an evolutionary perspective of HCI development, producing early operative versions (prototypes) of the HCI's for subsequent evaluation and revision (Budde et al. 1991). There are two basic approaches to prototyping: static and dynamic (Harken 1991). Static prototyping provides HCI's that can be demonstrated, but not used directly. This approach does not include the functionality of the target process or system. Dynamic prototyping results in a testable simulation that provides a fully functional HCI that can be "test flown" by the end user (Rouff and Horowitz 1991) and enables interactive usability studies and acceptance testing. The goal of prototyping, usability studies, acceptance testing, and so forth, is to force as much of the evolutionary development as possible into the preimplementation phase, when modifications are relatively easy and inexpensive (Schneiderman 1992).

The objectives of this project are to develop and assess a dynamic HCI prototyping environment with embedded evaluation capability. There are four key tools or capabilities necessary for the dynamic prototyping process. First, a tool is required to build and spatially arrange the various buttons, widgets, icons, menus, etc., that populate a computer display. A second tool is required to develop a simulation of the target system or process. Although the resultant simulation does not require the fidelity of a training simulator, it must simulate enough of the relevant functional attributes of the target system or process to enable usability studies and acceptance testing. Third is the capability to provide a dynamic, interactive interface between the prototype HCI, developed with the first tool, and the simulation of the target system or process, developed with the second tool. Finally, a capability to evaluate the prototype HCI is required. This includes not only verifying compliance to applicable styles, guidelines, and standards, but also measuring the adequacy of the HCI to enable the user to control and maintain situational awareness of the target system or process. Adequacy measures would consider such performance attributes as the type and frequency of errors, time and context of calls to "Help," subtask completion times, response times, and so forth. Figure 90 shows two users of the dynamic HCI prototyping system.

FIGURE 90.—Two users of the dynamic HCI prototyping system.

If done correctly, the evaluation would not only determine that an HCI is deficient, but point to specific aspects or attributes of the HCI that need improvement. A basic set of evaluation metrics will be developed and embedded in the integrated prototyping environment. Thus, relevant evaluation data, based on the user's interaction with the simulator through the HCI, will be automatically collected and logged during the evaluation session. The system will then produce evaluation reports following the session. This task is probably the most theoretically challenging aspect of this project.

The capability to efficiently engage in systematic dynamic prototyping will significantly enhance the quality and functionality of the resultant HCI's, while minimizing development costs. The improved HCI's will help reduce training costs and improve productivity in the operational environment (e.g., minimize errors, increase situational awareness, enhance science return, etc.). This project will develop and assess an integrated dynamic prototyping environment. The currently existing capability that comes closest to this is the interactive link between the CAVE Laboratory and the Payload Crew Training Complex (PCTC), where prototype displays can be developed and linked to existing Spacelab training simulators. The utility of employing this capability as a dynamic prototyping environment is diminished because the training simulators are delivered too late to be effectively used in prototyping the displays. Further, the development of the simulators requires the knowledge and skills of a computer programmer.

This project employs a graphical modeling approach to rapidly construct accurate models of complex systems and processes. It also includes an embedded evaluation capability. This will facilitate the data collection, reduction, and analyses during usability testing and guide the HCI modifications for the next cycle. The development of an integrated dynamic prototyping environment with embedded evaluation capability will be a significant advance in the field of HCI prototyping. By the end of this project, a capable prototype integrated system is anticipated. Further development and refinement will continue as the system is tested and applied.

Budde, R.; Kautz, K.; Kuhlenkamp, K.; and Züllinghoven, H. 1991. Prototyping: An Approach to Evolutionary System Development. New York: Springer-Verlag.

Harken, S. 1991. Requirements Specification and the Role of Prototyping in Current Practice. J. Karat (ed.). *Taking Software Design Seriously: Practical Techniques for Human-Computer Interaction Design.* Pp. 339–54. Boston: Academic Press.

Rouff, C., and Horowitz, E. 1991. A System for Specifying and Rapidly Prototyping User Interfaces. J. Karat (ed.). *Taking Software Design Seriously: Practical Techniques for Human-Computer Interaction Design.* Pp. 257–71. Boston: Academic Press.

Schneiderman, B. 1992. *Designing the User Interface.* Reading, MA: Addison-Wesley.

Sponsors: Marshall Space Flight Center Director's Discretionary Fund, Summer Faculty Fellowship Program, and Engineering Technology Base (Institutional)

■

Alternative Illumination Technologies for the Human Habitation of Space

Benita C. Hayes/EO23
205-544-9276

Phase I of this SBIR reviewed new light source and control technologies for applicability to interior spacecraft illumination. It investigated the innovative use of these sources which have not previously been used in task and ambient illumination systems in spacecraft occupied by humans.

In Phase II, various sources and controls were evaluated and tested, and recommendations made. The importance of this Phase II SBIR is that it addresses methods of minimizing lighting power consumption, mass, and volume, while being attentive to human factors requirements necessary to accomplish a range of visual tasks. As NASA plans longer duration missions and approaches a permanent human presence in space, spacecraft lighting systems will play a significant role in determining the habitability of human-occupied structures. Phase II is directed toward three main tasks, including prototype source development, prototype luminaire development, and sunlight delivery system development.

The first of these tasks—prototype source development—will identify and develop new light sources for use in spacecraft and habitats, or direct the use of existing sources to space applications not yet tried, and will be sensitive to size, weight, power, performance, and so forth. The sources currently being investigated include subminiature fluorescent tubes (7-mm diameter), twin-tube fluorescents, T-8 fluorescent tubes, and light-emitting diodes (LED's). Evaluation methodology includes performance assessment via computer modeling, procuring samples, photometrically testing and comparing the samples with computer models, and sending source samples to subcontractors for building luminaire prototypes.

The second task—prototype luminaire development—will produce prototype indirect and direct/indirect ambient luminaires, using one or more sources identified above. These luminaires will be high fidelity. Additionally, task luminaires will be manufactured using the 7-mm or twin-tube fluorescent subcompacts. A medium-fidelity-prototype task luminaire will be constructed using the LED source. Evaluation methodology includes computer modeling of luminaires, manufacture of the prototypes, and photometric measurements. The results of this will help identify potential uses in various enclosures and implications on a crew.

The third task is the development of a sunlight delivery system. Currently, two options are being pursued to include a proximate system and a remote system. The proximate system, which is directly accessible to sunlight via windows or skylights, will be accomplished by selecting a site in the solar system, generating a computer model—considering thermal, construction, deployment, and human-factor implications—modifying for electric lights, and building the device. The remote system, which accesses sunlight via fiber optics or another "piping" system, will be accomplished much the same way.

Sunlight delivery systems will be pursued since this source has an "infinite" performance life, widespread availability, and excellent color characteristics. These systems will consider sunlight only, as well as in combination with electric lighting, to produce integrated electric/sunlight delivery systems suitable for use in areas of intermittent sunlight availability.

This Phase II SBIR has far-reaching commercial applications. It has been estimated that approximately one-third of the energy consumed in the U.S. is used in building operations. In most commercial buildings, this use profile is dominated by the interior electric lighting system. The American Consulting Engineering Council estimates that a typical American now spends more than 90 percent of their total life in an artificial environment, yet most efforts to reduce energy costs of electric lighting systems have sacrificed human-factor criteria for cost savings. Development and utilization of new energy-efficient light sources that also satisfy human-factor requirements, such as color rendition and glare control, have the potential to alter current design and construction approaches to building illumination on Earth.

Sponsor: Office of Advanced Concepts and Technology, Small Business Innovation Research Program

■

Propulsion and Fluid Management

Advanced Main Combustion Chamber Development

Henry J. Dennis/EP33
205-544-4670

Kathy S. Tygielski/EP33
205-544-4055

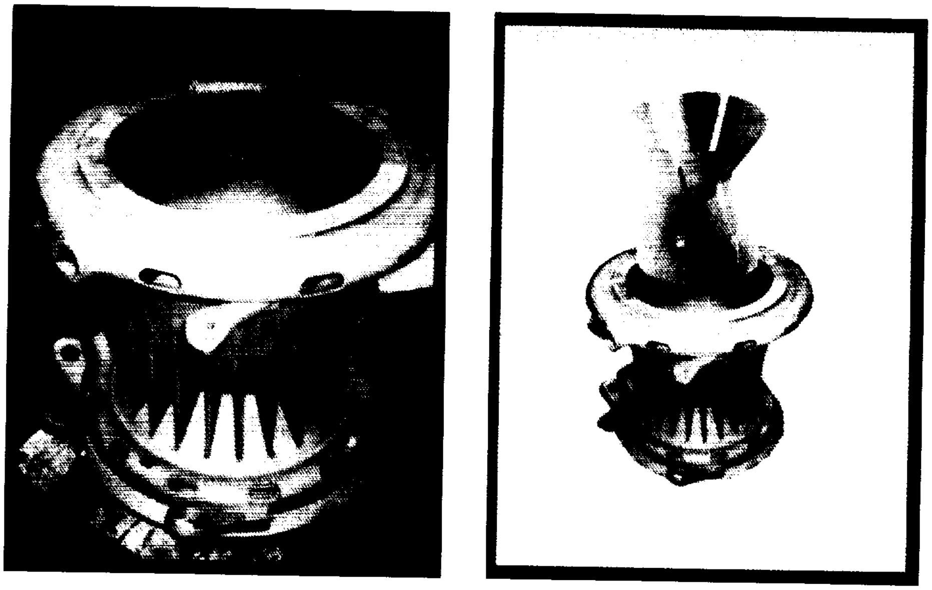

FIGURE 91.—Main combustion chamber fabricated by bonding formed platelet liner in cast structural jacket.

The Advanced Main Combustion Chamber (AMCC) Program was initiated to enhance the state of the art in design and fabrication of hydrogen-cooled combustion chambers for large liquid rocket engines. Using the current SSME combustion chamber as a baseline, the AMCC design goals are to increase hardware reliability, reduce critical failure modes, and reduce fabrication time, at a cost less than the current SSME combustion chamber. The AMCC incorporates a formed platelet coolant liner and a single-piece cast structural jacket, both assemblies greatly reducing the number of fabrication processes and part variation (fig. 91).

The formed platelet liner technology is being developed with Aerojet of Sacramento, CA. This forming process allows the liner to be made with complex internal flow passages that incorporate enhanced cooling features to increase the life and durability of the part. The investment cast structure is being developed with Precision Castparts Corporation of Portland, OR. The cast structure is a single-piece part incorporating both coolant manifolds, actuator lugs, instrumentation bosses, and the controller mounting bracket. It is made of a hydrogen-environment-resistant, nickel-based superalloy. Casting the structure as a single piece eliminates most of the welds normally required for this type of component.

These newer methods of fabrication have an added benefit of being able to produce a combustion chamber in 12 mo, compared to 40 to 60 mo for the conventional SSME combustion chamber. The cost for a production AMCC is projected to be less than $1 million, compared to over $3 million for the conventional SSME combustion chamber.

An aggressive schedule is in progress to demonstrate the lower fabrication time and costs by building the first AMCC prototype for full-scale testing in 1994.

Sponsors: Office of Advanced Concepts and Technology, Earth-to-Orbit Propulsion; Space Transportation Main Engine Project Office; and Space Shuttle Main Engine Project Office

Commercial Involvement: Aerojet, and Precision Castparts Corporation

■

Formed Platelet Combustor Liner Construction Feasibility

Fred W. Braam/EP11
205-544-7055

Rocket engine combustion chambers must be cooled to withstand the severe high-temperature environment that they contain. The construction of the cooling liners for the combustors is a time-consuming, intricate, and costly operation. Current practice employs the use of copper alloy liners with hundreds of axial grooves machined in the outer surface. These slots are closed out by an electroforming process, usually using nickel, to form the cooling passages. Machining tolerance capability currently limits the minimum hot gas wall thickness to approximately 0.635 mm, where wall temperatures are in the 732 °C range.

An alternate cooling liner fabrication approach is being investigated that has the potential for reducing liner fabrication time by an initial estimate of 50 percent and of improving the liner's cooling capability by lowering wall temperatures to 177 °C. This alternate approach is based on the use of diffusion-bonded stacks of copper alloy material sheets, called platelets, which are 0.20-mm thick or greater, and have been photoetched to form cooling passages. The platelet stacks are formed into contoured sections by a stamping process and are joined to form the desired combustion chamber liner.

A nozzle assembly containing a zirconium copper-formed platelet cooling liner and sized to fit a 178-kN thrust combustor has been hot tested to chamber pressures of 17.6 MPa (2,550 lb/in^2 absolute) to verify the design and fabrication approach. The platelet panels have been successfully scaled up to SSME size (figs. 92 and 93). These are being prepared for installation into an investment cast structure for assembly of a test article to demonstrate design integrity and manufacturing cost reductions of 80 percent over the current design.

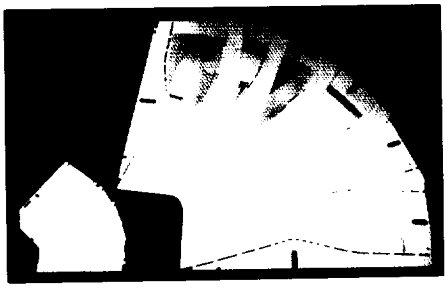

FIGURE 92.—Comparison of subscale platelets to large-scale platelets.

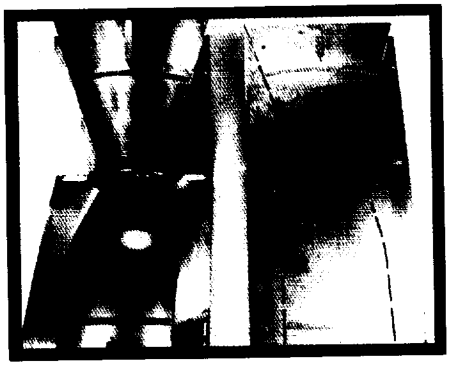

FIGURE 93.—Large-scale platelet cooling panels.

Sponsors: Office of Advanced Concepts and Technololgy, and Space Shuttle Main Engine Project Office

■

Liquid Rocket Injector Characterization

John J. Hutt/EP13
205-544-7125

Charles F. Schafer/EP13
205-544-1642

A program for studying the atomization and mixing characteristics of liquid propellant injector elements in cold flow has been established at MSFC. The program consists of experiments in three test facilities. The first facility is designed to flow water, air, or a combination of both through a single injector element. The flow exits the element to open air and is referred to as the Ambient Back Pressure (ABP) Facility. The second facility consists of a windowed high-pressure chamber designed to flow water and/or air through a single injector element at elevated back pressure and is referred to as the High Back Pressure (HBP) Facility. The third facility is based on acrylic models of liquid swirl injector elements that allow visualization of the internal flow field, and is referred to as the Acrylic Model (AM) Facility.

The ABP facility is currently operational and can be used for the following applications:

- To characterize liquid/liquid injector elements
- To measure discharge coefficients and flow uniformity for gas/liquid injector elements
- To develop diagnostic tools to be used in the HBP facility
- To study the self-atomizing characteristics liquid swirl elements.

The facility consists primarily of two separate air regulators, a water accumulator, an injector head, and a spray tank (fig. 94). The air regulators are dome loaders operated by hand valves. The air lines are 1.27-cm stainless steel tubing. The water accumulator is simply a set of 5.08-cm diameter stainless steel tubes with a thickness of 0.1661 cm. The accumulator is pressurized with air from two separate 17,225-kPa K-bottles. Maximum water pressure is 3,445 kPa, regulated. For safety, a relief valve set to 3,790 kPa has been placed in each output line.

A variety of diagnostic tools is available for use at the ABP facility:

- Planar laser-induced fluorescence (PLIF) imaging of sprays, using a 5–W argon laser and rhodamine 6–G dye
- Excimer-pumped dye laser for instantaneous (15 ns) imaging of high-speed sprays
- Phase Doppler particle analyzer (PDPA) for measuring droplet size distributions in sprays
- Intensified and unintensified video cameras for spray imaging
- High-speed film cameras (up to 5,000 frames/s) for spray imaging
- Stroboscopic imaging of sprays, using a 1-μs duration strobe.

The APB facility is currently being used to study optical methods for measuring liquid phase mass distribution by making PLIF measurements of swirl coaxial element flow fields. It was also recently used to study the effect of imposing a strong acoustic field on a thin liquid sheet.

The HBP facility is presently under development. It will be used to compare the atomization and mixing

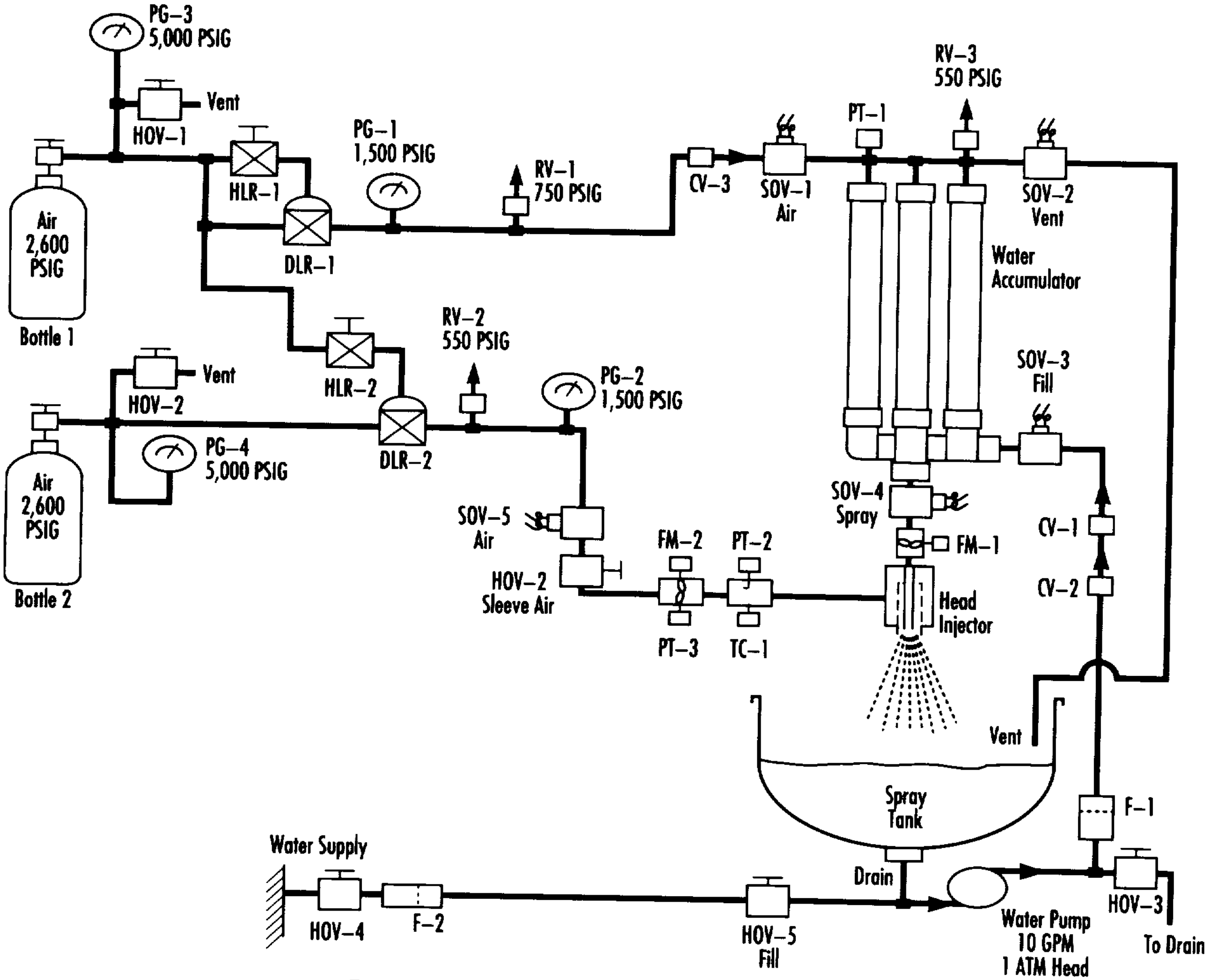

FIGURE 94.—Ambient Back Pressure Facility.

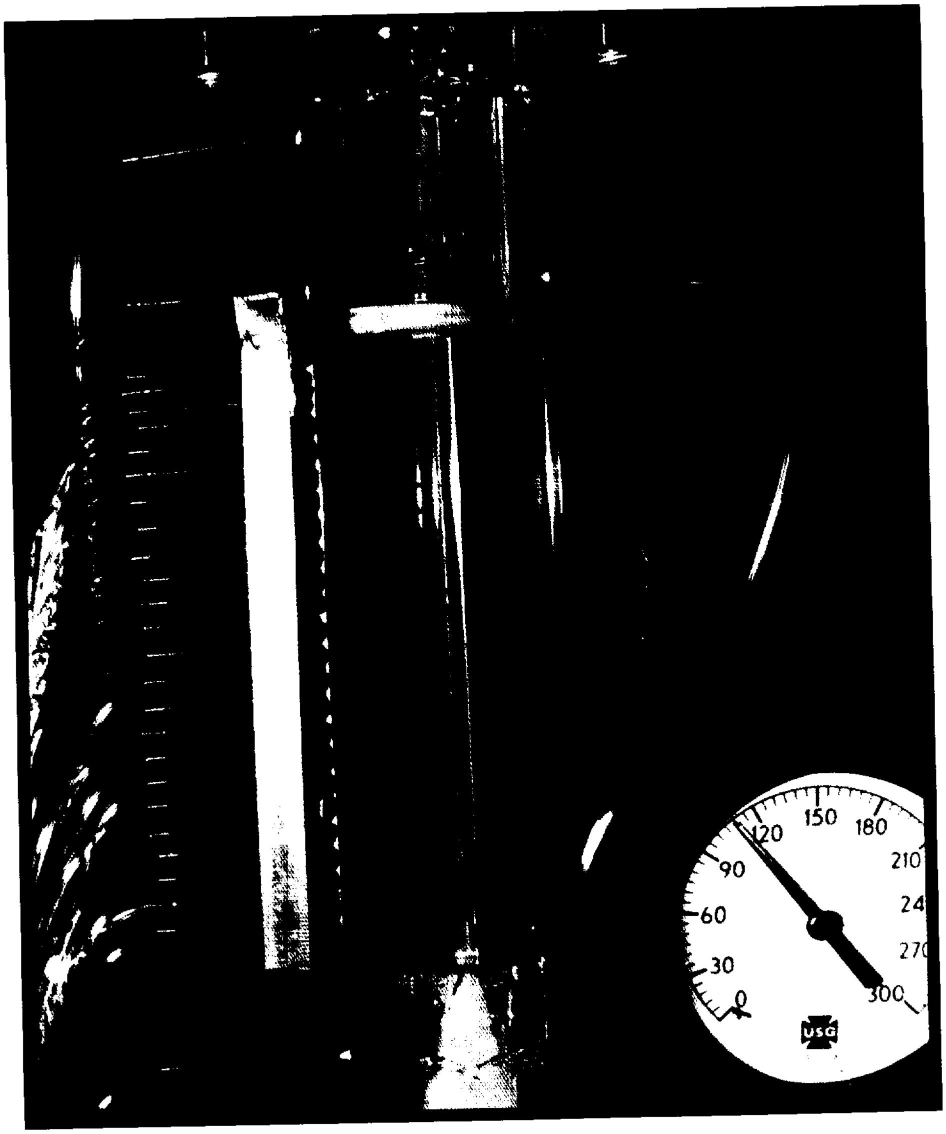

FIGURE 95.—Air core in a lox post.

characteristics of shear and swirl coaxial injector elements at conditions similar to the operating conditions of the SSME preburners. The objective of this study is to determine if swirl elements could reduce the temperature striations that exist at the turbine inlet.

The AM facility is a Center Director's Discretionary Fund project specifically designed to study some unique aspects of swirl coaxial injector elements. Typically, swirl coaxial elements involve swirling liquid oxygen (lox) in a central tube. The radial pressure gradient caused by the angular momentum causes low-density chamber gases to flow into the lox post. Understanding this flow behavior is necessary to make predictions of injector performance, as well as to evaluate the element for injection-coupled combustion instability. The AM facility uses water as a lox simulant to study these effects in cold flow, using clear models. Figure 95 is a photograph of the air core formed when testing a typical swirl lox post. The air core extends the entire length of the post. It becomes established at very low flow rates and, after becoming established, its shape remains independent of the flow rate.

Hutt, J.; Robertson, T.; McDaniels, D.; Eskridge, R.; and Fisher, M. June 1993. Rocket Injector Single Element Characterization at the Marshall Space Flight Center. AIAA 93–2337.

Sponsor: Marshall Space Flight Center Director's Discretionary Fund

■

Systematic Data Reconciliation in Rocket Engine Performance Predictions

John P. Butas/EP14
205-544-7057

Technology-derived power balance models are used to support the conceptual design of rocket engines and, ultimately, to correlate flight engine test data with previous analytical predictions. The primary purpose of engine modeling technology is to provide an accurate assessment of the characteristics of the individual engine components prior to and after experimental and flight engines are developed. These individual components are modeled using theoretical relationships which describe turbopump characteristics, pressure losses, and heat transfer effects. These theoretical relationships are adjusted to correlate them to test data. Thus, the quality and validity of the performance predictions generated rely primarily on the process in which test data are integrated with the theoretical relationships. If this process is flawed, the hardware characteristics and performance predictions generated from these models will be inaccurate, unreliable, and could steer the rocket engine development program on a costly and undesirable course. Hence, technology-derived power balance models are constantly being upgraded and modified to meet the growing demand for new engine cycle analysis and development.

The assumption that measured test data are absolutely accurate is implicitly incorporated within the computational strategy of most power balance models. However, the so-called "pristine data" assumption is flawed due to measurement system uncertainty. More importantly, individual engine component models are based on one-dimensional, uniform flow-averaged conditions. Local measurements in a complicated flow network such as a rocket engine are incapable of characterizing flow-averaged conditions with absolute accuracy. Computational predictions are forced to agree with the data at instrumented locations, often at the expense of satisfying the balance of the fundamental physical relationships (mass conservation, momentum, and energy conservation). If this occurs, the computed hardware characteristics no longer reflect the physical hardware. Consequently, use of the pristine data assumption can lead to inaccurate hardware characterization and engine system performance prediction. Such conditions could result in poor design decisions and inadvertently contribute to a catastrophic failure.

An effort is currently ongoing to develop performance analysis models that eliminate the shortcomings inherent in the assumption mentioned above. A new computational model, termed the Performance Reconciliation Model (PRM), is a general rocket engine performance analysis tool with test data integration capability. The solution procedure incorporates a system-level nonlinear mathematical optimization strategy. The optimization strategy requires uncertainty estimates for both test measurements and the balance of the fundamental physical relationships. The optimization procedure selects values for engine variables (flow rates, pressures, temperatures, speeds, etc.) within defined measurement uncertainty limits, while satisfying the fundamental physical relationships within defined balance uncertainty limits. The objective of the optimization procedure is to minimize adjustments in the engine variables from the initial test values. The PRM generates a set of performance predictions by reconciling test data with fundamental physical relationships within specified uncertainty limits. In effect, PRM predictions provide the most plausible set of engine performance conditions, recognizing the inherent uncertainties in both fundamental physical relations and test measurements.

The PRM has been under development for approximately 2 yr and is currently being used to evaluate SSME performance. The PRM was used to analyze performance characteristics of the SSME oxidizer preburner (OPB) and high-pressure oxidizer turbopump (HPOTP). Test data obtained from the Technology Test-Bed (TTB) facility at MSFC were used to support the analysis. A cursory uncertainty analysis was performed to determine uncertainty estimates for both the engine measurements, as well as the fundamental physical relationships. The uncertainty analysis indicated the uncertainty band for pressures, temperatures, and flow rates to be approximately 6 percent of the measured value, the mass balance uncertainty band to be approximately 0.50 percent of the total high-pressure oxidizer turbine (HPOT) flow, and the energy balance uncertainty band to be approximately 4 percent of the total HPOT horsepower.

A volume analysis was performed on the SSME HPOTP subsystem, using TTB test sequence 25 (TTB–25) test data. The purpose of the volume analysis was to check the test data with respect to mass and energy conservations. The results of the analysis indicated a small mass imbalance, but had a larger than

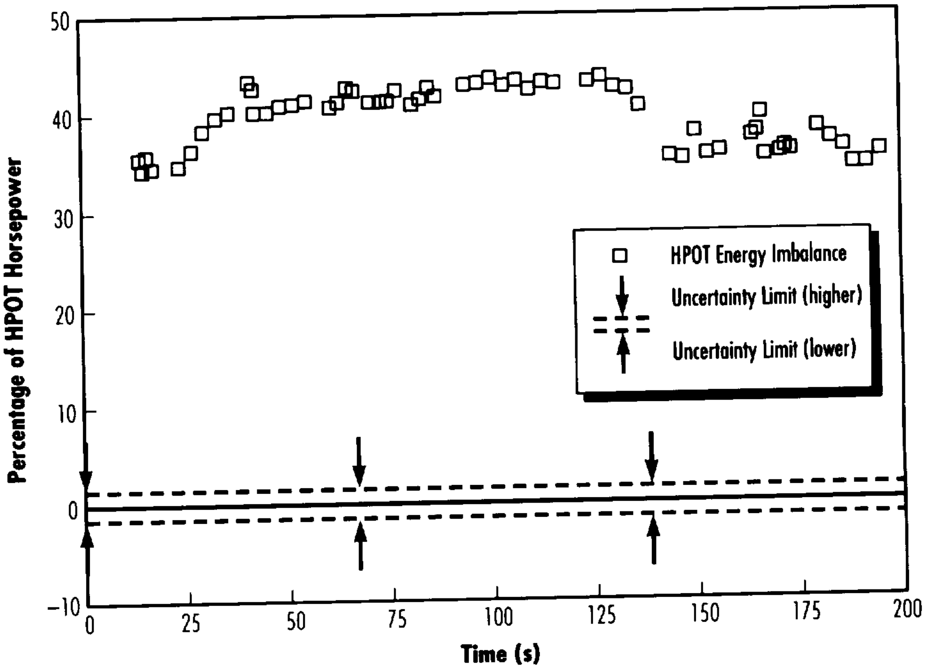

FIGURE 96.—SSME energy imbalance from TTB–25 test data.

acceptable energy imbalance. Figure 96 presents HPOTP energy imbalances with respect to the percentage of total HPOT horsepower. Based on flow, pressure, and temperature data, the HPOTP energy imbalance indicates that the turbine is delivering approximately 45 percent more horsepower than required by the pump.

A PRM subsystem analysis was performed on the SSME OPB and HPOTP. The PRM was used to reconcile the TTB–25 test data with fundamental physical relations by adjusting the HPOT flow and temperature to reduce the energy imbalance to within the acceptable uncertainty band. Figure 97 presents comparisons of PRM analysis predictions and TTB–25 test data. The PRM reduced the OPB total flow by approximately 0.7 lb/s. This indicates the PRM predictions agree well with the measured OPB venturi flow. In addition, the PRM reduced the temperature drop across the HPOT by approximately 110 °R. The HPOT temperature drop computed from TTB–25 test data is approximately 240 °R. This HPOT temperature drop is computed from individual temperature measurements at both the inlet and exit of the turbine. The PRM reduced the inlet HPOT temperature by 60 °R, which is approximately 4 percent of the measurement inlet temperature. The PRM increased the discharge HPOT temperature by 50 °R, which is approximately 4 percent of the measurement discharge temperature. The PRM predicted 110 °R reduction in the HPOT temperature drop corresponds to approximately a 45-percent reduction in total HPOT horsepower. This was the primary adjustment required to reduce the large energy imbalance observed within the measured TTB–25 test data. Using one-dimensional flow assumptions, the computed HPOT efficiency from the test data is unrealistic. The computed HPOT efficiency derived from the PRM predictions more closely matches theoretical performance.

The new PRM provides a systematic procedure for incorporating uncertain test data in computational procedures without corrupting physical balances beyond established and defined limits. This systematic procedure is a more accurate method for generating hardware characteristics. Results from the SSME subsystem analysis indicate the adjustments required to reconcile the TTB–25 HPOT flow rate and temperature measurements with the physical relations within the PRM. The predicted 4 percent adjustment in the HPOT temperature measurements could represent a delta between

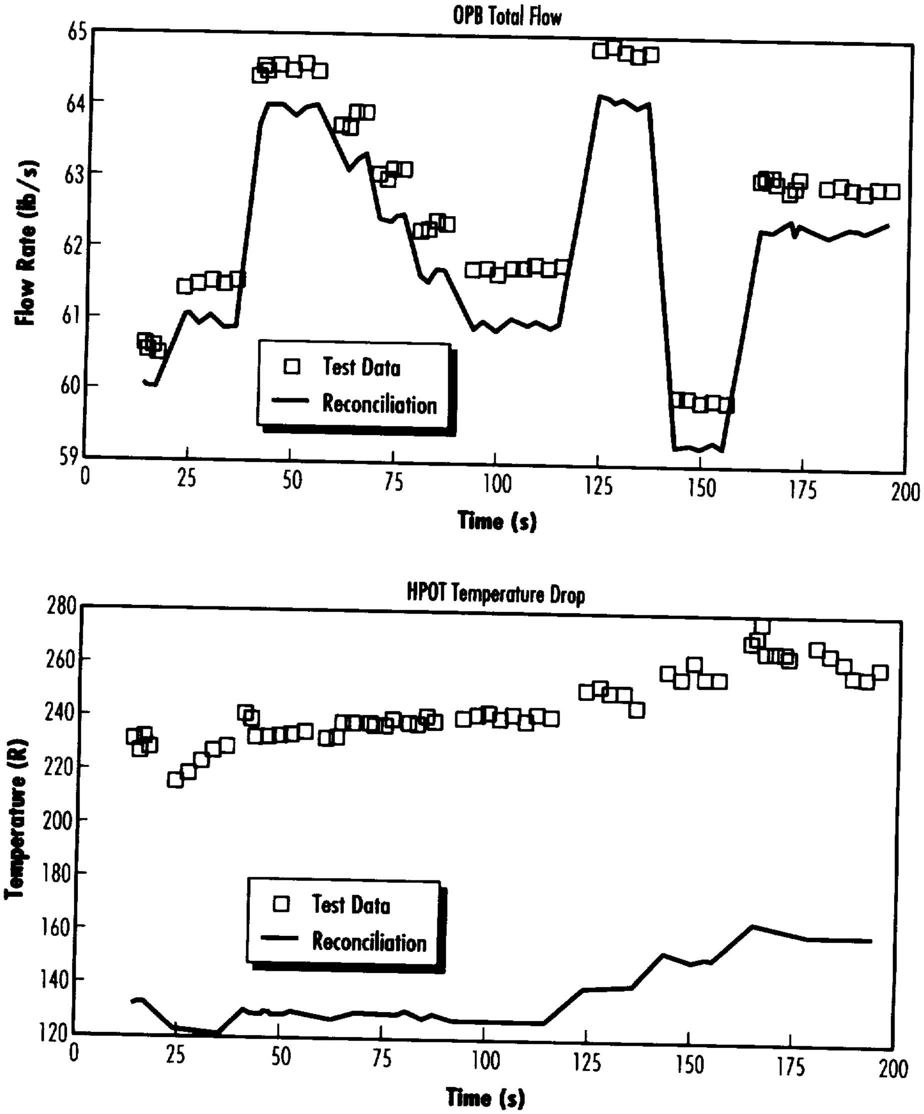

FIGURE 97.—Performance reconciliation model comparisons to TTB–25.

averaged and localized effects or could represent coolant effects that are not currently modeled within the theoretical relationships. Future analyses will be performed with better uncertainty estimates and more detailed engine component models in order to further improve engine hardware characterization. These types of measurement and hardware effects have been observed in the past and make it difficult to determine accurate hardware performance characteristics. The PRM provides a scheme to begin quantifying these effects and improve the engineer's understanding of the true flow environment within a rocket engine. This will ultimately improve performance predictions and enable the PRM to be a more useful rocket engine design tool.

Sponsor: Space Shuttle Main Engine Project Office, Office of Space Flight

University Involvement: Christian Brothers University

■

High Mixture Ratio Core Gas Generator Analysis

Huu P. Trinh/EP13
205-544-2260

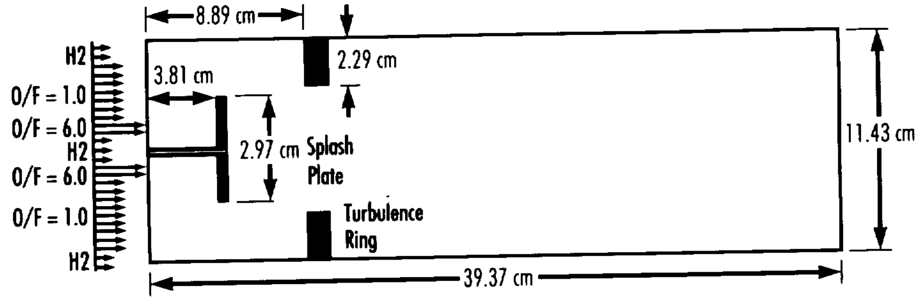

FIGURE 98.—Schematic diagram of a gas generator with a turbulence ring and a splash plate.

An advanced gas generator (AGG) with a high mixture ratio core, which has a potential use for future liquid rocket engines, has been studied. Because of the high mixture ratio core, such a generator can be ignited reliably during the start up. The generator, therefore, can be used for the no-bleed start operation, which has a low initial mixture ratio. Furthermore, the hot temperature streaks, which are also experienced on current gas generators, can be controlled and diffused by means of introducing enhancement mixing devices on the hot core gas generator. However, adding the mixing devices would increase the engine pressure loss and the engine complexity.

A number of combustion gas mixing techniques and mixing enhancement devices, including hot gas core impingement, auxiliary diluent injector, turbulence ring, splash plate body, etc., are numerically simulated using the existing reactive flow equation solver (REFLEQS). The criteria for the selection of mixing techniques are based on the minimization of the radial temperature variation at the generator exit and the generator pressure loss.

The AGG geometry and operating conditions are the same as the baseline of the gas generator of the space transportation main engine (STME) (Mercer and Hernandez 1993). The study included the effects of various mixing enhancement device geometries and various local mixture ratios (fig. 98), while the overall mixture ratio of the generator is maintained. The results indicate that placing a turbulence ring and a splash plate with reasonable height and at a proper location in the generator chamber could maximize the gas mixing. Therefore, this causes a nearly uniform gas temperature at the gas generator exit. When a gas generator is designed such that a turbulence ring with the height of 2.29 cm and a splash plate with the height of 2.97 cm are positioned at 8.89 and 3.81 cm, respectively, downstream of the injector face (case 1), the gas temperature variation is less than 6.0 °R at the exit (fig. 99), with the pressure drop across the generator at $7{,}924 \times 10^3$ Pa. However, if the turbulence ring height is reduced to 1.14 cm, and the ring and the splash plate are positioned at 6.35 and 8.89 cm from the injector face (case 2), the temperature variation at the exit increases up to 60.8 °R, while the pressure could drop by as much as $2{,}412 \times 10^3$ Pa.

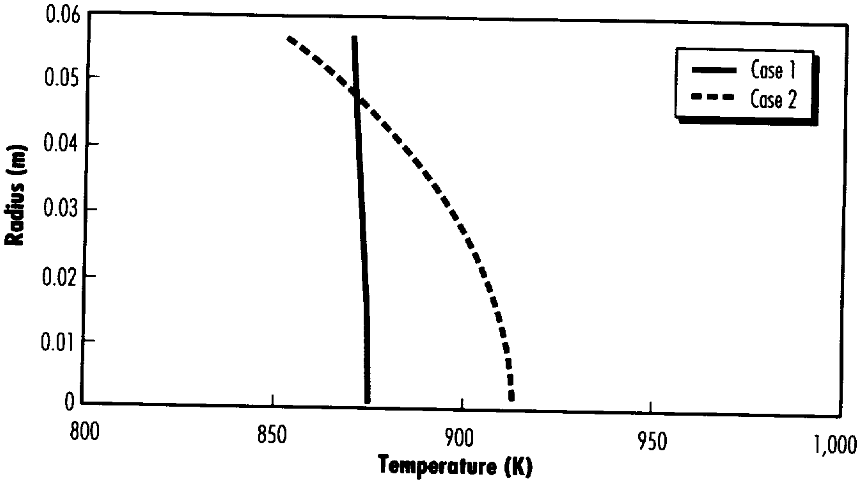

FIGURE 99.—Temperature distribution at exit.

The results also show that the maximum gas temperature at the generator exit decreases as the mixture ratio at the hot core region moves from a stoichiometric ratio to the fuel-rich condition. In addition, the maximum gas temperature at the exit is lowered by increasing the impingement angle of the hot core injector elements. Detailed results of this study are found in "Design Study of an Advanced Gas Generator," by Kim and Trinh, 1993.

Kim, S., and Trinh, H.P. June 28–30, 1993. Design Study of an Advanced Gas Generator. AIAA 93–2158, AIAA/SAE, ASME/ASEE 29th Joint Propulsion Conference and Exhibit.

Mercer, S.D., and Hernandez, R. February 1993. ALS Rocket Engine Combustion Devices GGA Test Plan. Contract NAS8–38080 GGA Test Plan DR–30.

Sponsor: Office of Space Systems Development

Commercial Involvement: Sverdrup Technology, Inc.

■

Combustion Stability Testing and Analysis

Marvin Rocker/EP13
205–544–4140

The in-house developed code Frequency Response of Admittance of Coaxial Injector Elements (FRACIE) is being used in conjunction with the Aerojet-developed high-frequency intrinsic (HIFI) code to predict combustion instabilities in Rocketdyne's 2–D Stability Research Combustor (2–DSRC). The FRACIE and HIFI codes are combined to form a control-theory-oriented model (fig. 100). The FRACIE-HIFI model has been reasonably accurate in matching frequencies of chamber and injector pressure oscillations exhibited in data obtained from a test firing of the 2–DSRC. The FRACIE code models the acoustics of a shear-coaxial injector given the total number of elements, element geometry, steady propellant flow conditions, and propellant thermodynamic properties. Plans to upgrade the FRACIE code to model swirl-coaxial injectors are in progress. The HIFI code models the acoustics of a combustion chamber given geometry, steady chamber conditions, and combustion products gas properties. Additionally, the HIFI code models acoustic cavities given the total number of cavities, cavity geometry, and local gas properties. The Colorado State University-developed RDORC code will be added to form a collection of codes that model chamber acoustics. The RDORC code has a more realistic combustion model and is currently being used by Rocketdyne in its combustion stability analysis.

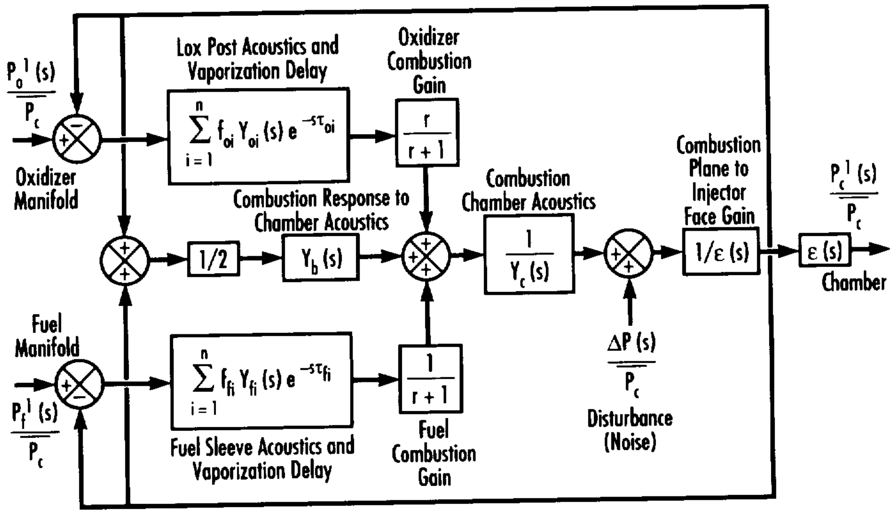

FIGURE 100.—Block diagram of chamber-injector-combustion interaction.

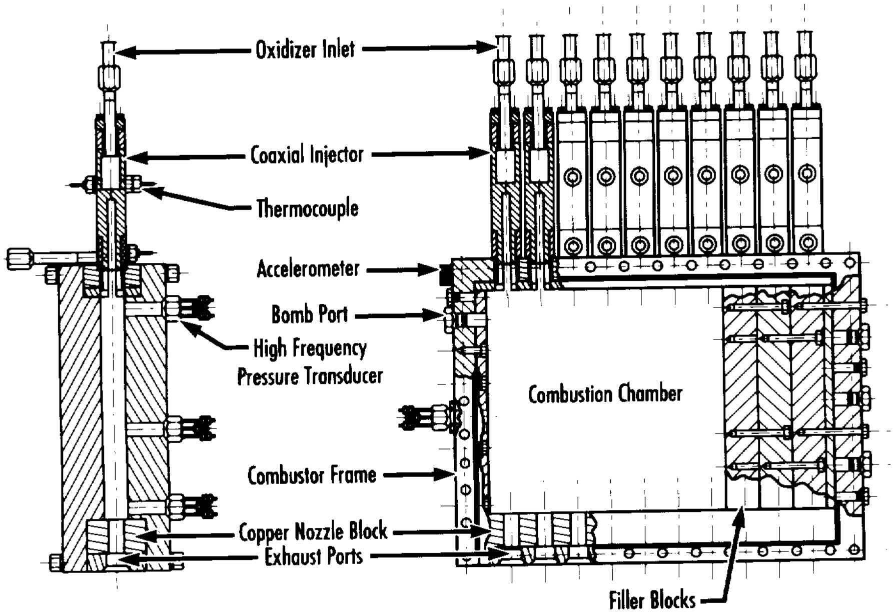

FIGURE 101.—Two-dimensional Stability Research Combustor assembly.

The 2-D Stability Research Combustor Test Program is a joint effort between MSFC and Rocketdyne to investigate the mechanisms responsible for combustion instabilities in liquid propellant rocket engines. The Rocketdyne-developed engine is a liquid oxygen/gaseous hydrogen (lox/GH_2) subscale combustor supplied by up to 10 shear-coaxial injector elements (fig. 101). The combustion chamber is rectangular and is 26.67 cm in length, 2.54 cm in thickness, and is adjustable up to 38.1 cm in width. The combustion chamber is also serviced at the aft end by 10 small nozzle-orifices about 1.778 cm in diameter. Testing, currently in progress at the MSFC test stand 115, investigates the effects of mixture ratio, chamber width, and chamber pressure on combustion stability. Tests at 1.38 MPA/in^2 chamber pressure exhibited some pressure oscillations both in the chamber and injector. Tests at chamber pressures of 2.07 MPA/in^2 and 2.76 MPA/in^2 are in progress. High-frequency test data were reduced to obtain dominant acoustic frequencies in the chamber and injector. Test data will be used to verify current empirical correlations, formulate new correlations, and verify the accuracy of the HIFI and FRACIE codes used to predict combustion instabilities.

Sponsor: Office of Aeronautics and Space Technology, Office of Advanced Concepts and Technology

University Involvement: Colorado State University

Commercial Involvement: Rockwell International; and Aerojet

■

Low-Cost Turbomachinery Technology

Matthew W. Marsh/EP32
205-544-1773

Turbomachinery used in liquid rocket engines typically are composed of complex geometries made from high-strength-to-weight superalloys. These high-performance machines usually have long design and fabrication cycle times, typically 3 to 5 yr. These factors increase development time and result in high costs for rocket engine turbomachinery.

A simple, low-cost turbopump is being designed in-house to demonstrate the ability to reduce the overall cost and life cycle of turbomachinery. The objective of this turbopump design, named "Simplex," is to minimize design complexity and to reduce design and fabrication time (fig. 102). The Simplex turbopump will be powered by gaseous nitrogen or gaseous oxygen. This eliminates the need for an interpropellant seal required to separate the fuel-rich turbine gases from liquid oxygen, which results in a simplified design. Materials used in the turbine flow paths will utilize existing characterized metals at 171 °C that are compatible with a warm-oxygen environment. The goal for this design is to complete the design and fabrication within 12 mo. The cost for the first unit fabrication and assembly is predicted to be less than $125,000.

This in-house design will demonstrate the capability of a low-cost liquid oxygen turbopump via an improved design and fabrication process. The prototype will also demonstrate a liquid oxygen pump driven by an oxidizer-rich turbine gas. Another benefit of this task is the increased ability to estimate the cost of rocket engine turbomachinery. The turbopump design would be suitable for integration with the hybrid motor, providing a warm-oxygen source from a tap-off location.

Sponsor: Office of Advanced Concepts and Technology, Earth-to-Orbit Technology Office

■

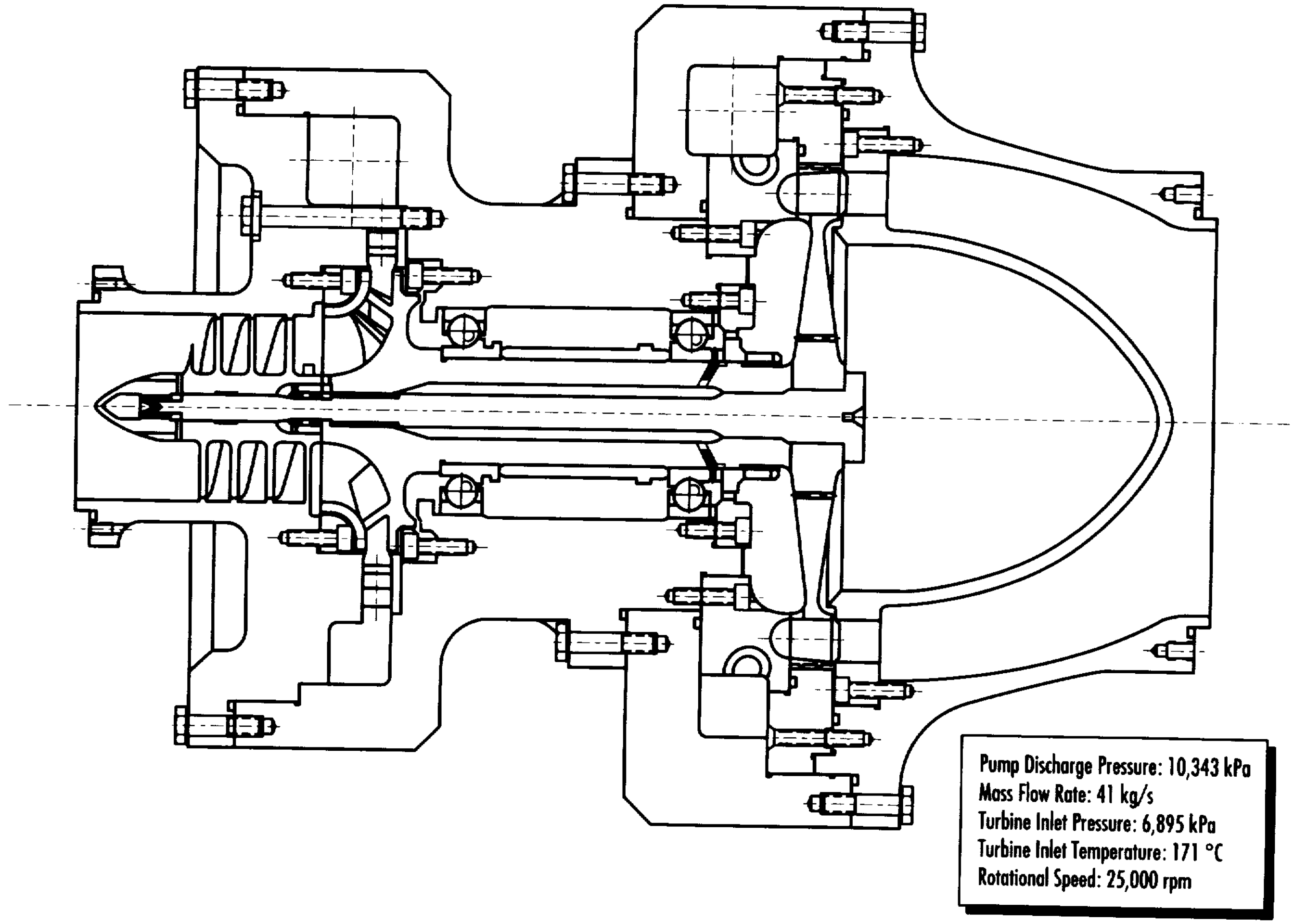

Pump Discharge Pressure: 10,343 kPa
Mass Flow Rate: 41 kg/s
Turbine Inlet Pressure: 6,895 kPa
Turbine Inlet Temperature: 171 °C
Rotational Speed: 25,000 rpm

FIGURE 102.—Simplex turbopump preliminary cross section.

Compliant Foil Bearing Technology Demonstration

Gary G. Genge/EP32
205-544-4941

For many years, rocket engine turbomachinery has relied on rolling element bearings (i.e., ball bearings or roller bearings) to support the rotor system. These bearings worked satisfactorily for engine systems that were on expendable rockets because the bearing life was limited to only a few starts and short operational time. As the desire to have reusable long-life cryogenic turbopumps became prevalent, the bearing system requirements for these machines became more difficult to attain.

The rolling element bearing is limited by the rolling contact stresses that cause fatigue and wear of the balls, rollers, and races. In order to keep these stresses low, the turbopump design often utilized a small diameter, more flexible shaft that complicated the rotordynamic problems of the design. Recent efforts have been made to eliminate the rolling contact problems by supporting the rotor on a film of fluid that the turbopump is pumping. This led to research in hydrostatic and hydrodynamic bearings that would eliminate the rolling contact fatigue and wear life issues, as well as allow the designers to enlarge the shaft diameters to simplify the rotordynamic design.

MSFC and Allied Signal Aerospace Company, Aerospace Systems and Equipment Division, have undertaken a program to demonstrate the capability of an alternative to the rolling element bearing. This alternative is a leaf-type compliant foil bearing developed by Allied Signal (fig. 103). For several years, Allied Signal has been using this type of hydrodynamic bearing in air cooling units used on many commercial airplanes. However, the bearings required several innovations to be able to carry the much higher loads found in cryogenic liquid turbopumps. Allied Signal's efforts have recently been tested at MSFC as a result of a cooperative agreement. A 4.445-cm diameter leaf-type compliant foil bearing has demonstrated a load capacity and direct damping in liquid nitrogen and oxygen capable of supporting a turbopump sized for an upper stage engine. The testing was performed with a bearing test rig designed specifically for obtaining these data.

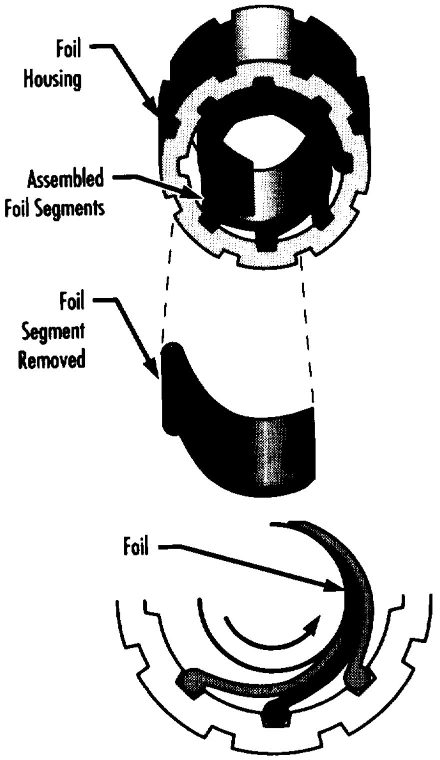

FIGURE 103.—Compliant foil journal bearing.

In addition to test rig work, MSFC and Allied Signal have a second cooperative agreement to demonstrate the bearing in an actual liquid oxygen turbopump. Allied Signal has built a turbopump equivalent to a turbopump needed on a 71,200–N thrust engine, and MSFC will be testing this pump at the test stand 500 facility. The data will be collected and the results published within a year.

Sponsors: Office of Advanced Concepts and Technology, Earth-to-Orbit Technology Office; and Advanced Chemical Engines

Commercial Involvement: Allied Signal Aerospace Company

■

Low-Temperature Testing of Static Seals and Leakage Characterization

Edward E. Litkenhous III/EP42
205-544-8387

This test program has two objectives: (1) to create a data base on the performance of static seals at low temperatures, and (2) to characterize leakage rates for inert gases and correlate these rates with cryogenic propellant leakage rates. Both the Static Seals Test and Phase I (inert gas leakage) of the Leakage Characterization Test will be performed using the same test fixture.

The Low-Temperature Static Seals Test will determine the actual performance of Viton™ elastomer Gask-O-Seals when exposed to temperature conditions from ambient to −101.1 °C. Additional testing will be conducted on static O-ring seals of several materials, including ethylene propylene, fluorocarbon, and silicone.

The Viton™ elastomer Gask-O-Seals, used to seal the flanges of the He system of the SSME, are designed to operate for the temperature range between −40 and +371 °C. The characteristics of this fluorocarbon seal are satisfactory during normal space shuttle flight conditions. It has been noted that in special cases during reentry (−56.7 °C) or during a return-to-launch site (RTLS) abort(−62.2 °C), the temperature of the seal could fall below −40 °C. At these low temperatures, the Viton™ Gask-O-Seal may lose much of its ability to stop leakage. Currently this condition is covered for the SSME by a change to Interface Control Document (ICD) 13M15000, which increases the allowable seal leakage rate. Static seal manufacturer data provide little information of the material characteristics of seals when exposed to low temperatures.

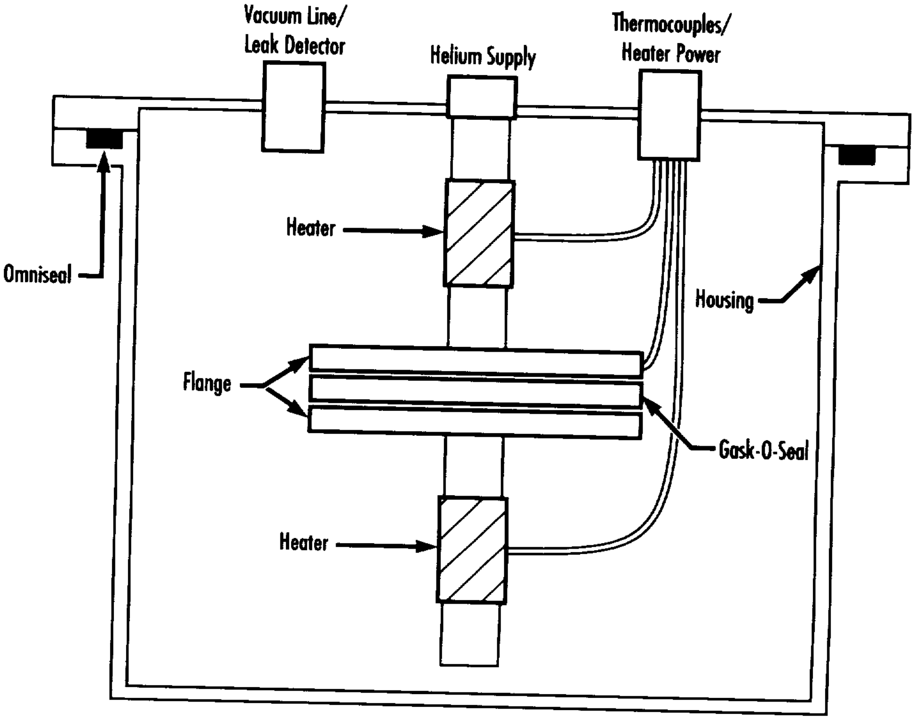

FIGURE 104.—Static seals test schematic.

There are two seal configurations to be tested. The first test configuration is the Viton™ Gask-O-Seal currently used in the SSME helium system. The second test configuration is for the static O-ring face seal test. The O-rings will conform to Parker size number 2–022 (2.51±0.025 cm outside diamater, 0.178±0.007 cm cross-sectional diameter).

The test configuration consists of a sealed fixture that contains two bolted flanges that are sealed with either Gask-O-Seals or O-rings. The inside surface of the seal will be pressurized to 5.86 MPa with gaseous helium (GHe). The outside of the test seal will be held in a vacuum. The fixture is placed inside an open drawer that is filled with liquid nitrogen (LN_2) to a maximum level of 5 cm above the top of the fixture. Kapton™ heaters are mounted inside the fixture to control the temperature of the test article, between ambient and −101.1 °C (fig. 104).

The test cycle will begin at ambient temperature. The temperature will then be reduced in 11±3 °C increments until the test article reaches −101.1 °C. The test article temperature will then be increased in 11±3 °C increments until the test article reaches ambient conditions. The helium leakage rate will be measured continously throughout the cycle.

The Gask-O-Seals will be tested first, and the amount of compression applied will not be varied. The flange compression of the O-ring seals will be varied to determine if increased compression will improve the ability to maintain a seal at low temperatures. This compression will be varied using shims. Three O-ring seal materials were chosen to be tested, four O-rings for each material and each compression level will be tested. The compression of the static seal O-rings will be varied from 10 to 40 percent, in 10-percent increments.

The Low-Temperature Static Seals Test will provide a data base of the properties of static seal materials when exposed to low temperatures. This data base will contain information useful for determining candidate materials in future low-temperature seal applications.

The Leakage Characterization Test will provide an experimental correlation between the leakage rates for inert gases and the leakage of propellant. This will be accomplished by subjecting these inert gases to varying temperatures and measuring the leakage rates through an orifice of a known size, while varying the temperature of the gas from ambient to cryogenic. GHe and gaseous nitrogen (GN_2) will be used initially (Phase I), and later testing (Phase II) will include propellant leak testing. A correlation will be developed for the leakage of H_2 and O_2. The test fixture designed for the static seals test will be modified for use in this test series (fig. 105).

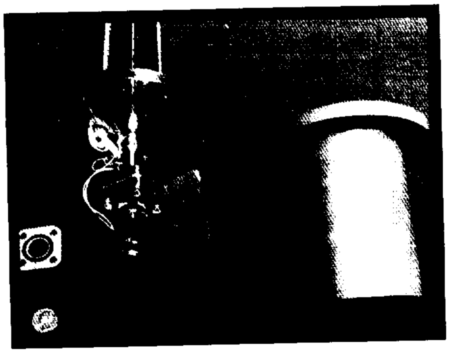

FIGURE 105.—Static seals test fixture.

A very small orifice will be used to simulate a leakage path. The test media will be chosen to correspond as closely as possible in temperature and physical properties with the intended propellant, initially using GHe and GN_2 and later expanding to perform propellant leak testing. The flow formulae will be given in volumetric form, and the gas formulae will be expressed in units that are a product of pressure and volumetric flow; e.g., atm-cm^3/s.

The leakage path will consist of an orifice plate welded to the flanged end of the static seals test fixture. The inside surface of the test article will be pressurized to 345 kPa with GHe. The outside of the test article will be held in a vacuum. The fixture will be submerged inside an open drawer filled with LN_2. A heater will be mounted to the fixture to vary the temperature of the test article between ambient and cyrogenic temperatures. The leakage rate will be measured at ambient conditions, originally to verify comparison with empirical data and to verify that there is no leakage elsewhere in the test setup. Leakage rates will be measured using a helium mass spectrometer or a flow meter capable of measuring a range of 0 to 16,400 standard cm^3/min.

The first test series will be conducted with an orifice size of 0.15 mm in diameter and a supply pressure of 345 kPa. The test cycle will be initiated after the test fixture has been thermally soaked for a minimum of 10 min at ambient conditions. The temperature will be reduced in increments of 14±10 °C until the test fixture reaches −195 °C. The leakage rate will be recoded at each increment. The test fixture temperature will then be increased in 14 °C increments until the test fixture reaches ambient conditions. After this test cycle, the pressure will be regulated to 690 kPa and the test cycle repeated. If additional data are desirable at other pressures, then the test cycle will be repeated. Identical tests will be run for additional orifice sizes not to exceed 0.38 mm in diameter.

The Leakage Characterization Test will provide a correlation between propellant and inert gases. By using the correlation, designers will be able to reduce the amount of testing done with propellant gases. Using nonvolatile substitutes will decrease cost by increasing safety.

Hord, J. Correlations for Estimating Fluid Leakage. May 19–22, 1968. American Institute of Chemical Engineers (AIChE), and Instituto de Ingenieros Quimicos de Puerto Rico, Joint Meeting Second Symposium on Cryogenic Advance in the Space Program, AIChE preprint 9E. Tampa, FL.

Sponsor: External Tank Program, Office of Space Flight

Commercial Involvement: Sverdrup Technology

■

Electromechanical Propellant Control Valve Actuator

Martha B. Cash/EP34
205-544-4282

Electromechanical actuating mechanisms for operation of propellant flow control valves are being developed for the next generation of propulsion systems and launch vehicles, as well as potential replacements for existing hydraulically operated actuating mechanisms. Alternatives to fluid power systems would potentially reduce operational costs associated with system fabrication, launch operations, and maintenance and refurbishment costs of maintaining precision fluid systems necessary to minimize contamination-related anomalies.

New control mechanism technologies are currently being developed to provide alternatives to the fluid power systems now in use. Developments in rare Earth permanent magnet motors, high-power switching devices, and electrical power sources of competitive weight and volume make electromechanical propellant flow control mechanisms viable candidates as potential replacements for existing vehicle propellant flow control mechanisms.

A high-fidelity prototype actuating mechanism has been designed and is currently undergoing preliminary performance and characterization testing. This unit is a dual-redundant mechanism designed to meet all operational performance requirements for use on the SSME. It utilizes two permanent magnet brushless motors, dual-channel control electronics, and special sensors for rate and position feedback. The actuating mechanism is shown in figure 106. The mechanical and electrical interfaces are such that the unit is functionally interchangeable with the currently used hydraulic actuation mechanism.

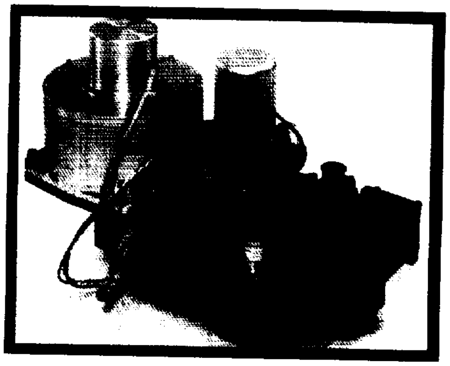

FIGURE 106.—Electromechanical propellant valve actuator.

Initial testing has been completed, and results are very promising. Lessons learned have resulted in a change to the control electronics in order to meet the positional rate and accuracy requirements for the SSME. Additional testing will be done to assess the overall suitability for functional verification on a Technology Test-Bed static firing. These additional tests will be vibration, thermal, and other environments, as well as functional verification in the engine simulation laboratory facility.

Sponsors: Office of Advanced Concepts and Technology

■

High-Power Electromechanical Thrust Vector Control Actuators

Rae Ann Weir/EP34
205-544-7146

Current launch vehicles, including the space shuttle orbiter and solid rocket boosters, use hydraulic-type systems for providing engine thrust vector control. Hydraulic fluid power systems are mature technology; however, their servicing and maintenance requirements are such that the costs associated with these operational systems are significant. This, along with the need to maintain stringent fluid cleanliness to minimize particulate contamination, make for relatively expensive systems.

New control mechanism technologies are currently being developed to provide alternatives to the fluid power systems now in use. Developments in rare Earth permanent magnet motors, high-power switching devices, and electrical power sources of competitive weight and volume, make electromechanical thrust vector control mechanisms viable candidates for the next generation of launch vehicles, as well as potential replacements for existing vehicles and systems.

A prototype configuration thrust vector control (TVC) actuator has been designed and is currently undergoing thorough evaluation and operational characterization testing (fig. 107). The unit is driven by two 19-kW three-phase permanent magnet motors driving a two-pass spur gear system. This in turn drives a roller screw device that converts the rotary motion into linear motion. The roller screw device, as well as all other mechanical components, are of a robust design capable of generating high forces on the order

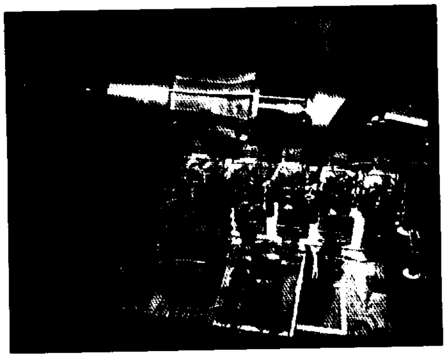

FIGURE 107.—MSFC 50-hp TVC electromechanical actuator.

of 178,000 N. Sensors provide rate and position feedback for closed-loop control.

The control electronics use pulse width modulation (PWM) technology. Insulated gate bipolar transistors are used as the high-voltage, high-current power switching devices. The electronic controller is rated at approximately 27 kW. Electric power is supplied by a battery bank of lead-acid-type batteries, configured to provide 270 V at 100 A.

Initial testing has been completed, and results are very promising. Lessons learned have resulted in a change to a single-pass gear system, as well as changes to the controller design and feedback sensors. Additional testing on this prototype unit is planned. In addition, a four-motor, 45.6-kW unit has been designed and is being fabricated. This unit will incorporate redundancy similar to flight systems now in use and will also be subjected to a rigorous test program culminating with engine gimbaling during a static test firing on the Technology Test-Bed engine facility.

Sponsor: Office of Space Systems Development

■

Multipurpose Hydrogen Test-Bed

George R. Schmidt/EP25
205-544-6055

The development of high-energy cryogenic upper stages is essential for the delivery of the large payloads envisioned in future programs. A key element in such spacecraft is cryogenic fluid management (CFM) technology. In response to this expected need, MSFC is conducting a development effort involving full-scale, ground-based testing of integrated CFM subsystems for space transportation applications. The approach is to develop and utilize a system-level test-bed, termed the Multipurpose Hydrogen Test-Bed (MHTB), which will be representative in size and shape of a fully integrated space vehicle liquid hydrogen propellant tank.

The MHTB tank, which was delivered to MSFC in December 1992, is 3.05 m in diameter, 3.05-m long, has an 18.09-m^3 capacity, and is made from 5083 aluminum. The tank is designed to accommodate a variety of different thermal control, pressure control, and liquid handling subsystems, either individually or simultaneously. Major accommodation features include several fill, drain, and vent ports; a 61-cm diameter opening for bulk access; sensors for liquid level, liquid temperature distribution, and ullage pressure; internal mounting brackets for future equipment; and low-heat-leak structural supports.

The first phase of MHTB testing will evaluate performance on a foam/multilayer insulation (FMLI) thermal control system (TCS). Although this concept offers a significant advantage for ground-based upper stages, test and operational experience is rather limited. The foam thermally protects the tank from ground-hold/ascent flight environments, and enables use of a dry nitrogen purge as opposed to a traditional, yet heavy and complex, helium purge subsystem. It consists of a 1.3-cm thick Isofoam SS–1171 layer bonded to the tank wall as shown in figure 108. The multilayer insulation (MLI) element provides protection in the space vacuum and is designed for an on-orbit storage period of 45 d. It consists of a double aluminized Mylar™ (DAM) blanket with an average layer density of approximately 10 layers/cm and is composed of 40 to 50 radiation shields with coarse Dacron™ net spacer material. Unique features of the MLI concept include a variable distance between the shields to reduce weight and fewer, but larger, perforations for venting during ascent to orbit.

Major objectives of MHTB thermal control tests are to: (1) establish—through hands-on experience—design and installation techniques for FMLI in full-scale applications, (2) define thermal performance and operational constraints during exposure to ground-hold environments, (3) prove that the MLI can be successfully evacuated to full-vacuum conditions during ascent and orbit injection phases, and (4) establish on-orbit performance of the FMLI concept. A major goal of the ground-hold testing is to ensure that the foam external surface temperature is maintained at or above 116 K to prevent gaseous nitrogen liquefaction. Also, saturation of the MLI with dry nitrogen must be ensured to prevent frost buildup. The on-orbit evaluation will include definition of steady-state thermal performance with minimum and maximum MLI surface temperatures of

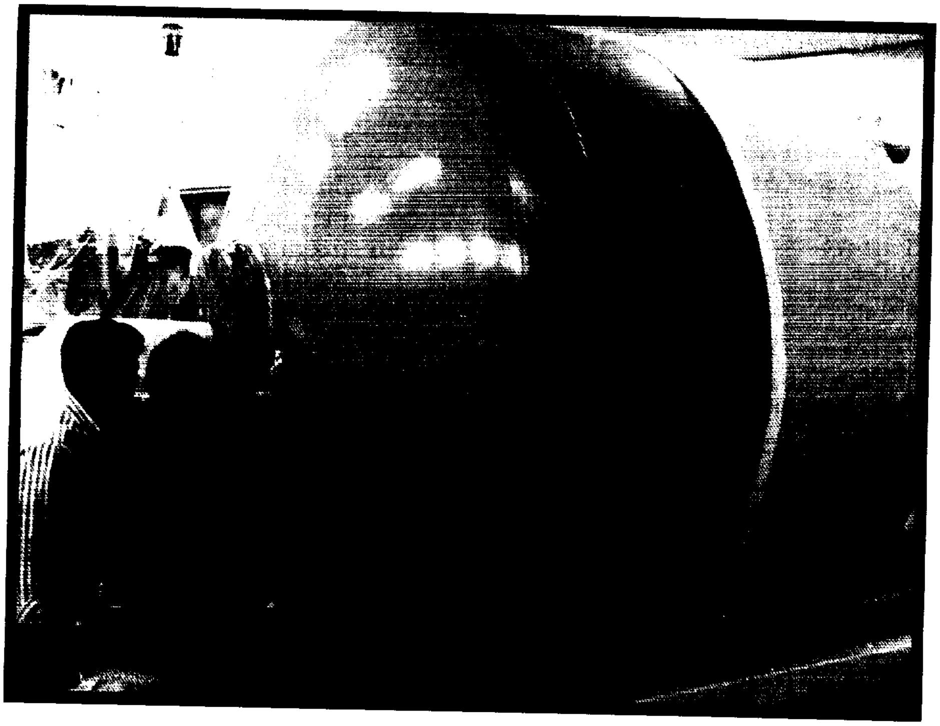

FIGURE 108.—MHTB tank following partial application of Isofoam SS-1171 spray-on foam.

140 and 300 K, respectively. A system-level thermal computational model, verified by MHTB testing, will enable definition of heat-leak contributions through each penetration and the FMLI.

MSFC is currently installing the TCS in-house. All foam application was completed in April 1993. Layup of the barrel and dome MLI sections, which is shown in figure 109, was finished in September 1993. Testing is scheduled to begin late in 1993.

The second phase of MHTB testing involves demonstration of an advanced thermodynamic vent system (TVS) for tank pressure control and zero-gravity venting. The concept selected for MHTB differs from more conventional designs in that the active components (i.e., Joule-Thompson expansion valve, pump, and isolation valve) are located externally in a stainless steel cylindrical enclosure attached to the bottom of the tank. This approach allows the pump to operate without adding heat to the propellants, and enables modification or changeout of TVS components without entering the tank. In the mixing mode, fluid is withdrawn from the tank by the pump and flows back into the tank through a spray bar positioned along the tank's longitudinal axis. Fluid expelled radially through the spray bar circulates and mixes tank contents regardless of liquid position, thus ensuring destratification and suppression of pressure rise. When pressure relief becomes necessary, a portion of the circulated liquid is passed sequentially through the expansion valve and spray bar heat exchanger element, and finally vented to space. The vented vapor cools the fluid circulated through the mixer element and removes thermal energy from the bulk liquid. In a low-gravity transfer application, the spray-bar concept could also be used to assist tank refill. By filling through the spray bar and heat exchanger, the inflowing fluid would be cooled and used to mix tank contents, thereby accomplishing a "no-vent fill" process.

A Critical Design Review (CDR) for the MHTB zero-gravity vent was successfully held in late June 1993. Hardware delivery at MSFC is scheduled for the spring of 1994, with testing to begin in 1995.

The third phase of MHTB tests addresses pressurization techniques needed to support engine startup and general liquid expulsion/transfer. Although considerable

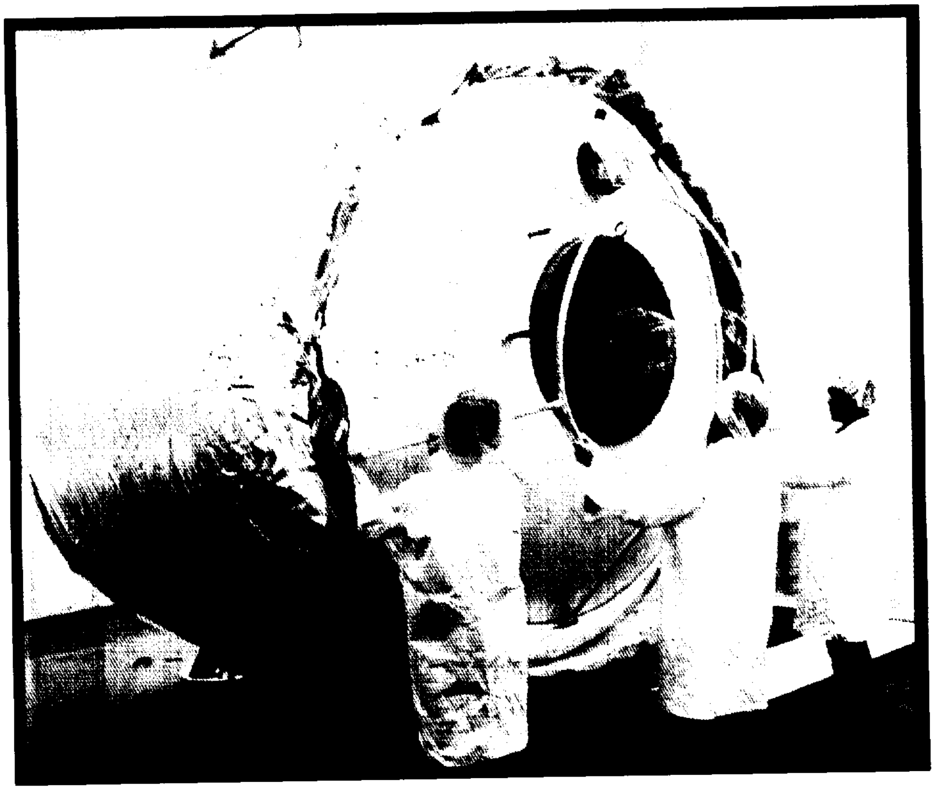

Figure 109.—Bottom view of MHTB tank following layup of multilayer insulation around barrel section.

experience with cryogenic pressurization systems exists, pressurization collapse due to liquid remaining on the walls following a propellant resettling maneuver is still a concern. Also, in several orbital transfer scenarios, pressurization with unsettled propellants may be required. Based on the preceding considerations, the MHTB pressurization subsystem includes provisions for evaluating both gaseous hydrogen and helium pressurants at various temperatures and flow rates. The MHTB pressurant inlet diffuser is based on the design used with the space shuttle external tank.

In-house design and fabrication of the pressurization system hardware is complete. Testing will be conducted concurrently with MHTB thermal control and zero-gravity vent subsystem tests.

Sponsors: Office of Space Systems Development, and Office of Advanced Concepts and Technology

■

Combined Foam/ Multilayer Insulation Demonstration

George R. Schmidt/EP25
205–544–6055

The propellant thermal control requirements for ground-based upper stages and servicing systems are unique. The thermal control system must operate effectively in all mission phases, namely ground-hold, launch/ascent, and orbit-hold, and provide thermal protection in both convection- and radiation-dominant environments. In convection-dominated or pressurized environments, a spray-on foam insulation (SOFI) that reduces heat conduction to the tank wall is usually selected. This approach is implemented on launch vehicles, such as the space shuttle external tank, and ground storage facilities. In space, a blanket consisting of very thin radiation shields separated by a low-conductance fabric is used to reflect radiation impinging on the outside of the spacecraft. The problem is that either form of insulation by itself is inadequate for a spacecraft that must function in both environments.

One promising solution is to implement the two insulation concepts simultaneously in one system. This combined foam/multilayer insulation concept is currently being investigated to assess its performance in simulated flight environments. The experiment apparatus, which is shown in figure 110, consists of a subscale, insulated liquid hydrogen

FIGURE 110.—Test tank installed in the 20-ft vacuum chamber.

tank installed in the MSFC 20-ft diameter vacuum chamber. The environment within the chamber is varied to simulate the pressure history and temperature within the shuttle cargo bay during ground-hold, rapid ascent, and on-orbit hold. Results will be compared to flight data from the shuttle ET and Centaur rocket upper stage, and analytical results from a systems improve numerical differencing analyzer (SINDA) computational model. Upon completion of tests, the insulation will be removed and thoroughly examined to assess the effect of repeated operational cycling. Testing will aid in determining the feasibility of employing the combined insulation concept on a reusable, wet-launched upper stage. It will also provide a means of validating analytical models for various launch environments.

To date, four ground-hold simulations have been performed while maintaining the vacuum chamber and environmental shroud under a gaseous nitrogen purge.

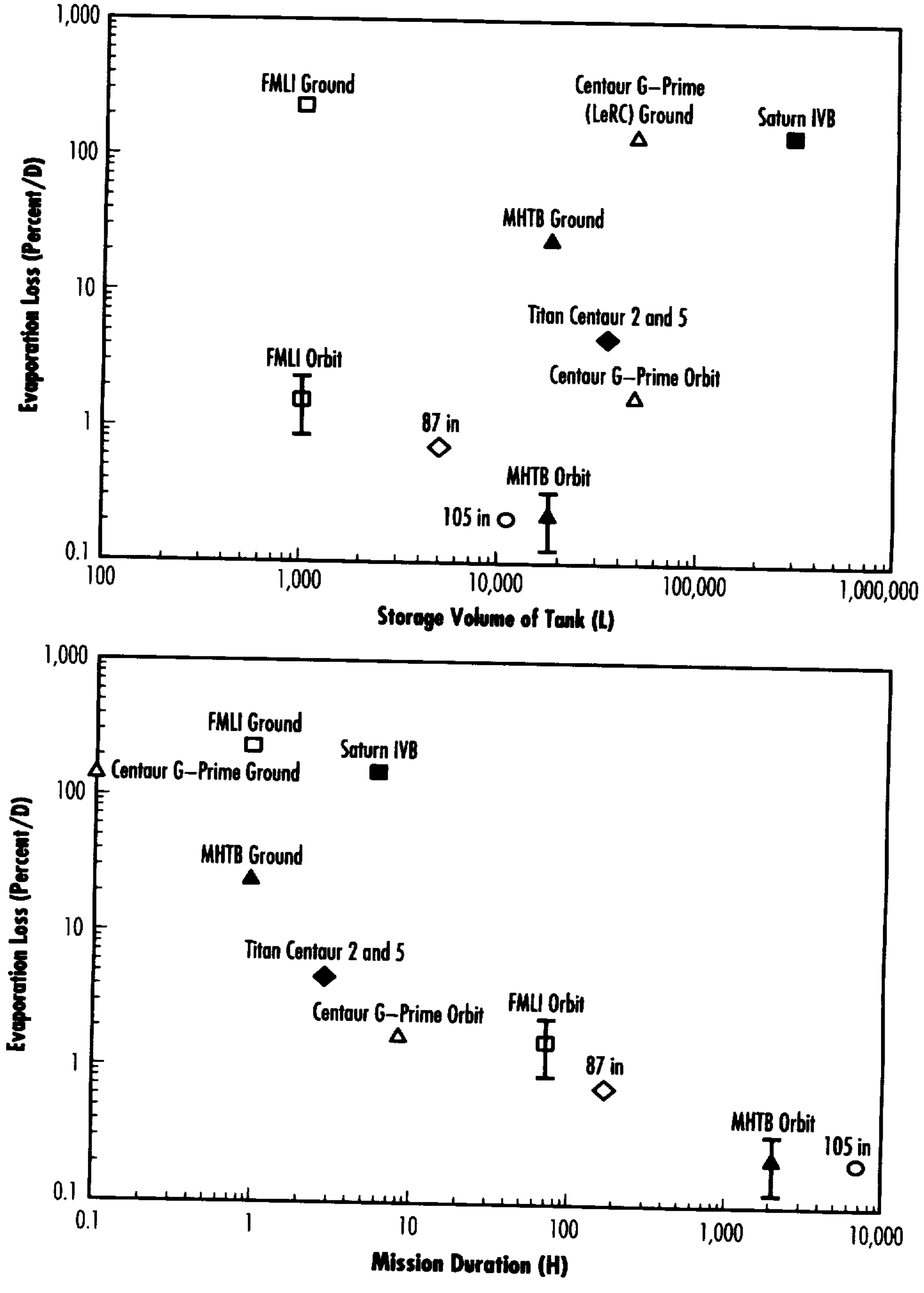

	Surface Area/Vol	Hot Boundary (K)	Insulation Content
■	0.37	155	Internal Foam
◆	0.59	144–311	Mylar™ (1 layer) and Doubly Aluminized Mylar™ (DAM) (2 layers)
△	0.50	222	Foam Panels (2-by-19 mm) and DAM MLI (3 layers)
◇	0.86	277	Goldized Kapton™ MLI (20 layers)
○	0.63	294	DAM MLI (70 layers)
□	1.60	166–255	SOFI (10.2 mm) DAM MLI (16 layers)
▲	0.57	166–300	SOFI (25.4 mm) DAM MLI (45 variably spaced layers)

FIGURE 111.—MHTB steady-state ground and orbit-hold boil-off losses compared with other programs.

Total average heating rates ranged from 752 to 882 W for shroud purge flow rates of 0 and 0.079 kg/s, respectively. This yielded propellant loss rates ranging from 8.8 to 10.4 percent of the tank volume/h. Results also indicated that the foam surface temperature, which varied from 172 to 189 K for the aforementioned purge rates, was sufficiently high to prevent liquefaction of oxygen and nitrogen.

Three steady-state orbital hold and heating simulations have also been performed. Electrical heaters installed in the environmental shroud allowed application of several warm boundary conditions during each test. Average insulation heating rates during orbit-hold simulations ranged from 3.1 to 8.2 W for boundary temperatures of 167 to 256 K, respectively. These rates corresponded to liquid losses of 0.9 and 2.3 percent of the tank's volume/d.

In June 1993, the test program concluded with four ascent tests. It will take several months to disseminate and process these data, which include transient estimates of heat loads and boil-off losses. The results obtained so far from ground- and orbit-hold tests appear to confirm the FMLI concept's flexibility in handling pressurized and vacuum environments, as shown in figure 111. However, the volume percent loss rates were higher than flight data for each insulation type in its respective design environment. This is because of the full-scale application's decreased surface area-to-volume ratio compared to the test tank. A more consistent comparison will be possible once full-scale FMLI tests are conducted in 1993, using MSFC's Multipurpose Hydrogen Test-Bed.

Sponsor: Office of Space Systems Development

Fluid Acquisition and Resupply Experiment

George R. Schmidt/EP25
205-544-6055

Propellant and fluid tankage operating in a low-gravity environment requires methods for acquiring and expelling vapor-free liquid. In addition, any orbital resupply and replenishment must be performed without venting liquid or exceeding tank pressure limits. Liquid acquisition devices (LAD's) that exploit surface tension are typically used to separate and orient liquid in the tank. Although both screen and vane LAD's have been successfully used in flight applications, performance limits remain undefined. For example, the space shuttle's Orbital Maneuvering System (OMS) uses screen channel LAD's, but the performance limits and design margins cannot be established during flight. Similarly, a vane LAD was used on the Mars *Viking* orbiter, but its low-gravity performance margins were never verified.

The purpose of the Fluid Acquisition and Resupply Experiment (FARE) is to demonstrate the performance of a screen and vane LAD aboard two different shuttle flights. The test objectives include: (1) evaluating and comparing the expulsion efficiency of both designs, (2) assessing how well each LAD orients the liquid and maintains surface stability during vented fills with different inflow rates, and (3) determining the response and rewicking capability of the devices when subjected to various orbiter accelerations.

FARE successfully flew on mission STS–53 in December 1992, and on STS–57 in June 1993. The facility was originally built by Martin Marietta as the Space Fluid Management Demonstration (SFMD), which was carried aboard STS 51–C in January 1985. The FARE hardware was mounted in five orbiter middeck lockers as shown in figure 112. Four of these contained the hardware, while the fifth provided space for stowage of a flowmeter display, vent hose, and cables. The test fluid was deionized, distilled water with food coloring and a wetting agent added. Test operations entailed transferring fluid between two transparent acrylic tanks. The receiver tank, which was videotaped during the experiment, contained the LAD, while the supply tank contained a bladder to ensure expulsion and recovery regardless of initial liquid orientation.

FIGURE 112.—Testing of fill performance through screen LAD aboard STS–53.

The first flight tested the screen device, and consisted of eight experiments examining different values of inflow rate, expulsion rate, receiver tank pressure, and imposed acceleration. Besides video, data included 35-mm still photography,

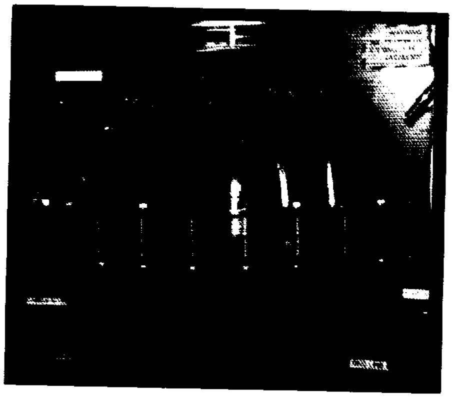

Figure 113.—Closeup of LAD tank during expulsion tests aboard STS–53.

crew comments, and recorded accelerations from the orbiter's microgravity acceleration measurement system.

The results indicated that the screen was highly effective in expelling gas-free liquid from the tank under a variety of conditions. A photograph of the receiver tank during expulsion through the screen LAD is shown in figure 113. In all expulsion tests, an expulsion efficiency of 96.5 to 98 percent was achieved. However, the vented fill tests were not as conclusive. It appeared that interfacial stability and fill percent was maximized at a Weber number (ratio of inertia to surface tension forces) of 2.3 or between the minimum and maximum tested of 0.6 and 5.2, respectively. It was also found that whenever an adverse acceleration was applied, regardless of whether the tank was 5- or 50-percent full, the liquid would wick back to its original position within 10 to 15 s. This demonstrated that the screen channel was relatively immune to acceleration.

The second flight tested the vane device and basically repeated the conditions examined on the first flight. At the time of this report, videotape data from the second had not been processed. However, a real-time downlink enabled preliminary observation and evaluation by the experiment's investigators. The results indicated that the expulsion efficiency for the vane was approximately 95 percent. Although this was somewhat less than that for the screen, the vane appeared to be more effective in stabilizing the surface and better suited for liquid control during the vented fill process. The most notable aspect of the vented fill tests was the astronaut's ability to adjust the inflow to the critical Weber number. At this point, the geyser emanating from the inlet jet reached its maximum penetration into the ullage bubble without breaking through. This value has been estimated before from previous analyses and drop-tower experiments, and the FARE results, once processed, will provide another data point to evaluate its validity.

Sponsor: Office of Space Systems Development

■

Liquid Acquisition Device Characterization

George R. Schmidt/EP25
205–544–6055

In the absence of gravity or large accelerations, channels and traps comprised of fine-mesh screens are used to foster liquid expulsion from spacecraft tankage. Operation of such devices with storable propellants is well understood and has been demonstrated in numerous applications. Designing these components for use with cryogens, however, is complicated by the fact that the fluid is stored at or close to a saturated state. Thus, mass, heat, and momentum transport between the liquid, screen, and pressurant gas can destabilize the liquid/gas interface between the screen pores (i.e., meniscus), and cause vaporization and retention loss around the screen.

The objective of this project is to research the underlying thermophysics governing retention of screened acquisition devices with cryogenic propellants and to improve the understanding of how such phenomena influence the surface stability and maximum sustainable pressure difference across simple screen-weave geometries. Rather than assessing performance of a particular device, the project focuses on effects at the screen-pore level and involves computational modeling and experimental observations of two-phase fluid behavior near the liquid/gas interface.

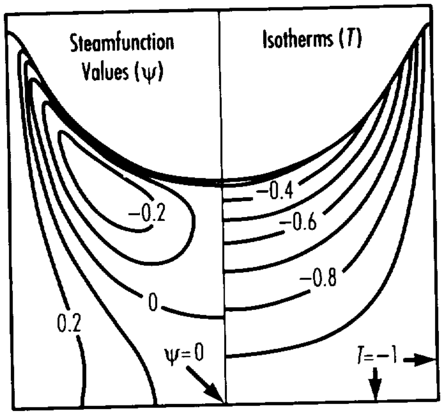

Sidewall Subcooling/Condensation

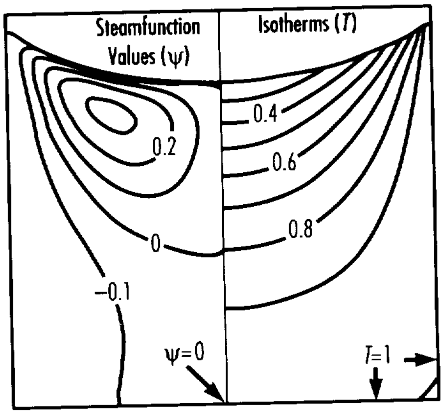

Sidewall Superheating/Evaporation

FIGURE 114.—Steady-state flowfield, temperature, and meniscus.

A major accomplishment was the development of a model that predicts combined thermocapillary, evaporation, and condensation flow in an isolated rectangular cavity. It also accounts for meniscus deformation and all the thermo-physical phenomena relevant to retention of a volatile liquid. The model was initially used to investigate the combined influence of thermocapillarity, evaporation, and condensation on the flow and heat transfer about superheated and subcooled meniscus bounded by isothermal sidewalls. This study provided useful insight into the physics of the flow field and served as a validation against the results from previous investigations. Figure 114 shows the steady-state stream function and isotherm (i.e., constant temperature) profiles for the three types of regimes considered in the study. Note that either the separate or simultaneous action of interfacial flow and/or thermocapillary stress produces distinct velocity and temperature distributions. An important result was that the interfacial heat transfer for all three regimes was greater than the case for a stationary fluid.

The results of this study have pointed to several causes for liquid acquisition device retention failure. It appears that evaporation and condensation, in conjunction with thermocapillary flow, exhibit opposite trends in terms of influencing surface stability and bubble-point pressure. That is, condensation tends to foster instability, while evaporation tends to suppress it. In the small pores considered here, all convection modes can cause a notable deviation from the hydrostatic solution for meniscus curvature due to temperature-dependent variation in surface tension, vapor recoil, and dynamic pressure along the surface. These effects have not been fully studied yet, but will be the emphasis of future analytical and experimental activity.

Sponsor: Marshall Space Flight Center Director's Discretionary Fund

Magnetically Actuated Propellant Orientation

George R. Schmidt/EP25
205–544–6055

In a low-gravity environment, acquisition of vapor-free propellant is complicated by the indeterminate location of bulk liquid with respect to the tank outlet. Proper design of engine feed or propellant transfer systems requires methods to control liquid orientation and an understanding of fluid motion in response to disturbances and imposed accelerations. Traditional approaches for controlling and positioning cryogenic liquids, such as period thruster firings and capillary retention devices, exhibit several drawbacks that could be mitigated by employing systems that exploit the inherent paramagnetism of liquid oxygen and diamagnetism of liquid hydrogen. With the advent of lightweight, high-temperature superconductors, and high-flux density, rare Earth magnets, the use of magnetic fields to control large fluid quantities in microgravity appears feasible, and could enable low-gravity settling, venting, filling, and acquisition without the need for capillary retention systems or propulsive firings. Some of these potential applications are shown in figure 115.

This project is currently evaluating the feasibility and practicality of magnetically actuated propellant orientation (MAPO) for spacecraft applications. The scope has been restricted to lox primarily because: (1) control of lox offers the near-term application of MAPO technology, (2) the magnetic properties of paramagnetic fluids are well known, and (3) lox behavior has been tested before in a low-gravity environment on a laboratory scale. One of the primary objectives is to determine the range of magnetic field strengths required to perform reorientation

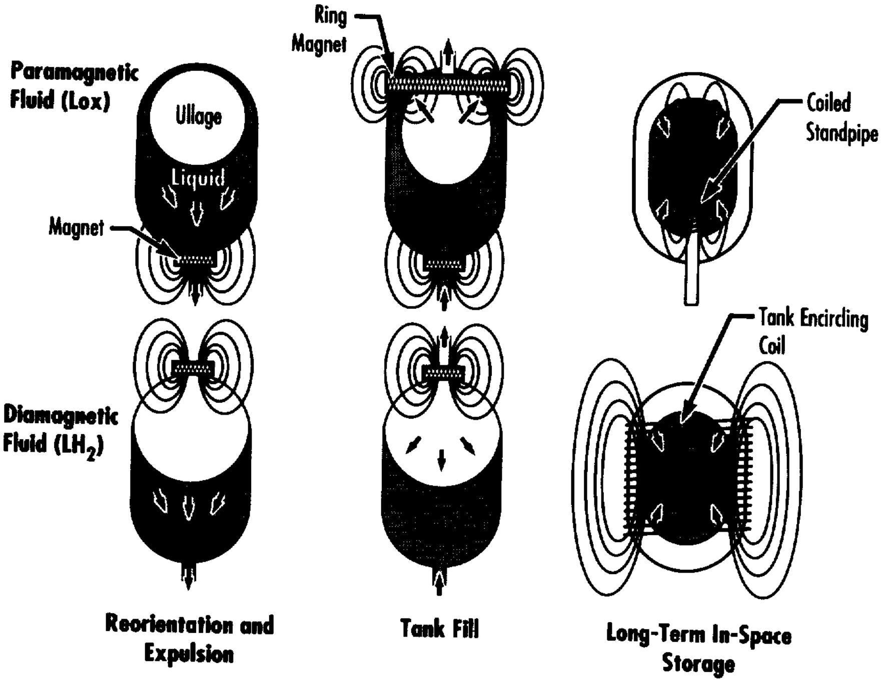

FIGURE 115.—Potential applications of magnetically actuated propellant control for spacecraft.

and maintain liquid orientation during tank fill and expulsion. This range will provide a basis for evaluating whether these magnetic field requirements fall within the capabilities of current or anticipated superconducting magnet technology.

The project involves low-gravity experiments utilizing the KC–135 low-gravity aircraft. All experiments employ the subscale hardware shown in figure 116 and a noncryogenic ferrofluid that simulates the paramagnetic behavior of lox. The ferrofluid is a commercially available kerosene-based solution containing a suspension of extremely fine ferrous particles. Several properties of this fluid (i.e., particle density, viscosity, and surface tension), along with tank diameter, flow rates, and magnetic field intensities, are being scaled to model lox behavior in a spacecraft-type application. Design and assembly of the test article is nearing completion, and the facility should be ready for preliminary tests in 1993. Two other series of tests will be conducted in 1994.

Scaling analyses have shown that magnets in the size range of 1 to 10 Tesla should be adequate for propellant reorientation in a full-scale lox application. These results, however, are rather limited since the fields can typically assume very complicated geometries, which are difficult to characterize in terms of dimensionless groupings. Consequently, another aspect of this activity is focused on modifying an existing computational fluid dynamics (CFD) model to include the body and surface forces arising from the interactions between the fluid and magnetic field. This will provide a more rigorous means of assessing fluid behavior, and will enable the modeling of more complicated field geometries and advanced concepts, such as liquid hydrogen. Videotaped recordings of fluid motions taken from the low-gravity tests will be used to validate the revised CFD model.

Sponsor: Marshall Space Flight Center Director's Discretionary Fund

■

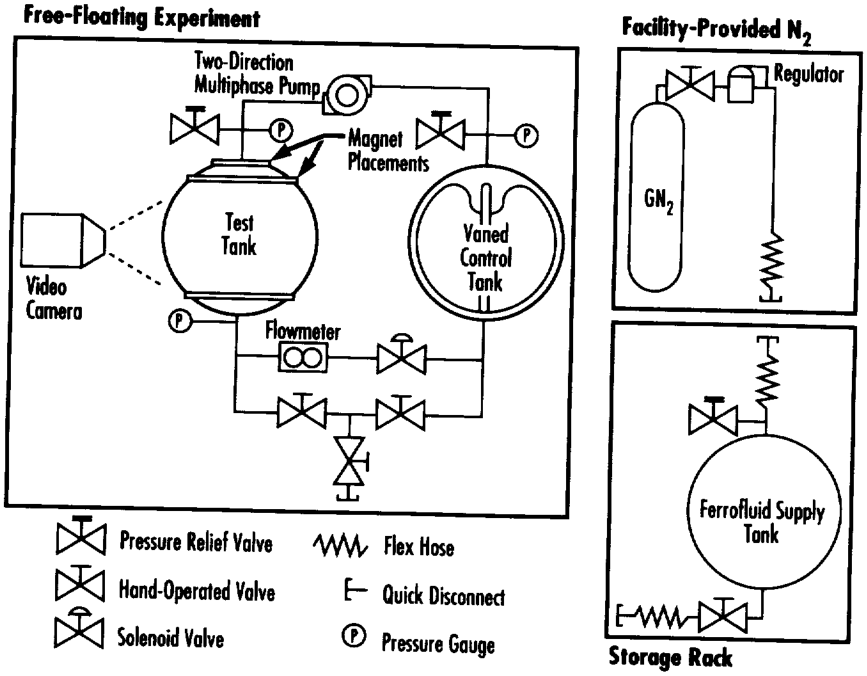

FIGURE 116.—Schematic of KC–135 test apparatus.

Structures and Dynamics

Computer Aided Grid Interface System

Theodore G. Benjamin/ED32
205-544-9402

NASA maintains an applications-oriented computational fluid dynamics effort complementary to, and in support of, aerodynamic propulsion design and test activities. This is especially true at MSFC where the goal is to advance and optimize present and future liquid-fueled rocket engines. Numerical grid generation plays a significant role in the fluid flow simulations that CFD utilizes. An overall goal of the current project is to develop a geometry grid generation tool that will help engineers, scientists, and CFD practitioners to analyze design problems involving complex geometries in a timely fashion. This goal is being accomplished by developing the computer aided grid interface (CAGI) system. The CAGI system is being developed by integrating computer aided design/computer aided manufacturing (CAD/CAM) geometric system output and Initial Graphics Exchange Specification (IGES) files (including all NASA–IGES entities), geometry manipulations and generations associated with grid constructions, and robust grid generation methodologies.

A multitude of techniques and computer codes have been developed for generating computational grids in arbitrary regions. However, in most of these codes and methodologies, the evaluation of the geometry input and realization of mapping between physical and computational space allowing appropriate zonal/block strategies are long, very laborious, and extremely time consuming. Geometry-grid generation is considered the most time- and cost-critical part in a typical CFD application. There is a need to develop a cost-effective and efficient computational geometry-grid generation capability applicable to complex geometries encountered in propulsion problems at MSFC, and one that is timely enough for engineering design; this is the motivation for the current CAGI development. This project was initiated on May 16, 1992, with the commitment to release a version of software each year.

CAGI is being developed in a modular fashion. A self-explanatory pictorial view of different modules and their linkage is provided in figure 117. The computer languages FORTRAN 77 and C in a UNIX window environment are utilized for portability.

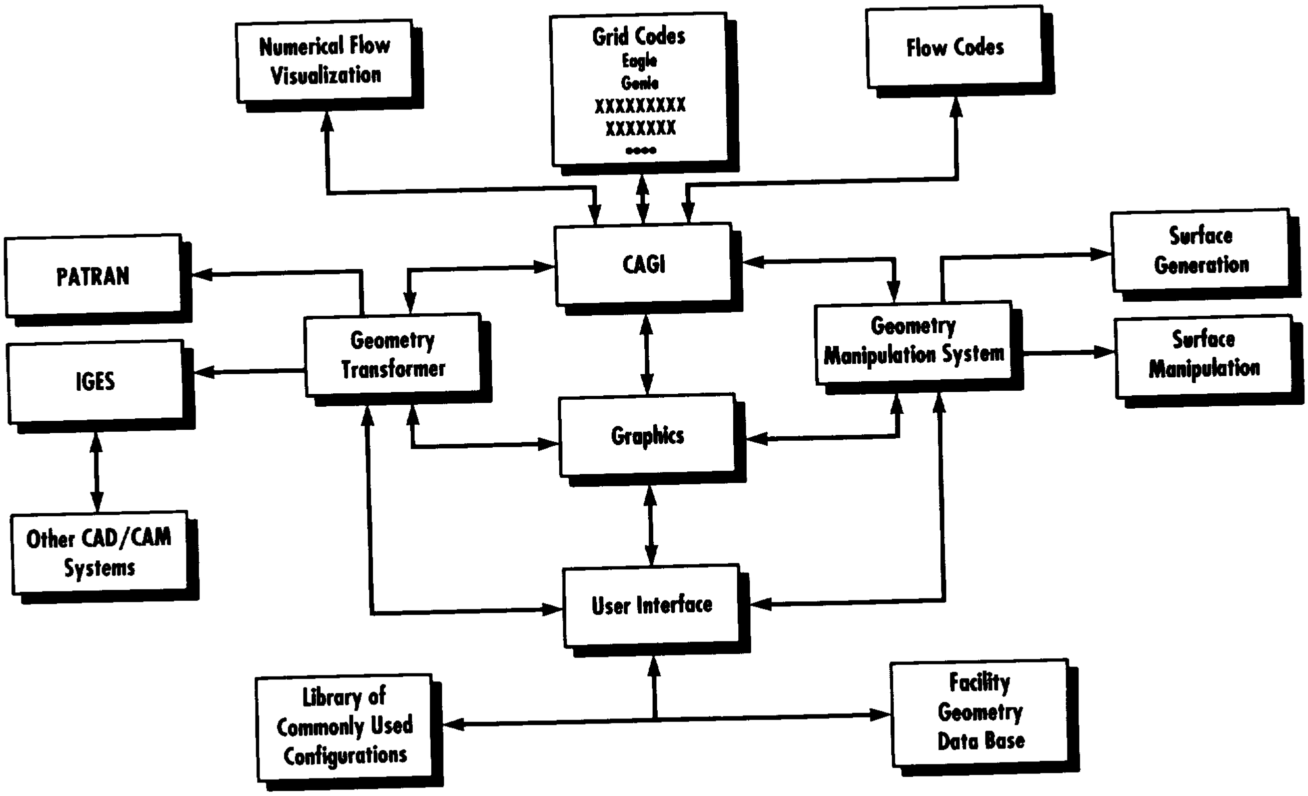

FIGURE 117.—CAGI modules.

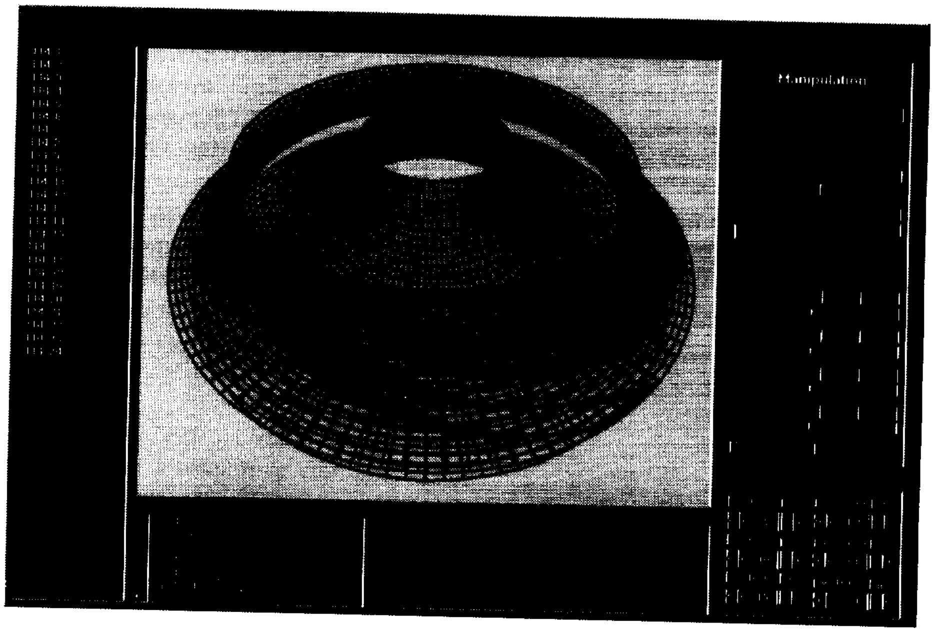

FIGURE 118.—CAGI user interface: surfaces created by IGES transformer for impeller data.

An X-based interface is provided, allowing Silicon Graphics, Inc. (SGI) Graphics Language (GL) library of X-graphics access by command-line argument. The dynamic allocation of memory and linked lists on a well-defined data structure is allowed in the CAGI development. A module, an IGES transformer, is developed allowing all critical geometrical entities. All NASA–IGES geometric entities have been considered in this development. The nonuniform rational b-spline (NURBS) curve/surface/volume representation is selected for the geometric description. The NURBS offers a control-point based parametric representation that is widely utilized for interactive design applications using CAD/CAM systems. An inverse formulation of NURBS is developed for evaluation of control points associated with the sculptured discretized specification of geometrical entities. The application of these developments in surface grid redistribution, adaptation, remapping, and optimization are being explored. The work continues on the development of multiblock strategies and the geometry manipulation system, along with the development of the NURBS tool kit for grid generation.

The initial (Beta) version of the CAGI system offering an IGES transformer, conversion of the geometric entities into the standard NURBS data structure, and various geometry manipulation and generation, was released to MSFC personnel in June 1993. The IGES transformer module was incorporated in the grid system GENIE++ and the National Grid System being developed at Mississippi State University. The current version of the CAGI system has been applied to various grid generation applications based on the IGES-supplied geometric information. An example representing a complex impeller configuration is presented in figure 118. In figure 118, the surfaces interpreted by the IGES transformer are presented using a CAGI graphical user interface; the pictorial view of the grid behavior is presented in the graphics window.

A scientific workstation-based, user-oriented, menu-driven software system, CAGI, that will aid in geometry preparation and establishment of zonal boundaries/surfaces for complex grid generation applications encountered in present and future liquid-fueled rocket engines is being developed. The progress to date has indicated that this system will help CFD practitioners analyze design problems involving complex CAD/CAM-generated geometries in a timely fashion.

Blake, Matthew W., and Chou, Jin J. April 1992. The NASA–IGES Geometry Data Exchange Standard. Proceedings of a workshop sponsored by the NASA, Langley Research Center, Hampton, VA.

Yu, T.Y. August 1992. IGES Transformer and NURBS in Grid Generation. Master's thesis, Mississippi State University.

Yu, T.Y., and Soni, Bharat K. April 1993. Computer Aided Grid Interface (CAGI). Computational Fluid Dynamics Workshop, NASA, MSFC, AL.

Sponsor: Office of Advanced Concepts and Technology

University Involvement:
Mississippi State University

Analysis of Residual Flexibility Modal Test Data

Paul S. Bookout/ED26
205-544-1490

Michael L. Tinker/ED26
205-544-4973

Historically, fixed-base testing has been used for verification of space shuttle payload models. Due to difficulties involved in the fixed-base approach, free-free modal testing augmented by residual flexibility measurements has been studied and, to a limited degree, applied in the model updating process. The purpose of the current research effort is to implement the procedure in-house beginning with a simple beam having a trunnion simulator attached (fig. 119). By using a very simple structure, high confidence should exist in the model, allowing the study team to focus on the accuracy of residual measurements. Successful measurement and calculation of residual flexibility for the simple beam is to be followed by test and analysis for a more complicated structure. The final phase would likely involve use of actual payload test data, after which the approach would be available as an alternative procedure when fixed-base testing proves undesirable.

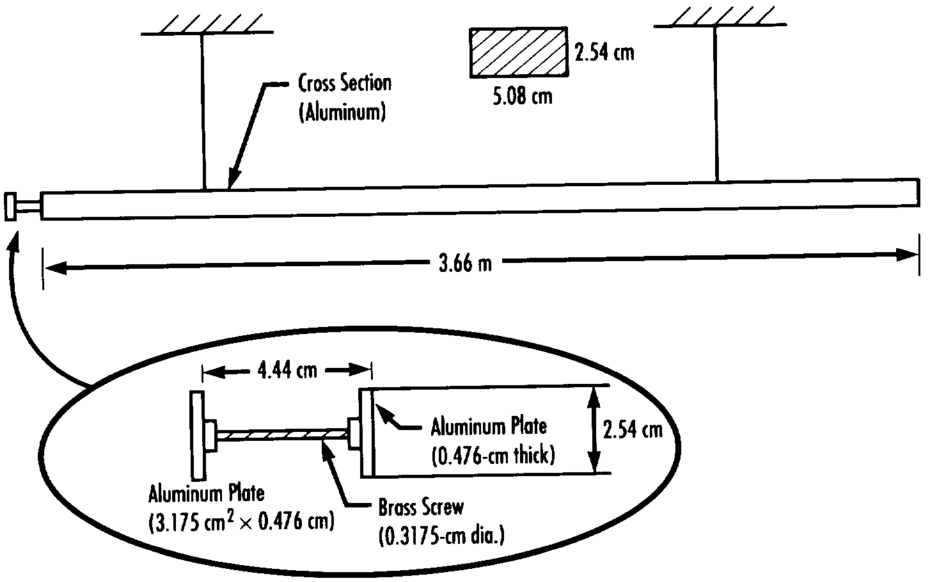

FIGURE 119.—Beam test article.

Modal test procedures for the residual flexibility approach involve the measurement of free-free modes as well as the residual functions for the structure interfaces or boundary degrees of freedom. Residual flexibility, or the value of a displacement/force residual function at zero frequency, approximates the higher-order modes that are not measured in the free-free test. Constrained-boundary modes of the payload are calculated using the measured free-free modes and residuals.

Implementation of the residual flexibility technique for the simple beam with trunnion simulator consisted of the following steps:

- Development of a finite element model
- Measurement of free-boundary frequency response functions (FRF) from which vibration mode shapes and frequencies are obtained
- Updating of the model to improve agreement with test frequencies
- Extraction of experimental residual functions by subtracting an FRF containing only the measured modes from the full measured FRF
- Comparison of experimental and analytical residual functions to assess measurement accuracy.

In applying the residual flexibility method to the simple beam, a number of problems were encountered in obtaining values for residual terms from measured residual functions. An analytical residual function in the displacement/force domain has the characteristics of a relatively flat line in the lower frequencies and a slight upward curvature in the higher frequency range. In the test residual function, the above mentioned characteristics can be seen, but due to the present limitations in modal parameter estimation, the residual function has regions of ragged data.

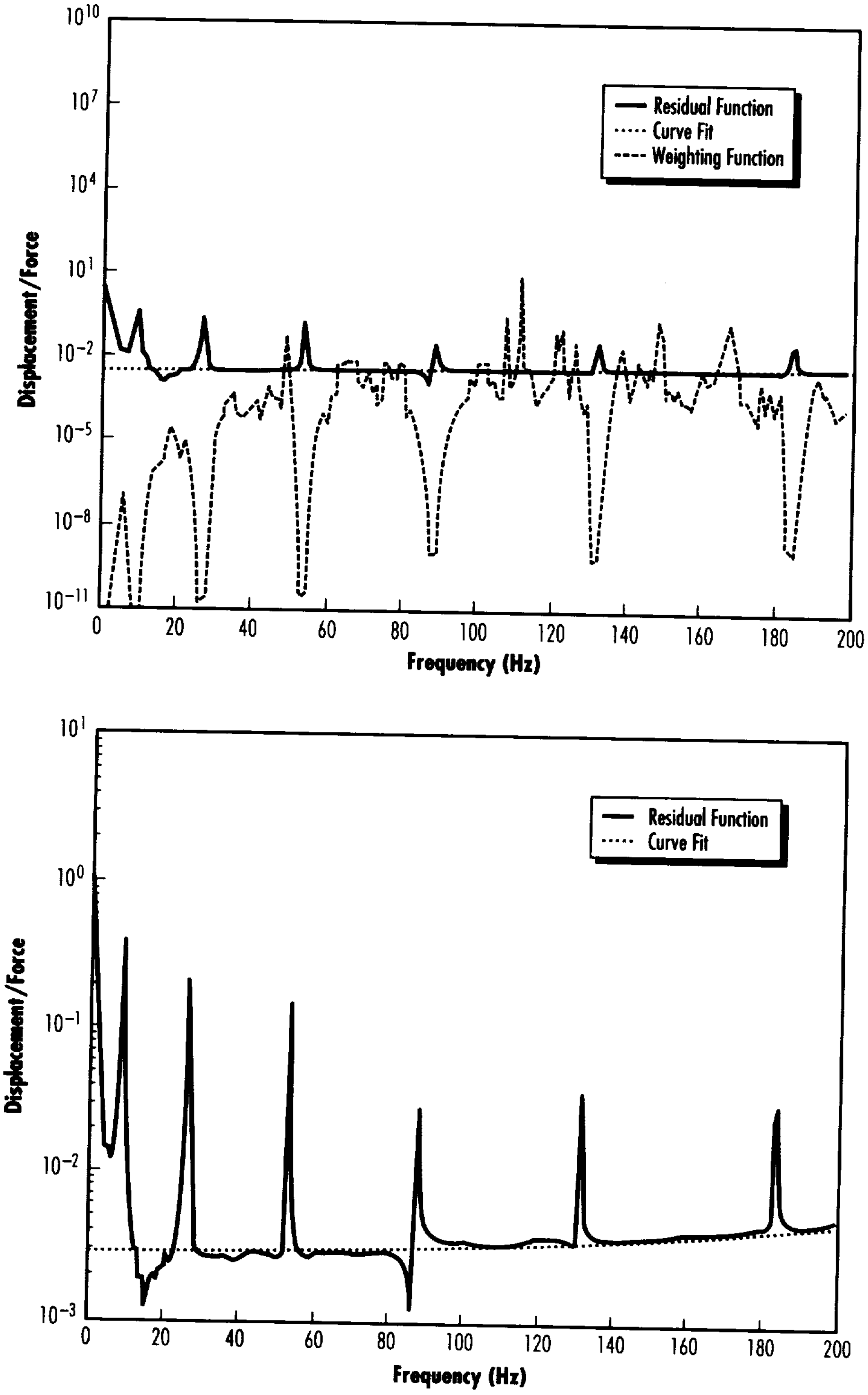

FIGURE 120.—Weighted curve fit, with (top) and without (bottom) weighting function plotted.

A second-order polynomial curve fit is required to obtain the residual flexibility and residual mass terms. As stated previously, the residual flexibility term is computed by evaluating the residual function at zero frequency, while the residual mass term is determined by the upward curvature of the residual function. Direct curve fits of the test data produce poor results due to the ragged data regions. A method of reducing the effect of the ragged data upon the curve fit process is necessary. A weighting function, which will reduce the effect of the ragged data, is generated by examining the variances between neighboring data points. Due to the characteristics of the residual function as stated above, the variance of the data should be small throughout the frequency span. The ragged data produce large variances. Taking the inverse of the variance, the weighting function is produced. From a weighted second-order polynomial curve fit, an accurate residual flexibility value can be obtained (fig. 120). The residual flexibility value and test free-free modes are used to update a mathematical model of the structure.

Admire, J.R.; Tinker, M.L.; and Ivey, E.W. April 13–15, 1992. Residual Flexibility Test Method for Verification of Constrained Structural Models. Proceedings of 33d Structures, Structural Dynamics, and Materials Conference. Pp. 1614–22. Dallas, TX.

Rubin, S. 1975. Improved Component Mode Representation for Structural Dynamic Analysis. *AIAA Journal* 13:995–1006.

Sponsor: Space Station Project Office

■

Investigation of Inducer Cavitation and Blade Loads

Wayne J. Bordelon, Jr./ED34
205–544–1579

During hot-fire development testing of the alternate turbopump development (ATD) lox turbopump, the lox pump experienced high pump-end vibrations, causing engine shutdown. It was determined that the pump was experiencing high rotor vibrations at super-synchronous (above shaft speed) frequencies that would suddenly shift to a high synchronous (shaft speed) frequency. The probable cause of these high vibrations was determined to be a fluid-structural coupling between the inducer cavitation and the rotor system.

As part of the effort to solve this problem, full-scale water flow inducer tests were conducted at MSFC. The test article (fig. 121) was instrumented with accelerometers and dynamic pressure measurements and was, in part, made of acrylic, allowing high-speed photography of the inducer cavitation patterns. As suspected, the inducer exhibited alternate blade cavitation, causing a two-times synchronous (2N) forcing function at a certain suction-specific speed (Nss). However, an unexpected finding revealed that this 2N cavitation mode would suddenly shift to a synchronous (1N) cavitation mode at a higher Nss condition. As revealed by high-speed film and measured dynamic pressures (fig. 122), there was a sudden drop in the 2N pressure amplitude followed by a sudden increase in the 1N amplitude. This cavitation mode change is believed to be a significant contributor to the sudden increase in pump vibration. Testing of five inducer configurations revealed that although this 1N cavitation mode could not be eliminated, the amplitude could be substantially reduced by increasing the inducer tip clearance—the eventual "fix."

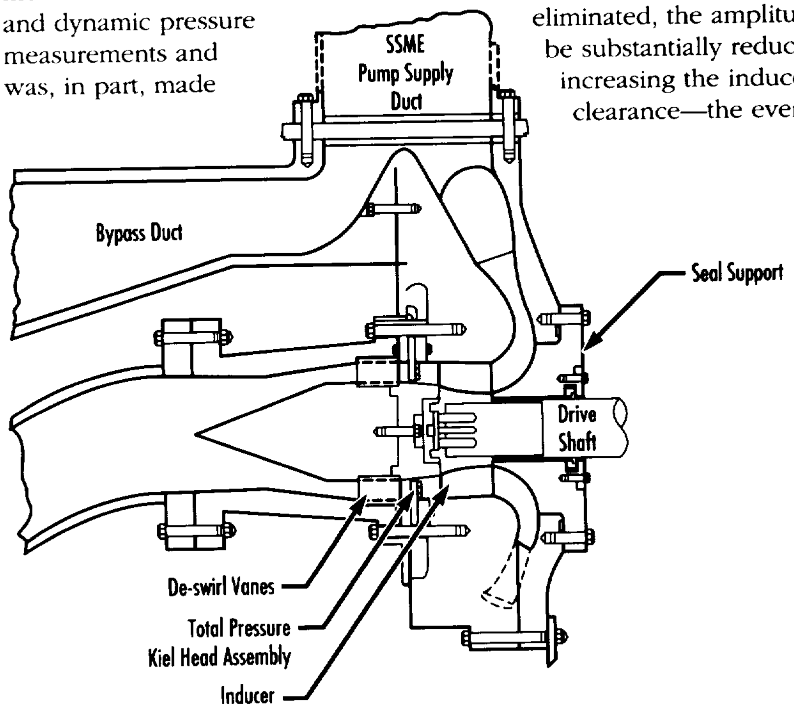

FIGURE 121.—MSFC inducer technology rig cross section.

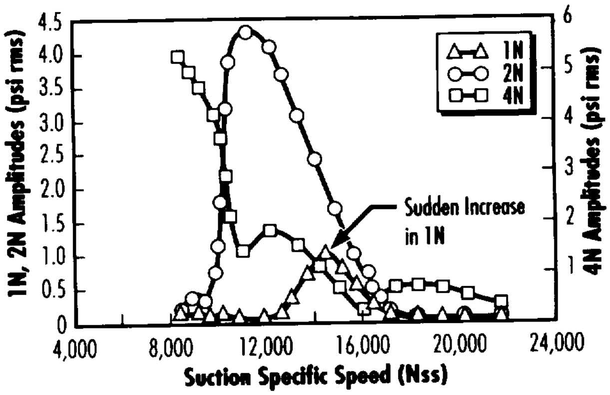

FIGURE 122.—ATD lox pump inducer shroud water flow dynamic pressure data.

The lox pump vibration investigation summarized above prompted renewed interest in turbopump inducer cavitation and the resulting rotor loads. To further investigate the various inducer cavitation modes and quantify the rotor loads, an effort has been initiated at MSFC to retest the ATD lox inducer with improved flow visualization access, additional inducer housing measurements, and on-rotor dynamic pressure and strain measurements. The objective of this effort will be to: (1) develop advanced testing and analysis methods for studying inducer cavitation and unsteady blade loads, (2) identify unsteady and destabilizing cavitation modes, and (3) quantify the noncavitated and cavitated inducer blade hydrodynamic loads. This effort is expected to directly benefit the ATD program in the short term and reduce the cost and risk to future turbopump development programs in the long term.

Sponsors: Office of Advanced Concepts and Technology, and Alternate Turbopump Development Project Office

■

Bosch Reaction Kinetics Research

Robyn L. Carrasquillo/ED62
205-544-7227

Recovery of O_2 from CO_2 is essential to enable closure of the O_2 loop in the space station Environmental Control and Life Support System's air revitalization subsystem. A promising method that was evaluated is the Bosch reactor. Improvements in the reactor design are needed to make this method more suitable.

The objective of this project was to investigate the reaction kinetics occuring in the Bosch CO_2 reduction subsystem reactor-furnace to obtain a quantitative rate expression based on catalyst quantity, reactor temperature, and constituent concentrations. This rate expression would then be used for analytically modeling the Bosch subsystem, which would lead to optimizing the Bosch process efficiency. A secondary objective was to identify alternate catalysts or enhancement to the present catalyst providing improved reaction rates, reduced startup time, and reduced catalyst degradation.

A thermodynamic computer model was developed to investigate the different regions of operating conditions (temperature, feed composition, etc.) to identify operating conditions where the thermodynamics for the Bosch reaction are unfavorable. Several catalysts including nickel and iron were then studied for transient rate effects at different temperatures and as carbon is deposited on them. Nickel was found to be a strong methanation catalyst at lower temperatures, but did not significantly decay in activity. Two iron catalysts were studied; both exhibited an initial rate drop followed by a sharp increase to levels comparable with nickel. Activity degradation occurred on iron, but was less severe on iron supported on gamma-aluminum oxide (Al_2O_3). The most significant finding in these studies was that under none of the conditions studied was the testing able to produce filamentous carbon as seen in all prototype Bosch subsystems. The carbon formed was amorphous, having a much higher inherent density than filamentous. Finally, a steady-state reaction rate expression was developed relating rate of carbon dioxide reacted to partial pressures of constituents and reaction temperature. This expression will be used to enhance phenomenological models of Bosch subsystems.

Sponsor: Office of Space Systems Development

■

Cylinder Optimization of Rings, Skin, and Stringers

Jeffrey L. Finckenor/ED52
205-544-7041

Patrick R. Rogers/ED24
205-544-4632

Neil E. Otte/ED24
205-544-7231

Cylinder Optimization of Rings, Skin, and Stringers (CORSS) is a computer program written to optimize the preliminary design of stiffened shells of skin-stringer construction. A commercially available optimization program called Design Optimization Tool (DOT) is linked to a skin-stringer analysis. The analysis uses closed-formed solutions and engineering design equations. DOT calls the analysis to evaluate the weight and limitations of a given configuration and iterates to find, numerically, the minimum weight design.

At the beginning of the National Launch System (NLS) program, a skin-stringer construction was baselined for much of the vehicle. Since there would be a number of design cycles, CORSS was written to enhance the turnaround time and accuracy of the primary structure designs.

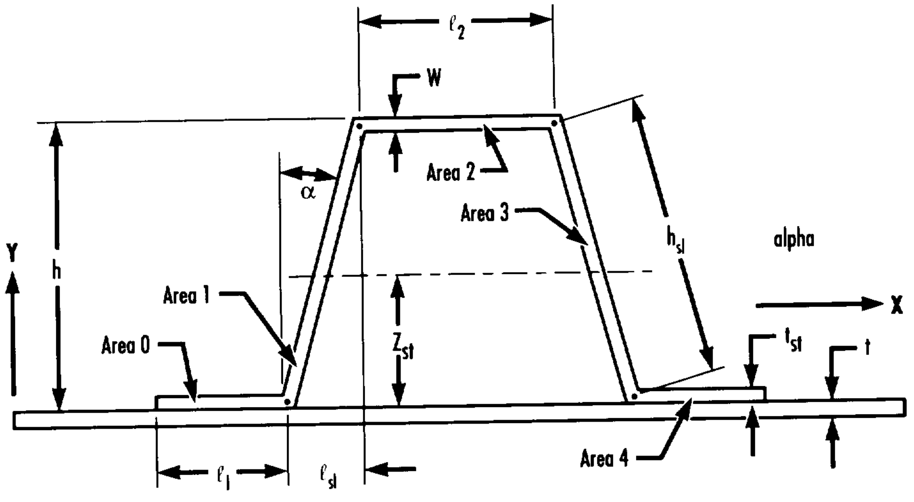

Hat-Stringer

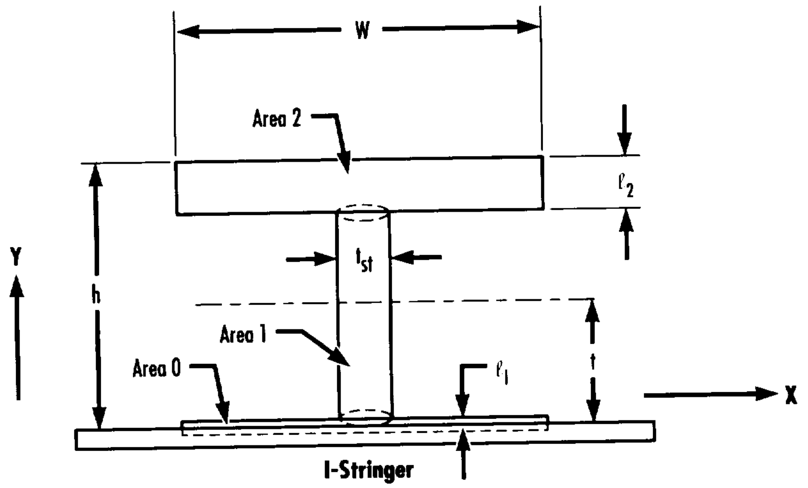

I-Stringer

FIGURE 123.—Stringer dimensions.

The analysis was written in the "C" language and linked to the DOT FORTRAN code. The optimizer varies the stringer dimensions (h, ℓ_2, tst) (fig. 123); the number of stringers (Nst); and the skin thickness (t). The failure modes considered are skin buckling, shell buckling, allowable stress, stringer crippling, and stringer local buckling. Figure 124(a) shows a typical optimization history of normalized design variables. Figure 124(b) shows the history of the constraint values. For DOT, a negative value means the constraint is satisfied. The variation of the values by DOT and the effect of the changes on the constraints can be clearly seen. The general decrease in weight during the optimization is also apparent. Depending on the initial conditions, run time varies from 6 s to 1.5 min.

Extensive use of CORSS was made during the NLS project. It was applied to every major component of the 1.5-stage vehicle and the 9,100-kg-payload (20,000 lb) vehicle, two-stage, NLS–3 vehicle. CORSS can be applied to any stringer-stiffened shell made of an isotropic material. This could include tanks for the railroad or trucking industries, farm silos, and so forth.

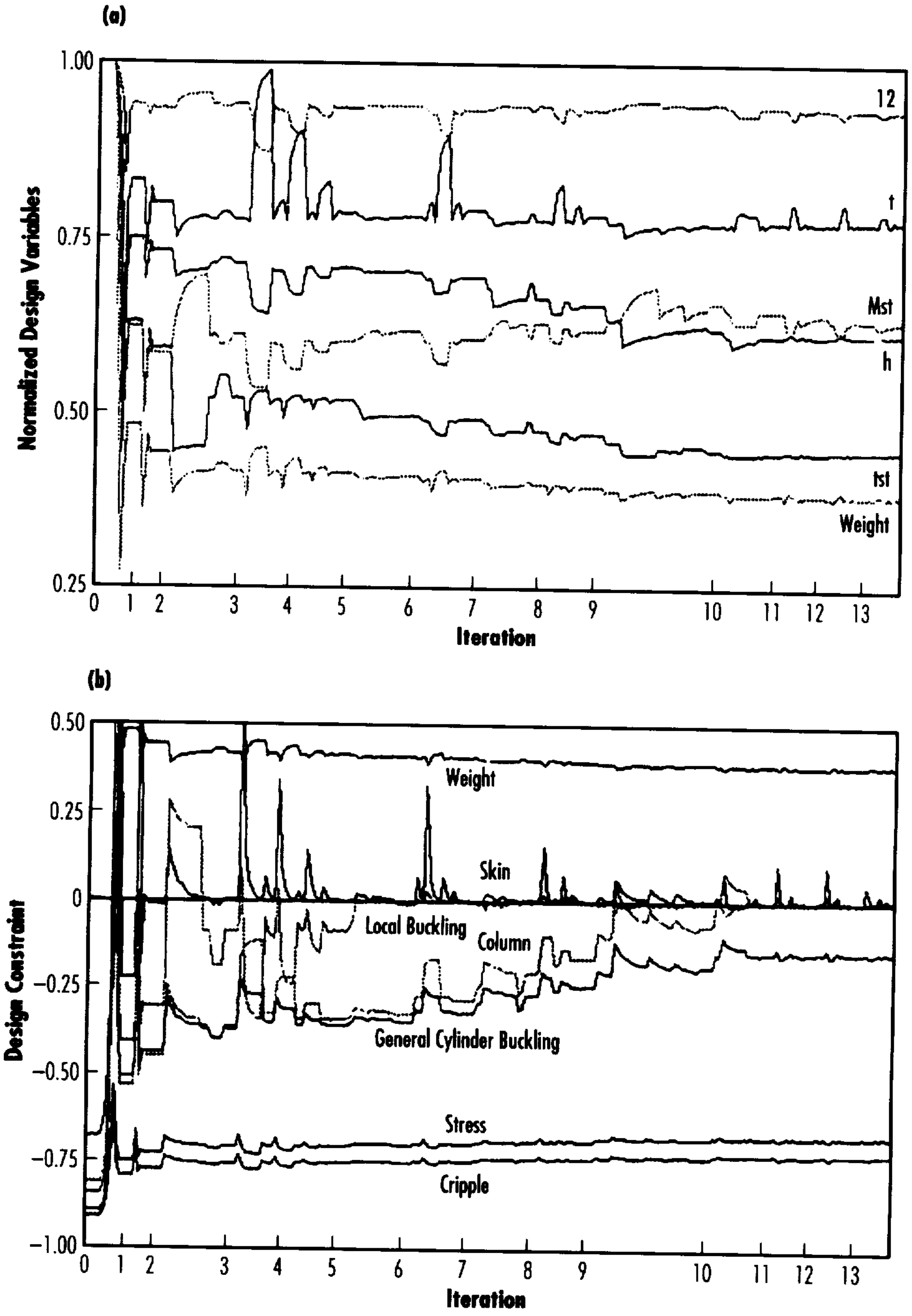

Figure 124.—Normalized design variable history (a) and design constraint history (b).

CORSS is a practical application of optimization theory to real-world uses. It provides an easy to use, efficient design tool that links the analysis of a skin-stringer construction with a numerical optimizer. It allows a large variety of different designs to be evaluated quickly and easily allows limits, such as those from manufacturing facilities, to be included. All the major failure modes are checked.

Bruhn, E.F. 1973. *Analysis and Design of Flight Vehicle Structures.* Jacobs Publishing, Inc.

Timoshenko, S. 1936. Theory of Elastic Stability. *Engineering Sciences Monograph.* McGraw-Hill.

Vanderplaats, G., and Hansen, S. 1985–88. Design Optimization Tool. VMA Engineering.

Sponsor: Office of Space Systems Development

Commercial Involvement: Martin Marietta Corporation

■

Optimum Design of Launch Vehicle Structures

Donald B. Ford/ED52
205-544-2454

Recent launch vehicle design activities and current trade studies emphasize the need for both quick turnaround time and the ability to evaluate synergistic effects of multiple design variables. A computer tool that can transform preliminary design data into an optimally feasible vehicle reduces the initial detail design time. MSFC, in a joint agreement with General Dynamics, is developing a tool to size major launch vehicle structural elements, such as propellant tanks and intertanks.

Minimizing the total mass or maximizing the performance are two main approaches of launch vehicle design. Numerical optimization techniques manipulate multiple design variables to arrive at the global optimum point within given constraints. Linking modular computer programs from several disciplines to a numerical optimizer is the basic framework for the development effort. Incremental results from each analytical module influence the overall vehicle as the design is driven to converge at the best solution. Thus, the optimum vehicle is better than that of a vehicle combining independent optimum elements.

The framework to perform the analysis consists of three components (fig. 125). First is a numerical optimizer to control the change of the design variables. Any one of several public or commercially available routines can perform the necessary calculations. Second is a management system to govern the variables being passed back and forth. All variables must be accounted for as they are changed. Third is a set of analysis modules to compute values for each variable. Each module represents the function of a design team within a given discipline. The framework allows fast low-fidelity calculations to be interchanged with more intense analysis routines.

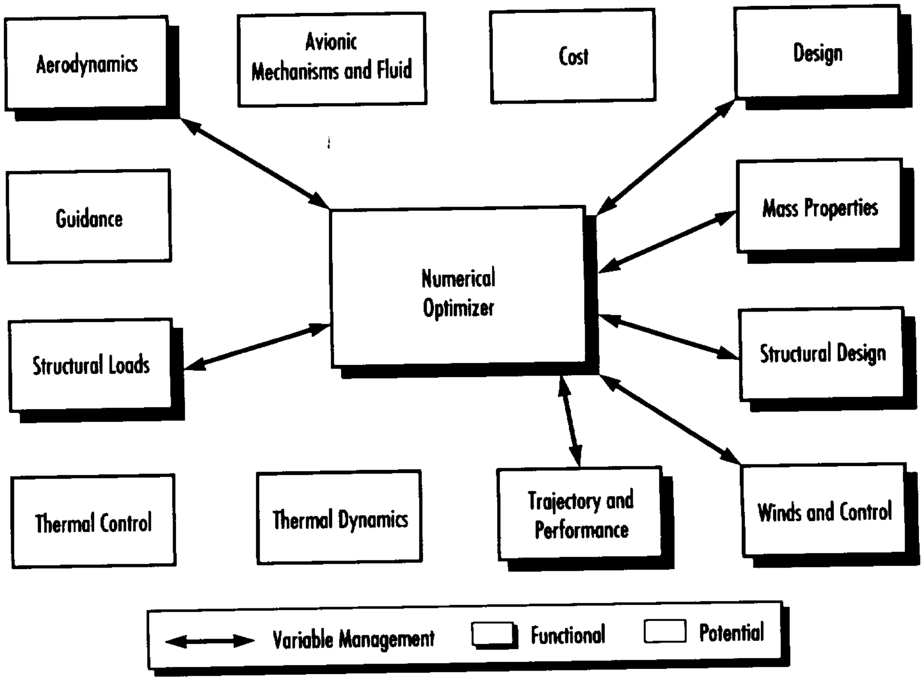

FIGURE 125.—Design tool framework.

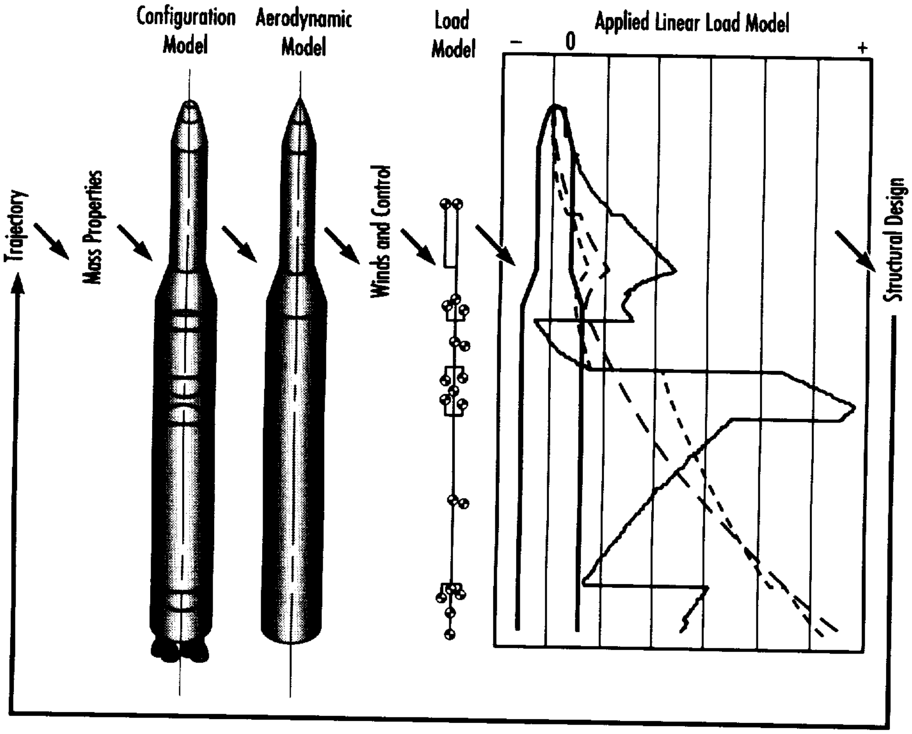

FIGURE 126.—Iterative design cycle.

The recent NLS study provided a configuration to benchmark the design tool capability. A test case successfully ran with the current functional modules and provided a working platform to add potential modules. An iterative cycle uses ground winds, maximum dynamic pressure, and maximum acceleration conditions to establish loads and size the major structures of the launch vehicle (fig. 126). This initial single-configuration tool is being further developed to handle a variety of vehicle configurations. Individual modules are already being used in the detail design of hardware. Both aerospace and other industries can apply this approach to any design effort.

Combining the expertise of separate disciplines with the speed of computers benefits the design process, as well as the design. The result is useful in three ways. It allows a vehicle concept to be quickly evaluated. It enables a variety of variables to be traded against each other. It also provides an accurate starting point for a detail design activity. The design cycle proceeds faster and produces a better total product.

Sponsor: Office of Space Systems Development

Commercial Involvement: General Dynamics

■

System for Anomaly and Failure Detection

Thomas H. Fox/ED14
205-544-1462

Since ground testing of the SSME began in 1975, there have been 36 major incidents. These failures occurred despite an extensive internal system of self-checking and measurement redlines designed to safeguard the SSME. This number almost seems insignificant when compared to the over 1,500 tests made without major incidents. However, these failures have costs associated with them that belie their small numbers. These include costs from engine damage, stand damage, analysis costs, engine component loss, loss of failure evidence, and schedule impacts.

An analysis of these failures showed that most of them could have been detected earlier than the present SSME redline method, with improved observability of engine operation. All the SSME failures were examined to determine which engine measurement, or suite of measurements, would indicate deteriorating SSME operation and incipient engine failure. It was found that almost all of the engines involved in these failures could have been shut down earlier than redline-initiated shutdowns. A small list of generic failures types was ascertained that covered these 36 failures. Work was initiated to develop an algorithm for the detection of incipient engine failure during the steady-state engine operation as a first cut. This algorithm has since been improved to include monitoring the nonlinear portions of engine operation.

Work has also started to extend monitoring to transient engine operation. This last improvement should be implemented in 1994. A ground-based computer system containing the System for Anomaly and Failure Detection (SAFD) algorithm has, to date, monitored 17 hot-fire tests on the Technology Test-Bed stand at MSFC. This system has also hosted other engine health monitoring algorithms during a part of this series of tests. The ground-based system can run the algorithms in a stand-alone mode or in parallel with other algorithms. The system has the capability to delegate engine shutdown authority to a selected set of these algorithms. Those algorithms not selected would be in a passive monitor mode only.

The SAFD algorithm has been tested against a mixture of successful and failed tests using a combination of simulations and tapes of real, hot-fire tests. In all cases, the SAFD algorithm showed an improvement over red-line methodology by issuing significantly earlier shutdown commands (tables 6 and 7), except in the cases where catastrophic failures occurred.

Sponsor: Earth-to-Orbit Technology Office, Office of Advanced Concepts and Technology

Commercial Involvement:
Rockwell International, A Division of Rockwell International

■

Table 6.—*SSME simulated actual and hypothetical failures—stand tests*

No.	TTB Test No.	Cut Request	Comments
1	26	No	First monitored test
2	27	No	Full duration test
3	28	Yes	Lack of compensation for mixture ratio shift
4	29	No	Full duration test
5	30	No	Redline cut made at 5.3 s (good test)
6	31	No	Full duration test
7	32	No	Full duration test
8	33	No	Full duration test. Hydrostatic bearing test
9	34	No	Full duration test. Hydrostatic bearing test
10	35	No	Full duration test. Hydrostatic bearing test
11	36	No	Pratt and Whitney (P&W) high-pressure fuel turbopump (HPFTP)
12	37	No	P&W HPFTP
13	38	No	P&W HPFTP
14	39	Yes	Large throat main combustion chamber (MCC). First instance check error
15	40	Yes	Large throat MCC. First instance check error
16	41	No	Large throat MCC. P&W high-pressure oxidizer turbopump (HPOTP)
17	42	No	Large throat MCC. P&W HPOTP and HPFTP

Table 7.—*Other tests*

No.	TTB Test No.	Redline	SAFD	Comments
1	750–175	116.06	116.06	High-pressure oxidizer duct
2	750–285	223.50	212.48	Feed line
3	901–173	201.17	201.02	Main injector; also run at Canoga Park, MD
4	901–183	51.00	50.35	Main injector
5	901–225	255.63	255.61	Main oxidizer valve
6	901–284	9.88	7.14	Controller
7	901–340	405.50	295.42	HPFTP
8	901–364	392.16	386.00	HPFTP, venting/repressurization
9	901–511	—	—	Nominal
10	901–551	—	—	Nominal
11	901–558	—	—	Run for United Technologies Research Center (UTRC), algorithms only, full duration
12	901–577	—	—	Run for UTRC, algorithms only, high-pressure oxidizer turbine (HPOT) total discharge temperature (TDT)
13	901–683	—	—	Nominal
14	902–249	450.57	350.32	HPFTP, venting/repressurization; Canoga Park, MD; Huntsville Simulation Lab
15	902–398	—	—	Nominal
16	902–428	204.12	190.00	Oxidizer preburner injector, venting/repressurization
17	902–461	—	—	Run to develop a statistical base
18	902–462	—	—	Run to develop a statistical base
19	902–471	147.68	146.76	Duct, flex joint
20	902–463	—	—	Run to develop a statistical base
21	902–519	—	—	Nominal
22	902–532	—	—	Nominal
23	902–149	109.86	109.78	Facility acceleration redline on HPOTP
24	DTM	—	—	Hypothetical preburner pump discharge duct
25	DTM	—	—	Hypothetical HPFT discharge flow block

Note: A simulation of engine 0215 in test 901–666 showed that a shutdown command issued only 0.38 s earlier than the redline shutdown would have avoided significant engine damage.

Cold Air Flow Turbine Testing of Advanced Turbine Designs

Stephen W. Gaddis/ED34
205–544–1612

The SSME alternate turbopump development high pressure fuel turbine test article (TTA) was configured with state-of-the-art aerodynamic design concepts and tested with the MSFC cold air flow turbine test equipment (TTE). The test program was a cooperative endeavor between MSFC and Pratt and Whitney's commercial and government divisions. Testing evaluated turbine aerodynamic performance and provided results to validate various CFD codes used during the design process.

The MSFC TTE is a cold air flow blowdown facility that operates by expanding high pressure air from 2.9 MPa (420 lb/in^2 gauge) to atmospheric conditions. This equipment can deliver air for run times from 30 s to over 30 min, depending on test conditions. The TTE can accurately control and measure pressures, temperatures, shaft speed, torque, and horsepower. Full-scale test articles can be tested at scaled performance conditions accurately measuring pressures, temperatures, gas path flow angles, blade tip clearances, dynamic pressures, and gas path velocities by hot-wire or laser velocimetry.

The test included the original baseline two-stage, axial-flow ATD fuel turbine TTA with modifications.

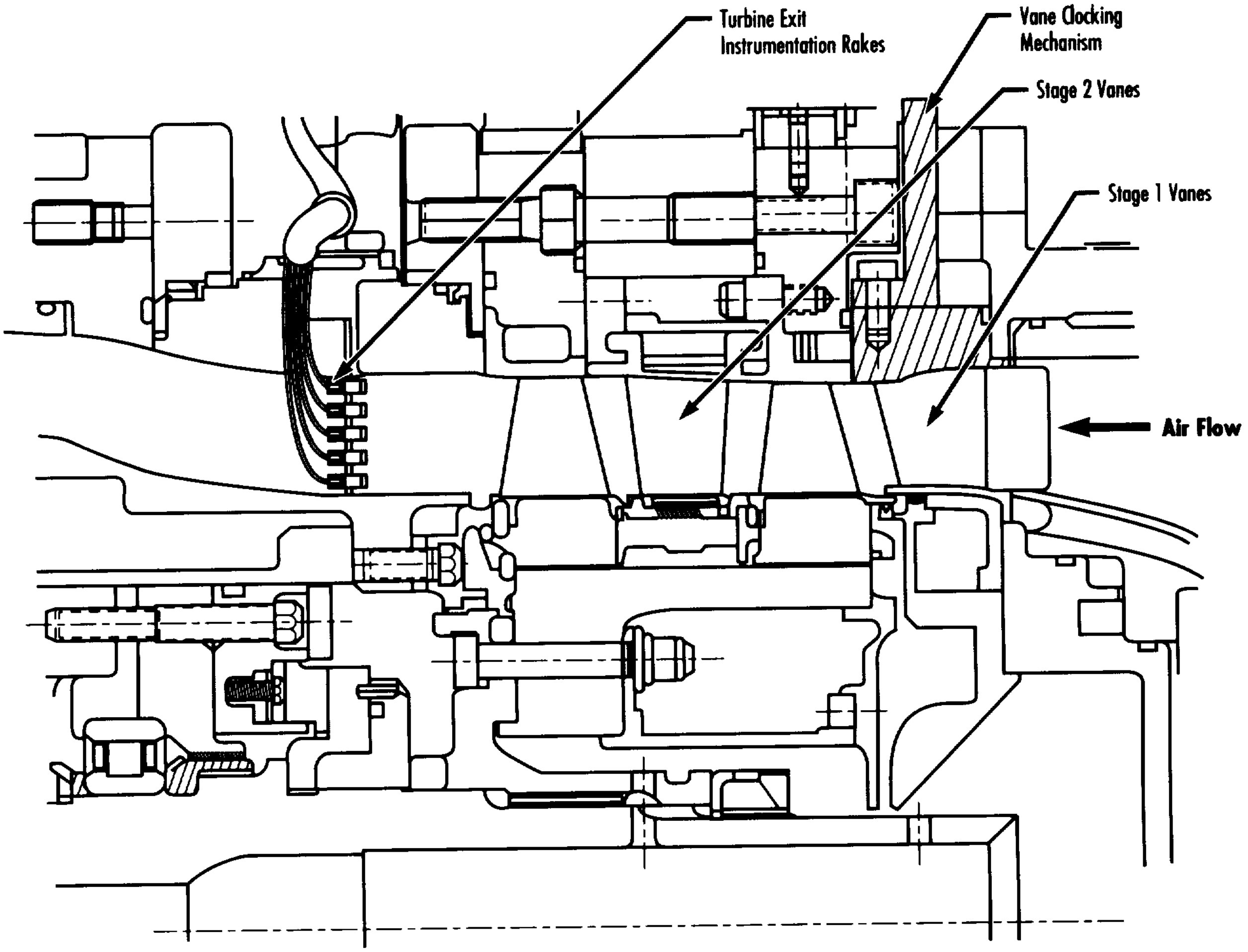

FIGURE 127.—Cross section of vane clocking turbine test article.

A mechanism was included in the test article design that allowed the first stage vane assembly to be rotated circumferentially in relation to the second stage vanes. Matching the number of first stage and second stage vanes in the test article incorporated an advanced design concept called vane clocking (fig. 127). The test article was configured with 54 first stage vanes, instead of the 52 vanes in the original baseline test. Thus, first stage vanes were aligned relative to the downstream second stage vanes to determine the performance effect of the first stage vane wake interaction with the downstream vanes. The test results were compared to the baseline test yielding a 0.5 percent increase in turbine efficiency at the design point. Results from the advanced design features incorporated in this test program are applicable to aircraft engines, liquid rocket engines, and land-based turbomachinery.

Sponsor: Office of Advanced Concepts Technology

■

Pump Computational Fluid Dynamics Code Validation Tests

Roberto Garcia/ED32
205-544-4974

A significant amount of performance data exists for many pump types. Empirical models have been created using the existing data, and it is these models that have been used to design pump components. Advances in pump design have been made by extrapolating from past experience, which inherently leads to increased developmental risk. The use of computational fluid dynamics codes in the design process can reduce the risks associated with advancing pump designs. However, before CFD codes are applied in the design process, they must first be benchmarked against test data to verify their applicability and to obtain a measure of their accuracy. Under this task, detailed velocity measurements are made at several stations in the flow path of selected pump components for comparison with the CFD predictions.

The SSME high-pressure fuel turbopump impeller was chosen as the first component to be tested. It was chosen because it represents the state of the art in impeller design and performance. Laser velocimeter measurements were made on a 1610 grid at the impeller inlet that was used by the CFD analysts as the upstream boundary condition in their models. Similar data grids were obtained at three radial planes downstream of the impeller. Also obtained were pressure measurements on the stationary walls. This data set is the first of its kind for a rocket engine impeller. The data have been used to assess seven CFD codes currently being used by either industry, academia, or the Government. The experimental results and some of the code comparisons have been published.

The second component tested under this task is a conventionally designed impeller that was optimized using CFD. Despite having 50 percent as many blades as the SSME impeller, this impeller was predicted to have increased performance and decreased distortion. Therefore, this test was conducted to verify the performance of a design arrived at using CFD. The data show that the velocity field and, hence, performance were very well predicted by CFD (fig. 128). Furthermore, the comparisons for this impeller

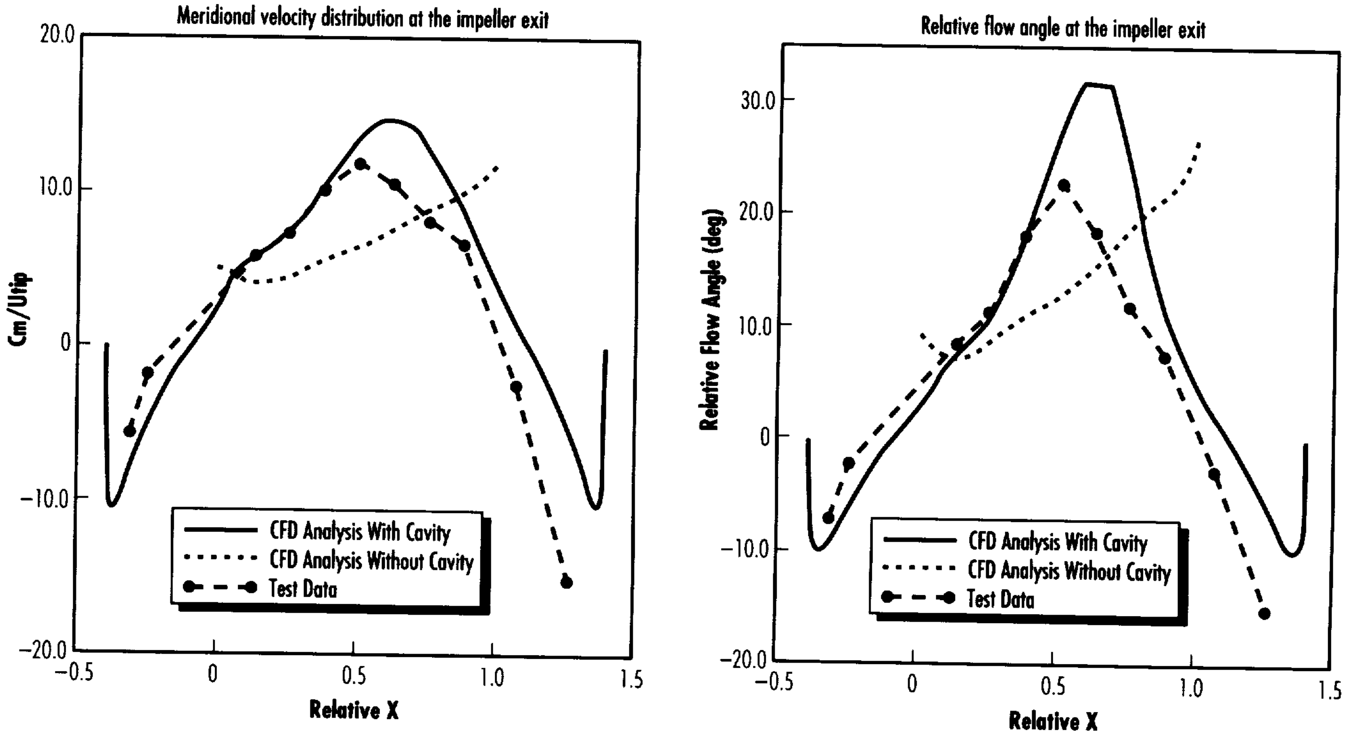

FIGURE 128.—Impeller CFD analysis comparison to data.

showed that while the average performance of an impeller is not affected by details of the geometry downstream of the impeller (such as a sudden expansion cavity), the distribution of performance from hub to shroud is significantly affected.

The data collected under this task have demonstrated the applicability of CFD codes for the design of centrifugal impellers. Presently, similar data are being collected for a typical rocket engine pump inducer. That experimental work will be followed by the acquisition of diffuser data.

Brozowski, L.A. et al. May 8–11, 1994. Impeller Flow Field Laser Velocimeter Measurements. To be presented at ISROMAC–5 Conference, Kaanapoli, Maui, HI.

Brozowski, L.A. et al. June 20–24, 1993. Laser Velocimeter Measurements of an Impeller Flow Field. Presented at the ASME Fluids Engineering Conference Second Pumping Machinery Symposium, FED, Washington, DC. 154:187–96.

Prueger, G.H. et al. June 28–30, 1993. Validation of Computational Fluid Dynamic Analysis of a Rocket Engine Turbopump Impeller. AIAA 93–2575. AIAA/Society of Automotive Engineers (SAE)/American Society of Mechanical Engineers (ASME)/American Society of Electrical Engineers (ASEE) 29th Joint Propulsion Conference and Exhibit, Monterey, CA.

Sponsor: Office of Advanced Concepts Technology

■

Hydrodynamic Design of Advanced Pump Components

Roberto Garcia/ED32
205-544-4974

The design of pump components has not significantly changed over the last 30 yr, while their operational requirements in rocket engines have increased. Today's rocket engine designs are requiring higher specific work pumps and lower dynamic loadings, while maintaining high efficiency. These requirements cannot be easily met using conventional design practices without incurring increases in development costs. Under this task, MSFC is applying CFD tools to the design process to produce higher performance pump components with reduced developmental risk.

This task has focused on centrifugal pump impellers as the pump component that could most readily benefit from the applications of CFD in the design process. As a demonstration case, a conventionally designed impeller was optimized using CFD (fig. 129). A comparison of the resulting impeller design and the SSME high-pressure fuel turbopump shows that this new impeller has nearly the same efficiency as the SSME impeller, but does 11 percent more specific work and its discharge flow field has 12 percent less distortion. Furthermore, the new impeller has 50 percent less blades than the SSME impeller, making it less expensive to produce. Subsequent testing of this new design confirmed the CFD predictions.

FIGURE 129.—Conventional design optimized using CFD: increased performance and reduced distortion.

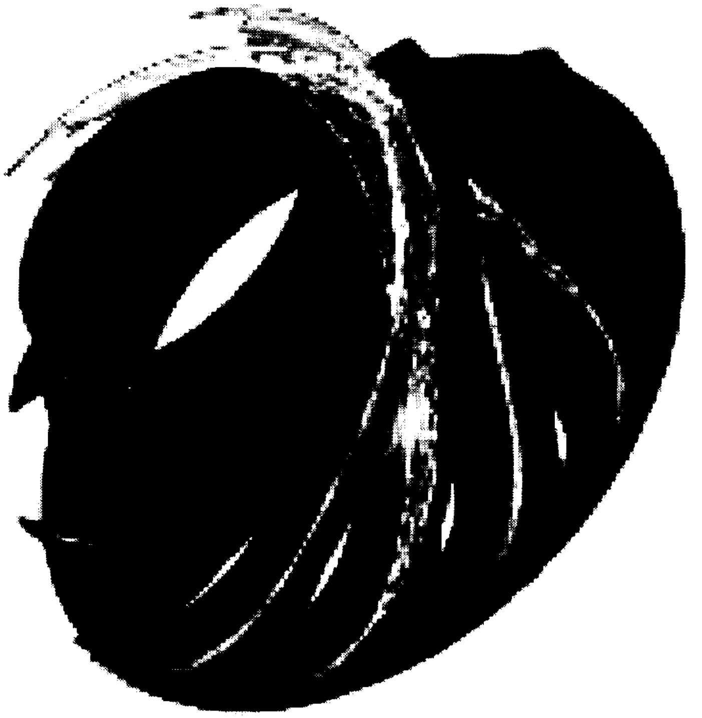

FIGURE 130.—CFD-developed advanced impeller concept: increased performance and uniform flow (white streak lines indicate the path taken by fluid particles).

The next step was to apply the new understanding on centrifugal impeller flows that were acquired during the optimization of the first impeller to the design of impellers incorporating new geometric concepts (fig. 130). Concepts evaluated included tandem blades, blade lean, repositioned partial blades, and tailored chordwise loading distributions. The final design of this advanced concept impeller is pending, but results obtained thus far show that leaning the blades leads to further distortion reductions (and, hence, lower dynamic loads) for the same specific work, without sacrificing efficiency.

The optimization of the conventionally designed impeller and the ongoing advanced concept evaluation have demonstrated the advantages of using CFD in the design process and have advanced the design of centrifugal impellers. The next step under this task is to make similar advances for the design of pump diffusers.

Sponsor: Office of Advanced Concepts and Technology

■

Elastic-Plastic Fracture Mechanics Methodology for Surface Cracks

M. Wayne Gregg/ED27
205-544-5501

Pressure vessels are an essential part of all propulsion systems. Failure of one of these vessels can be a catastrophic event resulting in the loss of millions of dollars, or human life. In order to ensure the safety of pressure vessels, safe-life analyses are often performed to ensure a flaw-tolerant design. In particular, pressure vessels of interest to NASA must comply with MIL–STD–1522A, *Standard General Requirements for Safe Design and Operation of Pressurized Missile and Space Systems.* However, pressure vessels are often used in operating conditions that produce significant plastic stress fields in the vicinity of the flaw. Because MIL–STD–1522A does not account for nonlinear stresses and is quite limited to the shape and growth characteristic of flaws, a research effort has begun to establish a methodology whereby pressure vessels may be designed to account for these effects.

Under the direction of a MSFC research grant, the Georgia Institute of Technology is performing testing and fractography in an attempt to develop an acceptable methodology for predicting "leak before burst" (LBB) in pressure vessels subjected to elastic-plastic fracture. In doing so, three major tasks are to be accomplished:

- The study of constraint and thickness effects in different specimen sizes and geometries
- The study of 3–D effects
- The development of a methodology to assess LBB.

Resistance curve testing of Inconel 718–STA1™ and Al 6061–T651 is currently under way to obtain curves that represent the energy required to grow the crack and to obtain fracture surfaces so that constraint and thickness effects may be measured. A preliminary assessment indicates that some flaw shapes do not grow self-similar, but instead tend to mushroom beneath the surface, thereby giving a false measure of the crack length. Leak-before-burst calculations on such flaws using the current method would erroneously predict a leak, whereas a burst situation may exist. In order to determine how 3–D effects create changes in crack extension, 2–D specimens are being tested.

Planar specimens have been observed to generate different fracture resistance curves when different thicknesses are tested. Because 3–D stress fields are present in planar configurations, mapping the crack face separation profiles at different locations throughout the cross section should produce parameters that can be generalized to the 3–D cases of interest. Several specimens have been tested, and characterization of the crack fronts is currently under way.

The research being conducted for this grant will result in an increase of the fundamental understanding of how surface cracks grow in the plastic region for a variety of crack shapes and sizes. More importantly, however, the knowledge gained will be an invaluable addition in ensuring the safe operation and design of pressure vessels.

Sponsor: Earth-to-Orbit Technology Office, Office of Advanced Concepts and Technology

University Involvement: Georgia Institute of Technology

■

Elastic-Plastic and Fully Plastic Fatigue Crack Growth

M. Wayne Gregg/ED27
205–544–5501

High performance demands placed upon launch vehicles and propulsion elements ultimately create an environment in which components experience stresses beyond the elastic regime. Life-prediction methods are needed to allow engineers to assess the longevity of these components under such conditions. Currently, knowledge about how flaw growth occurs is limited primarily to operating conditions that produce stresses in the elastic range. There exist, however, some independent solutions in the literature for prediction of cyclic plastic fatigue crack growth. These solutions are generally obtained via testing or finite element modeling and are valid only for a particular geometry and a defined set of boundary conditions. In order to obtain a practical method for predicting flaw growth in the plastic regime, an empirical or analytical model is needed that gives an acceptable solution for a range of boundary conditions.

Southwest Research Institute (SWRI) is currently working under contract for MSFC to develop analytical models for fatigue crack growth predictions in the plastic range.

By incorporating the reference stress method, along with modifications to existing linear elastic fatigue crack growth data, J-integral solutions are being formulated to allow quick solutions for crack growth problems. The objectives of this research are to:

- Review the literature and collect existing solutions for the J-integral, along with how the J-integral has been used for fatigue crack growth predictions
- Develop and verify new solutions for the J-integral for geometries of interest to the SSME program
- Collect information from previous research efforts about crack closure and develop schemes to incorporate this information into the estimation of governing parameters for elastic-plastic crack growth
- Develop and verify algorithms for calculating elastic-plastic fatigue crack growth life under variable load histories and combined load histories
- Develop and verify algorithms that account for time and temperature effects
- Develop damage rules for creep contributions to crack growth
- Develop and verify algorithms to predict the onset of final crack instability
- Incorporate the algorithms and new J solutions into a usable software package.

Several J-integral solutions have been collected along with a few newly developed ones of interest to the SSME. In particular, a closed-form equation for the deepest point of a semielliptical surface crack in a finite width plate has been developed using the reference stress approach. A comparison between finite element solutions and the reference stress estimate for J shows good agreement with published results for a variety of different crack depths, crack shapes, and material constitutive relationships. Currently, work is in progress to explore the applicability of the general methodology to other specific geometric configurations.

In addition to obtaining results for new J-integral solutions, an appreciable amount of work has been completed on the contribution of crack closure on fatigue crack growth. Most of the previous research on fatigue crack closure has been for center cracked panels, with a few studies having been performed on the single-edge cracked plate in bending, and the compact tension specimen. Results generally indicated that the crack opening stress is a function of the maximum stress. However, SWRI has found that different specimen geometries (center cracked panel, single-edge cracked plate in tension, and single-edge cracked plate in bending) exhibit different fatigue crack closure behaviors. Most specifically, the maximum stress does not correlate the effect of different geometries on the crack opening stress. This result indicates that a parameter other than the maximum stress is needed for describing the crack opening stress over a range of geometries. After further investigation, it was discovered that the normalized stress intensity successfully correlates crack opening stresses for the three different specimen geometries at three different crack lengths. The usefulness of the stress intensity approach to characterizing crack closure is readily apparent when considering the complexities and time involved in modeling many geometries and load configurations.

As work continues on elastic-plastic fatigue crack growth, there is no doubt that even more useful results will be brought forward. Once the algorithms are coded into a user-friendly software package, this new technology will enable engineers to more accurately predict the life of components that experience nonlinear stresses.

Sponsor: Earth-to-Orbit Technology Office, Office of Advanced Concepts and Technology

University Involvement: Southwest Research Institute

■

Advancement of Volute Design Techniques

Lisa W. Griffin/ED32
205-544-8972

Traditionally, volutes have been designed with limited analysis and a heavy reliance on an existing data base. This method of design has not always been successful for rocket engine turbopumps due to their complex flow paths and high pressures. Problems that can be encountered by poorly designed volutes are low performance and high side loads that have to be reacted by the bearings in both turbines and pumps. In order to enhance the state of the art in volute design and to mature computational fluid dynamics tools that have not been widely used for volute analysis, the Turbine Technology Team has initiated an advanced volute development program. The team is in the process of designing an inlet volute and an exhaust manifold system for the Gas Generator Oxidizer Turbine (GGOT). The GGOT, designed by the Turbine Technology Team, meets the requirements of the STME lox turbine (fig. 131).

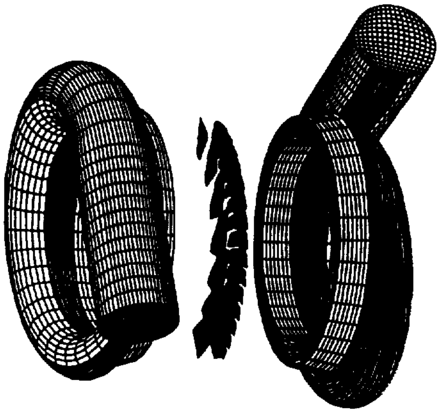

FIGURE 131.—Major elements of the GGOT.

Table 8.—*Exit volute design requirements*

	Annular Diffuser	Volute	Conical Diffuser
Inlet Mach Number	0.84	0.79	0.66
Exit Mach Number	0.79	0.66	0.30
Total Pressure Loss	2.50%	11.60%	3.40%

The baseline designs of the inlet and exit volutes have been completed. Integration of the inlet volute design with the turbine stators reduced the stator turning requirements, enabling an airfoil reduction count of approximately 50 percent. CFD analyses of the inlet volute are currently in progress, with the goals of minimizing the circumferential static pressure and gas angle gradients entering the turbine. Delivering uniform flow conditions to the stator is the key to minimizing radial side loads on the turbopump shaft.

The aerodynamic design of the GGOT exhaust manifold represents a formidable challenge. This component must not only efficiently collect a transonic turbine discharge flow, but it must perform its function with minimal interaction with the turbine stage. Undesirable interactions would cause performance degradations and could produce increased turbine side loads. Compounding the complexity of the volute design is the fact that rocket engine turbomachinery are generally operated at conditions off of their original design points. Therefore, the volute must be able to efficiently function over a range of conditions. The baseline exhaust manifold has been designed without guide vanes to reduce cost, weight, and complexity. Design requirements for the exit volute system are shown in table 8.

CFD analyses are currently being performed for the exit manifold. The most significant issue for the prediction of the exit volute performance is the application of the inlet boundary condition. The exit volute and the turbine are highly coupled. Therefore, calculations are being performed by various team members of the volute alone, with methods of simulating the turbine/volute interaction (such as by coupling the volute calculation with a one-dimensional turbine analysis), and of the entire turbine stage and volute. The results from these studies will provide guidance to analysts about what methods must be employed to generate accurate volute predictions. Initial results from the entire turbine/volute model show a predicted increase in radial pressure gradient over predictions from the stand-alone volute model by an order of magnitude.

Results from these analyses will be used to optimize the GGOT volutes. In 1994, the designs and numerical predictions will be verified with a test of highly instrumented volute models in the MSFC Turbine Airflow Facility. The volutes will be tested as a system with the GGOT so that proper boundary conditions will be maintained. This program will further volute aerodynamic design technology, demonstrate the capabilities of CFD in the volute design process, and provide a unique set of volute experimental data.

Sponsor: Office of Advanced Concepts and Technology

■

Development of Advanced Turbine Blades

Lisa W. Griffin/ED32
205-544-8972

In order to further the state of the art of turbine aerodynamic design, the Turbine Technology Team of the consortium for Computational Fluid Dynamics Application in Propulsion Technology initiated an advanced subsonic turbine development program. The purpose of this program is to demonstrate the benefits of CFD application during the turbine design process and to develop a turbine with increased efficiency and enhanced robustness. To ensure program output relevant to current needs, the team focused on design requirements consistent with the STME. Concentrating on requirements for an actual turbopump allowed the team to focus on a clear deliverable product and schedule. However, the resulting technology is generic.

The Turbine Technology Team consists of experts in turbine design, analysis, and testing representing the Government, industry, and academia. Each team member brings unique knowledge and expertise to the fuel and oxidizer turbines designed for the advanced subsonic turbine development program.

The STME employs a gas generator cycle requiring the turbines to operate at very high values of stage-specific work. Traditional designs for the turbines would be velocity-compounded or pressure-compounded impulse turbines. These types of turbines tend to be inefficient and have high Mach numbers. In order to meet the STME requirements and the team's performance and robustness goals, the Turbine Technology Team's fuel turbine design—called the Generic Gas Generator Turbine (G^3T)—incorporates reduced through-flow velocities and increased reaction relative to previous gas generator experience.

Reducing the through-flow velocities required blading camber of approximately 160 degrees. This turning angle is well beyond the maximum experience of approximately 140 degrees. CFD analyses of this design were performed by different team members. The findings from each analysis were incorporated into the final G^3T design, which was predicted to have significant performance and cost benefits over traditional designs (table 9). A particularly significant finding was the effect of airfoil spacing on efficiency and dynamic loading. Calculations performed for conventionally chosen axial spacing revealed an unsteady, inner row shock wave (fig. 132). A subsequent unsteady CFD study was performed to determine the optimal spacing. The G^3T redesigned with this predicted optimal spacing showed a predicted gain of a point in efficiency and a reduction in blade dynamic loading of 24 percent from the baseline design.

TABLE 9.—*Comparison of conventional design and G^3T (as predicted by a meanline analysis)*

	Conventional	G^3T
Number of Stages	2	2
Work Split	70/30	50/50
Blade Turning	140 degrees	160 degrees
Max Blade Mach Number	1.32	0.87
Efficiency	Base	+ 9.8 Percent
Airfoil Count	Base	– 55 Percent

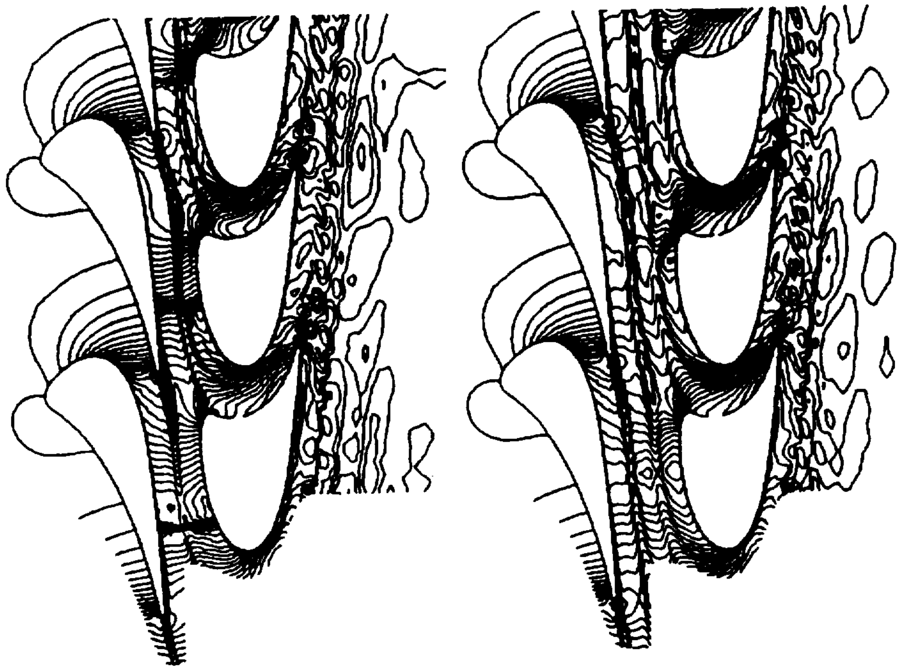

Predicted Preliminary Design

Final Baseline Design

FIGURE 132.—Temperature contours for the G^3T for two axial spacings.

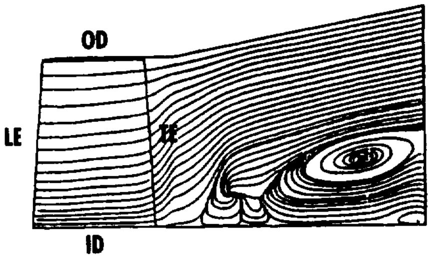

Preliminary Design

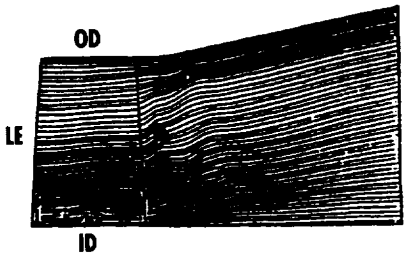

Final Baseline Design

FIGURE 133.—Predicted streaklines downstream of the GGOT rotor.

The team then incorporated the high cambered airfoils into a design meeting the STME lox turbine requirements. This design concept enabled a single-stage configuration, as opposed to the two-stage design baselined for STME. Analyses were again performed by various team members. Results from a 3–D Navier-Stokes analysis of the team's design, called the Gas Generator Oxidizer Turbine, indicated a flow separation downstream of the rotor at the hub (fig. 133). The lean of the airfoil was adjusted until calculations confirmed the elimination of the separation. The final design was predicted to have a gain in efficiency of two points over the baselined STME lox turbine. The STME Program decided to use the GGOT design concept for its lox turbine, resulting in an estimated life-cycle cost savings of $71 million. Verification of the design and the CFD analyses will be provided by cold-flow testing of a highly instrumented GGOT test article. The test will be performed in the MSFC short-duration Turbine Airflow Facility in 1993.

Griffin, L.W., and Huber, F.W. 1993. Advancement of Turbine Aerodynamic Design Techniques. ASME paper 93–GT–370.

Huber, F.W.; Johnson, P.D.; Montesdeoca, X.A.; Rowey, R.J.; and Griffin, L.W. 1992. Design of Advanced Turbopump Drive Turbines for National Launch System Application. AIAA paper 92–3221.

Sponsor: Office of Advanced Concepts and Technology

Verification of Analytical Methods—Single Cycle Versus Multicycle Proof Testing

Henry M. Lee/ED25
205-544-7245

The overall objective of this effort is to assess the relative advantages and disadvantages of single-cycle versus multicycle proof testing.

Rocketdyne, the current SSME contractor, uses a multicycle proof testing procedure that consists of the application of five proof cycles at a minimum pressure of 1.2 times the maximum operating pressure, each with a minimum hold-time of 30 s. The proof pressure is selected to keep nominal stresses below 85 percent of ultimate strength. A fracture mechanics-based theory of multicycle proof testing is being formulated in terms of crack resistance curve concepts. Crack resistance curves for surface crack panels of Inconel 718™ have been developed. Analytical and experimental work previously accomplished has clearly shown that the conditions of constraint and control on the local level around a crack have very significant influence on the subsequent behavior of that crack during single cycle or multicycle proof testing.

A component that satisfies local displacement control may be a poor candidate for proof testing of any type because significant flaw growth can occur on any cycle. An improved analytical model based on tear fatigue has been shown to be consistent with previous experimental and analytical observations. The new model shows great promise for unifying the framework to describe multicycle proof test behavior.

Work to date has primarily been focused on the high toughness, low hardening superalloy Inconel 718™. Other materials that exhibit low toughness characteristics, high hardening rates, or substantial cyclic softening will be studied. A practical engineering guidelines handbook will be developed that has a comprehensive formulations-of-proof test philosophy for service life.

Sponsor: Office of Advanced Concepts and Technology

Commercial Involvement:
Rocketdyne, A Division of Rockwell International

■

Fracture Control/Damage Tolerance Methods for Composite/Anisotropic Materials

Rene Ortega/ED25
205-544-5448

Composite/anisotropic materials are increasingly being considered for structural use in space systems. These materials are capable of providing many benefits to structural systems due to their strength capabilities, thermal properties, reduced weight, and so forth. However, there is an increased need to accurately establish their damage tolerance capabilities. Damage tolerance is the ability of a structure to sustain loads after crack initiation. Much research on the damage tolerance of composite/anisotropic materials has been carried out over the past 20 yr. However, a need remains to compile and consolidate the various aspects of the research that has been done in this area.

Damage tolerance consists mainly of three aspects: (1) residual strength provides the maximum damage the structure can resist under fail-safe loads, (2) crack propagation defines the time period in which a crack grows from a defined detectable length to the allowable length determined by the residual strength requirement, and (3) damage detection specifies inspection methods and intervals needed to identify flaws. The work reported here involves the residual strength and crack propagation aspects of damage tolerance of composite/anisotropic materials.

The objectives of this research are to develop a guidelines handbook for damage tolerance testing of composite/anisotropic materials and to test verified algorithms for calculating flaw growth in these materials. These algorithms are to be in a format that can readily be inserted into existing computer codes.

A review of current state-of-the-art testing methods for flaw growth and fracture toughness was initiated on composite/anisotropic materials. Initial literature surveys were conducted on damage tolerance involving single-crystal, laminated-metal, and laminated-fiber composites. Preliminary evaluation of the literature on single-crystal materials revealed that stress intensity factors and da/dN measurements are appropriate parameters for estimating fracture growth.

The characterization of damage is currently being explored for application on current programs using composite materials, such as the SSME combustion chamber for laminated metals.

Engineering algorithms for calculating fatigue crack growth life for composite/anisotropic materials will be developed. A wide range of crack type, geometry, and loading cases will be considered. Laboratory test data, when available, will be used to verify the accuracy of the developed algorithms.

Sponsor: Office of Aeronautics, Exploration, and Technology

■

Study of Trace Contaminant Control System Catalysts

Jay L. Perry/ED62
205–544–2730

Development of a more robust catalyst system for oxidizing atmospheric trace contaminants at ambient and moderately high temperatures without poisoning is needed. Such a system may eliminate the need for expendables, such as activated charcoal, and high power requirements associated with regenerable charcoal.

The major objectives of this project are to screen suitable coprecipitated catalyst candidates for metal/metal-oxide catalyst development, characterize activity and poisoning susceptibility, develop processing and fabrication techniques, and develop a suitable catalyst support. A co-precipitated catalyst was developed that is capable of oxidizing carbon monoxide at temperatures as low as –70 °C with no water vapor poisoning. The catalyst also exhibits greater activity than conventional platinum- and palladium-based catalysts for methane oxidation at high methane concentrations. The activity is essentially the same as palladium-based catalysts currently in use for low methane concentrations; however, the new catalyst exhibited significantly greater poisoning resistance. In addition, under humid conditions, the new catalyst showed higher activity than the palladium-based catalyst.

A performance prediction method was also developed that assesses the compatibility of the metal work function and metal oxide valence and conduction bands for electron transfer and, therefore, allows a prediction of which metal/metal-oxide combinations make the most suitable catalysts.

Sponsor: Office of Advanced Concepts and Technology, Small Business Innovation Research

Commercial Involvement: TDA Research, Inc.

■

C-3.

Dynamic Modeling of Bearings

Stephen G. Ryan/ED14
205-544-1467

Rolling element bearing models typically ignore race flexibility and clearance (deadband) in the bearing support. Enhanced mathematical models and associated computer programs have been developed that include the effects of race and support flexibility and outer race deadband on the force deflection relationships (stiffness) of ball and roller bearings.

This analysis tool, known as Flexibility Enhanced Rolling Element Bearing Analysis (FEREBA), utilizes ANSYS™ finite element models of the races, support structure, and the deadband (gap elements) to represent the flexibilities of these elements. These data are integrated into a classical quasi-static analysis formulation where general motion of all elements is allowed. Preload springs can be included in both simplex and duplex arrangements. This tool enables more accurate prediction of bearing mechanical behavior for use in rotor dynamic analyses.

Sponsor: Earth-to-Orbit Technology Office, Office of Advanced Concepts and Technology

■

Porous Wall Flow Experimental Facilities

Andrew W. Smith/ED36
205-544-4932

The simulation of the internal flow field of SRM's in cold-flow tests requires the prescription of a uniform blowing velocity injected through the wall. This blowing from the model wall simulates propellant burning within the rocket motor. The uniform blowing velocity distribution is usually simulated using porous wall tubes that are pressurized to yield different blowing rates. Knowledge of the flow behavior from porous materials is important for understanding the wall's contribution to the internal flow field.

Recognizing the need to support the MSFC cold flow Solid Rocket Motor Modeling Facility, laboratory-scale experimental facilities for investigating internal flows contributed by, or generated from, porous walls have been developed. The facilities include a flow resistance chamber, a shear flow water tunnel, and a duct flow air chamber.

The purpose of the flow resistance chamber is to obtain the mass flow and pressure loss relationship for a porous wall sample. This curve is important in the design of an SRM cold-flow model for determining air supply requirements. The chamber can test samples up to 10 cm in diameter at a maximum flow rate of 0.45 kg/s. Recent testing in this facility has focused on the reliability of pressure-drop information from the material supplier, and the discovery that upstream side surface conditions can influence the flow resistance of the material.

The shear flow water tunnel (fig. 134) was developed to investigate the near wall flow behavior of porous wall flow (y direction) in the

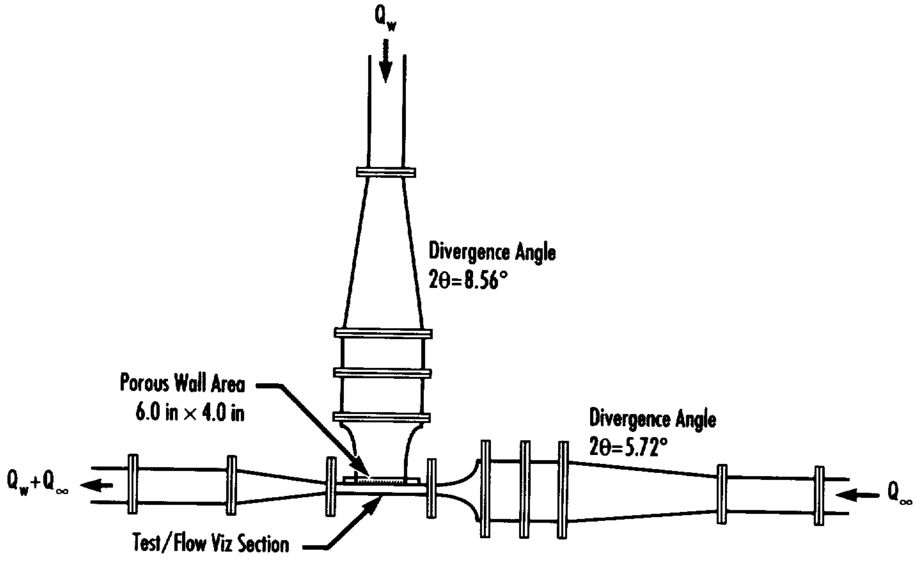

FIGURE 134.—Shear flow water tunnel.

presence of a shear flow (x direction). A combined flow rate of 17.6 L/s is possible. The two flow-conditioned legs meet in an acrylic test section, providing optical access for Laser Doppler Velocimetry (LDV) and flow visualization of the interaction region. Recent studies with various material porosities showed the dependence of near-wall flow behavior on the pore diameter Reynolds number and revealed recirculation regions very near the wall for nonuniform pore-sized materials.

The duct flow air chamber (fig. 135) consists of two porous walls (top and bottom of the duct) with acrylic side walls. The duct height is variable, with a maximum separation of 50 cm. One of the ducts is blocked, allowing the duct flow to shift from wall injection flow to axial shear dominated flow over a length of 610 cm. This rig is capable of a Reynolds number (based on duct half height) of 2 × 10E5 that affords the study of flow transition from laminar to turbulent flow. The predicted theoretical axial velocity (Culick's profile) was confirmed by LDV measurements. Initial results have also shown the dependence of flow not only on the axial and injection Reynolds numbers, but also on the porous material characteristics (fig. 135).

In addition to the development of these rigs, other bench tests have been conducted. Velocity field surveys of pressurized porous cylinders without axial flow led to the discovery of a critical velocity that can be used to predict jetting behavior (Ramachandran, Heaman, and Smith). This experience has been combined with the test rigs described in this article to provide the technical expertise required for understanding the internal fluid dynamics of an SRM.

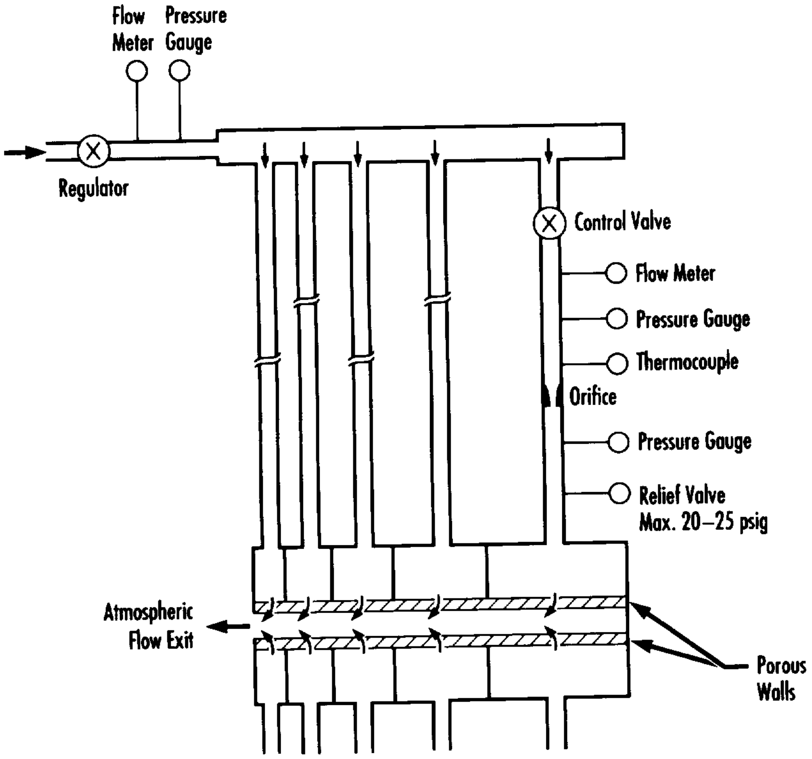

FIGURE 135.—Duct flow air chamber.

McDaniels, D. July 1993. Posttest Report of Test STM0008 (Porous Material Pressure Drop Characterization). NASA Memorandum ED34–20.

Ramachandran, N., Heaman, J., and Smith, A. 1992. An Experimental Study of the Fluid Mechanics Associated with Porous Walls. Presented at the 30th AIAA Aerospace Sciences Meeting, Reno, NV.

Yeh, Y.P. Quarterly Progress Report 4. Cold Flow Studies in Support of the ASRM Program. NAS8–38679.

Sponsor: Solid Propulsion Integrity Program

University Involvement: Universities Space Research Association

Commercial Involvement: Engineering Research Corporation

■

Verification of Analytical Methods: NASA Crack Analysis Code

Roderick Stallworth/ED25
205-544-7189

The NASA Crack Analysis Code (NASCRAC) is a state-of-the-art fracture mechanics analysis computer code. This research effort involves the verification and validation of the code and determination of the limits of applications, with the end result being the capability for more efficient fracture analysis. In the area of crack transitioning, the NASCRAC results were compared versus experimental testing. Figure 136 shows the fracture specimen with the prefatigue notch Figure 137 shows NASCRAC-predicted results and the results observed from testing. NASCRAC predicted that the crack would grow faster than was observed. Therefore, in this case NASCRAC proved to be conservative. For this case, the semi-elliptical surface flaw in a plate, NASCRAC predicted that the flaw would transition to a corner crack at 26,000 cycles, compared to observed experimental data that showed the crack growing to a corner flaw at 35,000 cycles. NASCRAC predicted transition from a corner flaw to a through flaw, and then failure at 73,000 cycles. Experimental results showed transitioning to a through crack at 138,000 cycles without failure occurring.

FIGURE 136.—Fracture specimen with prefatigue notch.

Analytical verification consists of comparing NASCRAC code results with literature sources and finite element model solutions. In the case of a surface crack in a solid cylinder, NASCRAC predicts a constant stress intensity (K) value across the crack front where 3–D finite element analysis showed the K values changing from the edge to the apex of the flaw.

Comparisons and results previously summarized help to quantify the limits of accuracy and application of the NASCRAC code. Verification and validation of the code is ongoing, with the end result being improved life prediction analysis capability.

Sponsor: Office of Aeronautics and Civil Technology

■

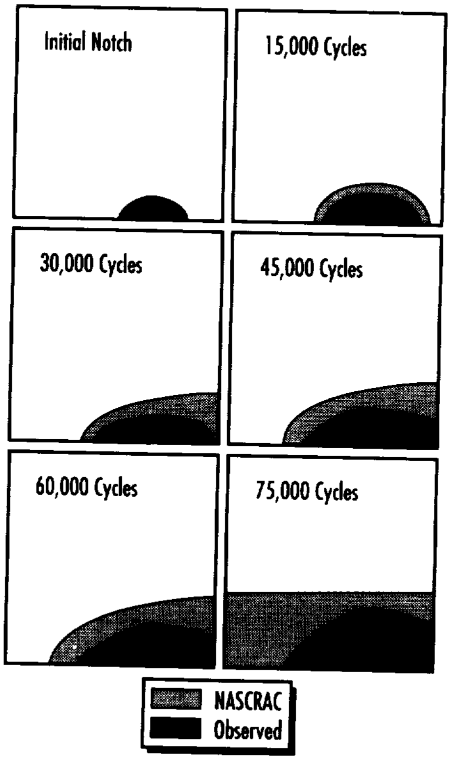

FIGURE 137.—NASCRAC-predicted results and results observed from testing.

Grid Optimization Tools for Complex Models

Gregory R. Swanson/ED25
205–544–7191

John M. Price/ED27
205–544–4645

Today, cost plays a decisive role in the design of aerospace structures. New computational tools are available, but are not being used routinely because of implementation costs. Probabilistic methods, large-scale design optimization of aerospace vehicle structures, structural sensitivity, and inverse design problems require repeated analysis. The practical implementation of these computational technologies depends on how much a single analysis costs. The goal is to seek the most cost-effective analysis.

An analysis can be divided into preprocessing, solution, and postprocessing tasks. In the past, much attention has been directed toward reducing the time required to obtain a solution. Today, most of the analysis time is spent in preprocessing and postprocessing activities. One of the most costly and time-consuming preprocessing tasks is the construction of the finite element model representing the physical problem. Grid quality directly affects the quality of the solution, but grid quality depends strongly upon the specific problem to be solved. Hence, a good grid for a specific load case becomes a poor grid for another load case. Current practice is to generate a grid for a specific problem. A more efficient approach would be to generate a generic grid and then to optimize it for a specific problem. The cost of preprocessing can be reduced through the development of software tools that allow the rapid modification and conditioning of finite element grids.

Under an SBIR Phase I contract, Alabama Research, Inc., of Huntsville, AL, is developing a grid optimization tool for complex structural models. The principle investigators are Mr. Lawrence Spradley, Dr. Rainald Lohner, and Mr. Jean Cabello. The objectives of this Phase I SBIR are to: (1) establish a practical strategy for improving grid quality, (2) show that optimization techniques can be used to improve the quality of finite element grids, (3) verify that this grid optimization strategy can be used with existing finite element models, and (4) demonstrate that this strategy can be used to reduce the cost (time and money) of analysis.

A practical strategy for grid optimization has been demonstrated that combines moving node methods, local remeshing, a simple user interface, and interfaces with an existing commercial finite element code (ANSYS44a). Spring and variational moving node methods are implemented. Both methods adjust existing interior grid points. The spring method treats each side of an element as a spring. These springs are relaxed in time, using explicit time-stepping, until an equilibrium of spring forces has been established. The variational moving node method optimizes the physical grid relative to a set of reference elements. An advancing front method is used for local remeshing. The user selects a region of the existing grid to be refined or coarsened.

Phase I has been successfully completed. The results, presented in a final report, indicate that the mesh optimization strategy has been demonstrated as a practical tool for reducing the cost of analysis.

Cabello, J.; Lohner, R.; and Jacquotte, O.P. June 3–6, 1991. A Variational Method for the Optimization of Directionally Stretched Elements Generated by the Advancing Front Method (AFM). The 3d International Conference on Numerical Grid Generation in CFD and Related Fields, Barcelona, Spain.

Lohner, R., and Parikh, P. 1989. Three-Dimensional Grid Generation by the Advancing Front Method. *International Journal of Numerical Methods in Fluids* 8:1135–49.

Spradley, L.W.; Lohner, R.; and Cabello, J. 1993. Grid Optimization Tools for Complex Structural Models. NASA AR–93–01.

Sponsor: Office of Advanced Concepts and Technology, Small Business Innovation Research Program

Commercial Involvement:
Alabama Research, Inc.

■

Combustion Chamber Analysis Code

P. Kevin Tucker/ED32
205-544-4185

The overall objective of this project was to develop a 3–D computational fluid dynamics code that could be used as an analysis tool in designing liquid propellant rocket engine thrust chambers. Until recently, thrust chambers were designed using method of characteristics (MOC) techniques and boundary layer approximations. In the last two decades, new prediction methodologies based on solutions of Navier-Stokes equations have evolved. Thus, CFD has become one of the viable tools for the design of rocket engines.

Three major activities of this project included: (1) development of a new generation REFLEQS CFD code with colocated (nonstaggered) formulation, (2) code verification and validation against high-fidelity benchmark data, and (3) computational studies supporting STME engine development. A state-of-the-art numerical methodology was developed by implementing nonstaggered grid arrangement, strong forms of the conservation equations expressed in terms of Cartesian velocity components, higher-order total variation diminishing (TVD)-type numerical schemes, and noniterative pressure-implicit split operator (PISO) solution procedure. Fundamental development, testing, and validation efforts were directed to the development of robust numerical techniques, as well as physical models. Parallel to the code development, continuous support was provided for analyzing flows and heat transfer problems during the STME development effort; e.g., National Launch System manifold study, STME nozzle cooling, vehicle base heating, and so forth.

The main features of the REFLEQS code are:

- Numerical Techniques
  - Finite-volume approach of solving Favre-averaged (steady state/transient) Navier-Stokes equations for compressible/incompressible flows
  - Cartesian, polar, and nonorthogonal body-fitted coordinates (BFC)
  - Colocated (nonstaggered) grid arrangement
  - Pressure-based methodologies such as semi-implicit method for pressure linked equations (SIMPLEC) and noniterative PISO algorithms for all flow speeds
  - Blockage technique for flows with internal solid objects
  - Four differencing schemes: upwind (first/second order), central (with damping terms), monotonic upstream schemes for conservation laws (MUSCL), and third-order Osher-Chakravarthy
  - Fully implicit and conservative formulation
  - Stationary and rotating coordinate systems
  - Symmetric whole field linear equation solvers and conjugate gradient solvers.
- Physical Models
  - Advanced turbulence models with boundary layer treatment (with standard/extended wall functions): (a) Standard k-e Model, (b) Extended k-e Model, (c) Multiple Time Scale Model, and (d) Low-Reynolds Number k-e Model
  - Instantaneous reaction (diffusion-controlled combustion) model
  - Equilibrium chemistry model (based on element potentials method)
  - One-step finite rate chemistry models and two-step reduced mechanism models for O_2/H_2 and O_2/hydrocarbon propellants

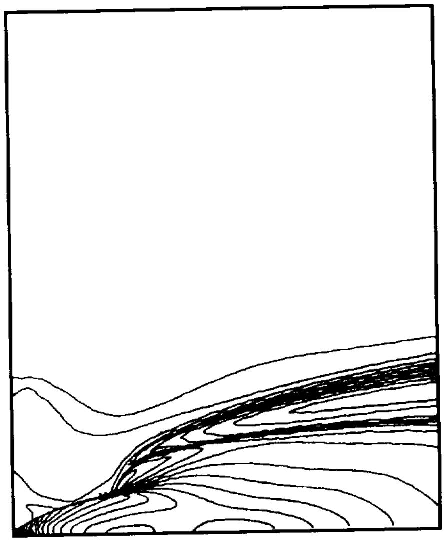

FIGURE 138.—Temperature distribution in the computational domain.

- Eulerian/Lagrangian, two-liquid evaporating reactive spray dynamics model with turbulent disperson effects
- Turbulence-combustion interaction models using the probability density function (pdf) method
- Discrete ordinate thermal radiation model.

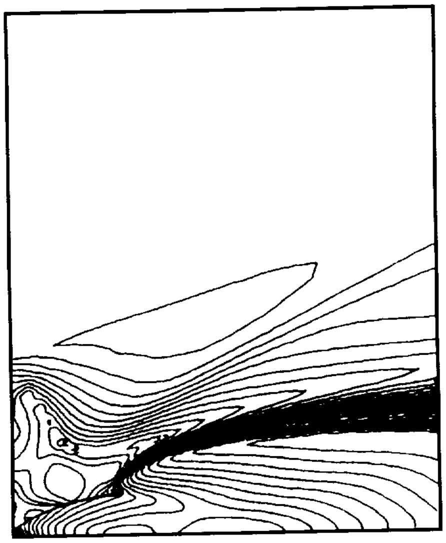

FIGURE 139.—Mach number distribution in the computational domain.

Results obtained from REFLEQS for the modeling of the flow in the base region of the space vehicle and STME nozzle are given in temperature and Mach number distributions, respectively (figs. 138 and 139).

Sponsor: Office of Advanced Concepts and Technology

Commercial Involvement: CFD Research Corporation

■

High-Accuracy CFD Methodology for Fast Flow Transients and Nonlinear Instability Phenomena

P. Kevin Tucker/ED32
205-544-4185

Analysis of nonlinear combustion instability problems requires the use of nonoscillatory, high-accuracy numerical algorithms. Development of numerical methods for the treatment of high-speed flows has received much attention during the last 10 yr. Methods are now available that are capable of simulating compressible flows in two and three dimensions in complex geometries. A comprehensive assessment study was performed under a Phase I SBIR project in which all advanced shock-capturing CFD techniques were implemented and tested for one-dimensional test problems, such as shock tube and resonant tube simulations. In the follow-up SBIR Phase II project, a modular CFD code Fast Transient Analyses (FASTRAN) was developed for 2–D and 3–D flows. The algorithms used in the code are of second-order accuracy in time and at least second-order accuracy in space, and include the flux-corrected transport (FCT), TVD, essentially nonoscillatory (ENO), and Godunov approaches.

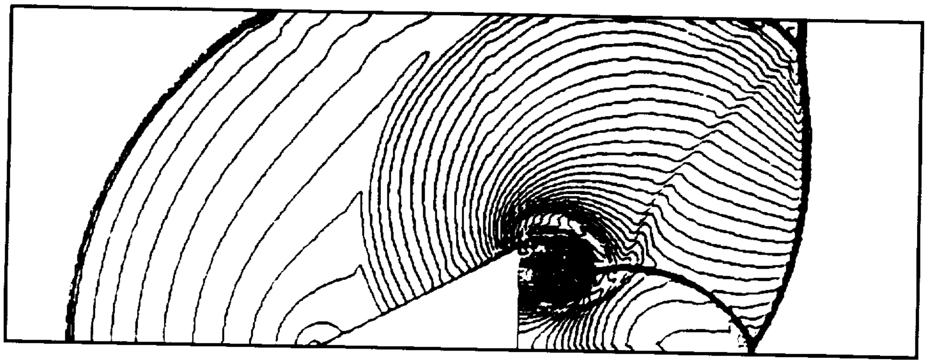

FIGURE 140.—Computed density contours for a Mach 1.3 shock wave.

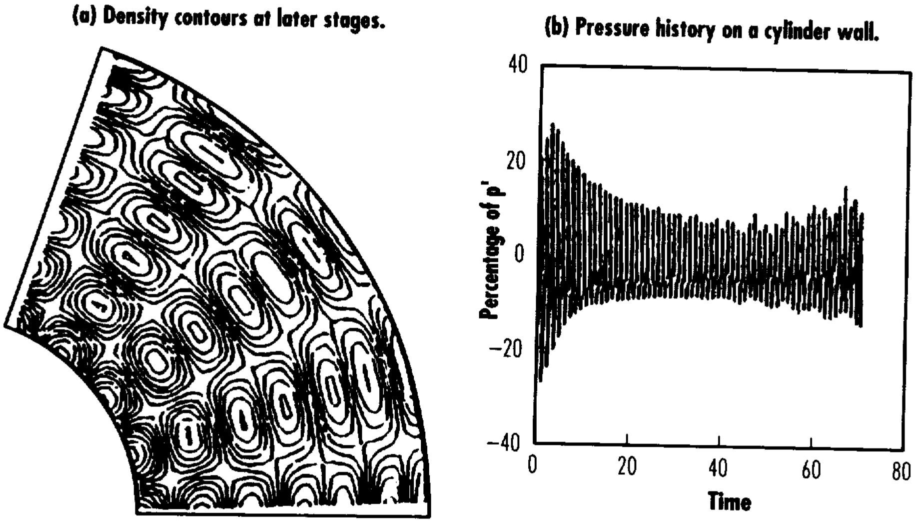

(a) Density contours at later stages.

(b) Pressure history on a cylinder wall.

FIGURE 141.—Wave propagation in an annular cylinder.

Results of simulations that have been performed using FASTRAN for purposes of algorithm comparison show the comparison of experimental shadowgraphs with computed density contours for shock diffraction over a 55-degree wedge (fig. 140), and the nonlinear resonant acoustics within a chamber cross section in the form of multiple wave reflections induced by an initially plane pressure wave (fig. 141). The scattering of a plane wave by the curved walls prevents formation of shocks and leads to formation of large amplitude, undissipative pressure waves. Existence of such pressure waves can have an adverse effect on performance of liquid rocket engines; and, therefore, it is essential that a numerical simulation can correctly account for their formation and behavior.

Sponsor: Office of Advanced Concepts and Technology, Small Business Innovation Research Program

Commercial Involvement: CFD Research Corporation

■

A General Computational Fluid Dynamics Code for All Mach Numbers

Ten See Wang/ED32
205–544–0503

An extension of the preconditioning techniques of Van Leer and Roe to 3–D inviscid flow with generalized chemistry has been developed and implemented in the CFD code General Aerodynamic Simulation Program (GASP). As a result, GASP is now capable of efficiently solving problems over the entire Mach number domain. A plot is presented for flow over a circular arc airfoil that demonstrates the savings achieved with preconditioning over a Mach number range of $0.1<M<1.0$ (fig. 142). The use of preconditioning for this Mach number range resulted in a 25- to 80-percent savings in central processing unit (CPU) time. Although not presented in this report, similar savings can also be observed for supersonic flow.

An $M=0.001$ flow was chosen to demonstrate the capability to predict incompressible flowfields through the use of preconditioning (fig. 143). Not only does GASP with preconditioning accurately predict the results (when compared to potential function results), it is able to converge the problem with the same efficiency as the compressible flow problems. To put this in perspective, without adding preconditioning techniques a density-based code is not capable of accurately or efficiently solving incompressible flow problems. The use of preconditioning makes it possible

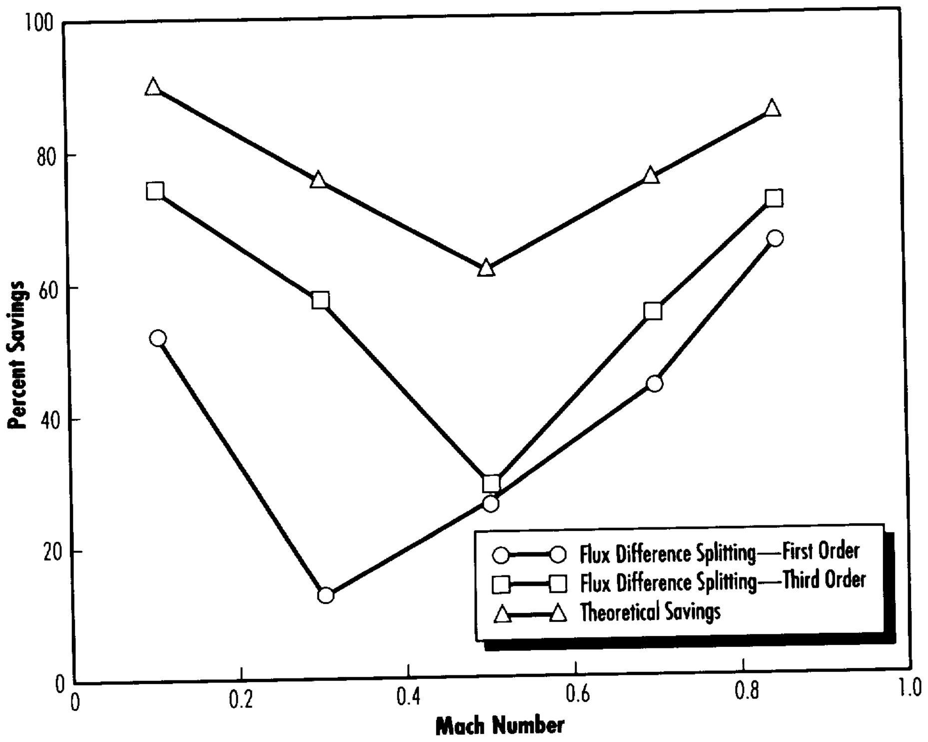

FIGURE 142.—CPU savings due to preconditioning for flow over a circular arc airfoil.

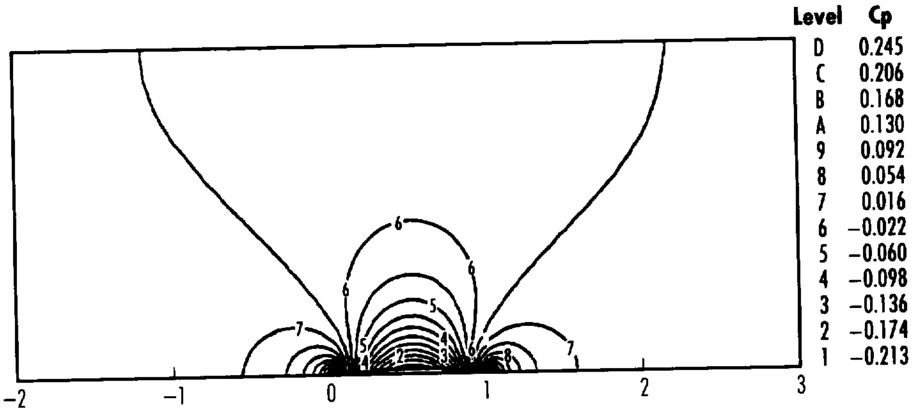

FIGURE 143.—Pressure contours for M_∞=0.001 flow over a circular arc airfoil.

to efficiently solve incompressible flow calculations without making assumptions that would prevent the flow solver from accurately predicting compressible flowfields.

In addition to providing incompressible capabilities, preconditioning has the added benefit of significantly improving the convergence rate for problems at all Mach numbers.

Sponsor: Office of Advanced Concepts and Technology, Small Business Innovation Research

Commercial Involvement: Aerosoft, Inc.

■

Fast Algorithm Combustion Modeling

Ten See Wang/ED32
205-544-0503

Numerical accuracy and computational efficiency of a time-accurate, pressure-based computational fluid dynamics (CFD) methodology, with physical models describing the finite-rate chemistry and spray evaporation and combustion, have been evaluated. An operator-splitting predictor, plus multiple correctors viscous flow solution method with 3–D multizone capability, has been employed for solving finite-rate chemistry and spray combustion-related problems.

Two approaches to solving a finite-rate chemistry system of equations, including a point implicit integration method and a penalty function method, have been incorporated and evaluated for various types of reacting flow problems (fig. 144). Steady state and transient test cases with premixed and/or diffusion flame flow conditions have been investigated to validate the accuracy and robustness of the physical models incorporated. Very efficient solution algorithms have been identified for steady state and transient flow applications. Models for the droplet breakup, evaporation, and combustion have also been implemented and tested using the same CFD model.

The results of benchmark evaluation cases have shown good comparisons between the computational predictions and the measured data for evaporating spray. Further development and testing work for the dense spray physical models using the method of volume of fluid, which has been planned for future study, will complete most of the requirement to make the present CFD combustion model to be a user-friendly, robust, accurate, and efficient engineering tool for the design and analysis of rocket engine combustion-related problems.

Sponsor: Office of Advanced Concepts and Technology, Small Business Innovation Research Program

Commercial Involvement: Engineering Science, Inc.

■

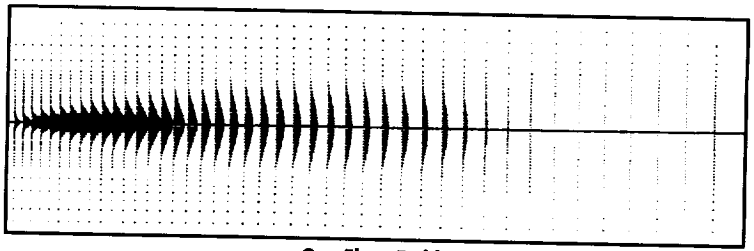

Gas Flow Field

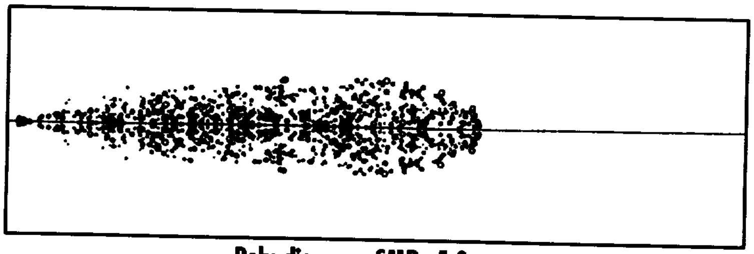

Poly-disperse, SMR=5.0 µm

FIGURE 144.—Solid-cone spray simulation at P=1.1 MPa and t=4.5 ms.

Hubble Space Telescope Pointing Controller Redesign

Mark S. Whorton/ED12
205-544-1435

Control system design for flexible space structures (large space structures (LSS)) is a challenging task that motivates today's intense research in modern robust control theory. The performance objectives of many spacecraft are quite ambitious, as is the case with the Hubble Space Telescope (HST), launched in April 1990. The HST is the most complex and advanced space observatory ever built. More than 1,900 observations of nearly 900 astronomical objects were carried out in the first 18 mo of operation. To achieve the science objectives, alignments of HST optical components must be maintained to within 1/400 mm and pointing stability must be maintained to within 0.007 arc seconds radian means per second (RMS) (or an angle less than the width of a dime seen from 300 km away).

After initial deployment, the HST experienced severe pointing disturbances due to thermal excitation of the solar arrays. Since this problem was first recognized, several control system redesigns have been carried out by the pointing control system team at MSFC and Lockheed Missiles and Space Company. These redesigned controllers have been uplinked to the spacecraft with increasing degrees of success.

Since this challenging controller design problem was representative of control/structure interaction (CSI) issues, an HST Pointing System Performance Enhancement Study was conducted. The results of this study were presented along with a tutorial paper in a session sponsored by MSFC at the 16th Annual American Astronautical Society Guidance and Control Conference held February 6–10, 1993, in Keystone, CO. The purpose of this study was to apply advanced modern control methodologies that have been developed under the MSFC CSI program funding to a challenging "real world" problem. Five principal investigators from four universities and one contractor were provided with detailed models, simulations, and flight data from the HST and asked to apply their control methodology to the pointing control system to explore possible performance enhancements. The solar panel thermal snap disturbances were to be minimized or eliminated in the resulting closed-loop system design.

The tutorial was an overwhelming success. The editor of the AIAA *Journal of Guidance, Control, and Dynamics* has requested that a special issue of the journal be compiled highlighting the study and its results.

The continued development of modern control theory, coupled with practical applications to challenging CSI problems, is an essential element in preparing the control community to design systems for the more ambitious spacecraft that are envisioned for future development.

Sharkey, J.; Nurre, G.; Beals, G.; and Nelson, J. August 1992. A Chronology of the On-Orbit Pointing Control System Changes on the Hubble Space Telescope and Associated Pointing Improvements. AIAA paper 92–4618

Sponsor: Office of Advanced Concepts and Technology

Commercial Involvement: Lockheed Missiles and Space Company

■

Quantifying Spacecraft Crew Safety From Orbital Debris Penetration

Joel E. Williamsen/ED52
205-544-7007

Pedro I. Rodriguez/ED52
205-544-7006

The penetration by meteoroids or orbital debris of small module volumes occupied by crew members in space, has often been associated in the past with immediate crew loss. However, with the advent of large, multichambered spacecraft designs, crew loss need not necessarily follow spacecraft penetration by orbital debris particles. A computer simulation tool, MSCSurv™, can be used to identify interior spacecraft designs, crew work and sleep schedules, and other factors that affect crew safety following the remote possibility of spacecraft penetration by orbital debris.

This program quantifies the hazards of decompression, injury, and spacecraft structural failure, given the input parameters of spacecraft geometry and shielding, crew location, strike location, and crew protection afforded by internal equipment. The hazard analysis and quantitative output from this safety study should be valuable to crewed spacecraft designers.

Sponsor: Space Station Program Office

■

Augmented Orbital Debris Shield Concepts for Space Station Critical Elements

Joel E. Williamsen/ED52
205-544-7007

Pedro I. Rodriguez/ED52
205-544-7006

With the recent increase in the orbital debris population, spacecraft in low-Earth orbit require advanced shield concepts employing maximum overall protection-to-weight ratios. Toward this goal, a team of MSFC and JSC engineers designed and tested a family of weight-efficient orbital debris shield concepts that could augment existing space station shields either on orbit or prior to launch (fig. 145).

Shield concepts generally employed advanced materials (such as Nextel™ AF52 and Kevlar™ 49 cloth) combined in layers to maximize protection capability. This study also minimized shield support structure weight within the framework of minimizing total shield system weight. Astronaut extravehicular activity (EVA) compatibility with orbitally augmented shields was verified through neutral buoyancy testing.

Shield concepts resulting from this study are broadly applicable to other government or industry spacecraft designs.

Sponsor: Space Station Program Office

■

Modified Baseline	Conformal, Augmented Baseline		
Option 1 (≈1 CM Protection Level)	**Option 2** (≈1 CM Protection Level)	**Option 3** (≈1.5 CM Protection Level)	**Option 4** (≈2 CM Protection Level)
.05 in 6061–T6 2.25 in Al Mesh Nextel AF62 Kevlar 710 2.25 in MLI .125 2219–T87	.05 in 6061–T6 8-in standoff 50 mil MLI 125 MLI Baseline (4.5-in pkg.)	.05 in 6061–T6 4 in Nextel 4 in Nextel 50 mil MLI 125 mil Baseline (4.5-in pkg.)	.05 in 6061–T6 4 in Nextel 4 in Nextel 50 mil MLI 125 mil Baseline (4.5-in pkg.)
Additional shield wt. 0.458 g/cm^2	Additional shield wt. 0.345 g/cm^2 ≈14.3 lb/shield	Additional shield wt. 0.665 g/cm^2 ≈34.5 lb/shield	Additional shield wt. 1.445 g/cm^2 ≈56.5 lb/shield

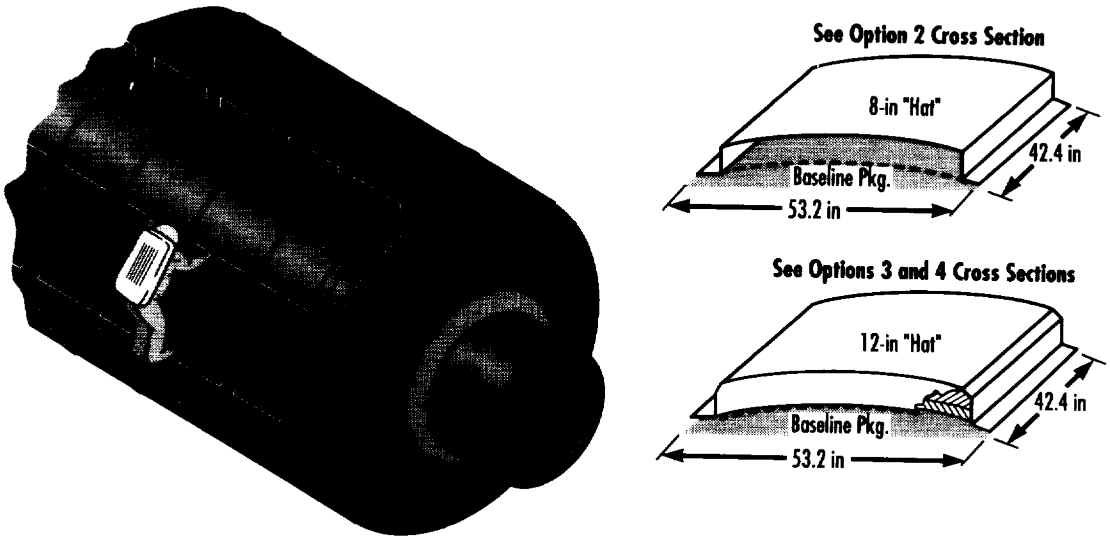

Figure 145.—Habitable module shield concept summary.

Systems Analysis and Integration

Autonomous Reconfigurable Navigation and Attitude Filter

James J. Lomas/EL58
205-544-8305

The integrated Global Positioning System/Conical Earth Sensor/Sun Sensor (GPS/CES/SS) system being developed under the SBIR Phase II Program supports the NASA spacecraft autonomy goals. This research addresses the spacecraft autonomy issue from two technical directions: (1) selection and integration of navigation and attitude sensors that are applicable to a wide variety of missions, and (2) incorporation of real-time software reconfiguration technology to address mission contingencies.

The complementary performance features of the GPS and CES/SS will provide continuous, accurate 3–D navigation and attitude estimates irrespective of the location of the spacecraft with respect to the Earth, Sun, and Moon. Another important mission benefit of integrating GPS with CES/SS (via the real-time reconfigurable software) is the resulting improvement in functional redundancy (fig. 146). The reason for this benefit is that the physical phenomena that limit the performance of one sensor do not affect the other sensor and that the failure of one sensor still permits the mission to continue, albeit at a degraded level. The use of reconfiguration software technology, in the proposed integration approach, "fuses" the solution from the two sensors and allows a smooth transition from one sensor operation to the other, depending on the mission timeline, geometry, and sensor health and status.

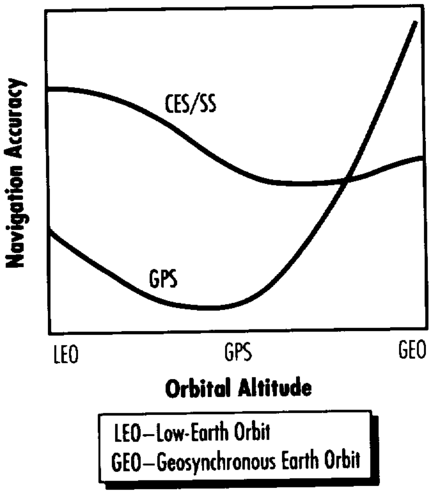

FIGURE 146.—Performance crossover characteristics.

This research will demonstrate the innovative sensor integration and software reconfiguration concepts through proof-of-concept demonstration hardware. The demonstration hardware will be a hardware-in-the-loop simulator that will be used to validate the performance benefits of the integrated, autonomous, reconfigurable GPS/CES/SS system.

Sponsor: Office of Advanced Concepts and Technology, Small Business Innovation Research Program

Commercial Involvement: Mayflower Communications Company, Inc.

■

Signal Analysis and Modeling System

James W. Parker/EL56
205-544-2340

The objectives of this effort are to design, develop, validate, demonstrate, document, and deliver a signal analysis and modeling system (SAMS) data base methodology and modeling tool for detailed modeling, simulation, analysis, technical management, and archival of spacecraft and/or experiment signal requirements and characteristics. This tool is capable of accommodating a minimum of 10,000 signals per program, which include both hardware and software measurements and commands that comprise the instrumentation program and command list (IPCL). SAMS consists of three models: (1) the data base development model, (2) the data base analysis model, and (3) the simulation model.

Many large systems, such as the space station, contain increasing numbers of complex systems and science instruments that demand an enormous increase in the number of signals. The signal requirements are driven by ambitious national and international science demands, the inclusion of a crew on board, the increased emphasis on safety, and high-tech, computer-driven flight hardware. A major responsibility of systems engineering is to manage and account for a signal complement expected to exceed 10,000 measurements and commands (scientific, operations, test, and housekeeping data and commands) over a duration of 10 yr or more. The complement of signals will change at regular intervals as additional facilities are attached during the buildup and as experiments are changed out or augmented. The large number of signals that must be analyzed and tracked cannot be efficiently handled by manual sorting and comparison of signal lists. Currently, no computer-automated tool exists that provides a specialized procedure of analyzing and managing complex signal lists.

The SAMS is a computerized systems engineering tool designed to archive and manage IPCL data bases, provide traceability of requirements and design changes throughout the program life, and develop selected subsets and data reports in support of trade studies, changes, growth, and evolution. The tool provides increased efficiency in monitoring and assessing data management systems requirements, verifying and making visible adequate systems resources such as signal bandwidth, memory, CPU throughput and margins, and other architectural compatibility with mission data models. The generalized functional requirements allocated for SAMS are as outlined below.

The data base development model provides a standard signal data base architecture and the tools needed to load, monitor, manage, and access this data base. This architecture is capable of including and accounting for every signal used to test, verify, and operate a system.

The data base analysis model consists of three integrated subtier models. The first is a data archival model that provides for requirements traceability and defines the computer memory data base architecture and software hierarchy associated with the manipulation, archival, and output of multiple IPCL data bases. The second is a data correlation model that performs the setup, selection, processing, generation, and storage of data for reports that compare IPCL data bases representing the configuration of a system at different stages of development, and reports the selectable differences in the data-base format. The third is the performance analysis model that provides the capability to statistically analyze the performance and validate the technical composition needed to support trend analysis and to ensure adequate margins in data-handling resources.

The simulation model is called the data systems dynamic simulator (DSDS) and allows the development of a data management system model that simulates the functions of the system on an events/timeline basis to provide statistical performance analysis and trades. These analyses and trades yield a prediction of the performance of the system and identify incompatibilities early in the design so that problems can be corrected at a minimum of cost.

The software is being developed by Stanford Telecommunications, Inc., in Seabrook, MD, under contract to MSFC, and is hosted on a UNIX-based Digital Equipment 5000 workstation. The software builds are nearly complete. Planned work remaining includes completing the documentation of the design of the software code, the users guide, and a step-by-step software configuration guide. In addition, the software functions will be validated and any bugs discovered during the validation will be corrected.

SAMS is currently in use and contains the space station signal data base. The software/hardware system validation will be performed as this program data base is manipulated.

The SAMS provides a computerized methodology for storing, sorting, and analyzing the signal requirements and characteristics. The tool greatly improves the efficiency of a systems engineer to perform analyses and trades, and to assess and ensure compatibility of data management system resources with data flow requirements.

Sponsor: Office of Space Systems Development

Commercial Involvement: Stanford Telecommunications, Inc.

■

Thermospheric Density Variations Simulator

B. Jeffrey Anderson/EL54
205-544-1661

For most engineering applications, NASA has adopted the Marshall Engineering Thermosphere model to define the total mass density at orbital altitudes. Total mass density determines the drag on the vehicle, thus the MET model is most often thought of in terms of orbital lifetime calculations. However, drag on the vehicle also can cause torques and affect the microgravity environment, so the model is also used to analyze control system designs and space-based experiment microgravity levels—applications where rapid variations in the environment are important. The shortest time scale variations within the MET model are those occurring every 3 h as a result of the geomagnetic storm index (a_p) variations. The only neutral density variations at orbital altitudes with time periods less than the orbital period are those associated with internal gravity waves; however, these had not been modeled until this study.

As the design of the space station experiment complement evolved, it became evident that design engineers needed more information about density variations with time periods on the order of a few minutes to a few hours, shorter than the MET model provided. This was because: (1) the basic design was significantly different than previous satellites, and (2) the microgravity experiment requirements were more stringent. A simulator—a computer code that would generate realistic data emulating density variations—was also required so the systems could be analytically exercised to ensure that they would meet the requirements.

This problem was complicated by the fact that the MET model is based on proxy input parameters that are imperfect representations of the parameters that actually control the thermosphere, and predictions of these proxy inputs are unavailable for future time periods, when the space station will be in orbit. The only predictions currently possible are for the 13-mo smoothed values of the input parameters and, until this effort, no research had addressed how they should be used to produce design-to-density values that would ensure reasonable risk levels without an over-design.

The aim of this activity was to develop: (1) statistics of the distributions of "actual" values of neutral densities about MET model-estimated values (derived from using 13-mo smoothed input parameters) so that program managers could determine risk levels associated with specific design-to-density values; (2) statistics of the perturbations with periods of 3 h or longer to determine both the frequency and duration of neutral density deviations greater than the design-to-values, for use in designing and testing the guidance, control, and navigation (GN&C) systems required to conduct microgravity experiments; and (3) a computer simulator to be used with the MET model that would produce perturbations in neutral density with periods from a few minutes to 3 h, for optimizing and verifying GN&C system software.

The historical solar activity indices were used to generate values of the minimum, mean, and maximum exospheric temperatures on the globe (which the MET model relates to density) for every 3-h period from 1947 through 1991. These temperatures were indexed to five different levels of solar activity—as defined by the 13-mo smoothed 10.7 cm solar radio noise flux values—and cumulative percent frequency (CPF) distributions were computed for each of the five different levels of solar activity (Smith et al. 1991). These CPF's can be used to select the proper risk levels in design trade studies.

These same CPF's were used to: (1) determine how frequently specified density levels were likely to be exceeded and their duration, and (2) establish files of input parameters that would generate 90-d density profiles for use in design and tests of both control systems and operations methods, to determine if mission requirements can be attained (Hickey and Smith 1992).

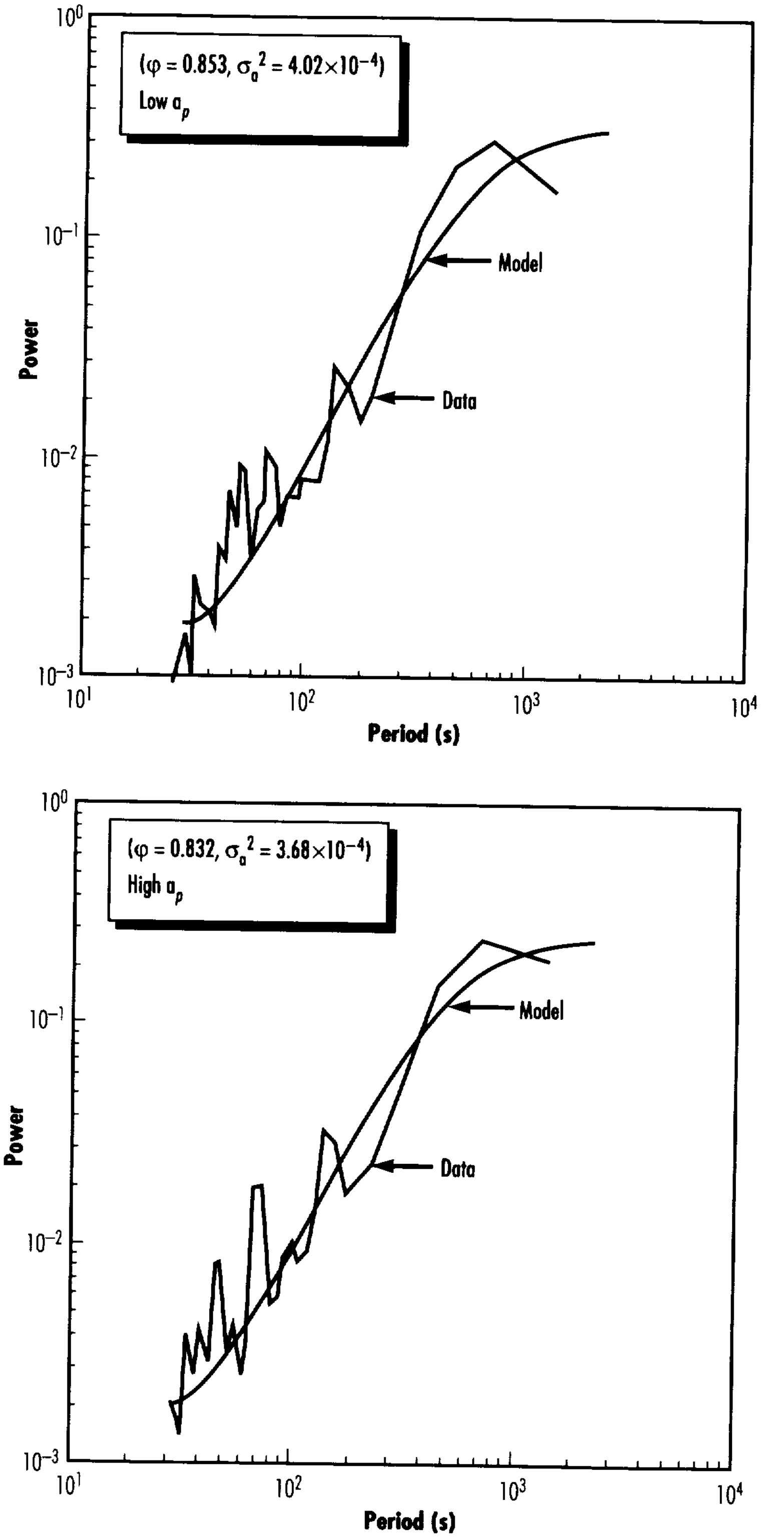

FIGURE 147.—First-order autoregression fit to average power spectral densities for low solar activity.

A definition and simulation method for the small-scale, within orbit, variations due to internal gravity waves was still needed. This led to the development of a wave model that can be used in conjunction with the MET model (Hickey 1993). Data from the Neutral Atmosphere Composition Experiment mass spectrometer on the Atmosphere Explorer-E satellite, flown from December 1976 to April 1981, was binned according to the 3 hourly a*p* and the 13-mo smoothed 10.7-cm flux (F_{13}) values. Four bins were produced, two for each of the a*p* and F_{13} values. After filtering the combined atomic oxygen and molecular nitrogen (the major constituents in the middle to upper thermosphere) density values, and then analyzing the spectral content using the Fast Fourier Transform technique, average power spectral densities were derived by averaging over at least one hundred such spectra for each of the four a*p*–F_{13} bins. The length of each individual data string from which these spectra were derived corresponds to about 15,000 km along the satellite track.

First and second order autoregression models were fit to the average power spectra density curves by utilizing and modifying the Maximum Entropy Method equations, from which the "best-fit" autoregression parameters were derived (fig. 147). The result is a subroutine that can be used with the MET model to provide realistic simulation of the minute-to-minute density variations a satellite will experience in low-Earth orbit. Model restrictions/limitations are: (1) F_{13} must be <210, (2) orbital altitude 250–500 km, (3) inclinations <30 degrees, (4) results show little dependence on a*p*. Additional work is needed to extend the simulation to high-inclination orbits.

Hickey, M.P. September 1993. Simulation of Small Scale Thermospheric Density Variations for Engineering Applications. PHY–93R044.

Hickey, M.P., and Smith, R.E. 1992. Ninety-Day Solar and Geomagnetic Activity. Input filed for Thermospheric Variation Simulation: Simulation Data Files/Release 2. PHY–92R103.

Smith, R.E.; Anderson, B.J.; and Catlett, K. 1991. The Marshall Thermosphere Model Atmosphere: Statistical Analysis Mode (MET–SAM). AIAA 91–0453.

Sponsor: Space Station Program Office

■

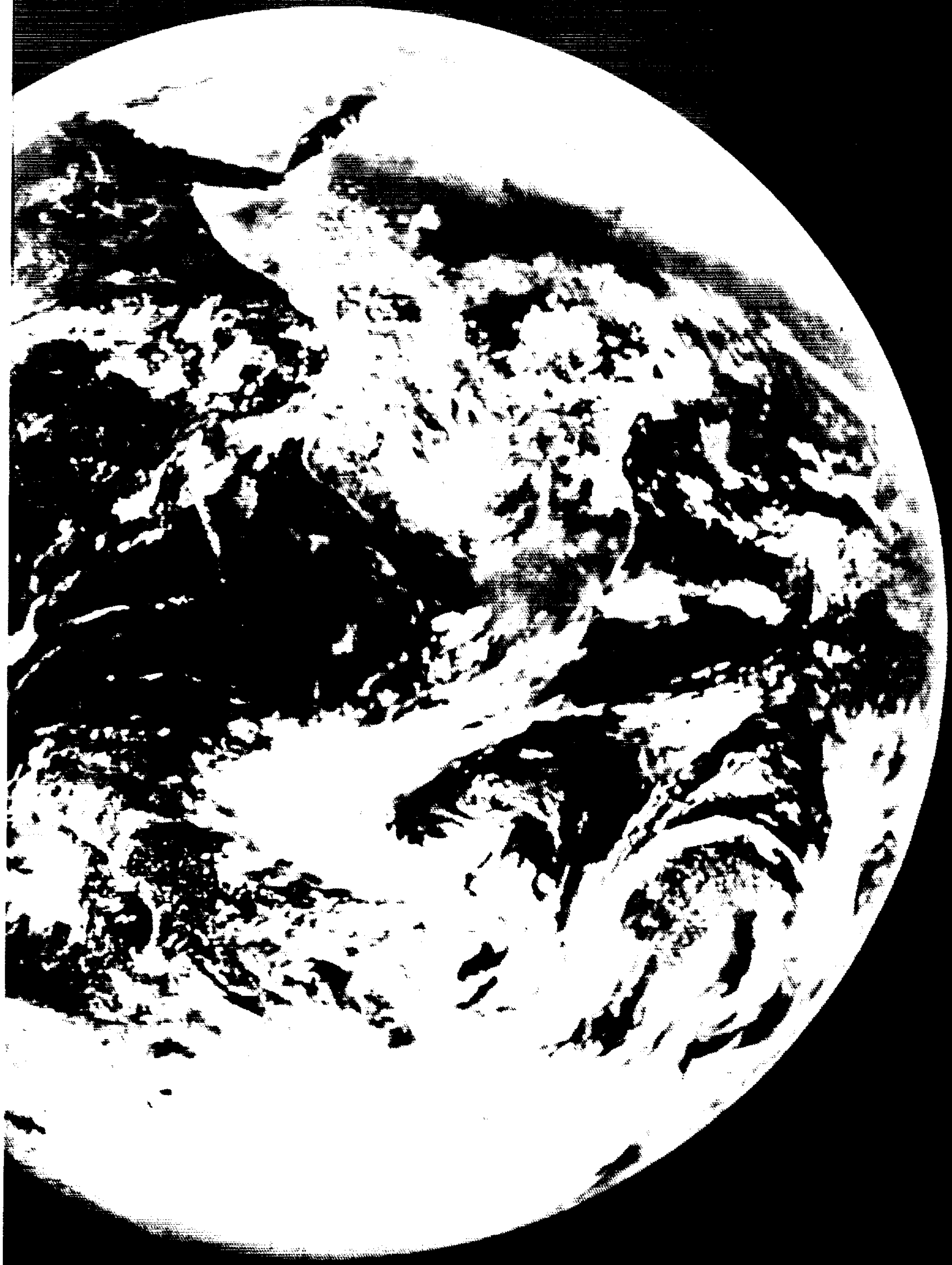

Technology Transfer

NASA-developed technology represents an immensely valuable bank of know-how on which American companies may draw to bring new products and processes to the world market, at more competitive prices because the technology has already been developed. MSFC is an active partner with many businesses, assisting in the transfer of Government-funded technology to the private sector. The following summary includes only a few selected examples of programs and instances of technology transfer during this past year and is not meant to be comprehensive.

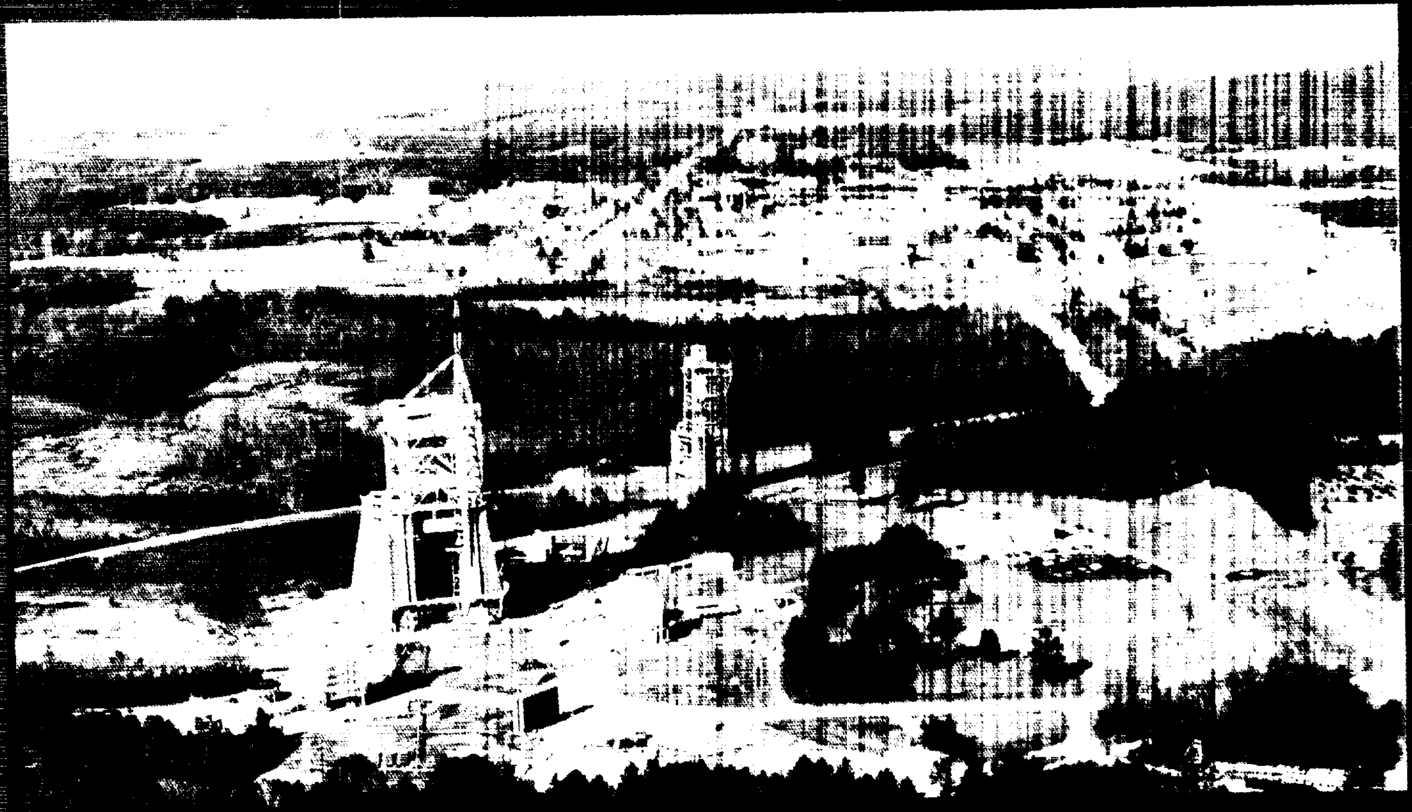

Marshall Space Flight Center offers more than just state-of-the-art laboratories and facilities—we offer a diverse experience base of people working to develop new ideas and solve problems using the extensive resources at hand.

MSFC Technology Transfer Opportunities and Successes

Technology transfer is recognized as a vital aspect of every MSFC organization. Businesses are encouraged to team with project offices, laboratories in the Science and Engineering Directorate, and offices in Program Development to adapt technologies for commercial use.

The major research and technology thrusts at MSFC include:

- Propulsion systems
- Structures and dynamics
- Materials and manufacturing processes
- Avionics and optical systems
- Automation and robotics
- Astronomy and astrophysics
- Earth science and applications
- Solar terrestrial physics
- Microgravity sciences.

Within these areas are numerous activities that are applicable to a wide range of the commercial sector. Industrial partners may transfer technology already developed by NASA toward new product development or process enhancement, or can team with MSFC in research to address an industry-identified need. Whatever the chosen method of technology transfer, the result is a major cost savings to industry. An excellent example of a technology transfer "enabler" mechanism is the Productivity Enhancement Complex operated by the Materials and Processes Laboratory at MSFC. Here, NASA and industry work together to develop new materials, processes, and assembly techniques.

Technology Utilization Program

The MSFC Technology Utilization (TU) Office accepts problem statements and technical inquiries from all facets of the private sector—from large and small industries, research organizations, academia, private entrepreneurs, and inventors.

The TU Office will consider requests for help with industrial or technical problems or for information in a specific technical field. Additionally, the TU Office will accept proposals for cooperative projects where the Government joins with private companies or organizations to modify space technology for other uses. Within these projects, proprietary information is honored and patent rights are negotiated to benefit the private-sector partner.

The TU Office has access to a nationwide technology transfer network. Some of the services available include:

- Computer Software Management and Information Center (COSMIC®) through which computer programs from NASA and other federal agencies are available for commercial use.

- National Technology Transfer Center (NTTC) and Regional Technology Transfer Centers (RTTC) which conduct technology searches and offer many other technology planning services.
- NASA inventions are available for licensing. The TU Office can direct you to patent counsels who can license NASA patents.
- *NASA Tech Briefs* magazine is free to qualified business, technical, and academic professionals. The TU Office can provide subscription information.
- NASA Center for Aerospace Information (CASI) provides technical support packages that contain additional information to supplement *NASA Tech Briefs*.
- Federal Laboratory Consortium (FLC) can be your doorway to more than 700 federal institutions and their technology expertise.

When NASA-developed technology is used for secondary applications, everyone benefits.

- A manufacturer of compressors experienced a high rejection rate of hermetically sealed units. MSFC assisted in applying automated, laser-guided welding.
- A Tennessee manufacturer of electric motors experienced production and quality control problems. An MSFC engineer suggested designs to improve the manufacturing process.

- A textile mill experienced frequent power surges that damaged equipment. MSFC led a team that solved the problem.
- MSFC developed expert systems to aid the design of superplastic forming have been sought by and supplied to industry.
- Environmental concerns lead to numerous requests for chlorofluorocarbon (CFC) substitutes. MSFC experience with substitutes for foaming, cleaning, and refrigeration products has been compiled in *Focus on the Future*, a publication available through the TU Office.
- One of the world's largest industrial computed tomography systems has been used by the logging, energy, and automotive industries for nondestructive inspection and testing.
- Water-jet stripping technology developed at MSFC has resulted in the formation of a private company that has sold units to the airline and other industries.
- MSFC expertise in field testing resulted in the successful design of test procedures to simulate take-off and landing pressures on composite aircraft ducting needed by a small Alabama firm.

Small Business Innovation Research Program

The Small Business Innovation Research (SBIR) program offers another avenue to access technology transfer. The SBIR program objectives include: stimulating technological innovation in the private sector, strengthening the role of small business concerns in meeting federal research and development needs, increasing commercial application of federally supported research results, and fostering and encouraging participation by socially and economically disadvantaged persons and women-owned small business in technological innovation.

One major national objective for the SBIR Program is broad commercial applications for the results of research and development (R&D) sponsored by the Federal government and performed by small businesses. Structured in three phases, the SBIR program uses Phase I to assess the technical feasibility of novel ideas proposed by small companies and Phase II to conduct R&D on the best concepts. Phase III, not funded by SBIR, is the utilization and/or commercialization phase.

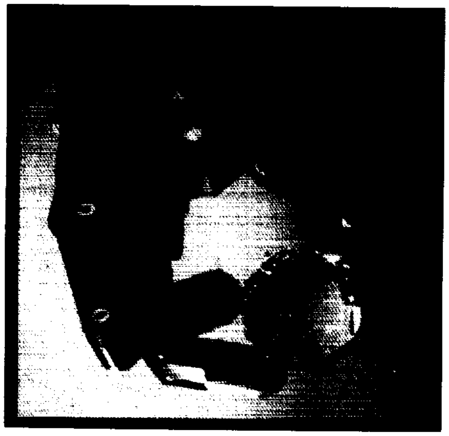

Some examples of products produced under the SBIR program include:

- "Dry-Film Lubricant for Bearings Using Ion Implantation," which has applications in orthopedic implants, aerospace bearings, and semiconductor wafers.
- "Control of Manual Data Entry Accuracy in Management and Engineering Information Systems," in business practice, can be used in tasks where at least 2,000 characters of data per day are manually entered into computers or reviewed by management for accuracy or sign-off. Other applications are education curriculum development and textbook publishing for unified keyboarding, in personnel management, and in psycho-medical research.
- "Tethered Satellite Video Monitoring System" applications include space flight hardware, remote monitoring and security systems, and environmental monitoring.

Publications available through the SBIR program are:

- Annual NASA SBIR solicitation for each program year, which specifies the application requirements and describes the R&D of interest to NASA for that particular program year.
- The NASA *SBIR Product Catalog* of products that have been produced as a result of projects supported under the SBIR program. This catalog assists small business firms in making the community aware of products emerging from their efforts in the SBIR program.
- *Abstracts of Phase I Projects* describes the objectives of projects placed under contract by the NASA SBIR program within a specific program year.
- The NASA *SBIR Composite List of Projects* includes all projects, both Phase I and Phase II, selected for funding by the SBIR program.

Small Business Innovation Research

Helen Stinson, SBIR Program Manager
Mail Stop ER41
Marshall Space Flight Center, AL 35812
205–544–7239

Technology Utilization

Ismail Akbay, Director
Mail Stop AT01
Marshall Space Flight Center, AL 35812
Toll Free: 1–800–437–5186
Commercial: 205–544–2223
FAX: 205–544–3151

Abbreviations and Acronyms

1N	synchronous
2N	two-times synchronous
2–D	two dimensional
2–DSRC	Two-Dimensional Stability Research Combustor
3–D	three dimensional
4–D	four dimensional
5–D	five dimensional
AAP	Advanced Automation Project
ABP	ambient back pressure
ac	alternating current
AFM	atomic force microscope
Ag	silver
AGC	automatic gain control
AGG	advanced gas generator
AGU	American Geophysical Union
AIAA	American Institute of Aeronautics and Astronautics
AIChE	American Institute of Chemical Engineers
AIP	Algorithm Intercomparison Project
Al_2O_3	gamma-aluminum oxide
AM	acrylic model
AMMC	advanced main combustion chamber
AMPR	Advanced Microwave Precipitation Radiometer
AMS	American Meteorological Society
AMU	atomic mass unit
AOCI	Advanced Ocean Color Imager
AP	ammonium perchlorate
Ap. J.	Astrophysics Journal
AS	ammonium sulfate
ASEE	American Society of Electrical Engineers
ASME	American Society of Mechanical Engineers
ATD	alternate turbopump development
ATLAS	Atmospheric Laboratory for Applications and Science
ATM	Apollo Telescope Mount
AU	astronomical units
AVHRR	Advanced Very High Resolution Radiometer
BATSE	Burst and Transient Source Experiment
BFC	body-fitted coordinates
BRDF	bidirectional reflectance distribution function
C–BIT	conical bond-in-tension
CAD	computer aided design
CAGI	computer aided grid interface
CAM	computer aided manufacturing
CaPE	Convective and Precipitation/Electrification
CASI	Center for Aerospace Information
CAVE	Computer Applications and Virtual Environments
CCD	charge coupled device
Cd-An-Te	cadmium zinc telluride
CDR	Critical Design Review
CDRA	Carbon Dioxide Removal Assembly
CERN	European Center for Nuclear Research
CES	Conical Earth Sensor
CFC	chlorofluorocarbon
CFD	computational fluid dynamics
CFM	cryogenic fluid management
CGF	Crystal Growth Furnace
CGRO	Compton Gamma Ray Observatory
CIRS	Composite Infrared Spectrometer
CMV	cloud motion vector
CO_2	carbon dioxide
COARE	coupled ocean-atmosphere response experiment
CORSS	Cylinder Optimization of Rings, Skin, and Stringers
COSMIC®	Computer Software Management and Information Center
CPF	cumulative percent frequency
CPU	central processing unit
CRF	cloud radiative forcing
CRIMS	Cometary Rendezvous Ion Mass Spectrometer
CSI	control/structure interaction
CSWA	conic section wave approximation
CTV	cargo transfer vehicle
Cu	copper
DAAC	Distributed Active Archive Center
DAM	doubly aluminized Mylar™
dc	direct current
DCR	Data Control Room
DE	Dynamics Explorer
DIF	Differential Ion Flux
DIFP	Differential Ion Flux Probe
DMSP	Defense Meteorological Satellite Program
DOT	Design Optimization Tool
DSDS	data systems dynamic simulator
DV	dependent variable
EB	electron beam
ECLSS	Environmental Control and Life Support System
ECMWF	European Center for Medium Range Weather Forecasts
EDCS	Electrostatic Deflection and Collimation System
ELV	expendable launch vehicle
ENO	essentially nonoscillatory

EOF	Empirical Orthogonal Functions
EOS	Earth Observing System
EOSDIS	Earth Observing System Data and Information System
EP	Earth Probe
EPA	Environmental Protection Agency
EPDM	ethylene propylene diene monomer
EPS	Electrical Power System
ESA	European Space Agency
ESCA	electron scanning analysis
ET	external tank
EUV	extreme ultraviolet
EVA	extravehicular activity
EST	Experiments Systems Test
EXVM	Experimental Vector Magnetograph
FARE	Fluid Acquisition and Resupply Experiment
FASTRAN	Fast Transient Analysis
FCT	flux-corrected transport
Fe	iron
FEL	free electron laser
FELES	front end load enabler schedule
FEREBA	Flexibility Enhanced Rolling Element Bearing Analysis
fgr	face growth rate
FLC	Federal Laboratory Consortium
FMLI	foam/multilayer insulation
FOV	field of view
FPC	forty-pound charge
FRACIE	Frequency Response of Admittance of Coaxial Injector Elements
FRAMES	fault recovery and management expert system
FRF	frequency response function
FTIR	Fourier Transform Infrared
ftp	file transfer protocol
g	gravity
G^3T	Generic Gas Generator Turbine
Ga-As	gallium arsenide
Ga-In-Sb	gallium indium antimonide
GASP	General Aerodynamic Simulation Program
GCIP	GEWEX Continental International Project
GEO	Geostationary Earth Observatory
GEOSIM	Geophysical fluid flow simulator
GEWEX	Global Energy and Water Cycle Experiment
GFFC	Geophysical Fluid Flow Cell
GGOT	Gas Generator Oxidizer Turbine
GGS	Global Geospace Science
GH_2	gaseous hydrogen
GHe	gaseous helium
GL	Graphics Language
GLOBE	Global Backscatter Experiment
GN&C	guidance, navigation, and control
GN_2	gaseous nitrogen
GOES	Geostationary Operational Environmental Satellite
GPIB	general purpose interface bus
GPS	Global Positioning System
GRAM	Global Reference Atmosphere Model
GSF	Goddard Space Flight Center
GTAW	gas tungsten arc welding
H	hydrogen
H^+	singly ionized hydrogen
H_2	slush hydrogen
H_2O	water
HBP	high back pressure
HCFC	hydrofluorocarbon
HCI	human-computer interface
HDF	hierarchial data format
He^+	singly ionized helium
He^{++}	doubly ionized helium
Hg-Cd-Te	mercurous cadmium telluride
Hg-Zn-Te	mercurous zinc telluride
HIFI	high-frequency intrinsic
HIV	human immunodeficiency virus
HNC	heavy nuclei collector
HOSC	Huntsville Operations Support Center
HPOT	high-pressure oxidizer turbine
HPOTP	high-pressure oxidizer turbopump
HST	Hubble Space Telescope
HTPB	hydrozy-terminated polybutadiene
IAU	International Astronomical Union
ICD	Interface Control Document
ICRC	International Cosmic Ray Conference
IFOV	instantaneous field of view
IGES	Initial Graphics Exchange Specification
IMI	Inner Magnetosphere Imager
In-Sb	indium antimonide
I/O	input/output
IPCL	instrumentation program and command list
IR	infrared
IR&D	independent research and development
IRTF	Infrared Telescope Facility
ISCCP	International Satellite Cloud Climatology Project
ISO	Imaging Spectrometric Observatory
ISO	Infrared Space Observatory
ITCZ	Intertropical Convergence Zone
IV	independent variables
JACEE	Japanese-American Cooperative Emulsion Experiment
JANNAF	joint Army, Navy, NASA, and Air Force
JPL	Jet Propulsion Laboratory
JSC	Johnson Space Center
KANT	knowledge and negotiation tool
KAO	Kuiper Airborne Observatory
KNOMAD	knowledge management and design
KO	knock on
KSC	Kennedy Space Center
LAD	liquid acquisition device
LAMPS	Limited Area Mesoscale Prediction System
LaRC	Langley Research Center

LAWS	Laser Atmospheric Wind Sounder
LDEF	Long Duration Exposure Facility
LDV	Laser Doppler Velocimetry
LED	light-emitting diode
LEIF	Low Energy Ion Facility
LEO	low-Earth orbit
LeRC	Lewis Research Center
LGS	laser glazed surface
LH_2	liquid hydrogen
lidar	light detection and ranging
LIS	Lightning Imaging Sensor
LLB	leak before burst
LLP	lowest level processor
LMS	Lightning Mapping Sensor
LN_2	liquid nitrogen
LO	lift-off
LON	local operating network
LOPC	laser optical particle counter
lox	liquid oxygen
LSS	large space structures
LTC	low thermal conductivity
LUTE	Lunar Ultraviolet Telescope Experiment
MACAWS	Multicenter Airborne Coherent Atmospheric Wind Sensor
MAMS	Multispectral Atmospheric Mapping Sensor
MAPO	magnetically actuated propellant orientation
MAS	MODIS–N Airborne Simulator
MCC	main combustion chamber
MET	Marshall Engineering Thermosphere
MHTB	Multipurpose Hydrogen Test-Bed
MLE	Mesosphere Lightning Experiment
MLI	multilayer insulation
MLT	magnetic local time
MLT	mesosphere/lower thermosphere
MNASA	modified NASA
Mo	molybdenum
MOC	method of characteristics
MSAD	Materials Science and Applications Division
MSA	Marshall sprayable ablator
MSFC	Marshall Space Flight Center
MSU	Microwave Sounding Unit
MSV	Mechanisms of Solar Variability
MTPE	Mission to Planet Earth
MUSCL	monotonic upstream schemes for conservation laws
N^+	singly ionized nitrogen
N^{++}	doubly ionized nitrogen
NaCl	sodium chloride
NASA	National Aeronautics and Space Administration
NASCRAC	NASA Crack Analysis Code
Nb	niobium
NCSA	National Center for Supercomputing Applications
NDE	nondestructive evaluation
NEΔT	noise equivalent change in temperature
NESDIS	National Environmental Satellite Data and Information Service
NGDC	National Geophysical Data Center
NIR	near infrared
NITM	nozzle insulation test motor
NLS	National Launch System
NMR	nuclear magnetic resonance
NOAA	National Oceanic and Atmospheric Administration
NTTC	National Technology Transfer Center
NURBS	nonuniform rational b-spline
O^+	singly ionized oxygen
O^{++}	doubly ionized oxygen
ODP	ozone depletion materials
OH	hydroxyl
OLS	Optical Linescan System
OMS	Orbital Maneuvering System
OPB	oxidizer preburner
OPS	optical pulse sensor
OSHA	Occupational Safety and Health Act
OSS	Office of Space Science
OTD	Optical Transient Detector
PAN	polyacrylonitrile
PAO	Public Affairs Office
PCA	Payload Control Area
PCTC	Payload Crew Training Complex
PDCU	power distribution control unit
pdf	probability density function
PDPA	phase Doppler particle analyzer
PGSC	Payload and General Support Computer
PHOT	Photopolarimeter Instrument
PI	principal investigator
PIP	Precipitation Intercomparison Project
PISO	pressure-implicit split operator
PLIF	planar laser-induced fluorescence
PLM	Pressurized Logistics Module
PMAD	power management and distribution
PMG	Plasma/Motor Generator
PMW	pulse width modulation
POCC	Payload Operations Control Center
POIC	Payload Operations Integration Center
PRM	Performance Reconciliation Model
QVS	quick-view system
R&D	research and development
Ra	Rayleigh number
radar	radio detection and ranging
RAM	random access memory
REFLEQS	reactive flow equation solver
RGA	residual gas analyzer
RIMS	Retarding Ion Mass Spectrometer
RMS	radian mean per second
RMS	Remote Manipulator System
ROPE	Research on Orbital Plasma Electrodynamics
RPA	retarding potential analyzers
RPC	remote power controllers
RSRM	redesigned solid rocket motor

RTEP	real-time event processor
RTG	radioisotope thermoelectric generator
RTLS	return-to-launch site
RTTC	Regional Technology Transfer Center
RWA	rectangular wave approximation
SAA	South Atlantic Anomaly
SAC	sample ampoule cartridge
SAE	Society of Automotive Engineers
SAFD	system for anomaly and failure detection
SAFiRE	Sensing and Force-Reflecting Exoskeleton
SAMPE	Society for Manufacturing and Process Engineering
SAMS	signal analysis and modeling system
SBIR	Small Business Innovation Research
SCN	succinonitrile
SCSI	Small Computer Systems Interface
SEDS	Small Expendable Deployer System
SEDSAT	Students for the Exploration and Development of Space Satellite
SELENE	Space Laser Energy
SFMD	Space Fluid Management Demonstration
SGI	Silicon Graphics, Inc.
Si	silicon
SiC	silicon carbide
SIMPLEC	semi-implicit method for pressure linked equations
SINDA	systems improve numerical differencing analyzer
SMEX	Small Explorer
SMM	Solar Maximum Mission
SMMR	Scanning Multichannel Microwave Radiometer
SNR	signal-to-noise ratio
SOFI	spray-on foam insulation
SOURCE	Solar Ultraviolet Radiation and Correlative Emissions
SPES	Soft Particle Energy Spectrometer
SPIE	Society of Photo-Optical Instrumentation Engineers
SPIP	Solid Propulsion Integrity Program
SPN	Shared Processing Network
SRM	solid rocket motor
SS	Sun Sensor
SSF	silicone seal material
SSM	space station module
SSM/I	Special Sensor Microwave Imager
SSME	space shuttle main engine
SSR	solid state recorder
SST	sea surface temperature
SSTO A/R	single-stage-to-orbit: air breathing plus rocket
SSTO R	single-stage-to-orbit: all rocket
SSTO	single-stage-to-orbit
STME	space transportation main engine
STORM–FEST	Storm-Scale Operations and Research Meteorology-Fronts Experiment System
TA	antenna temperature
Ta	tantalum
TABI	tailored advanced flexible blanket insulation
TB	brightness temperature
TCS	thermal control system
TDK	two-dimensional kinetics
THC	Temperature and Humidity Control
TIDE	Thermal Ion Dynamics Experiment
TIMED	Thermosphere, Ionosphere, Mesosphere, Electro-Dynamics
TIROS	Television Infrared Operations Satellite
TMS	Thematic Mapping Sensor
TOF	time of flight
TOGA	Tropical Ocean Global Atmosphere
TOVS	TIROS Operational Vertical Sounder
TPS	thermal protection system
TQCM	temperature-controlled quartz crystal microbalances
TRL	technology readiness level
TRMM	Tropical Rainfall Measuring Mission
TSS	Tethered Satellite System
TSTO A/R	two-stage-to-orbit: air breathing plus rocket
TSTO	two-stage-to-orbit
TTA	turbine test article
TTB	Technology Test-Bed
TTE	turbine test equipment
TU	Technology Utilization
TUFI	toughened rigid ceramic insulation
TVC	thrust vector control
TVD	total variation diminishing
TVS	thermodynamic vent system
TWA	triangular wave approximation
U of I	University of Illinois
UARS	Upper Atmosphere Research Satellite
ULC	Unpressurized Logistics Carrier
USBI	United Space Boosters, Inc.
USI	USBI Sprayable Insulator
USML	United States Microgravity Laboratory
UTSI	University of Tennessee Space Institute
UV	ultraviolet
UVI	Ultraviolet Imager
VAS	visible infrared spin-scan radiometer atmospheric sounder
VDCR	Virtual Data Control Room
VI	virtual instrument
VPOCC	Virtual Payload Operations Control Center
VPPA	variable polarity plasma arc
VPS	vacuum plasma spraying
VR	virtual reality
VW	virtual world
W	tungsten
WMO	World Meteorological Organization
XTM	X-ray Transmission Microscope
Zr	zirconium

Index of Contacts

Index of Key Words

About Key Words

To broaden the availability of this report, the text is placed on-line on the FEDIX Technology Information System computer, which can be easily accessed by phone and terminal. This enhances the opportunities for technology transfer to the private sector.

For further information about FEDIX, contact:

Office of the Associate Director for Science
Mail Stop DS01
Marshall Space Flight Center, AL 35812
205–544–3033